TEL AVIV UNIVERSITY אוניברסיטת תל-אביב

RAYMOND AND BEVERLY SACKLER
FACULTY OF EXACT SCIENCES
GEOPHYSICS AND PLANETARY SCIENCES

הפקולטה למדעים מדוייקים
ע״ש ריימונד ובברלי סאקלר
המחלקה לגיאופיזיקה ומדעים פלנטאריים

Thermal and Structural Evolution of Small Bodies in the Solar System

Thesis submitted for the degree *Doctor of Philosophy*

by

Gal Sarid

This work was carried out under the supervision of

Prof. Dina Prialnik

Dept. of Geophysics and Planetary Sciences

Submitted to the Senate of Tel Aviv University

October 2009

Thermal and Structural Evolution of Small Bodies in the Solar System

By Gal Sarid

October 2009

Abstract

The designation "small bodies" in Solar System studies refers to astronomical bodies smaller than planets, for which the Sun is the main gravitational attractor. The diversity in the dynamical properties of these bodies may be a result of the specific accretion locations of each class of bodies, or their subsequent orbital evolution, mainly due to gravitational perturbations by the planets. There are many dynamical classes of small bodies, but the ones that share a common dynamical evolution scheme, or a widely accepted chain of origin, are Comets, Centaurs and trans-Neptunian objects.

In the work presented here we followed the thermo-chemical evolution of the relevant small bodies. This was done through the use of a sophisticated 1-D or quasi-3D numerical code, which solves the heat transfer and flow equations for a porous multi-component object, with full consideration of interior and exterior boundary conditions.

We applied this general thermal evolution code to the modeling of several specific trans-Neptunian objects, which represent a sample of the various physical characteristics attributed to this population. Results indicate a general trend of more compacted, thermally-processed and volatile-depleted interiors, as the size and density of the object is larger. However, in the sub-surface layers, a mixed and intricate composition of volatile compounds can be found. An interesting and notable result is the viable and relatively robust occurrence of conditions for liquid water in the deep interior of the larger objects.

Another application of the thermal evolution code is to the modeling of several specific Centaurs. We examined the effect of initial conditions on the thermal evolution on different unstable orbits. For this purpose, we set various scenarios for the succession of Centaur origin and emplacement – either as 'a chip of the old block' of larger trans-Neptunian objects, which scattered inwards, or as a 'rolling stone' from out beyond Neptune, which leisurely diffused inwards. The end results of these sets of simulations should provide insight into the current internal state of Centaurs and the initial configurations of evolving Jupiter-family comet nuclei.

The dynamical state of several specific Centaur objects is also examined, through N-body integrations. Since these objects are highly prone to gravitational interactions with the outer planets, their orbits are highly chaotic. As such, characterizing their orbital stability is a challenging task. We show some representative results of this effort here, and determine several global orbital evolution properties for each object.

We conclude with a detailed examination, through quasi-3D modeling, of two typical Jupiter-family comets. In the case of 9P/Tempel 1, we study the internal evolution, activity and impact modeling. In the case of 22P/Kopff, we study the dust activity and its connection to internal thermal evolution. The outstanding feature emerging from the quasi-3D thermal simulations is that even at relatively high cometocentric latitudes the nucleus will develop a complex pattern of volatile stratification with depth.

We suggest that our detailed results of the thermal processing, which altered the internal configurations of trans-Neptunian objects, Centaurs and Jupiter-family comets, provide some insight into both the history of large ice-rock planetesimals and the prenatal constitution of cometary material.

Acknowledgments

The work presented here is a product of the last six years of my main occupation – research in planetary science, and specifically into cometary science. Thus, it is only natural and obvious to acknowledge ones advisor. However, as it turns out, I went looking for an advisor and found one of the most special people I imagine I'll ever meet (and one of the foremost experts in the field). Dina, for your kindness, your attention, your patience, your caring, your guidance and imparting of both 'know-how' and 'know-when', there is not enough I can say. So a simple 'thank you' will have to suffice.

Since this is the more personal part of the thesis, I will try to keep it simple. This is a necessary constrain, as this part is not meant to be the largest in bulk. So, i would just like to say, to all of you out there (you know who I mean), if you are reading this: I care for you and I appreciate you. Some more than others, naturally.

I would like to mention by name, those closest to me, who helped me the most, mentally and otherwise, during this long period. And the nominees are: Ofer, David, Sharon, Elinor, Shachar and Yonit. Friends, the above statement refers to you especially!

It is a pleasure to thank several faculty members who helped me along the way with a kind word, a logistic nudge, a rewarding grade, or some professional advice. Thank you Eyal, Morris, Attay, Peter and Shay.

Almost last, but certainly not least is my family. My parents, who gave me the freedom to pursue my ambitions and desires and the confidence and insight to know how to use it. Oh, and also endless love to make all the freedom and confidence worth it. My sisters, who supported my endevours, sometimes quietly and sometimes with a bang, but always with appreciation and love. Don't think it went unnoticed. I love you, mom. I love you, dad. I love you, Hadar and Adva.

To my grandparents, passed and living, thank you for nurturing me and making me feel like a unique grandson.

If I forgot someone, and most chances are that I did, don't be offended. As you know me, I'm doing this at the last moment and I am probably preoccupied. Also, I wanted to keep it short.

And then there is, of course, Yael. What can I say to avoid a cliche? You are ny sunshine, my only sunshine, you make me happy when skies are gray. I am only ecstatically joyful that we spend our time together.

I love you, buba!

Contents

Abstract **I**

Acknowledgments **III**

List of Figures **XI**

List of Tables **XIII**

1 Introduction **1**

1.1 Sketch of This Work . . . 1

1.2 The Classes Of Small Bodies . . . 2

1.2.1 The Cometary Population . . . 2

1.2.2 The Centaur Population . . . 3

1.2.3 The Trans-Neptunian Population . . . 7

1.3 The Dynamical Scheme Of Small Bodies . . . 10

1.3.1 Cometary Taxonomy . . . 10

1.3.2 The Link Between TNOs And JFCs . . . 11

1.3.3 The Structure And History Of The Trans-Neptunian Region . . . 12

1.3.4 Number Estimates For The Dynamical Classes . . . 15

1.3.5 The Size-Distribution Of The TNOs Population . . . 16

2 Methodology **17**

2.1 Governing Equations . . . 17

2.2 Numerical Scheme . . . 21

2.3 Porous Structure and Composition . . . 21

2.4 Pore-Size Distribution . . . 24

2.5 Radioactive Heat Sources . . . 27

2.6 Self Gravity . . . 29

2.7 Equation of State . . . 33

2.7.1 Birch-Murnaghan EOS . . . 33

2.7.2 Vinet EOS . . . 36

2.7.3 Stability Analysis . . . 37

2.8 A “Thermal” Impact . . . 40

3 Evolution of Trans-Neptunian Objects 43
3.1 The Inner-Workings of Trans-Neptunian Objects 43
3.1.1 Introduction 43
3.1.2 Model assumptions and choice of key parameters 44
3.1.3 Results of Internal Evolution 46
3.1.4 Re-distribution of Pore Sizes 56
3.1.5 Effect of the Equation of State 58
3.1.6 Effect of Various Radioactive Species 61
3.1.7 Possible Liquid Water 63
3.2 End-States of Some Evolved Objects 67
3.2.1 (50000) Quaoar - Extended Evolution 67
3.2.2 1992 QB_1 and 1998 WW_{31} – Smaller and Colder Objects 72

4 Evolution of Centaurs 79
4.1 Dynamics Within the Centaur Population 79
4.1.1 Introduction 79
4.1.2 Integration Scheme 83
4.1.3 Initial Configuration 85
4.1.4 Summary of Results 90
4.2 Thermal Evolution In the Region of the Outer Planets 103
4.2.1 Introduction 103
4.2.2 Initial Parameters 103
4.2.3 Initial State Scenarios – The Fragment and Immigrant Cases 107
4.2.4 Thermal Evolution As A TNO Fragment 108
4.2.5 Thermal Evolution As A TNO Immigrant 114

5 Evolution of Jupiter-Family Comets 119
5.1 Thermal Evolution and Activity of Comet 9P/Tempel 1 and Simulation of a Deep Impact 119
5.1.1 Introduction 119
5.1.2 Some Ground-Based Observations 120
5.1.3 Numerical Model and Initial Parameters 122
5.1.4 Results of Evolutionary Calculations 125

5.1.5 Simulation of a Thermal Impact 131
5.2 Internally-Driven Dust Activity of Comet 22P/Kopff 135
5.2.1 Introduction 135
5.2.2 Dust-Dynamical Modeling Results 136
5.2.3 Numerical Model and Initial Parameters 138
5.2.4 Thermal Evolution Modeling Results 141

6 Summary and Conclusions 147

Bibliography 153

List of Figures

1.1 Distribution of JFCs, HFCs and Centaurs in the orbital phase space of a vs. e. 5
1.2 Distribution of JFCs, HFCs and Centaurs in the orbital phase space of e vs. i. 6
1.3 Distribution of TNOs in the orbital phase space of a vs. e. 8
1.4 Distribution of TNOs in the orbital phase space of e vs. i. 9
1.5 Distribution of KBOs in the orbital phase space of a vs. e. 13

2.1 Relation between ρ, Ψ and X_{dust}/X_{ice}. 23
2.2 Correction factor for the SVR parameter. 26
2.3 Relative importance of hydrostatic pressure for the solid matrix of a cometary object. 30
2.4 Hydrostatic profiles for a 500 km object ($\rho = 1.5g\ cm^{-3}$) 34
2.5 Hydrostatic profiles for a 1000 km object ($\rho = 2.5g\ cm^{-3}$) 35
2.6 Magnitude of the exponential term in the Vinet EOS. 37
2.7 Comparison of B-M and Vinet equation-of-state. 39

3.1 Pressure profiles for the solid matrix of four modeled TNOs. 48
3.2 Evolution of internal profiles for models of QB1, Varuna and Quaoar. 50
3.3 Depth profile of temperature and porosity for a model of Eris. 55
3.4 Profiles of permeability and surface-to-volume ratio for a model of Quaoar. 58
3.5 Comparison of the effect of the EOS on internal temperature distribution. . 59
3.6 Comparison of the effect of the EOS on internal porosity distribution. . . . 60
3.7 Evolution of T_{max}, T_c and T_s, for different radioactive sources. 62
3.8 Thermodynamic conditions of H_2O phases for the modeled TNOs. 64
3.9 Liquid phase saturation map for the modeled TNOs. 66
3.10 Thermal, compositional and structural profiles of the outer layers, for a model of Quaoar. 70
3.11 End-state configuration for long-term evolution of a 1998 WW31 model . . 75
3.12 End-state configuration for long-term evolution of a 1992 QB1 model . . . 77

4.1 Ecliptic plane projection of the Orbits of five sample Centaurs 81
4.2 Orbital phase space distribution of known Centaurs 86

4.3 Comparison of orbital stability of Chiron's clone population, for different planetary distances 88
4.4 Comparison of orbital elements evolution for an Asbolus clone, for different planetary distances 89
4.5 Cumulative distribution function of the lifetimes of Centaur objects 91
4.6 Snapshots of the evolution of the clone population of 10199 Chariklo 94
4.7 Snapshots of the evolution of the clone population of 8405 Asbolus 94
4.8 Evolution of orbital elements for 10199 Chariklo clone 163 96
4.9 Evolution of orbital elements for Chariklo clone 251 97
4.10 Evolution of orbital elements for Chariklo clone 399 98
4.11 Mean value of eccentricity, for the clone populations of each Centaur object 99
4.12 Mean value of inclination, for the clone populations of each Centaur object 100
4.13 Temperature profile for 8405 Asbolus. 110
4.14 Internal profiles of structure and composition for 8405 Asbolus. 110
4.15 Internal profiles of structure and composition for 5145 Pholus. 112
4.16 Internal profiles of structure and composition for 32532 Thereus. 113
4.17 Temperature profile for 10199 Chariklo. 114
4.18 Internal profiles of structure and composition for 10199 Chariklo. 115
4.19 Comparison of final depth distributions of temperature, volatile ice and amorphous ice for immigrant TNO case. 116
4.20 Comparison of final depth distributions of temperature and volatile ice abundance for immigrant TNO case. 117

5.1 Composite images of comet 9P/Tempel 1. 121
5.2 Finson-Probstein contour fits to 9P/Tempel 1 composite images. 121
5.3 Comparison of observations and model results for initial model fitting of 9P/Tempel 1. 125
5.4 Dust production rate for a fitted 9P/Tempel 1 model. 126
5.5 Evolution of internal temperature and amorphous ice abundance for a model of 9P/Tempel 1. 128
5.6 Evolution of production rates and surface temperature for a model of 9P/Tempel 1. 130

5.7 Quasi-3D surface maps of simulated H_2O and dust production rates, along the orbit of 9P/Tempel 1. 131
5.8 Results of a thermal impact simulation of a model of 9P/Tempel 1. 133
5.9 Dust modeling contour profiles for 22P/Kopff. 137
5.10 Dust production rates around perihelion, for different models of 22P/Kopff. 142
5.11 Internal temperature, porosity and ice abundance distributions for several Kopff models, pre-perihelion. 143

List of Tables

1.1 Orbital elements of the known active Centaurs 6
1.2 Mean orbital elements of TN populations 9

2.1 Thermodynamic coefficients of various volatile compounds 19
2.2 Radioactive isotope characteristics 28

3.1 Known properties of the modeled TNOs 44
3.2 Initial physical parameters for the modeled TNOs 45
3.3 Common input physics parameters for all models of TNOs 46
3.4 Results of model calculations for modeled TNOs - end of evolution (100 Myr) 49
3.5 Bulk composition (by mass fractions), for an extended model of Quaoar . . 69
3.6 Initial model parameters for TNO models 73
3.7 Common input physics parameters for TNO models 74

4.1 Orbital elements of Centaur objects 80
4.2 Orbital classification of Centaur objects 83
4.3 Lifetimes (in Myr) and statistics for the different Centaur objects 92
4.4 Last planetary encounters for each Centaur object 93
4.5 Known parameters for each of the modeled Centaurs 104
4.6 Common input physics parameters for all models of Centaurs 106
4.7 Initial internal configurations for the fragment and immigrant cases 109

5.1 Finson-Probstein model fit to 9P/Tempel 1 images 122
5.2 Orbital elements and nucleus properties for 9P/Tempel 1 123
5.3 Initial compositions for 9P/Tempel 1 evolution models. 124
5.4 Properties of the simulated impact for a model of 9P/Tempel 1. 132
5.5 Finson-Probstein model fit to 1992 Kopff observations 138
5.6 Orbital elements and nucleus properties for 22P/Kopff 140
5.7 Variants of the basic thermal model of 22P/Kopff 140

1 Introduction

1.1 Sketch of This Work

In this work we present several studies into the thermal, compositional and structural properties of small bodies, as they evolve from various initial states.

In the following sections, we present an introduction to the classes of Comets, Centuars and TNOs, and the overall picture, which defines their interrelations and histories.

Chapter 2 describes the equations of the model we use to simulate the thermal evolution of a cometary-like object and the physical assumptions that provide the crucial input to the model, to relate it with observations.

Chapter 3 describes the study of the thermal evolution of several specific TNOs. They are followed from initial homogeneous states, until further internal variations are minor. We also detail the end states of various-sized KBOs, pertinent to their current configurations, as thermally-processed objects.

Chapter 4 describes two studies into the intrinsic population of Centaurs. The first deals with the orbital evolution of several specific Centaurs and their dynamical properties. The second describes thermal evolution models of several Centaur objects, assuming different initial conditions. These are due to different histories, prior to their inclusion in the dynamical population of Centaurs.

Chapter 5 presents studies of two sample JFCs. These examples should be typical of this cometary population and were chosen as representing characteristic properties. Comet 9P/Temple 1 is evolved and its activity followed, as it experiences the effect of a collision onto its surface. Comet 22P/Kopff is evolved through various initial models, in order to try and explain its peculiar dust activity near perihelion, as previously observed.

1.2 The Classes Of Small Bodies

In this section, a brief presentation will be given on the three main classes of objects, which this research is concerned with. The main characteristics of comets, Centaurs and TNOs are described, in terms of their origin, dynamics, structure and composition, and presumed evolution. Each of these classes merits an evolutionary study of its thermal and structural phases on its own, in order to better understand what we learn from ongoing observations and discoveries.

1.2.1 The Cometary Population

Comets are ice-rich small bodies, that orbit the Sun and become prominent when heat from the Sun causes their trapped volatiles to sublimate. These bodies have characteristic sizes of 1-15 km, and they consist of varying, yet to be confirmed, proportions of non-volatile solids (silicates, refractory organics) and volatile ices. Cometary ices are dominated by water ice, but CO_2 and CO are also present at significant levels. Other volatiles, notably including H_2S, NH_3, HCN and CH_4, have also been detected in the atmospheres of comets. The presence of such a wide array of high-volatility species strongly suggests that comets originated in the cool, outer regions of the proto-planetary nebula, and perhaps ever since been stored in exterior cryogenic conditions (Stern, 2003). Thus, comet nuclei are of high interest because of their possible identity as planetesimals from the outer regions of our solar nebula.

The small size of cometary bodies and their short lifetime, due to the dominant sublimation process controlling their evolution (typically $\sim 10^4$ yr), suggests that the ones we observe (quiescent or active nuclei) were presented recently to the inner solar system. If a steady-state population is to be maintained, the comets must be continuously re-supplied from one or more long-lived reservoirs.

The peculiar distribution of semi-major axes of long period comets (LPCs), and the related observations of the nearly isotropic orientation of their orbits relative to the ecliptic plane, led Dutch astronomer Oort, in the 1950's (Oort, 1950), to the conclusion that such comets must be derived from an essentially spherical reservoir. This "Oort cloud" (OC) supplies the flux of LPCs to the planetary region, and is of characteristic length scale $R_{OC} \sim 10^5$ AU and orbital periods $\tau_{OC} \sim 10^6 - 10^7$ yr . Modern estimates (Dones *et al.*, 2004) place the number of OC comets, larger than ~ 1 km, in the range of $10^{11} - 5 \times 10^{12}$, corresponding to a total mass of order $1 - 50M_\oplus$. These objects are thought to have originated in the region between Jupiter and Neptune and scattered outwards mostly by Uranus and Neptune (Hahn and Malhotra, 1999; Dones *et al.*, 2004).

Not all comets, however, have the highly extended orbits indicative of an extremely distant, spheroidal reservoir. On the contrary, many comets are observed to be on much more tightly bound orbits that are either trapped among the planets, or never stray to the OC. These short-period comets (SPCs) are divided into two groups: Halley-family comets (HFCs), which have a wide spread of inclinations, including retrograde orbits (and thus may be related to the OC), and Jupiter-family comets (JFCs), which display shallow, prograde orbital inclinations relative to the ecliptic plane. The latter constitute the predominant group, and are the subject of this research. These facts were used to infer that a second cometary reservoir must exist, in the region beyond Neptune. By the early 1990's it became possible for ground-based techniques to detect moderate-sized bodies in this region directly (Jewitt and Luu, 1993), which is now known as the Kuiper belt.

At least some nuclei of JFCs are now thought to be produced collisionally from interactions in the trans-Neptunian region (Davis and Farinella, 1997). They are fragments of "parent" KBOs, chipped off by mutual collisions in the KB. This view is interesting because it allows the possibility that the material in the JFCs nuclei might have been modified from its primordial condition. It could have been cooked by intrinsic heating in the larger KBOs, or in some transition phase, on its way from the KB to the inner solar system. It could also have been shocked and altered by the collision responsible for creating the small nucleus fragment. Another hypothesis is that JFC nuclei represent the small-end members of the TNOs size distribution, which have dynamically diffused towards the Sun, due to remote gravitational interactions with Neptune (Morbidelli, 2008).

1.2.2 The Centaur Population

If JFCs originate in the KB and eventually end up with orbits not much larger than Jupiter's, one would expect to find objects that are in the process of making the journey from the KB to the inner solar system. These transition objects have probably been found in the Centaurs.

In the past decade, there has been a rapid increase in the number of discoveries of a transitional population of minor bodies in the outer solar system called the Centaurs.

The first object in this population, Chiron, was discovered in 1977 (Kowal, 1989), and several dozens are now known, most discovered within the last several years. As of November 2008, the MPC listed 153237 Centaurs and scattered-disk objects (SDOs) in a single table (http://cfa-www.harvard.edu/iau/lists/Centaurs.html). Following a standard dynamical division between Centaurs and SDOs (Tiscareno and Malhotra, 2003), in which the perihelion distance is either interior or exterior to Neptune's orbit, a subset of ~ 120 objects belong to the population of Centaurs. Following another standard dynamical division (Jewitt, 2004), in which the perihelia and semimajor axes satisfy $q > a_J$ and $a < a_N$, with $a_J = 5.2$ AU (Jupiter) and $a_N = 30$ AU (Neptune), a subset of ~ 80 objects belong to the family of Centaurs.

The dynamical lifetimes of Centaurs are much shorter than the age of the solar system, and thus they must have a source in a more stable reservoir elsewhere in the outer solar system (Duncan *et al.*, 2004). The prevailing view is that Centaurs are objects that have escaped from the trans-Neptunian region of the KB and represent the dynamical population intermediate between the relatively stable KBOs and the short-lived JFCs.

Fig. 1.1 depicts the distribution of the three close dynamical classes of JFCs, HFCs, and Centaurs. This picture is based upon a number of theoretical investigations that have explored the KBO-JFC relations by means of numerical simulations. Once trapped as Centaurs the dynamical lifetimes are limited by strong gravitational scattering by the giant planets to $\tau_{Cen} \sim 10^7$ yr (Tiscareno and Malhotra, 2003). Most Centaurs are ejected from the solar system. The survivors that become trapped inside Jupiter's orbit tend to sublimate and are observationally re-labeled as JFCs (Jewitt, 2004). Overall, the dynamical evolution is mostly chaotic and the reverse transition from JFC to centaur is common. The specific dynamical picture of the whole intrinsic Centaur population, as well as the dynamical evolution of individual objects, is based on two recent and comprehensive investigations by Tiscareno and Malhotra (2003) and Horner *et al.* (2004a,b).

Fig. 1.2 shows how, in terms of the intrinsic orbital elements (e, i), the connection between Centaurs and JFCs is clear, as well as their distinction from the HFC group.

Another recent evidence for the origin of these objects comes from broadband photometry and spectral observations of the brightest Centaurs. This sample exhibits a wide diversity in color, from neutral/blue for 2060 Chiron, to ultra-red for 5145 Pholus (Barucci *et al.*, 2005), much like the color diversity known for the KBOs (Luu and Jewitt, 2002). The color diversity, together with the evidence for spectral similarity between Centaurs

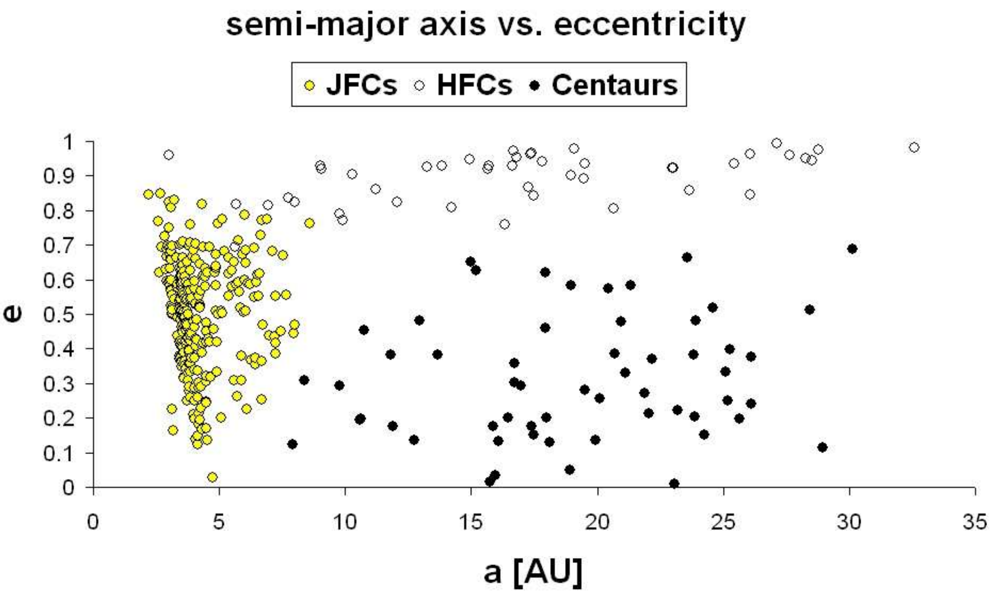

Figure 1.1 Distribution of JFCs, HFCs and Centaurs in the phase space of semi-major axis (a) and eccentricity (e). Note the clear distinction between the classes and the transition objects at the boundaries of each two groups. The data plotted here is taken from the MPC database (http://cfa-www.harvard.edu/iau/lists/centaurs.html) and from Yan Fernandez's website (http://www.physics.ucf.edu/ yfernandez/cometlist.html).

and KBOs (Groussin *et al.*, 2004; Barucci *et al.*, 2004), are consistent with an origin in the KB for the Centaurs.

Most known Centaurs have an asteroid-like appearance, as dormant, rocky objects. However, several such objects have been observed to show cometary activity, in the form of observable comae. These objects are listed in Table 1.1 (based on Jewitt, 2009).

The increasing rise in discoveries of Centaur objects and measurements of their physical properties, along with the observed activity of a sample of these objects, make good arguments for modeling efforts of the thermal and structural evolution of such bodies, on their own. Their conjectured dynamical role as a transition phase between KBOs and JFCs put these modeling efforts in a wider context, as a natural intermediate evolutionary phase between the very distinct "parents" (KBOs) and "offsprings" (JFCs).

There are some previous investigations dealing with the thermal evolution and resulting inner structure of the best observed and measured centaur 2060 Chiron (Capria *et al.*, 2000; Prialnik *et al.*, 1995; Fanale and Salvail, 1997). These models were done through the prism of an isolated body, with complete amnesia of its origin, and blindness to its future.

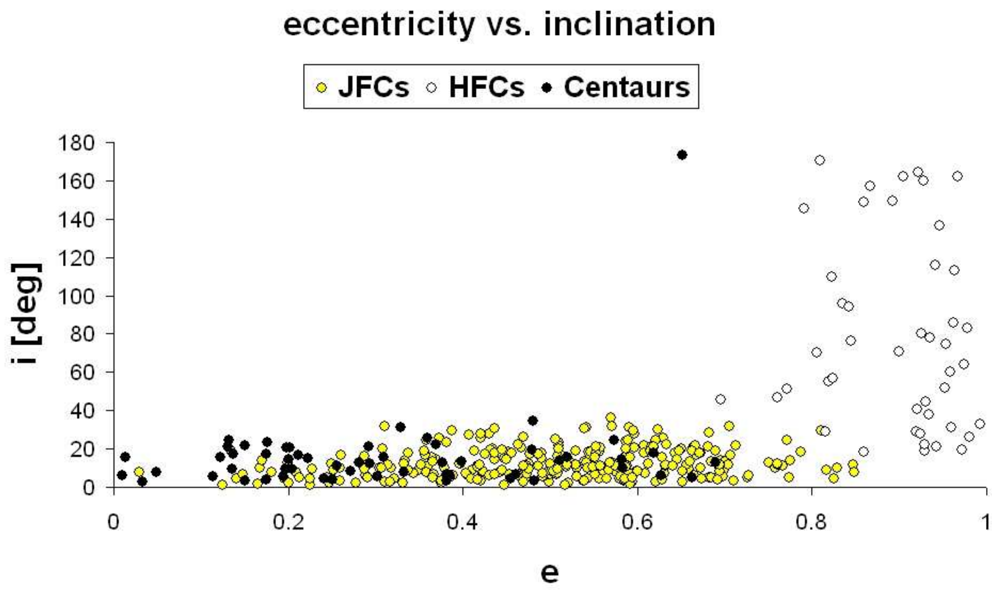

Figure 1.2 Distribution of JFCs, HFCs and Centaurs in the phase space of eccentricity (e) and inclination (i). Note the almost indistinguishable nature of Centaurs and JFCs, in this dynamical sense. This is in contrast to the clear distinction of HFCs. The data plotted here is taken from the MPC database (http://cfa-www.harvard.edu/iau/lists/Centaurs.html) and from Yan Fernandez's website (http://www.physics.ucf.edu/ yfernandez/cometlist.html).

Table 1.1 Orbital elements of the known active Centaurs

Object	q (AU)	a (AU)	e	i (deg)
29P/SW1	5.722	5.986	0.044	9.4
39P/Oterma	5.471	7.256	0.246	1.9
166P/2001 T4	8.564	13.880	0.383	15.4
167P/2004 PY42	11.784	16.140	0.270	19.1
C/2001 M10	5.303	26.660	0.801	28.0
P/2004 A1 (LONEOS)	5.463	7.895	0.308	10.6
174P/Echeclus (60558)	5.849	10.740	0.455	4.3
2003 QD112	7.935	18.974	0.582	14.5
(2060) 95P/Chiron	8.511	13.709	0.379	6.9

Data compiled from Jewitt (2009).

A slight exception, is part of the work carried out by Capria *et al.* (2000), which used an initial structure derived from previous KBO simulations, but suffered from over-simplified assumptions, short duration of simulation runs ($\sim 10^4$ yr), and lack of relevant physical processes. The thermal evolutionary path of Centaurs implemented by these models, as well as the evolutionary path for the progenitor KBOs, is different in this study. The differences arise from the physical processes taken into account, the initial compositions and material properties considered, and the updated dynamical input (median lifetimes and orbital elements).

1.2.3 The Trans-Neptunian Population

The first trans-Neptunian object to be discovered was Pluto, in 1930 by Clyde Tombaugh at Lowell Observatory. At the time of the discovery, it was believed that it was 'Planet X' that Percival Lowell proposed as the the cause of the deviations in Neptune's orbit. Despite later findings that Pluto was actually too small to have caused the suspected perturbations, it was generally considered to be a full-fledged planet. A number of individuals in the early 20th century speculated about the possible existence of objects beyond the known planetary region. These included the Irish aristocrat Edgeworth, who suggested that the origin of short-period comets might be beyond Pluto (Edgeworth, 1949). Later, the Dutch-American astronomer Kuiper discussed a ring of small bodies beyond Pluto, which was considered by him to be a massive planet, responsible for scattering small bodies formed in the trans-Neptunian region out to the Oort cloud (Kuiper, 1951). For reasons that remain unknown, Kuiper did not refer to the prior suggestion by Edgeworth. Finally, neither Edgeworth nor Kuiper cited the even earlier writing of Leonard, who correctly speculated that Pluto would prove to be the first of many objects to be discovered beyond Neptune (Leonard, 1930). The first bona-fide TNO had to wait for more than 60 years to be discovered. After many previous attempts failed, Jewitt & Luu found in 1992 the object designated $1992QB_1$ (Jewitt and Luu, 1993). Thus started the KBO hunt that has led to over 1000 observed object today in the TN region (according to the records of the IAU MPC).

The orbits of the known TNOs may be naturally divided into three distinct groups. Classical objects, with semimajor axes $42 \leq a \leq 47$ AU and small eccentricities ($e_{median} = 0.07$), constitute about 2/3 of the observed KBOs. About a third of the better-observed objects reside in the 3:2 mean motion resonance with Neptune at $a \simeq 39.4$ AU; these are known as Plutinos because of their dynamical similarity to Pluto. The rest possess large, highly eccentric and highly inclined orbits. These are designated "scattered disk objects" (SDOs). The SDO population is probably at least comparable in number to that of the

KBOs (Luu and Jewitt, 2002). The SDOs are hypothesized to be the population scattered by Uranus and Neptune, during the stage of planet formation. As already mentioned in Sec. 1.2.1, many nearby planetesimals were scattered to large distances, and subsequently formed the OC. Planetesimals scattered to more modest distances formed the SD and remained weakly interacting with Neptune. These objects may also be responsible for at least some of the influx of short-period comets (Duncan and Levison, 1997).

Fig. 1.3 and 1.4 depict the distribution of TNOs, in the 3 main orbital elements (a, e, i).

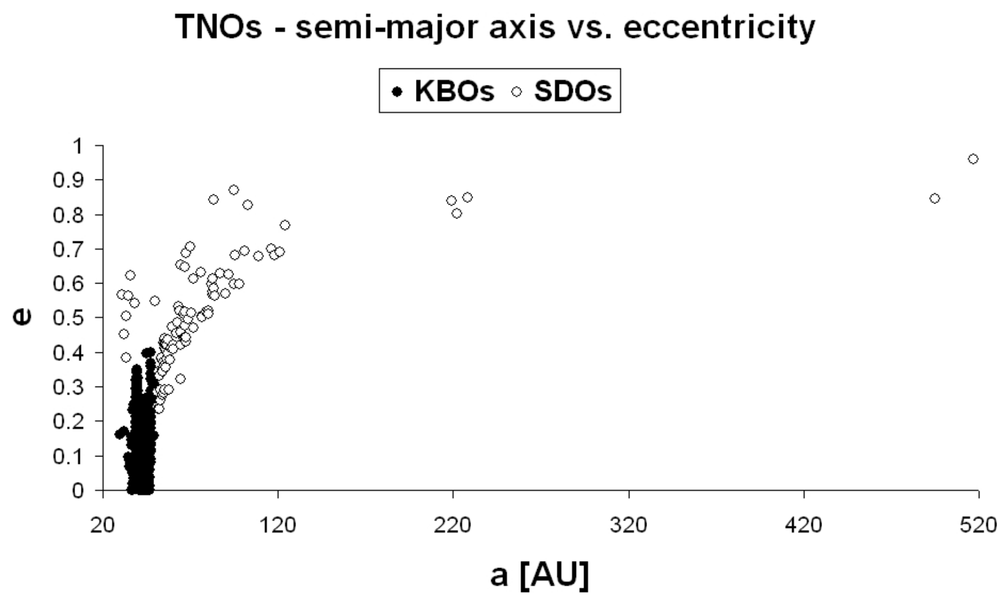

Figure 1.3 Distribution of TNOs (KBOs and SDOs) in the phase space of semi-major axis (a) and eccentricity (e). Note the high eccentricities and "scattered" nature of the SDOs, extending over $\sim$ 500 AU. The second most distant object in this plot is Sedna. The data plotted here is taken from the MPC database (http://cfa-www.harvard.edu/iau/lists/TNOs.html, for KBOs, and http://cfa-www.harvard.edu/iau/lists/Centaurs.html, for SDOs).

Table 1.2 gives a more detailed account of the mean orbital elements of distinct groups of objects in the disk region beyond Neptune.

The trans-Neptunian population is rapidly taking shape, and ,as a result, its dynamical evolution and structure are examined extensively by means of both simulations and observations. These dynamical investigations yielded the, more or less, consistent and acceptable model for the structure and long-term behavior of TNOs and their (intricate) relationships with the JFCs and the transient centaurs.

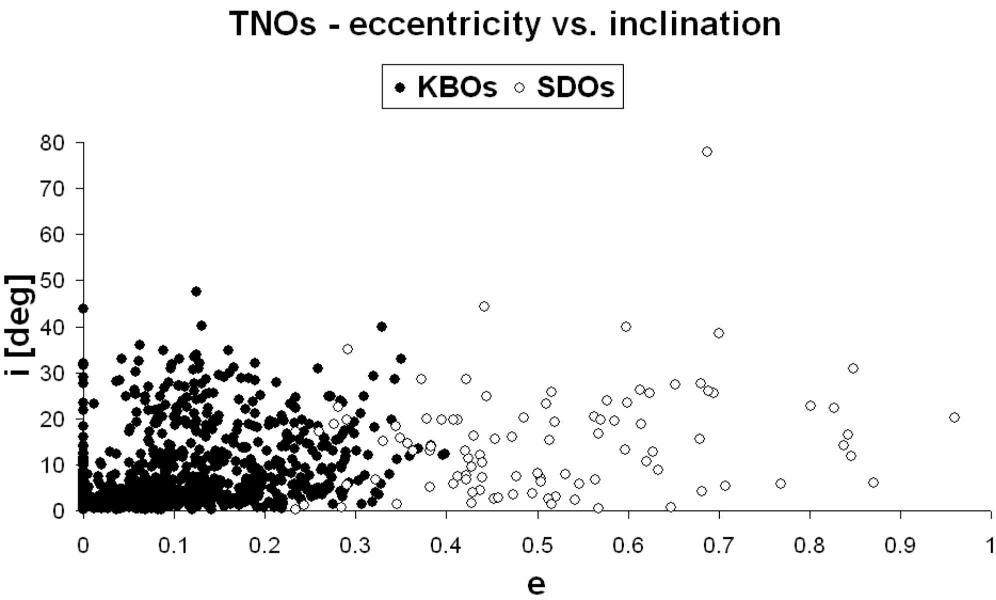

Figure 1.4 Distribution of TNOs (KBOs and SDOs) in the phase space of eccentricity (e) and inclination (i). Note the similar distribution of inclinations. Note that most KBOs are concentrated in a low-eccentricity and low-inclination region. The data plotted here is taken from the MPC database (http://cfa-www.harvard.edu/iau/lists/TNOs.html, for KBOs, and http://cfa-www.harvard.edu/iau/lists/Centaurs.html, for SDOs).

Table 1.2 Mean orbital elements of TN populations

Dynamical group	a (AU)	e	i (deg)
Classical	$\gtrsim 42$	0.09	7.11
4:3 resonance	36.4	0.22	7.81
3:2 resonance	39.4	0.36	12.87
2:1 resonance	47.8	0.14	9.83
Scattered	$\gtrsim 30$	0.49	14.08

Taken from Luu and Jewitt (2002).

It is widely believed that TNOs are remnant planetesimals from the solar system's early accretion phases and constitute an important reservoir of primitive materials (Luu and Jewitt, 2002; Malhotra, 1996). This population of small bodies, having been formed farthest out from the Sun, is believed to constitute the most primitive, least thermally processed matter. In recent years, various groups have reported discovering evidence for water ice in the spectrum of several large KBOs (e.g. Brown *et al.*, 1999; Jewitt and Luu, 2004; Schaller and Brown, 2008; Pinilla-Alonso *et al.*, 2009). These, and other, observations indicate a more direct physical kindship of TNOs and comets.

1.3 The Dynamical Scheme Of Small Bodies

Comets have dynamical and physical lifetimes that are short compared to the age of the solar system. This fact suggests that observed comets must have an origin in reservoirs, somewhere in the outer solar system. These reservoirs should retain enough objects to be stable over the solar system's age, but still allow objects to dynamically diffuse inwards.

The current viewpoint is that the three main reservoirs of observed comets are: the Kuiper belt (KB), the scattered disk (SD), and the Oort cloud (OC). The latter is considered as the source of long-period comets (Stern, 2003), whereas the KB and the SD are regarded as the sources of ecliptic comets (Levison and Duncan, 1997; Duncan *et al.*, 2004). The abridged dynamical scheme is that the giant planets perturb some TNOs into unprotected Neptune-crossing orbits after the TNOs have spent billions of years on non-crossing orbits beyond Neptune. Some of the Neptune-crossers eventually evolve inward to become Centaurs. Some Centaurs, in turn, become "observable" JFCs. By convention, an "observable" comet is defined in the dynamical literature as a comet with a perihelion distance less than 2.5 AU (Dones *et al.*, 1999).

1.3.1 Cometary Taxonomy

The classification of comets was historically based on the distinction of orbital period: comets with $P_{orb} > 200$ yr were considered as long-period (LPCs), whereas comets with $P_{orb} < 200$ yr were considered as short-period (SPCs). A further sub-division was made in the SPCs group, where objects with $P_{orb} < 20$ yr designated as Jupter-family (JFCs) and the rest were designated as Halley-family comets (HFCs). However, such classification was recognized as somewhat inappropriate, following numerical integrations that showed that most SPCs, classified in this manner, shifted in and out of the JFC class many times during their dynamical lifetimes (Duncan *et al.*, 2004). A better criterion for this kind of classification was suggested by several authors to be the Tisserand parameter, which was shown to be fairly constant during a typical dynamical evolution of a comet (see Levison and Duncan, 1994; Jewitt, 2004). The Tisserand parameter, with respect to Jupiter, is defined as

$$T_J = \frac{a_J}{a} + 2\sqrt{(1-e^2)\frac{a}{a_J}}\cos(i), \tag{1.1}$$

where a_J is the semi-major axis of Jupiter, and (a, e, i) are the orbital elements of the comet. The Tisserand parameter can be derived as an approximation to the integral of motion (Jacobi constant) of the circular restricted 3-body problem (Murray and Dermott, 2000). We note that when $e = 0$, $i = 0$ and $a = a_J$, then $T_J = 3$ and the orbit of the comet is similar to that of Jupiter. Thus, for values of the Tisserand parameter close to 3, the giant planet can strongly influence the comet's orbit.

In this scheme of taxonomy, comets with $T_J > 2$ are ecliptic comets, since they must have small inclinations. These most likely originated in the KB (Fernandez, 1980; Duncan *et al.*, 1988; Quinn *et al.*, 1990) or the SD (Duncan and Levison, 1997). Comets with $T_J < 2$ are believed to be mainly derived from the OC (Dones *et al.*, 2004). A subdivision of the ecliptic group follows:

- JFCs: $2 < T_J < 3$, where comets are mainly on Jupiter-crossing orbits that are obviously dynamically dominated by Jupiter.
- Centaurs: $T_J > 3$ and $a > a_J$, where the orbit is exterior to that of Jupiter.
- Encke-type: $T_J > 3$ and $a < a_J$, where the orbit is completely interior to the orbit of Jupiter.

1.3.2 The Link Between TNOs And JFCs

Much as the main belt asteroids are the ultimate source population of most near-earth asteroids, TNOs are the source of most, if not all, JFCs. Even before the discovery of KBOs, many researchers demonstrated that the orbital distribution of JFCs was consistent with a low-inclination disk of material beyond the orbit of Neptune (e.g. Fernandez, 1980; Duncan *et al.*, 1988; Quinn *et al.*, 1990). Subsequently, several studies involved more detailed simulations that gave estimates of the number of precursor bodies that must exist in the trans-Neptunian region in order to explain the observed number of JFCs, and assuming different source region (Holman and Wisdom, 1993; Levison and Duncan, 1997; Duncan and Levison, 1997; Morbidelli, 1997).

In one of the earliest numerical models of the KB-JFC connection, Holman and Wisdom (1993) estimated a population of 4.5×10^9 JFC precursors. Levison and Duncan (1997) refined this value to 7×10^9 JFC precursors using essentially the same physical model. These calculations were based on a dynamically "cold" KB, which means that most objects were considered to be in low-eccentricity, low-inclination orbits. Modeling the SD population as the source of JFCs, Duncan and Levison (1997) calculated that there are 6×10^8 JFC precursors in the SD, with $\sim 1/4$ of them found at any given time between heliocentric distances $30 - 50$ AU. In yet another calculation, Morbidelli (1997) calculated that if the Plutinos population (the 3:2 resonant objects in the KB) is the source of JFCs, it should contain 4.5×10^8 precursors.

A commonality of these models is the assumption that the various classes of the trans-Neptunian region constitute stable reservoirs of cometary precursors, and that some fraction of these objects escape into the inner solar system on Gyr timescales as a result of slow orbital chaos induced by the gravitational perturbations of the giant planets. The models differ only in the initial conditions of the precursor objects, that is, in the choice of the dynamical class for the putative sources of the JFCs. The instability that triggers the ejection of TNOs from long-lived orbits beyond Neptune may be dynamical chaos (Levison and Duncan, 1997), collisional scattering (Stern, 1995), or some form of stirring due to migration of the giant planets (Levison and Morbidelli, 2003).

As the trans-Neptunian population is rapidly growing, its dynamics is examined extensively by means of both simulations and observations (Morbidelli *et al.*, 2008; Gomes *et al.*, 2008; Kavelaars *et al.*, 2008). These investigations yield a consistent model for the structure and long-term dynamical evolution of TNOs and their (intricate) relationships with Jupiter-family comets (JFCs) and the transient Centaurs population (Duncan *et al.*, 2004). Thus JFC nuclei are thought to be either produced collisionally by interactions in the trans-Neptunian region (Davis and Farinella, 1997), as fragments of "parent" TNOs, chipped off by mutual collisions, or the small-end members of the TNO size distribution, diffusing inwards (Levison and Duncan, 1997; Duncan and Levison, 1997).

1.3.3 The Structure And History Of The Trans-Neptunian Region

Numerical studies of the stability of low-eccentricity, low-inclination orbits of objects in the KB, subject to the gravitational perturbations of the giant planets, have shown that the inner edge of the KB is at ~ 34 AU (Fernandez, 1980; Morbidelli and Brown, 2004). Beyond this edge, and up to ~ 42 AU there are interwoven regions of stability and instability (Morbidelli and Brown, 2004). This structure has a complex correlation with the locations of Neptune's orbital resonances (Malhotra, 1996). Other studies suggested that early in the history of the solar system, the majority of KBOs were swept into eccentric orbits located at the orbital resonances of Neptune (for a full critical account of these studies, see Morbidelli and Brown, 2004). The regions between these resonances would have been largely cleared of residual planetesimals. The relatively isolated first and second order Neptune resonances beyond ~ 34 AU provide narrow stable libration regions for the long-term storage of TNOs in eccentric orbits, often Neptune-crossing. Typical libration periods are $\sim 10^4$ yr, and these zones are surrounded by narrow chaotic zones where orbits are unstable on timescales of $\sim 10^5$ yr (Malhotra, 1996).

Fig. 1.5 shows the dynamical structure of the KB.

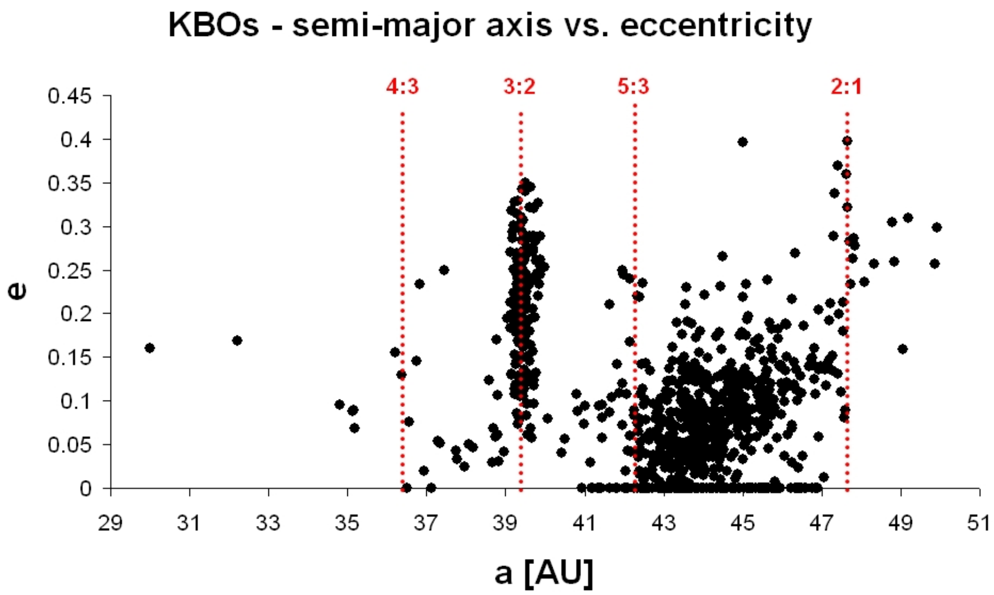

Figure 1.5 Distribution of objects in the Kuiper belt, in the phase space of semi-major axis (a) and eccentricity (e). Note the locations of the four strongest mean-motion resonances and the accumulation of objects near the 3:2 one. The data plotted here is taken from the MPC database (http://cfa-www.harvard.edu/iau/lists/TNOs.html).

Brown (2001) showed that the KB can be sub-divided into a 'cold' population with inclinations $i \leq 4°$ and a 'hot' population with inclinations as large as $50°$ (see Fig. 1.4). The cold KB is most similar to what was envisioned by early theories on the nature of the KB, and thus it is termed 'classical'. Observational evidence seems to point to an edge to the classical KB around 50 AU, just outside the 2:1 resonance with Neptune, but this may just be due to observational biases and a lack of sufficient orbital data (Trujillo and Brown, 2001; Gladman *et al.*, 2001; Kavelaars *et al.*, 2008).

The different sub-populations of TNOs were likely emplaced in different ways. Malhotra (1996) showed that gravitational interactions with planetesimals early in the history of the solar system could have caused Neptune to migrate outward, trapping bodies in mean-motion resonances, such as the 3:2 and 2:1. As those resonances would be moving outwards as Neptune migrates, bodies trapped in the resonances would be swept outwards as well, forming the resonant populations. Duncan and Levison (1997) showed that during its migration, Neptune would gravitationally scatter some bodies into highly eccentric and inclined orbits, thus forming the scattered disk population. Gomes (2003) showed that a subset of Neptune-scattered planetesimals could experience resonant effects that reduce their eccentricity and leave them in the KB region, albeit with fairly large inclinations, as the hot KB population.

Levison and Morbidelli (2003) showed that resonant effects combined with the migration of Neptune could cause planetesimals to migrate outwards under the action of the 2:1 resonance, without increasing their inclinations and having their eccentricities oscillate rather than monotonically increase. This was necessary because the cold KB is significantly depleted in mass relative to the mass necessary to form 1000 km-scale bodies (Stern and Colwell, 1997; Kenyon and Luu, 1998). The behavior of eccentricities would give rise to a wide range of values, comparable to that seen in the cold KB. Since the migration of Neptune is not assumed to be perfectly uniform, there will be jumps in the location of the 2:1 resonance. These jumps would cause some of the bodies trapped in the resonance to be freed, and those bodies that escape from the cold KB. A large number of bodies would be lost in this process due to inefficient resonance capture, the probability of being released from the resonance, and scattering by Neptune, explaining the observed mass depletion of the cold KB relative to the primordial population. In addition, Levison and Morbidelli (2003) provides an explanation for why the classical KB may end at, or very near, the 2:1 resonance with Neptune.

An interesting and important implication of all of these models is that all TNOs formed well inside their current positions and were pushed outwards by interactions with Neptune. In addition, there was potentially much more mass in the initial TNO population than is seen in the current population. This has important implications for modeling the collisional, and subsequent thermal, history of TNOs. It is possible that a substantial amount, or even a majority, of the collisional evolution of some of the TNO sub-populations occurred very early on in the history of the solar system and in a different region than those objects currently populate. The timescale for the migration of Neptune, and hence the processes described above, is on the order of 50 – 100 Myr (Hahn and Malhotra, 1999). In turn, the implication of these processes on the early thermal evolution of TNOs should be taken into account, with regards to the insolation at the regions of origin and the radioactive heating during accretion/erosion by collisions.

1.3.4 Number Estimates For The Dynamical Classes

Very roughly speaking, the probability that a small body will be scattered inward following its encounter with a planet is $p \sim 1/2$ (Fernandez, 1980). This means that every scatter of a small body past a perturbing planet adds a factor of p to the probability. Assuming TNOs have an effective lifetime comparable to that of the solar system, $\tau_{SS} \approx 4.5 \times 10^9$ yr, a crude estimate of the steady-state population of Centaurs (N_{Cen}) relative to TNOs (N_{TNO}) can be given by (Jewitt, 2004)

$$\frac{N_{Cen}}{N_{TNO}} \sim p\frac{\tau_{Cen}}{\tau_{SS}} \sim 10^{-3}. \tag{1.2}$$

where τ_{Cen}, the Centaurs population mean dynamical lifetime, is constrained by frequent close encouters with the giant planets and is on the order of 10^7 yr, with a large dispersion due to the chaotic nature of the orbital phase space (Tiscareno and Malhotra, 2003).

An estimate of bodies with diameter larger than 100 km, $N_{TNO} \sim 7 \times 10^4$, gives $N_{Cen} \sim 70$, which is in good agreement with observational estimates of centaur objects with the same size (Jewitt, 2004; Sheppard *et al.*, 2000).

Following the above approximation, the JFC steady-state population is

$$\frac{N_{JFC}}{N_{TNO}} \sim p^4\frac{\tau_{JFC}}{\tau_{SS}} \sim 5 \times 10^{-6}, \tag{1.3}$$

where the median dynamical lifetime of JFCs is $\tau_{JFC} = 3.25 \times 10^5$ yr (Duncan *et al.*, 2004). Numerical integrations by Levison and Duncan (1997) found that the source region of the JFCs must contain 7×10^9 objects, of diameter larger than 1 km. This gives $N_{JFC} \sim 10^4$, which is in agreement with the (very uncertain) observational estimates (Jewitt, 2004). A significant problem in comparing source models with population measurements is that the sizes of the objects being compared (cometary nuclei & TNOs) are not well determined because the albedos are not well known, and surveys are yet uncertain and incomplete.

1.3.5 The Size-Distribution Of The TNOs Population

The size distribution of the TNO population is usually expressed as a fitted differential power-law distribution of the form

$$n(r)dr = \Gamma r^{-\alpha} dr, \tag{1.4}$$

where $n(r)$ is the number of objects in the range $(r, r + dr)$, Γ is the normalization coefficient and α is the slope of the distribution. Luu and Jewitt (2002) presented number estimates for the bodies in the classical Kuiper belt, derived from the surveys done until then: Small objects, with $R > 1$ km, should have $N \sim 10^{10}$; large objects, with $R > 50$ km, should have $N \sim 3 \times 10^4$; and the largest objects, with $R > 1000$ km, should be on the order of $N \sim 10$.

Bernstein *et al.* (2004) performed a survey for TNOs, which covered 0.02 $\deg^2$ of the invariable plane in the sky beyond 25 AU, with a limiting R-band magnitude of 28.8. The size distribution can be estimated from the R-magnitude data, assuming that an R-magnitude of 28.5 corresponds to $D \sim 10$ km for an albedo of 4% and a heliocentric distance of 40 AU. As values are given in number per square degree of sky, the absolute number can be estimated by multiplying the 'classical' population (inclinations between $-5°$ and $+5°$) by $360 \times 10 = 3600$ square degrees and the 'excited' population by $360 \times 30 = 10800$ square degrees. Their analysis represents the current best estimate of the TNO population at small sizes. The observed sky surface density of the largest objects, with radii $300 - 1000$ km, and the location of the break in the size distribution are still uncertain, and there is also some evidence that different classes of TNOs have different size distributions (Luu and Jewitt, 2002). However, it can be said, based on the data presented in Bernstein *et al.* (2004), that the change in the slope of the size distribution occurs at a break radius $r \sim 10 - 30$ km. The current range for the mass of the KB, based on the deduced size distributions, is $M_{KB} \simeq 0.05 - 0.2\ M_{\oplus}$ (Stern, 1996; Luu and Jewitt, 2002; Bernstein *et al.*, 2004).

2 Methodology

In this chapter we describe the model we applied for the thermo-chemical evolution of the icy objects in question. We detail the governing equations, numerical scheme of the computer code, computational assumptions, input physics for the various processes that were implemented.

2.1 Governing Equations

Numerical modeling of the evolution of icy-rocky objects involves the simultaneous solution of energy and mass conservation equations, as well as momentum conservation, in the form of the hydrostatic equation, assuming a spherical object. When dealing with relatively large objects ($R \geq 100$ km), as discussed in Sec. 2.6, self-gravity prevails throughout most of the object, thus encouraging the use of a spherical shape, not only for computational ease. At heliocentric distances characteristic of TNOs ($q \geq 39$ AU) solar energy is a negligible heat source (Choi *et al.*, 2002), orbital periods are long and eccentricities relatively low (at least for classical KBOs), we can safely assume a "fast rotator" model (i.e., spherical symmetry - see Prialnik *et al.*, 2004), for the duration of the evolution.

The density ρ and porosity Ψ (either bulk or local) are given, respectively, by

$$\begin{aligned} \rho &= \rho_a + \rho_c + \rho_v + \sum_\alpha (\rho_{s,\alpha} + \rho_{g,\alpha}) + \rho_d, \\ \Psi &= 1 - (\rho_a + \rho_c)/\varrho_{\text{ice}} - \sum_\alpha \rho_{s,\alpha}/\varrho_\alpha - \rho_d/\varrho_d, \end{aligned} \tag{2.1}$$

where ϱ is the specific density of a species α. The other indices represent amorphous water ice (a), crystalline water ice (c), water vapor (v), solid and gaseous phases (s and g) of volatile species (α), and dust (d). The mass conservation equations for water ice in both phases and for the other volatile species are

$$\frac{\partial \rho_a}{\partial t} = -\lambda \rho_a, \tag{2.2}$$

$$\frac{\partial \rho_c}{\partial t} = (1-f)\lambda \rho_a - q_v, \tag{2.3}$$

$$\frac{\partial \rho_v}{\partial t} + \nabla \cdot \mathbf{J}_v = q_v, \tag{2.4}$$

$$\frac{\partial \rho_{g,\alpha}}{\partial t} + \nabla \cdot \mathbf{J}_\alpha = f_\alpha \lambda \rho_a + q_\alpha, \tag{2.5}$$

$$\frac{\partial \rho_{s,\alpha}}{\partial t} = -q_\alpha, \tag{2.6}$$

where λ is the temperature-dependent amorphous-crystalline transition rate (Schmitt *et al.*, 1989) and f is the total fraction of volatiles occluded as gas in the amorphous ice, $\sum_\alpha f_\alpha = f$. The mass flux, $\mathbf{J}$, represents the flow of gas, which is driven by sublimation from the pore walls or crystallization of amorphous ice and subsequent diffusion through the porous medium (Huebner *et al.*, 2006). The rate of sublimation (mass per unit volume of cometary material per unit time) is given by

$$q = SVR(\Psi, r_p)\left[(\mathcal{P}_{\text{vap}} - P)\sqrt{\frac{\mu}{2\pi \mathcal{R}_g T}}\right], \tag{2.7}$$

where SVR is the surface to volume ratio, which is a function of the given porosity (Ψ) and pore size (r_p) distribution (Sarid *et al.*, 2005), $\mathcal{R}_g$ is the gas constant and μ is the molecular weight of the volatile species. The pressure expressions are for the saturated vapor pressure (given by the Clausius-Clapeyron equation), $\mathcal{P}_{\text{vap}}$, and the partial pressure for each component (assuming an ideal gas), P, which are both a function of the temperature T, and are given by

$$\mathcal{P}_{\text{vap}} = Ae^{-B/T}, \qquad P = \frac{\mathcal{R}_g \rho_g T}{\Psi \mu}, \tag{2.8}$$

where A and B are coefficients for the different ice components (see Prialnik *et al.*, 2004). Table 2.1 lists these coefficients, as well as sublimation temperatures and their correpond-ing pressures, for some of the most commonly used and most abundant volatile species in planetary environments and observations of cometary volatiles (Bergin *et al.*, 2007; Bockelée-Morvan *et al.*, 2004).

Taking into account energy conservation throughout the nucleus, and combining with the mass conservation equations, we obtain the heat diffusion equation in the form

$$\sum_\alpha \rho_\alpha \frac{\partial u_\alpha}{\partial t} - \nabla \cdot (K \nabla T) + \left(\sum_\alpha c_\alpha \mathbf{J}_\alpha\right) \cdot \nabla T = \lambda \rho_a \mathcal{H}_{\text{ac}} - \sum_\alpha q_\alpha \mathcal{H}_\alpha + \dot{Q}, \tag{2.9}$$

Table 2.1 Thermodynamic coefficients of various volatile compounds

	T [K] [1]	P [dyn/cm^2] [2]	A [dyn/cm^2] [3]	B [K] [3]
H_2O (Water)	180	7.6×10^{-4}	3.56×10^{13}	6141.667
CO (Carbon monoxide)	25	6.7×10^{-4}	1.263×10^{10}	764.16
CO_2 (Carbon dioxide)	80	8.8×10^{-5}	1.079×10^{13}	3148
CH_4 (Methane)	31	1.3×10^{-6}	5.97×10^{10}	1190.2
C_2H_6 (Ethane)	44	3.4×10^{-9}	4.59×10^{10}	1938
CH_3OH (Methanol)	99	4.2×10^{-9}	8.883×10^{11}	4632
HCN (Hydrogen cyanide)	95	1.5×10^{-7}	3.8665×10^{11}	4024.66
H_2S (Hydrogen sulphide)	57	8.4×10^{-10}	1.2631×10^{11}	2648.42
NH_3 (Ammonia)	78	5.3×10^{-8}	6.1412×10^{12}	3603.6
C_2H_2 (Acetylene)	57	1.2×10^{-8}	9.831×10^{11}	2613.6

[1] Sublimation temperature (see Meech and Svoren, 2004).
[2] Pressures corresponding to the quoted sublimation temperatures.
[3] Coefficients for the saturated vapor equation, $\mathcal{P}_{\rm vap}$ (see Prialnik *et al.*, 2004).

where $u = \int cdT$ is the specific heat energy and c and K are the specific heat and thermal conductivity of the various components. The right-hand side includes all the available energy sources and sinks, primary (radioactive decay), as well as secondary, or induced (crystallization of amorphous ice, sublimation). Here $\mathcal{H}_{\rm ac}$ and $\mathcal{H}_\alpha$ represent the heat released upon crystallization and sublimation, respectively, and

$$\dot{Q} = \sum_j X_{0,j}\mathcal{H}_j\tau_j^{-1}\exp -t/\tau_j \tag{2.10}$$

is the rate of radiogenic energy release. Here τ_j is the decay time of the j'th radioactive isotope, $X_{0,j}$ is its mass fraction (initial abundance of radionuclide multiplied by the mass fraction of dust), and $\mathcal{H}_j$ is the energy released per unit mass upon decay (see Sec. 2.5 for the relevant properties of the radionuclides).

The above set of time-dependent equations is subject to constitutive relations: $u(T)$, $\lambda(T)$, $q_\alpha(T,\Psi,r_p)$, $\mathbf{J}_\alpha(T,\Psi,r_p)$, $K(T,\Psi,r_p)$, which require additional assumptions for modeling the structure of the nucleus. The additional assumptions refer to physical processes such as heat conduction and gas flow in a porous medium, crystallization of amorphous ice and dust drag, as well as mechanical and structural properties, such as compressive and tensile strength and pore-size distribution (Prialnik *et al.*, 2004; Sarid *et al.*, 2005; Prialnik *et al.*, 2008).

Dust is assumed to be, in part, dragged along with the gas flowing through pores and, in part, lifted off the nucleus surface by the sublimating vapor. For the former, the dust velocity is assumed to be equal to the gas velocity (Podolak and Prialnik, 1996). An efficiency factor is calculated, to take account of a dust size distribution that allows only grains up to a critical size to be dragged or lifted off. The rest may accumulate to form a dust mantle. The efficiency factor may be adjusted so as to allow or prevent the formation of a sealing mantle.

The evolution equations are second-order in space, and hence each require two boundary conditions. One obvious boundary condition is vanishing heat flux at the center. The second one is obtained from the requirement of energy balance at the surface:

$$F(R) = \epsilon\sigma T(R,t)^4 + \mathcal{F}P_{\mathrm{vap}}(T)\sqrt{\frac{\mu}{2}\pi R_g T}\mathcal{H} - (1-\mathcal{A})\frac{L_\odot}{4\pi d_H(t)^2}\cos z, \tag{2.11}$$

where the factor $\mathcal{F} \leq 1$ represents the fractional area of exposed ice, since the surface material is a mixture of ice and dust (Crifo and Rodionov, 1997), $\mathcal{A}$ is the surface albedo, $L_\odot$ is the solar luminosity, d_H is the heliocentric distance and z is the local solar zenith angle.

Similarly to the heat flux, the mass (gas) fluxes vanish at the center. At the surface the gas pressures are those exerted by the coma; in the lowest approximation these may be assumed to vanish: $P_\alpha(R,t) = 0$ (Prialnik *et al.*, 2004; Sarid *et al.*, 2005). However, it should be mentioned that the simple (and commonly used) outer boundary conditions for both energy and gas fluxes have been recently examined in more detail by Davidsson and Skorov (2002, 2004). Back-scattering of molecules leaving the nucleus surface and penetration of solar radiation into a thin sub-surface layer of the nucleus have been shown to affect the surface and sub-surface temperatures. These temperatures, however, are equally affected by the other approximations of the model (such as sphericity or homogeneity of surface structure), not to mention the uncertainty in the thermal conduction coefficients. Nevertheless, production rates are far less affected by these factors. For example, if back scattering reduces the net amount of sublimation at a given temperature, the surface temperature increases, but with it the sublimation rate increases as well. In fact, at low heliocentric distances, the amount of sublimation may be quite accurately calculated simply by $(1-\mathcal{A})L_\odot \cos z/(4\pi d_H^2 \mathcal{H})$, independently of the surface temperature.

2.2 Numerical Scheme

The numerical code solves the set of dynamical equations of the model (see Sec. 2.1) using a fully implicit difference scheme (Prialnik, 1992). The model is evolved from an initial homogeneous configuration. Thus, no predetermined states of differentiation or stratification are assumed. In order to obtain a better resolution near the surface, where the temperature gradient is steeper, the layers are progressively thinner towards the surface. The time steps are automatically adjusted in order to keep the changes in temperature during one time step confined. The time scale for thermal evolution simulations is usually limited by computational constraints. The evolution equations are coupled through the sources and fluxes. These are functions of both temperature and pressure, and must be solved simultaneously. Details on computational approximations and on the numerical scheme may be found in Prialnik (1992) and Prialnik *et al.* (2004). A few particularly relevant factors are discussed in the following sections.

2.3 Porous Structure and Composition

For the purpose of modeling the thermal evolution of icy objects we regard them as similar to comet nuclei. A comet nucleus is generally portrayed as a porous aggregate of ices and solids (Weidenschilling, 2004). As such, its structure can be modeled as an agglomeration of grains made of volatile ices and solids at some mixing ratio, with a wide spread in the size distribution of the components. The most general composition of a comet-like object is assumed to consist of water ice (amorphous and crystalline), water vapor, dust (grains of silicates and minerals), and other volatiles (mainly CO, CO_2, HCN, NH_3, etc.). These volatile compounds may be frozen, free or trapped in the amorphous water ice (Bar-Nun *et al.*, 1987). Observations of highly volatile species in the comae of comets attest to the possible persistence of amorphous phases (Bockelée-Morvan *et al.*, 2004). Adding to this indirect evidence, direct observations of the spectral features of two new comets, C/Hale-Bopp O1 (Davies *et al.*, 1997) and C/2002 T7 (LINEAR) (Kawakita *et al.*, 2004), have been inferred to indicate amorphous water ice. Thus, water ice is assumed to be initially amorphous, but will crystallize at a temperature-dependent rate (Schmitt *et al.*, 1989) and gradually release the trapped volatiles. The dust component may include radioactive elements in abundances typical of meteorites, as will be discussed in Sec. 2.5.

The equilibrium temperature at distances corresponding to the Kuiper belt region (between $\sim 30-60$ K) are above the condensation temperature of highly volatile species, such as CO or CH_4, but low enough for water ice to be amorphous. For the moderately volatile species, such as CO_2, HCN and NH_3, the initial ice phase is usually considered negligible. This is because the heat deposition during the accretion phase of KBOs may be sufficient for preventing condensation of these volatiles, but not so strong as to drive the temperature above the crystallization threshold (Shchuko *et al.*, 2006). Thus, water ice remains amorphous for the initial configuration of most of our thermal models (cf. McKinnon, 2002).

These cometary materials may not be tightly packed, resulting in a large fraction of voids in the volume of an object. A high ratio of the volume of voids to the bulk volume, the porosity of an object, has been confirmed by every relevant measurement made on a comet nucleus (Weissman *et al.*, 2004; A'Hearn *et al.*, 2005). If we determine, in some way, an estimate for the bulk density, we can constrain the proportions of ice, dust (solids) and voids (porosity), using the relation

$$1-\Psi = \frac{\rho}{1+\mathcal{R}_{d/i}}\left(\frac{1}{\varrho_i}+\frac{\mathcal{R}_{d/i}}{\varrho_d}\right), \tag{2.12}$$

where Ψ is the bulk porosity, $\mathcal{R}_{d/i}$ is the ratio of mass fractions of dust to ice and ρ, ϱ_i, ϱ_d are the bulk density, specific density of water ice and specific density of dust, respectively.

Fig. 2.1 shows the parameter space for Eq. 2.12. In order to set the initial conditions for each object, we need to choose two of the parameters and the third is uniquely given. From this relation we can also conclude that for $\Psi \gtrsim 0.6$, as derived for Comet 9P/Tempel 1 (A'Hearn *et al.*, 2005), the bulk density should be less than that of water ice, no matter how much dust we assume the object contains. On the other hand, for $\Psi \lesssim 0.25$, the bulk density would be at least that of water ice, for any appreciable mass fraction of dust. Cold compaction of water ice, as occurs in icy satellites and TNOs, can reduce porosities to these levels (Durham *et al.*, 2005). This is consistent with the estimated ranges of densities for mid-size icy satellites and large TNOs (Brown, 2008).

Having a porous medium affects not only the structural properties of an object, but also its thermal behavior. This holds for any model of the porous medium and also affects some diffusove properties (see Sec. 2.4). We include this effect of porosity by applying a thermal conductivity correction factor. This factor describes how the overall conductivity of a medium is reduced due to the null or inefficient transport of energy of the pores. Generally, if K_{bulk} is the bulk conductivity of the material, then the actual conductivity

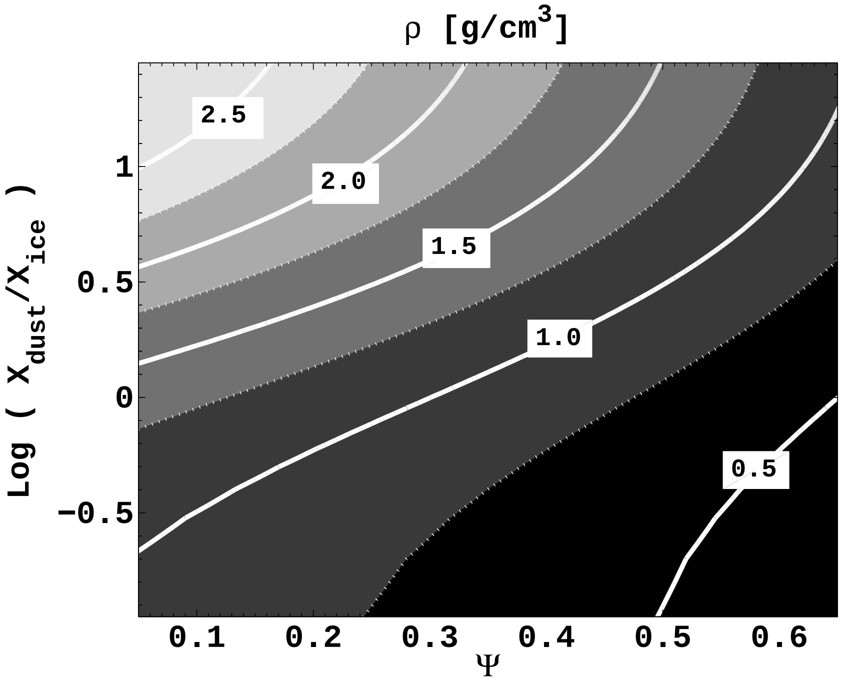

Figure 2.1 Relation between bulk density (ρ), porosity (Ψ) and dust-to-ice ratio (X_{dust}/X_{ice}). Note that for porosities greater than 0.6, very low density is expected, regardless of the abundance of "rocky" material inside an object. For porosities lower than 0.25, the bulk density of an object would be at least that of water ice.

of the same material with some porous structure in it will be $K = \phi K_{bulk}$ ($\phi \leq 1$). In order to determine ϕ we need to know the exact configurations and interactions of the grains and voids that comprise the porous medium. There are various approaches to modeling this problem, but for the sake of simplicity, we choose the simplest form of correction factor as $\phi = 1 - \Psi^{2/3}$ (Smoluchowski, 1981), as it gives a reasonable upper limit for most expressions and does not require additional unkown parameters to be included in the model (see Prialnik *et al.*, 2004, for a more complete discussion of all the above).

We should mention that all the pores mentioned in this and the following sections are a result of the structure of the solid matrix, comprising of grains or small ruble piles of rock-mineral aggregates and ices. Obviously, there are additional microscopic voids, within the sub-units of the solid matrix, and their conbined influence is commonly reffered to as "micro-porosity". This property may be due to the inherent structure of ice formed under thermodynamic conditions in space (Kouchi *et al.*, 1994), a result of slow dissociation of clathrate structures in the ice (Blake *et al.*, 1991), or due to the aggregation mechanism and brittle fragmantation of small planetesimals in the early phase of solar system formation (Blum and Wurm, 2008). However, micro-porosity should have very little direct influence on the thermal conductivity, unless the rock/ice sub-units of the solid matrix become correlated through adjacent layers and form continous cracks through the volume of the object (an effect that is not included in the current model). A more appreciable effect would be enabling gases to flow through the porous medium more effectively. However, this effect is not easily tractable and we do not have enough information about the interaction of micro-porous flow with ice and dust grains in low-pressure and low-temperature environments.

2.4 Pore-Size Distribution

An icy porous medium allows for sublimation from the pore walls and condensation onto them, as well as for flow of gas through the pores. The structural parameters that affect these processes are the porosity (Ψ), the surface to volume ratio (SVR) and the permeability (Φ) (Prialnik *et al.*, 2004). The first is defined as the total volume of pores per given bulk volume, and the second, as the total interstitial surface area of the pores per given bulk volume. The permeability is, up to a numerical constant, the proportionality coefficient between the mass flux and the gradient of $P/\sqrt{T}$ that drives the flow of mass, where P and T are the gas pressure and temperature, respectively.

In order to determine these properties, a model of the porous structure is required. Commonly used in the modeling of cometary interiors is the model of a bundle of unconnected cylindrical tortuous capillary tubes (Mekler *et al.*, 1990). The free parameters of this model are the tortuosity ξ, defined as the ratio of capillary length to linear distance, and the pore (capillary) radius r, for which some reasonable average pore size is assumed. These result in very simple expressions for SVR and Φ, in terms of Ψ, ξ and r,

$$SVR = \frac{2\Psi}{r}, \qquad \Phi = \frac{\Psi r}{\xi^2}. \tag{2.13}$$

However the above expressions imply that all capillaries are of the same radius. If r represents the mean of a distribution of pore sizes, the simple formulae above cease to be correct, a fact that has been largely overlooked. There is, however, a price to pay for a more realistic approach to pore sizes, and it involves a larger number of parameters for defining the medium. Nevertheless, the deviations from eqs.(2.13) may be quite considerable and thus worth the price.

Assuming the radii of the capillaries to vary according to some size distribution, we consider a volume of unit thickness and define $N(r)dr$ to be the number of capillaries with radii between r and $r + dr$ crossing a unit area. Keeping in mind that for a capillary tube, $\phi \propto r^3/\xi$ (Gombosi, 1994), the three fundamental properties of a porous medium are, in fact, moments of the distribution function (cf. Prialnik *et al.*, 2004):

$$
\begin{aligned}
SVR &= \xi \int 2\pi r N(r) dr \\
\Psi &= \xi \int \pi r^2 N(r) dr \\
\Phi &= \frac{\pi}{\xi} \int r^3 N(r) dr.
\end{aligned}
\tag{2.14}
$$

We can re-arrange the above expressions to have

$$
\begin{aligned}
\Phi &= \frac{\Psi}{\xi^2} \frac{\int r^3 N(r) dr}{\int r^2 N(r) dr} = \frac{\Psi}{\xi^2} \bar{r} \\
SVR &= 2\Psi \frac{\int r N(r) dr}{\int r^2 N(r) dr} = 2\Psi \overline{\left(\frac{1}{r}\right)},
\end{aligned}
\tag{2.15}
$$

where where $\bar{r}$ is the mean pore radius weighted by the volume fraction occupied by capillaries of radii in the range $(r, r + dr)$. We note that the expressions in Eq. 2.15 are similar to those in Eq. 2.13, except that SVR depends on the harmonic mean of $(1/r)$, rather than on the inverse of the mean. If we adopt $\bar{r}$ as the free parameter, then the expression for SVR in Eq. 2.13 should be corrected by a factor

$$
C = \bar{r} \overline{\left(\frac{1}{r}\right)} = \frac{\int r^3 N(r) dr \int r N(r) dr}{\left(\int r^2 N(r) dr\right)^2}. \tag{2.16}
$$

A reasonable distribution function for the pore sizes (their radii, r_p) is a power law, since grains ejected from comet nuclei have a power law size distribution (Fulle, 1997; Sarid *et al.*, 2005), and cometary bodies are believed to be formed by un-compacted aggregations of grains (Weidenschilling, 2004), in which case the grain and pore size distributions should be similar. Thus, if the number of capillaries with radii between r and $r + dr$, crossing a unit area is $N(r)dr$, we assume

$$
N(r_p) \propto r_p^{-\alpha} \qquad \text{for} \qquad r_{p,\min} < r < r_{p,\max}. \tag{2.17}
$$

The distribution function depends on four parameters: the exponent α, the normalization factor, and the size range $[r_{p,\min}, r_{p,\max}]$. The last three parameters may be replaced by values for the porosity Ψ (serving as a normalization factor), the average pore radius $\bar{r}_p$, and the ratio $X \equiv r_{p,\min}/r_{p,\max} < 1$. The resulting correction factor takes the form,

$$C_X(\alpha) = \frac{(3-\alpha)^2}{(4-\alpha)(2-\alpha)} \frac{(1-X^{4-\alpha})(1-X^{2-\alpha})}{(1-X^{3-\alpha})^2}. \tag{2.18}$$

Fig. 2.2 shows the distribution of the correction factor. Following the distribution of dust grains inferred from observations, typical parameter values are $X = 10^{-3} - 10^{-4}$ and $3 \leq \alpha \leq 4$ (Fulle *et al.*, 1997; Jockers, 1997; Harker *et al.*, 2002). These values correspond to the range where large corrections to the SVR are expected. Thus, a distribution of pore sizes – rather than a fixed average size – may have an important effect on the rate of sublimation and, in turn, on internal properties, such as abundances and migration of volatiles (water and other compounds), as well as external properties, such as fluxes of ejected material (gas and dust). Sec. 5.1.4 presents a comparison between a model of a JFC with and without the SVR correction, in terms of time-dependent external activity (Fig. 5.6) and internal evolution (Fig. 5.5).

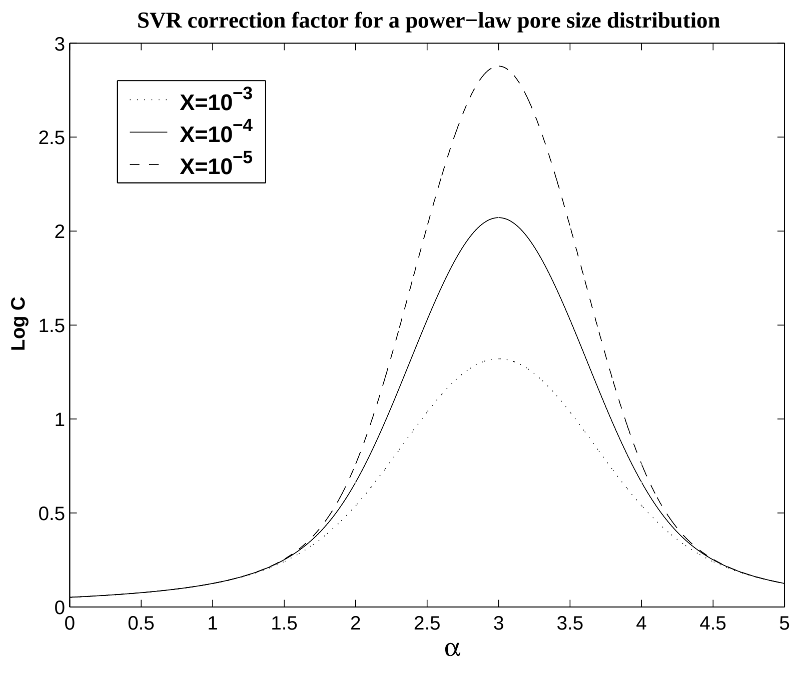

Figure 2.2 The correction factor of the SVR parameter, as a function of the power law exponent, for different ratios of minimal to maximal pore size. Note that the interval commonly used for pore size distribution ($3 < \alpha < 4$) gives a factor ≥ 10.

Pore radii may shrink or grow as a result of condensation or sublimation at each layer depth, respectively. In this case, the change in each pore's radius is by a uniform amount, independent of r_p. Thus, the effect of pore size change may be easily incorporated in modeling, by calculating the change in Ψ, from the mass conservation equation, and SVR (Prialnik *et al.*, 2008). Pores may also be squeezed or broken due to accumulation of internal pressure, in which case the material strength and its history become involved. Since we assume the full range of pore sizes does not change appreciably, the changing values of porosity are related to a changing exponent of the power-law distribution, α, as in Eq. 2.17. Thus, porosity is always considered (either as micro-, or macro-porosity) and the basic model (Eq. 2.15) is only altered through changing the number of available pores at each size.

Our treatment of compaction takes into account only the reduction of void volume (i.e., decrease in porosity), due to the shrinkage or growth of the capillary pores. It is not compaction per se, followed by changes in bulk radii and densities, as for planet-sized bodies, but rather a re-arrangement of the grain-size distribution and changes to the micro-porosity by random fracture configurations (see Durham *et al.*, 2005). As various volatiles sublimate and recondense, or different layers experience pressures that exceed the tensile strength (determined by material properties and local porosity), we re-calculate the local density and porosity (see Eq. 2.1). Pressures are calculated as either the gas pressure of vapor (Eq. 2.8), the hydrostatic pressure of the solid component (see Sec. 2.6), or a combination of both. If the layer becomes denser (less porous), we refer to it as 'compacted'.

2.5 Radioactive Heat Sources

The main energy source taken into account, when considering the thermal evolution of icy objects, is the internal heating generated by radioactive decay (Choi *et al.*, 2002). Radioactive heating has been shown to cause an appreciable rise of internal temperatures in small bodies of the solar system (Wallis, 1980; Prialnik *et al.*, 1987; Prialnik and Podolak, 1999; McKinnon *et al.*, 2008). Besides the major radionuclides, which constitute the main heat source for terrestrial planets – ^{40}K, ^{235}U, ^{238}U and ^{232}Th – the isotope ^{26}Al has been recognized as a heat source, capable of significant bulk thermal processing in bodies of radii between 100 and 1000 km (Urey, 1955; Ghosh and McSween, 1998). Its lifetime is comparable to the formation timescales of comets and comet-like bodies, but short enough as to generate sufficient heating for overcoming cooling by conduction (Prialnik and Podolak, 1999). An additional short-lived radionuclide, which may have had an appreciable effect on the thermal evolution of planetary objects is ^{60}Fe (Mostefaoui *et al.*, 2005). Evidence for the presence of ^{60}Fe in undifferentiated bodies, from analysis of chondritic meteorites, suggest a delayed incorporation into the disk during the early phases of the solar system's evolution, although there is still uncertainty about the actual enrichment mechanism and timescale (Tachibana and Huss, 2003; Mostefaoui *et al.*, 2005; Bizzarro *et al.*, 2007; Gounelle and Meibom, 2008). Estimates of the exact initial abundance of ^{60}Fe vary, but for our purposes we take an average of the values presented in Tachibana and Huss (2003). Table 2.2 summarizes the properties of all radioactive isotopes used in this work.

Table 2.2 Radioactive isotope characteristics

Isotope	τ(yr)	$X_{rad.}(0)$	$\mathcal{H}$(erg g^{-1})	Q_0(erg g^{-1} yr^{-1})
^{40}K	1.82(9)	1.1(-6)	1.72(16)	10.4
^{232}Th	2.0(10)	5.5(-8)	1.65(17)	0.454
^{238}U	6.50(9)	2.2(-8)	1.92(17)	0.65
^{235}U	1.03(9)	6.3(-9)	1.86(17)	1.14
^{26}Al	1.06(6)	6.7(-7)	1.48(17)	9.4(4)
^{60}Fe	2.15(6)	3.4(-7)	4.92(16)	7.8(3)

See Tachibana and Huss (2003) and Choi *et al.* (2002) for references related to the table values above.

For all of the radioactive species, we take the initial abundances as their estimated values, from meteoritic analysis, attenuated by a factor of 5×10^6 yr of accretion time. Objects with radii larger than 100 km are formed from smaller icy planetesimals. These smaller objects are inefficient in storing internally produced heat (Prialnik and Podolak, 1999) and so radioactive decay causes a decrease in the abundances of radionuclides without much thermal alteration of the interior, prior to their accretion. When a larger object is formed, large enough to retain its internal heating, the effective initial abundance of radionuclides is the original one attenuated by the accretion time span. In a minimum-mass solar nebula, calculations of planetesimal accretion and coagulation predict formation timescales of a few 10^7 yr, for objects with radii larger than 100 km, at distances of $30 - 50$ AU (Kenyon, 2002). However, the formation process should be more rapid if the nebula is more massive, or the formation zone more compact, as some models suggest (Desch, 2007; Kenyon *et al.*, 2008). Thus, to account for these, and other, uncertainties we take a shorter accretion time for objects such as large TNOs. However, it should be noted that this is an approximation, as it would be strictly correct only if the build-up of the objects considered was very slow for the duration of the accretion time and very rapid afterwards (Merk and Prialnik, 2003).

2.6 Self Gravity

Comet nuclei, although probably having low material strength (Weissman *et al.*, 2004), should be held together by material forces, as they are not massive enough to promote self-gravity. However, this neglect of self-gravity is only justified for small icy bodies, where the hydrostatic pressure is lower than the material strength (Prialnik *et al.*, 2004). When considering the larger objects of the TNO and Centaur population, self-gravity can become important and would affect the structure and composition of the interior.

Assuming a rotating body of constant density, hydrostatic equilibrium implies a pressure distribution,

$$P(r) = 2\pi^2 \rho R^2 \left(\frac{G\rho}{3\pi} - \frac{1}{p_{rot}^2} \right) \left[1 - \left(\frac{r}{R} \right)^2 \right], \tag{2.19}$$

where ρ, R and p_{rot} are the bulk density, radius and spin period, respectively. For the average bulk densities typical of large TNOs, between $1.5 - 2.5$ g cm^{-3} (Brown, 2008), the limiting spin period is between $2.69 - 2.08$ hr, respectively. This is, of course, amply satisfied by measured spin periods (Lacerda and Luu, 2006; Lacerda and Jewitt, 2007).

Comparing the pressure distribution in (2.19) with the material strength σ_s, assuming no spin, we find to what extent will an object become compressed under its own gravity (the largest radial distance z for which we still have $P(r) > \sigma_s$). If the central pressure, $P_c = \frac{2\pi}{3} G\rho^2 R^2$, is lower than the material strength, self-gravity may be safely neglected. On the other hand, when close to the surface, even at a depth of $0.9R$, the pressure given by Eq. 2.19 becomes greater than the material strenth, then the interior of the object can experience hydrostatic compression under its own gravity. By examining different values of σ_s and ρ, and demanding $r/R \gtrsim 0.9$, we conclude that self-gravity can be quite safely neglected below radii of $\sim$ 30 km, but has to be taken into account for bodies greater than $\sim$ 100 km in radius.

Fig. 2.3 shows the dependence of r/R on R (with $z \equiv r$, to denote the depth) for a density of 1.5 g cm^{-3} and several values of the material or tensile strength (in CGS units, dyne cm^{-2}). There is quite some evidence indicating that small bodies in the solar system have low tensile strengths (Blum *et al.*, 2006). However, these values are not well constrained and could be derived from various sources (tidal break-up, as in the case of S-L 9, measurements of IDPs and meteorites, rotational stability analysis and lab experiments on cometary material analogues). The excepted range for the values of the material/tensile strength in cometary bodies is between $\sim 3 \times 10^3$ and $\sim 10^6$ dyne cm^{-2} (e.g. Weissman *et al.*, 2004; Toth and Lisse, 2006; Blum *et al.*, 2006; Trigo-Rodriguez and Blum, 2009). Considering different values for the ρ and/or p_{rot}, the curves in Fig. 2.3 will shift slightly, but the characteristic size scale of $R \simeq 100$ km, for non-negligible self-gravity, will be the same.

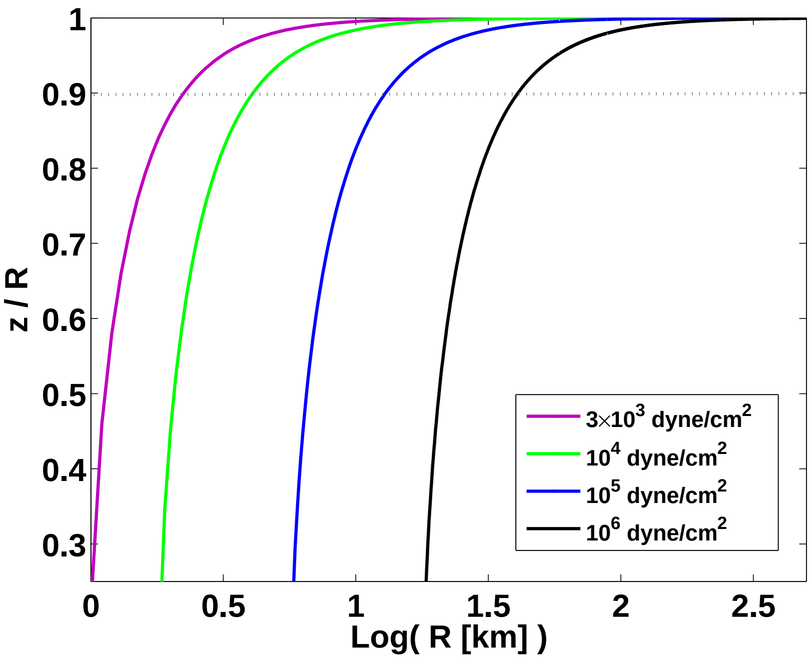

Figure 2.3 Relative importance of hydrostatic pressure for the solid matrix of a cometary object, with a density of 1.5 g/cm^3. The compressibility of self-gravitating objects (of over 10-100 km in radius) is evident by comparing hydrostatic pressure to compressive strength. Note that for $R \geq 100$ km, the curves for the various values of the compressive strength all lie close to $z/R = 1$. Thus for these radii most of the object experiences hydrostatic compression.

Self-gravity implies the release of specific gravitational energy, which is related to the compaction of solids and reduction of void volume (Leliwa-Kopystyński and Kossacki, 2000). In principle this should be taken into account when calculating heat diffusion with all available energy sources, as in Eq. 2.9. However, the specific energy input of this process is orders of magnitude smaller than that of other available energy sources (Czechowski and Leliwa-Kopystyński, 2005), even for the largest and bulkiest TNO considered in this work.

When self-gravity is taken into account, the density is no longer uniform, and the solution of the hydrostatic equation requires an equation of state (EOS), i.e. a relation $P(\rho)$ for the solid matrix. The density distribution throughout the object is then obtained by solving (numerically) the hydrostatic equation, Eq. 2.19, combined with the mass conservation equation, $dm/dr = 4\pi r^2 \rho$, which leads to

$$\frac{d}{dr}\left[\frac{r^2}{\rho}\frac{dP(\rho)}{dr}\right] = -4\pi r^2 G\rho. \tag{2.20}$$

The solution of this second-order equation requires two boundary conditions or related properties. If we can derive from observations the object's radius and average bulk density (R and ρ), we can set one condition as $\int_0^R (4/3)\pi r^2 \rho(r) dr = M$.

Internal pressures in large icy objects (like the TNOs, discussed in Sec. 3.1, or some larger Cenraurs) are not expected to be high enough as to compress the solid component (rocks and/or ices), but only to reduce the porosity. In our numerical implemenatation this is achieved by using the density at each layer to calculate the related hydrostatic pressure from the EOS. The density distribution is affected by the porosity at each layer, which can vary due to thermal evolution effects of sublimation, gas flow and condensation in and through the porous medium. We then insert this pressure distribution into the hydrostatic equation, Eq. 2.20. The solution of the hydrostatic equation is constrained by demanding a user-supplied convergence accuracy (ϵ_{HY}, usually taken to be 10^{-5} in our models) for the central pressure, assuming porosity to be $\leq 1\%$. As we compute a density distribution, we can calulate the resulting total mass M and compare it to the boundary condition (see above) – We do not expect hydrostatic pressures to either compress or inflate the entire object, but only re-distribute the available pore spaces in the interior.

Since we set a vanishing porosity ($\leq 1\%$) as the convergence condition for the hydrostatic calculation, the corresponding pressure for this would be our adopted central pressure. This holds for all sizes of objects and has the same order of magnitude as the simple calculation of a spherical object with constant density, $P_c = \frac{2\pi}{3} G\rho^2 R^2$. For large objects (on the order of $500 - 1000$ km) with densities in the range of $1.5 - 2.5$ g cm^{-3} (see Brown, 2008), the corresponding central pressures are $\sim 0.1 - 1$ GPa.

In the deeper layers down to the core the material strength is at least comparable to the hydrostatic pressure. Thus, according to the values of the central pressure, we assume that the material strength is at the upper limit of the tensile strength range increased by an 1-2 orders of magnitude. This is done to take into account that the compressive strength may be greater than the tensile strength. The material strength in the outer layers, where self-gravity is negligible, is taken in the range of $10^4 - 10^5$ dyne cm^{-2}, which is also considered as the critical pressure for tensile fracture (see Prialnik *et al.*, 2004).

If we deal with a coupled calculation of thermal evolution and hydrostatic structure, we may need to consider the effects of temperature on the pressure. This thermal pressure can be defined as $\Delta P_T = \alpha K_T \Delta T$, where K_T the isothermal bulk modulus, T the local temperature and α is the thermal expansion coefficient, which has values on the order of $10^{-5}/K$, in planetary-related silicates (Poirier, 2000). Thus, is we take the bulk modulus to have an upper limit corresponding to the central pressure (for details see Sec. 2.7.3), the thermal pressure contribution would be several orders of magnitude lower than the gravity-induced pressure in the deep interior.

Solving Eq. 2.20, with the procedure described above, implies a porosity distribution, which in turn implies a distribution throughout the object of the thermal conductivity correction factor (see Sec. 2.3 and Prialnik *et al.*, 2008). Thus, the thermal and subsequent compositional evolution of an object large enough to be at least partly self-gravitating depends on the hydrostatic conditions in the interior.

In Fig. 2.4 and 2.5 we show the radial distributions of density, porosity, thermal conductivity correction factor (see Sec. 2.3) and hydrostatic pressure, for two models, representing the range of sizes and densities relevant for this work – 500 km radius and 1.5 g cm^{-3} bulk density (Fig. 2.4) and 1000 km radius and 2.5 1.5 g cm^{-3} bulk density (Fig. 2.5). In each figure, 3 dust/ice mass ratios have been adopted: for $\rho = 1.5$ g cm^{-3}, a range of 2-10, and for $\rho = 2.5$ g cm^{-3}, a range of 10-100. The minimum values correspond to nearly vanishing bulk porosity and the maximum values correspond to a bulk porosity greater than 0.5 (see Fig. 2.1 and the related discussion in Sec. 2.3). The larger object was assigned with the larger bulk density, as it is the conjectured trend for large TNOs (Brown, 2008). In each of the hydrostatic calculations we applied the Birch-Murnaghan EOS (see Sec. 2.7.1). The dust/ice mass ratio has an appreciable effect on the porosity profiles of self-gravitating large icy objects, especially in the outer layers of an object. Although the interior has very low average porosity, the outer layers are characterized by considerably high values of porosity, comparable to the small comet nuclei. This, in turn, affects the thermal evolution and composition of the outer layers, as the bulk thermal conductivity is less effective in the outer layers, where the correction factor is smaller (see Sec. 2.3). It is clear from both figures that as the porosity decreases with increasing depth, due to the hydrostatic pressures involved, the conductivity correction factor approaches unity and the relevant layers in the model become more and more convective. A complete closure of the pores is not allowed in our calculations and so a situation involving a fully convective layer is never reached.

2.7 Equation of State

Since the icy objects in question (mainly the TNOs) are relatively small and cold objects, with comparison to planets, an isothermal equation of state (EOS) may be used. Also, in the implementation of the EOS, we restrict our treatment to include only the "dust" component and the crystalline/amorphous phase of water ice (see Sec. 2.3). We are aware that there could be a density variation effect due to different phases of water ice, at pressures exceeding a few 10^8 Pa (Petrenko and Whitworth, 1999). However, different phases imply different specific densities and inclusion of all possible phases of water ice would mean adding them as separate components, due to the requirement of mass conservation (see Sec. 2.1). Each addiitonal component adds two more equations to solve and (2N-1) components to the matrix that we inverse each time step in the numerical code. Thus, in order to keep the computation manageable, but still include other volatiles other than water, we need to constrain the number of composition components we implement.

2.7.1 Birch-Murnaghan EOS

The most commonly used universal EOS is the finite strain Birch-Murnaghan (B-M) equation. It is based on a finite hydrostatic compression, under an Eulerian scheme (Birch, 1947). It is derived from a power series expansion of the Helmholtz free energy to second order in the form

$$P = \frac{3K_{0T}}{2}\left[\left(\frac{\rho}{\rho_0}\right)^{(7/3)} - \left(\frac{\rho}{\rho_0}\right)^{(5/3)}\right], \tag{2.21}$$

where ρ_0 is a reference value for the the density and K_{0T} is the isothermal bulk modulus, both at $P = 0$ (Poirier, 2000). The bulk modulus can be derived by using $K = \rho\,(dP/d\rho)$, and the pressure derivative of the bulk modulus is given by $K_0' = (dK/dP)_{P=0}$.

Poirier (2000) notes that for the infinitesimal case, where the compression tends to zero, the application of finite strain theory yields $K_0' = 4$. This is the measured value

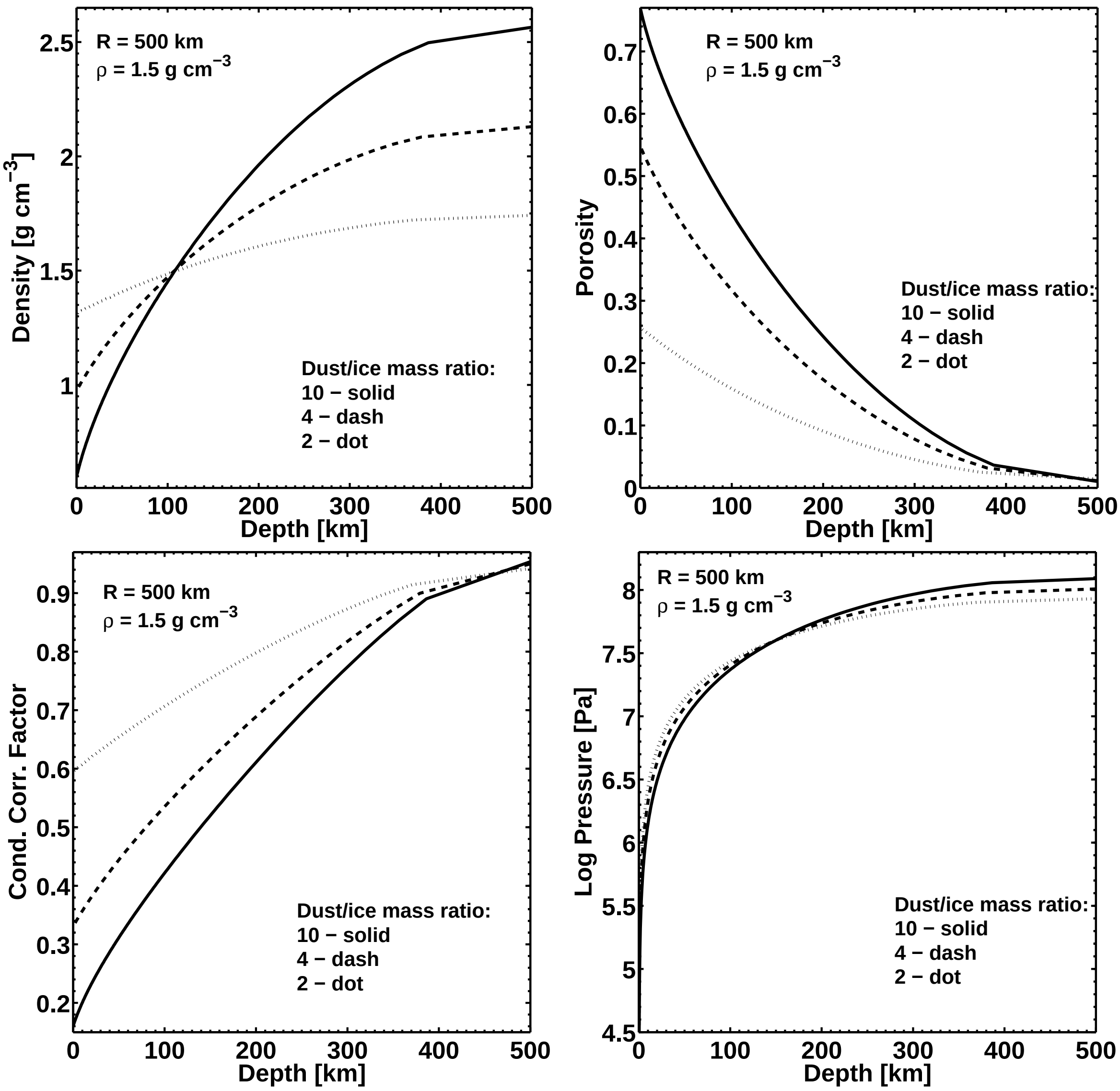

Figure 2.4 Radial distributions of density, porosity, thermal conductivity correction factor (Cond. Corr. Factor) and pressure, for an object with a 500 km radius and 1.5 g cm^{-3} bulk density. The solid, dashed and dotted curves represent initial dust/ice ratios of 10 (for bulk porosity ¿ 0.5), 4 and 2 (for a vanishing bulk porosity), respectively, with the surface at depth zero. Note that all density curves intersect at the value of the bulk density. Also note that the porosiy at the center reaches the convergence condition (porosity of 1%) set for the hydrostatic calculation (see Sec. 2.6).

for many mantle-comprising minerals, namely Perovskite and Enstatite, which are also representatives of meteoritic chondrits and cometary silicate dust compounds (Hanner and Bradley, 2004; Scott, 2007). Higher term expansions can be performed to the B-M EOS, which are mostly used for higher-pressure cases (for a recent example see Valencia *et al.*, 2006). However, as noted by Poirier (2000), for the case of $K_0' = 4$, the higher term

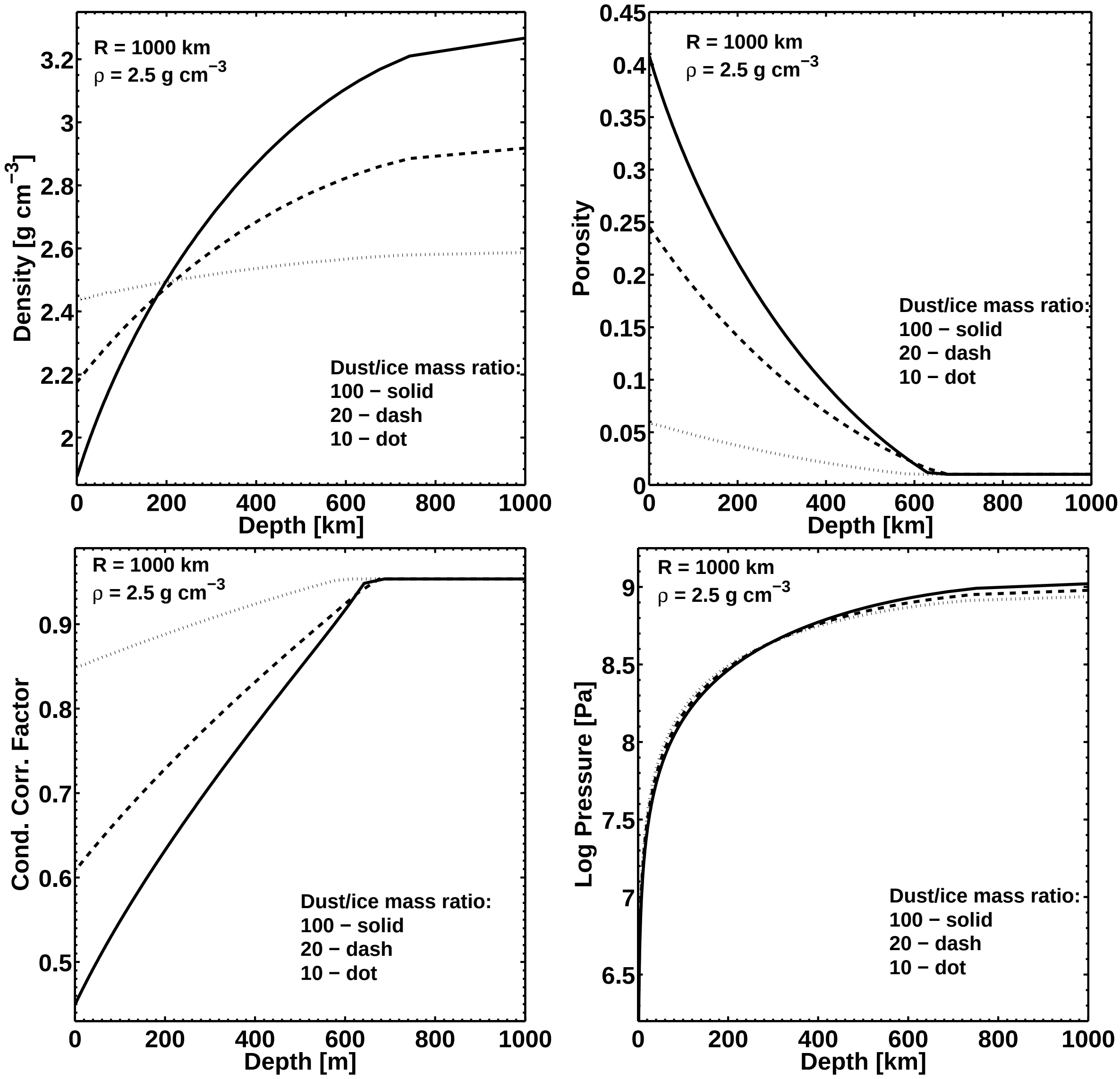

Figure 2.5 Radial distributions of density, porosity, thermal conductivity correction factor (Cond. Corr. Factor) and pressure, for an object with a 1000 km radius and 2.5 g cm^{-3} bulk density. The solid, dashed and dotted curves represent initial dust/ice ratios of 100 (for bulk porosity ¿ 0.5), 20 and 10 (for a vanishing bulk porosity), respectively, with the surface at depth zero. Note that all density curves intersect at the value of the bulk density. Also note that the porosiy at the center reaches the convergence condition (porosity of 1%) set for the hydrostatic calculation (see Sec. 2.6).

vanishes and we are left with the second-order B-M EOS.

2.7.2 Vinet EOS

Another fairly common choice is the Vinet equation (Vinet *et al.*, 1987), which is derived from an empirical potential. It is appropriate for high-pressure and very compressible solids, but also provides a good fit for Perovskite (Hama and Suito, 1998). Thus, it has been recently applied in modeling of planetary objects (Valencia *et al.*, 2007). The complete form of the EOS is given by (Poirier, 2000)

$$P = 3K_{0T}\left(\frac{\rho}{\rho_0}\right)^{2/3}\left[1-\left(\frac{\rho}{\rho_0}\right)^{-1/3}\right]\exp\left\{\frac{3}{2}\left(K_0'-1\right)\left[1-\left(\frac{\rho}{\rho_0}\right)^{-1/3}\right]\right\}. \tag{2.22}$$

Since for objects relevant to our studies we expect moderate-to-low compressions (ρ/ρ_0), we may expand the exponent term and neglect second order terms, to derive an approximated form of the Vinet EOS as

$$P = 3K_{0T}\left[\left(\frac{\rho}{\rho_0}\right)^{(2/3)}-\left(\frac{\rho}{\rho_0}\right)^{(1/3)}\right]. \tag{2.23}$$

Although this approximation is strictly valid only for compressions close to unity, the exponential term from Eq. 2.22 can still be neglected for a wider range of ρ/ρ_0. Fig. 2.6 demonstrates that the exponential term in the Vinet EOS (Eq. 2.22) results in a factor on the order of unity, for the adopted range of ρ/ρ_0. This holds for the different values of K_0', wihch represent our knowledge of mantle-comprising minerals and cometary silicates (Poirier, 2000; Scott, 2007). We should note that the adopted value of $K_0' = 4$, from the B-M EOS discussion (Sec. 2.7.1), results in a factor of 1-5. This value for K_0' is also about the average for the pyroxene silicate minerals (Poirier, 2000), which are one of the most common cometary silicate compounds (Hanner and Bradley, 2004).

Poirier (2000) notes that for $K_0' \approx 3.5$, the expressions of B-M and Vinet (complete form, Eq. 2.22) give practically the same results. Also, by following the analysis in Poirier (2000) of "universal" EOSs and comparing it with Eq. 2.23, we conclude that the B-M and approximated Vinet equations serve as upper and lower limit cases for most EOSs, respectively. This holds for most of the relevant ranges of K_0' and ρ/ρ_0 (low-to-moderate compression icy objects) and relevant rock/silicate components.

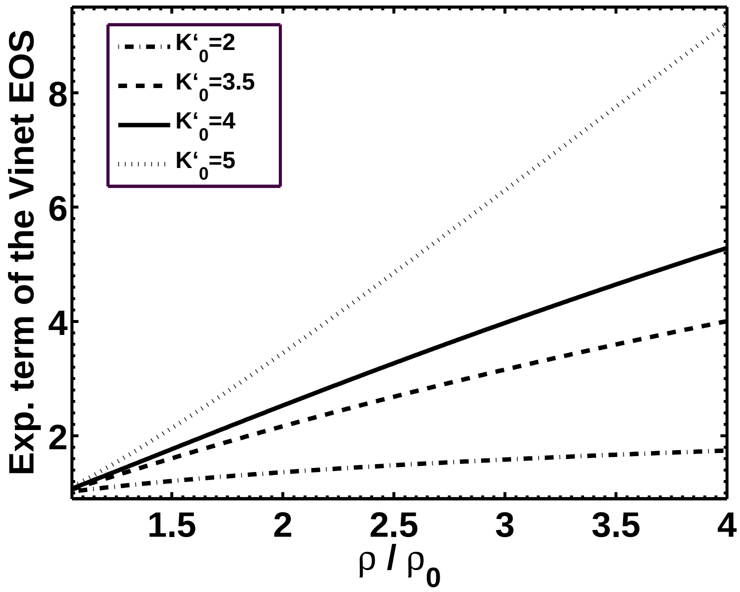

Figure 2.6 Magnitude of the exponential term of the Vinet EOS (see Eq. 2.22 in the text) as a function of ρ/ρ_0, for different values of the pressure derivative of the bulk modulus. Note that for all the acceptable values of K_0', the exponential term contributes a factor of a few at most. For the adopted value of $K_0' = 4$ (solid curve), the factor is 1–5.

2.7.3 Stability Analysis

We may write a general expression for the pressure-density polytropic relation, as a second order approximation, in the form

$$P(\rho) = K\left[\left(\frac{\rho}{\rho_0}\right)^{\alpha_1} - \left(\frac{\rho}{\rho_0}\right)^{\alpha_2}\right], \tag{2.24}$$

where $\alpha_1 > \alpha_2$ and ρ_0 is the density at a reference plane where the pressure vanishes. By defining P_c as the central pressure, where $\rho = \rho_c$, we can re-write the above expression as

$$(1-\beta)\, y = x^{\alpha_1} - \beta x^{\alpha_2}, \tag{2.25}$$

where we have defined the following:

$$\begin{aligned} y &= \frac{P}{P_c}, && 0 \le y \le 1, \\ x &= \frac{\rho}{\rho_c}, && \beta^{\left(\frac{1}{\alpha_1-\alpha_2}\right)} \le x \le 1, \\ \beta &= \left(\frac{\rho_0}{\rho_c}\right)^{\alpha_1-\alpha_2}. && \end{aligned} \tag{2.26}$$

In order to examine the stability of hydrostatic equilibrium, we use the stability condition for a polytropic relation (Prialnik, 2000), $\gamma > 4/3$, where the adiabatic index,

$\gamma = (d \ln P / d \ln \rho)$, may be expressed as

$$\gamma = \frac{x}{y}\frac{dy}{dx} = \frac{\alpha_1 x^{\alpha_1} - \beta \alpha_2 x^{\alpha_2}}{x^{\alpha_1} - \beta x^{\alpha_2}}, \tag{2.27}$$

We now differentiate γ with respect to the independent variable x

$$\frac{d\gamma}{dx} = \frac{-\beta \left(\alpha_1 - \alpha_2\right)^2 x^{\alpha_1 + \alpha_2 - 1}}{\left(x^{\alpha_1} - \beta x^{\alpha_2}\right)^2}. \tag{2.28}$$

and look at the gradient of the adiabatic index. The denominator of (2.28) is always positive, whereas the numerator is always negative. Thus γ is a decreasing function of x, and the minimal value is given by γ

$$\gamma_{min} = \gamma(x = 1) = \frac{\alpha_1 - \beta \alpha_2}{1 - \beta}. \tag{2.29}$$

The stability condition now becomes

$$3\alpha_1 - 4 > \beta \left(3\alpha_2 - 4\right). \tag{2.30}$$

Since $\beta > 0$ by its definition, we conclude the following:

(i) Having $\alpha_1 > 4/3$, requires that also $\alpha_2 > 4/3$ and we have $\beta < n$, with $n > 1$. Since $\rho_0/\rho_c < 1$ (the density at the surface is always smaller than the central density), there is no restriction on this ratio set by the stability condition(of course, we must note that the actual value of n is set by the exponents of the EOS). This is the case for the B-M EOS ($\alpha_1 = 7/3$, $\alpha_2 = 5/3$), where we have $\beta < 3$, which results in $\rho_0/\rho_c < 5.2$.

(ii) Having $\alpha_1 < 4/3$, requires that also $\alpha_2 < 4/3$ and we have $\beta > m$, with $0 < m < 1$. The restriction on the density ratio is now $m^{1/(\alpha_1 - \alpha_2)} < \rho_0/\rho_c < 1$. This is the case for the approximated Vinet EOS ($\alpha_1 = 1/3$, $\alpha_2 = 1/3$), where we have $\beta > 2/3$, which reaults in a narrow range of accepted values for the density ratio, $0.3 \lesssim \rho_0/\rho_c < 1$.

Condition (i) should always be met by the icy dwarf planets in question. According to condition (ii), if we choose ρ_0 and evolve an object, under hydrostatic conditions, the Vinet EOS might not be stable for the whole duration of the evolution, as the central density (pressure) varies in time.

Fig. 2.7 shows a comparison between the B-M and approximated Vinet formulations, in terms of the dependence of the pressure and the density gradient of the pressure, on the density. All physical quantities are normalized (pressure by the isothermal bulk modulus, K_{0T}, and density by the reference density, ρ_0). From the trends of the curves we can conclude that the two EOSs may be regarded as "stiff" (B-M) and "soft" (Vinet), where "stiff" means a strong dependence of pressure on density, while "soft" implies a shallow slope for $P(\rho)$. In the "soft" case, as density increases, $dP/d\rho$ remains constant, indicating that the propagation velocity of perturbations in the material is almost constant. Thus, in the "soft" case perturbations are almost undamped, while in the "stiff" case, perturbations dissipate and damp significantly, as the matrix becomes denser.

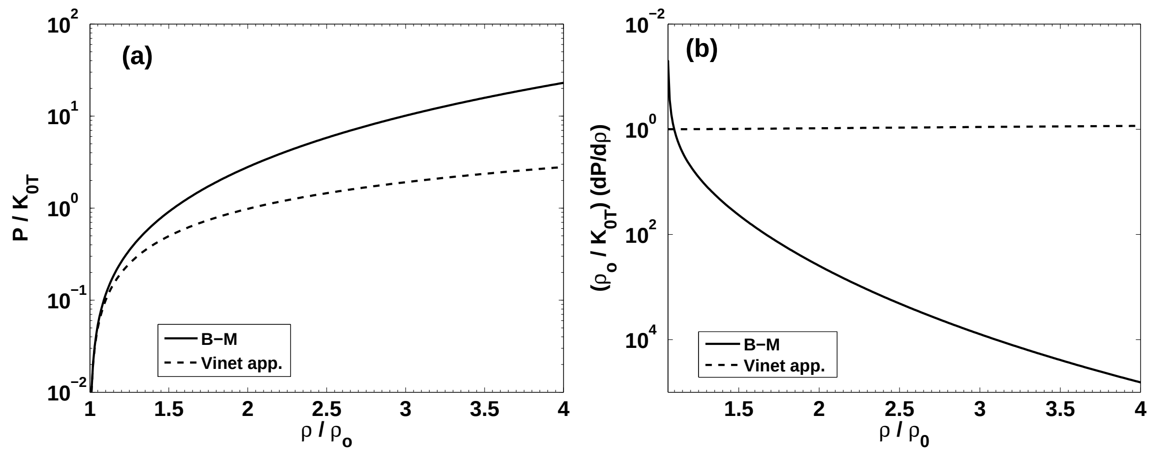

Figure 2.7 EOS curves, for the B-M (solid) and Vinet (dashed) formulations. *(a)*: Pressure-density relation, on a log scale. Note that for the B-M formulation the pressure is much more steeply dependent on the density, thus making it a "stiffer" EOS. *(b)*: $dP/d\rho$-density relation, on a log scale. Note that for the Vinet formulation $dP/d\rho$ remains almost constant, thus enabling perturbations to retain the same propagation velocity as the matrix becomes denser, and making it a "softer" EOS.

Finally, both equations of state have two material parameters: K_{0T} and ρ_0. We do not have sufficient information on the material properties of the objects we are modeling to set these as independent input to the model. However, we have from observations estimates of the masses and radii of the different objects and this is sufficient for determining the two parameters iteratively, by demanding $\int_0^R (4/3)\pi r^2 \rho(r) dr = M$ and $\rho(R) = \rho_0$. Our iterataive scheme follows: (i) Set ρ_0/ρ_c (according to the abovev stability analysis) and $K_{0T} = P_c$, initially; (ii) Solve the hydrostatic equation and derive the hydrostatic radius, $R_{HS} = \left(\frac{3M}{4\pi\rho_b}\right)^{1/3}$, where ρ_b is the 'known' bulk density of the object; (iii) If

$1 - R_{HY}/R_b > \epsilon_{HY}$, where R_b is the object's radius, adjust K_{0T} and repeat the former step; (iv) If after a certain number of iterations, there is no convergence of the numerical hydrostatic solution, adjust ρ_0/ρ_c and start the iterations again. Eventually, what we have are the EOS parameters that best reproduce the size and mass of the object.

We repeat the iterative process every pre-set number of time-steps (usually, a few 10^4 steps). Thus, if the internal configuration changes dramatically, due to onset of sublimation or migration of volatile species, the density changes affect the properties of the EOS. However, in all of our models, the changes have never been greater than a few percent.

2.8 A "Thermal" Impact

We simulate the thermal effect of an impact or collision by assuming an additional energy influx, for an infinitesimal period of time. The known input parameters for calculating the impact are the total (kinetic) energy of the projectile/impactor (E_{tot}), the estimated area that will be affected by the collision (A) – which is needed in order to obtain an energy flux – and the location in the orbit, stated as a heliocentric distance, where the impact is expected to occur (d_0). The total energy absorbed per unit area is $E_A = E_{tot}/A$. We note that the relevant parameter is E_A, hence the calculation is not sensitive to the total impact energy or the area, separately. In order to take into account some of the complexities of internal energetics of the impact/cratering process, we can express the total energy due to the impact as $E_{tot} = \epsilon E_k$. Here, E_k represents the projectile's kinetic energy and ϵ is the efficiency of conversion of kinetic energy to the internal energy available for thermal alteration. However, due to the lack of any further data and/or modeling, we take an upper limit assumption of maximal efficiency, $\epsilon = 1$.

Since numerical calculations do not allow for singularities, we assume the energy deposition rate to be in the form of a narrow time-dependent Gaussian (rather than a delta function), **centered** at the time of the collision, with a width corresponding to the timescale for the formation of an impact crater,

$$F(t) = F_0 e^{-\pi[(t-t_0)/\tau]^2}. \tag{2.31}$$

Here τ is a free numerical parameter that may be interpreted as the impact timescale. Normalizing the deposition rate,

$$\int_{-\infty}^{\infty} F(t)dt = E_A, \tag{2.32}$$

we obtain $F_0 = E_A/\tau$. Thus, the amplitude of the energy deposition rate is related to the physical parameters of the impact. The time of impact t_0 is calculated by

$$\begin{aligned} t_0 &= \sqrt{a^3/GM_\odot}(2\pi n - \pi - \vartheta_0 + e\sin\vartheta_o) \\ \vartheta_0 &= \cos^{-1}[(1 - d_0/a)/e], \end{aligned} \tag{2.33}$$

where a and e are the semi-major axis and eccentricity of the target object and n is the number of orbital revolutions calculated prior to the collision.

At the onset of an impact – defined to occur at a time $t_0 - \nu\tau$, where $\nu > 1$, so that $F(t \pm \nu\tau) \ll F_0$ – we remove from the model of the target object a layer of thickness ΔL, to simulate the formation of a crater. Thus the thermal energy is deposited below the original target surface, where the composition had been either preserved, or altered by earlier evolution. We should bear in mind that the kinetic energy of the collision is not necessarily transformed completely to thermal energy available for heating. It could also be partitioned into mechanical (or elastic) energy for the deformation of the impacted material and kinetic energy for the launching of debris. Since our model does not track the mechanical deformation of material or the disruption of objects, we can treat this energy partition by assigning an efficiency factor, h, that determines what fraction of the original kinetic energy energy is actually transformed into thermal energy. In order for the thermal effect of a collision to be maximized, we can assume h to be close to, or equal, to unity. Another amplification of the thermal effect is due to the deposition of heat at a depth corresponding to the bottom of the impact crater, ΔL.

3

Evolution of Trans-Neptunian Objects

In this chapter we utilize the general thermal evolution model described in Ch. 2 and apply it to the modeling of specific trans-Neptunian objects. These objects represent a sample of the various physical characteristics attributed to TNOs.

Section 3.1 presents long-term thermo-chemical and structural simulations of several large ($R \geq 100$ km) TNOs. These objects span the range of size-density-composition expected from this population and are among the best observed objects in this group.

Section 3.2 presents what we consider as the end states of a 1000-km scale object, (50000) Quaoar, and two 100-km scale objects, 1992 QB_1 and 1998 WW_{31}. These are records of the internal configuration, up to the sub-surface layers, after almost all of the thermal processing has been quenched.

3.1 The Inner-Workings of Trans-Neptunian Objects

3.1.1 Introduction

Considered as remnant planetesimals, from the early accretion phases of the solar system, formed farthest out from the Sun, TNOs are believed to constitute an important reservoir of primitive material (Luu and Jewitt, 2002), perhaps the least thermally processed. But although TNOs are among the coldest objects known in the Solar System, and are mostly considered to be geologically and thermally inert (McKinnon, 2002), some of them show evidence of internal activity to some extent (Jewitt and Luu, 2004; Brown, 2008; Stern and Trafton, 2008).

Evidence for water ice was discovered in the spectrum of two KBOs (Jewitt and Luu, 2004), indicating a more direct physical kinship of these objects to comets. This view is interesting because it allows for the possibility that the material in JFC nuclei may have been modified from its primordial condition. It could have been internally "cooked", within the larger TNOs, during their lifetime. It could also have been shocked and altered by some of the collisions responsible for creating the small nucleus fragment.

The purpose here is to model the thermal evolution of a sample of representative TNOs for extended times, in order to assess the extent of internal processing that such objects may have undergone and thus gain insight into the initial conditions (structure and composition) of comets originating from the trans-Neptunian zone.

3.1.2 Model assumptions and choice of key parameters

In order to follow the thermo-chemical evolution in the trans-Neptunian region we need to choose the parameters of the objects to be modeled. The TNOs chosen for this study, are among the best observed objects of this group. This means that although our parameter space of physical characteristics is still large, these objects represent a group for which we know at least some of the basic attributes.

The main parameters are listed in Table 3.1, along with the appropriate references. We have chosen the initial parameters so as to take in consideration the estimated mass and compositions of these objects. Briefly stated, the values in Table 3.1 span over the range of the size-density-composition parameter space for large icy objects. Table 3.2 lists the initial physical parameters chosen for each object.

Table 3.1 Known properties of the modeled TNOs

Designation	a (AU), e [1]	R (km)	A [2]	ρ (g cm^{-3})	Ref. A [3]
1992 QB1	44.08, 0.073	100	0.04	0.75	Jewitt and Luu (1993) Luu and Jewitt (2002)
(20000) Varuna	42.82, 0.056	300	0.21	1.0	Stansberry *et al.* (2005) Jewitt and Sheppard (2002)
(50000) Quaoar	43.53, 0.039	630	0.1	1.5	Brown and Trujillo (2004) Luu and Jewitt (2002)
(136199) Eris	67.96, 0.435	1200	0.85	2.3	Brown (2008) Brown *et al.* (2006)

[1] Semi-major axis and eccentricity (from MPC database).
[2] Average albedo.
[3] References from which R, A and ρ are taken.

Table 3.2 Initial physical parameters for the modeled TNOs

Object	$T_{init.}$ [1]	$X_{am.}$ [2]	$X_{d.}$ [3]	$X_{CO,CO_2,HCN}$ [4]	$\Psi_{init.}$ [5]	Rad. [6]
1992 QB1	48	0.45	0.55	(0.005, 0.005, 0.0025)	0.5	^{26}Al, ^{60}Fe
Varuna	45	0.35	0.65	(0.005, 0.005, 0.0025)	0.4	^{26}Al, ^{60}Fe, All
Quaoar	46	0.3	0.7	(0.005, 0.005, 0.0025)	0.2	^{26}Al, ^{60}Fe, All
Eris	28	0.08	0.92	(0.005, 0.005, 0.0025)	0.1	All

[1] Initial (uniform) temperature (radiative equilibrium, at aphelion).
[2] Initial mass fraction of amorphous water ice.
[3] Initial mass fraction of dust (rock/mineral).
[4] Initial fraction of occluded volatile gases in the amorphous ice.
[5] Initial bulk porosity.
[6] Active radionuclides considered (All meaning short and long-lived species).

In order to have a common ground to compare the different results of the evolution calculations, we have to take the leading structural and compositional parameters to be the same. These are listed in Table 3.3. For the composition, other than water ice, we take the three most common volatile compounds in planetary environments – CO, CO_2 and HCN (Bergin *et al.*, 2007). These are also among the most abundant cometary volatiles observed (Bockelée-Morvan *et al.*, 2004). We assume that water ice is initially in an amorphous phase and the volatile compounds are trapped as occluded gas in the ice (Prialnik *et al.*, 2008).

In this study we attempt to investigate the combined effects of self-gravity and thermal evolution, on the internal configurations of relatively large TNOs. Thus, an equation of state that has greater dependence on the internal conditions, may lead to internal evolution processes that can be examined by observation. Following the analysis in Sec 2.7.3, we explore in some more detail the application of the Vinet EOS (see Sec. 2.7.2 for a description). The B-M EOS has been applied to the models of larger objects ($R > 100$ km) with all possible radionuclides included (see Table 3.4). This is because we would like to examine the maximum influence this "stiffer" EOS has on the thermal conditions at the early and late stages of TNO internal evolution. Specifically for the model of Eris, the hydrostatic properties that we fit from the convergence of the hydrostatic equation (see discussion at the end of Sec. 2.7.3) are very similar between the Vinet and B-M EOS.

Table 3.3 Common input physics parameters for all models of TNOs

Parameter	Symbol	Value	Units
Specific H_2O ice density	$\varrho_{\rm ice}$	0.917	g cm^{-3}
Specific dust density	$\varrho_{\rm dust}$	3.25	g cm^{-3}
Ice heat capacity	$c_{\rm ice}$	$7.49 \times 10^4 T + 9 \times 10^5$	erg g^{-1} K^{-1}
Dust heat capacity	$c_{\rm dust}$	1.3×10^7	erg g^{-1} K^{-1}
C-Ice conductivity	$K_{\rm C-ice}$	$5.67 \times 10^7/T$	erg cm^{-1} s^{-1} K^{-1}
Dust conductivity	$K_{\rm dust}$	10^6	erg cm^{-1} s^{-1} K^{-1}
A-Ice diffusivity	$\kappa_{\rm A-ice}$	3×10^{-3}	cm^2 s^{-1}
Pore-size distribution [1]	α	3.5	
Pore size range [2]	X	10^4	

[1] Exponent for initial power-law distribution of pore sizes, as in comets (Sarid *et al.*, 2005).
[2] Ratio of maximal to minimal pore radius, as in comets (Sarid *et al.*, 2005).

These result in a factor of ~ 1.2 comparing the bulk moduli and essentially the same reference density.

The time scale for thermal evolution simulations is limited by computational constraints. Thus, we have chosen it so as to enable a sufficiently long evolution duration for each object (i.e., to track long-term trends) and to be in agreement with collisional and orbital diffusion time scales in the Kuiper belt, as derived from dynamical studies (Durda and Stern, 2000; Morbidelli, 2008).

3.1.3 Results of Internal Evolution

Each evolution run of the TNOs presented in Table 3.1 covers a period of time starting at an early epoch and ending when a slowly-evolving state is reached. By slowly-evolving we mean that compositional and/or structural configuration no longer varies and the cooling rate decreases monotonically, as a function of the decreasing temperature alone. These times exceed the half-life times of the short-lived radioactive isotopes, which constitute the main energy source. We present results as a function of depth, $z = R - r$, or relative depth, z/R.

The three classical TNOs in our sample have radii and bulk densities such that self-gravity plays a significant role (see Table 3.1 and Sec. 2.6). The orbital elements of these objects place them well inside the Kuiper belt, which means that their long-term thermal evolution is controlled by radiogenic heating and, subsequently, by the phase transition of amorphous to crystalline water ice (Choi *et al.*, 2002). Since the evolution times are only a small fraction of the dynamical stability timescales (a few 10^9 yr for dynamically “cold” classical TNOs, following Lykawka and Mukai, 2005), the orbital parameters are kept constant.

The forth object, Eris, has a radius which is an order of magnitude larger than that of the other objects modeled in this study. Consequently, the central pressure exceeds 1 GPa, which only permits very low to negligible porosity close to the core (McKinnon, 2002). Since the numerical computation of gas flow requires a lower limit for the porosity ($\sim 1\%$), for the purpose of maintaining a continuous flow, we follow the thermal evolution of Eris only until the bulk porosity near the center ($z/R \geq 0.8$) has reached this limit. This results in a shorter evolution time for this simulation, which also agrees with its classification as a scattered-disk object (SDO). This dynamical population has, on average, a shorter dynamical stability timescale than classical TNOs (Gomes *et al.*, 2008).

Fig. 3.1 shows pressure profiles of the four objects. These curves present the hydrostatic equilibrium pressure attained within the objects, as a function of relative depth. This is done in order to enable a clear comparison of the pressure distributions. These are the values of the solid matrix pressure obtained at the end of the simulation for each object, where a B-M EOS was used with an energy input from all available radioactive isotopes.

Gas pressures were included but are exteremely negligible, because at these long evolution times all volatiles have either escaped, re-condensed or are sublimating at a very slow rate.

Table 3.4 summarizes some key results from the various model simulations we ran for the four objects in our sample. We record here the compositional, thermal and structural properties at the end of each evolution run. The third column, Z(am.$\Leftrightarrow$cry.), shows the minimal distance, below the surface, at which amorphous and crystalline water ice can be found in similar abundances. This means that if we go deeper inside the object, amorphous ice will be at negligible abundances or depleted altogether. The layers between this depth and the surface are predominantly amorphous. The fourth column, Z(vol. ice), shows the minimal sub-surface depth, at which the first non-negligible concentration of re-frozen volatile ices is found. We choose a value $\gtrsim 0.1\%$ because it is of the order of the initial

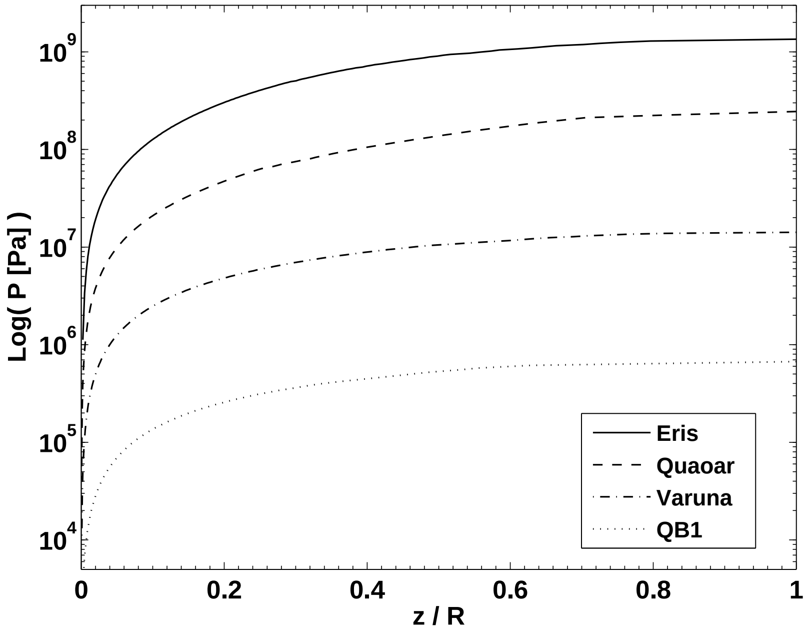

Figure 3.1 Pressure profiles for the solid matrix of the four TNOs. Profiles (on a log scale) are presented as a function of relative depth inside the object, from surface (z/R=0) to core (z/R=1). These are results of models implementing the B-M EOS and the energy input of all available radionuclides.

fraction of the occluded volatile gases in the amorphous ice (see Table 3.2). The fifth and sixth column are the temperature and total density, respectively, for each of the minimal depths mentioned. These are taken as averages of the values (temperature or density) in the layers adjacent to the minimal depths.

All of the objects reached a slowly-evolving state, where the cooling rate remains constant and low (or very close to it). Since further structural or compositional evolution is negligible (barring external effects), these end-configurations should represent the expected range of sub-surface conditions within relatively large icy TNOs.

Fig. 3.2 shows results of long-term evolution calculations for the three classical TNOs, with an application of the Vinet EOS and ^{26}Al. Each column displays the profiles of temperature, porosity, mass fraction of amorphous ice, and total mass fraction of CO_2 and HCN ices; CO ice is very rapidly depleted, as its sublimation temperature is lower than any temperature found inside the objects. Profiles are shown as a function of time ($\sim 10^5$ to 10^8 yr, on a logarithmic scale) and relative depth z/R, from surface ($z/R = 0$) to center ($z/R = 1$). Fig. 3.3 shows the temperature and porosity profiles for Eris, as a function of relative depth, at the end of the evolution run ($\sim 10^7$ yr), with an application of

Table 3.4 Results of model calculations for modeled TNOs - end of evolution (100 Myr)

Object	(model) [1]	Z (am.⇔cry.) [2] [km]	Z (vol. ice) [3] [km]	T(Z) [4] [K]	ρ(Z) [5] [g cm^{-3}]
1992 QB1	(Vinet, ^{26}Al)	7	9	78 ; 90	0.70 ; 0.70
	(Vinet, ^{60}Fe)	9	15	74 ; 90	0.70 ; 0.70
Varuna	(B-M, all)	2	38	45 ; 72	1.00 ; 1.04
	(Vinet, all)	5	7	57 ; 61	0.95 ; 0.96
	(Vinet, ^{26}Al)	4	14	50 ; 62	0.95 ; 0.96
	(Vinet, ^{60}Fe)	7	9	60 ; 65	0.96 ; 0.96
Quaoar	(B-M, all)	3	44	46 ; 74	1.21 ; 1.35
	(Vinet, all)	4	29	48 ; 76	1.01 ; 1.09
	(Vinet, ^{26}Al)	11	16	56 ; 61	1.03 ; 1.04
	(Vinet, ^{60}Fe)	12	16	57 ; 61	1.03 ; 1.05
Eris *	(B-M, all)	10	61	92 ; 119	1.06 ; 1.34

[1] EOS and radioactive energy source of the model.
[2] Shallowest depth (distance from the surface) of the transition layer between amorphous and crystalline water ice.
[3] Shallowest depth (distance from the surfae) of a layer with non-negligible abundance of volatile ices ($\gtrsim 0.1\%$ by mass).
[4] Temperature corresponding to the third and forth columns, respectively.
[5] Desnsity corresponding to the third and forth columns, respectively.
* This object has a shorter evolution time than the others (see Sec. 3.1.3).

the B-M EOS and all radioactive isotopes. In what follows we detail the results of internal evolution from the simulations we ran for each of the objects, with various configurations.

1992 QB1

QB1 is the smallest object of our sample, and has a low bulk density. We have thus taken its initial porosity to be high, $\Psi = 0.5$, corresponding to an ice to dust ratio of ~ 0.8. Two models of this object were evolved, with different radioactive sources (see Table 3.2), both considered short-lived. The differences in the results of these calculations are marginal.

The model evolved with ^{26}Al as a sole heating source, experiences an earlier onset of heating and a sharper initial gradient of temperature, due to the fact that the characteristic lifetime of ^{26}Al is about half that of ^{60}Fe and their specific powers differ by

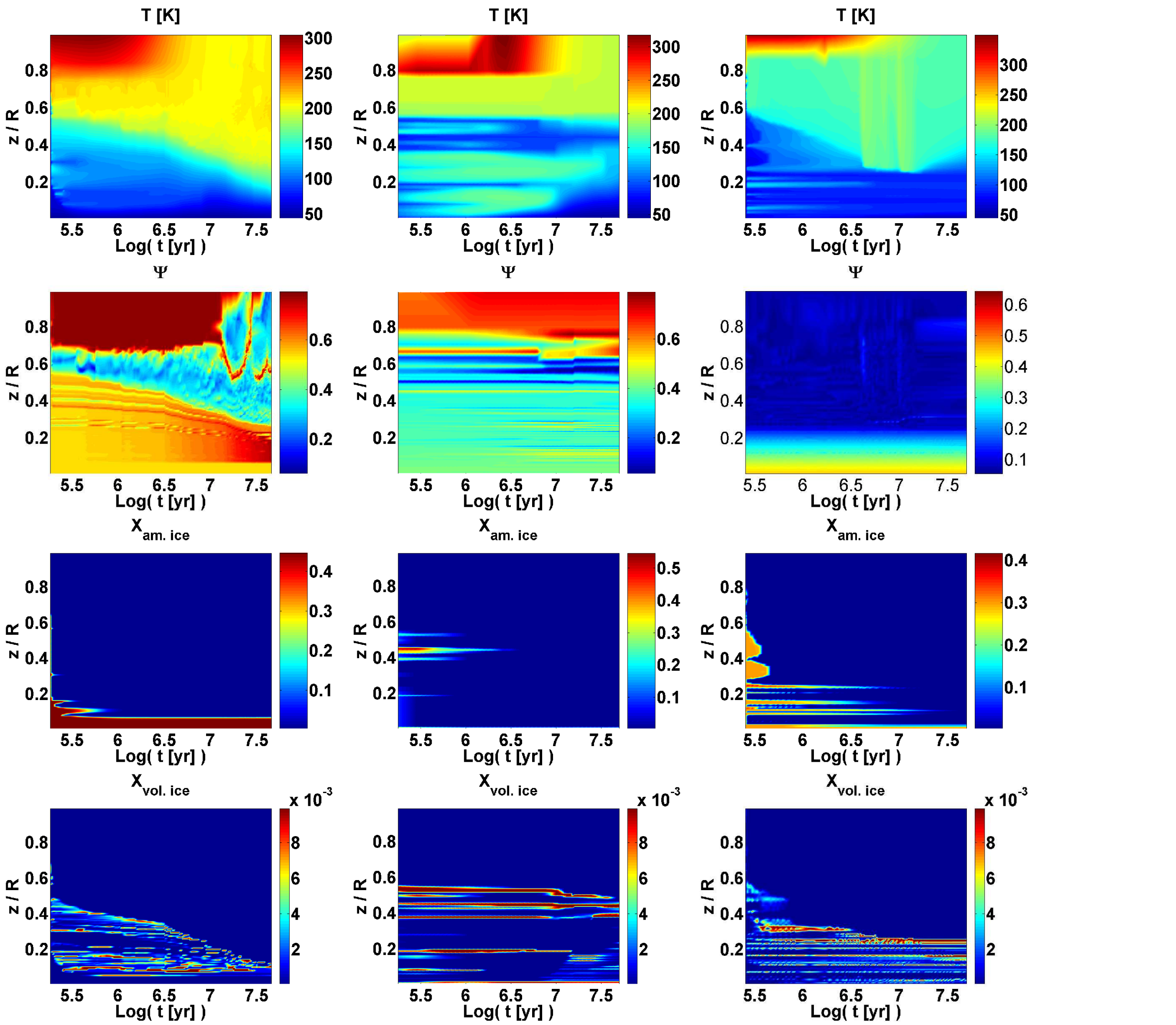

Figure 3.2 Evolution of the internal profiles of 1992QB1 (left column), (20000) Varuna (middle column) and (50000) Quaoar (right column). Profiles are shown for temperature (top row), porosity (second row), abundance of amorphous ice (third row) and abundance of volatile ices (bottom row). Time is given on a logarithmic scale, up to ~ 100 Myr and the depth scale is normalized by the objects radius, R, from surface (denoted by 0) to core (denoted by 1). Note that color scales may vary, between panels representing the same physical value.

about an order of magnitude (see Sec. 2.5). However, after the initial phase of heating ($\sim 10^5 - \sim 10^6$ yr), the rate of cooling is essentially the same, as the maximal temperature, density distribution and porosity-dependent conductivity attained are similar. This is also true for the gas flow and pressure. After an initial rapid build-up of pressure in the deep interior, due to the release of trapped gases during crystallization and sublimation of water ice, the pressure is quickly dissipated by the gas flow towards the outer layers. When gases reach the outer regions, where temperature are significantly lower ($\lesssim 120$ K), the pressures and fluxes subside and become negligible.

The left column of Fig. 3.2 shows the thermal, structural and compositional evolution of QB1 (using the Vinet EOS), with ^{26}Al as the primary heat source. The peak temperature attained is ~ 300 K and it is maintained in the deep interior ($\sim 80-100$ km below the surface) for up to $\sim 2-3\times10^6$ yr. From this point on the deep interior cools, while the mid-layers accumulate heat, due to energy released by crystallization of amorphous ice and the residual radioactive heating. This results in most of the interior reaching a temperature of ~ 200 K, with the outer layers ($z/R < 0.2$) remaining at temperatures lower than 100K and the immediate sub-surface layers remaining in the radiative equilibrium temperature of ~ 50 K.

Porosity remains constant and high (> 0.5) in the sub-surface layers for the entire duration. In the mid-layers it is high at the beginning, declining to slightly lower values ($\sim 0.3-0.4$) towards the end of the evolution. The distinct "cavity" in the core ($\Psi \geq 0.7$) for over 10^7 yr of evolution is due to the sublimation of water ice and subsequent outflow of all material except for the large dust grains. This is because compression is not strong enough to quench porosity in the deep interior, so material leaves relatively easily. Eventually, as temperatures decrease, there is slow condensation of residual vapor on the pore walls and the porosity decreases.

In terms of composition, amorphous ice can be found only in the outer layers ($z/R < 0.1$), where it retains its initial abundance. All of the interior has crystallized, with intermediate "pockets" of volatile ices. These intermittent layers of volatile ices are slowly depleted, until they are only found in the outer layers ($z/R < 0.2$), somewhat deeper than the amorphous ice layers.

(20000) Varuna

For this object we have taken a slightly higher dust/ice ratio than for QB1, so it would reflect its larger size and mass (see Table 3.2). Thus, in accordance with its estimated bulk density, the initial bulk porosity was set to 0.4. Models of this object were evolved with three different radioactive heating sources (^{26}Al, ^{60}Fe and a combination of all available short-lived and long-lived isotopes), and with two different EOSs (B-M and the approximated form of Vinet, see Sec. 2.7).

The middle column of Fig. 3.2 shows the evolution of Varuna (using the B-M EOS), with ^{26}Al as the only heat source. A peak temperature of ~ 320 K is reached in the deep interior ($240-300$ km below the surface) after 10^6 yr, persisting for $\sim 3\times10^6$ yr. After this period, the interior starts to cool, with a tendency towards an almost steady temperature of ~ 200 K within 50% of the bulk. The mid-layers experience a rise in temperature, to ~ 150 K, during the first 10^7 yr of evolution, due to heat release by radioactive decay and ongoing crystallization of amorphous ice. The surface and near-surface layers (~ 3 km below the surface) are kept at the equilibrium temperature with the environment, ~ 50 K. After 10^7 yr there is gradual cooling at all depths. At the end of the evolution, the outer regions (from the surface down to ~ 30 km) are cooled to the equilibrium temperature with the environment and are maintained so.

The porosity map shows a stratified structure with slightly varying values, between $0.4-0.5$, down to ~ 150 km. The deep interior ($z/R \gtrsim 0.8$) is entirely depleted of water ice and small dust grains; it is left with only rock/silicate components, with large pores where ice used to fill the gaps. This configuration should remain almost unchanged for the rest of the object's evolution, as no further thermal changes will occur (further heating by long-lived radionuclides will be too slow to cause any significant changes).

The amorphous ice is depleted throughout, except for regions very close to the surface, down to a depth of ~ 3 km (not clearly visible in Fig. 3.2), and probably on the surface itself, barring any irradiation or collisional processing. Crystalline ice is the dominant ice component, with an abundance exceeding the initial value, located around $z/R = 0.5$. This is a result of the outward flow of vapor from the deep interior and subsequent re-condensation on the pore walls. This is clearly visible in the porosity map, where around $z/R = 0.5$ there is a sharp, localized decrease of porosity ($\lesssim 0.2$).

Re-condensation patterns are also apparent for the other volatile ices, concentrated in three regions. The deeper region, at $\sim 120-180$ km below the surface, has a high abundance of CO_2 and HCN ices, which is maintained throughout the entire evolution. The shallower volatile-enriched region, at a depth of ~ 60 km, results from sublimation of the deeper region's volatile ices and re-condensation in the cold layers closer to the surface. As such, it is thinner than the deeper layer, it accumulates at a slower rate and persists for only $\sim 1.5\times10^6$ yr. The third layer, very close to the surface, survives for a limited time as well, with the volatile ices sublimating very slowly until they completely disappear close to the end of the evolution run ($\sim 9.5 \times 10^7$ yr).

(50000) Quaoar

At Quaoar's size and bulk density (see Table 3.1), some degree of pressure-induced densification is to be expected, at least during its early accretion phases (McKinnon, 2002). Thus, we have taken its initial bulk porosity to be 0.2, constraining its initial dust/ice ratio to be slightly higher than that of Varuna (see Table 3.2). Models of this object were evolved with three different radioactive heating sources (^{26}Al, ^{60}Fe and a combination of all available short and long term isotopes), and with two different EOSs (B-M and the approximated form of Vinet, see Sec. 2.7).

The right column of Fig. 3.2 shows the evolution of Quaoar (using the Vinet EOS), again with ^{26}Al as heat source. A peak temperature of ~ 350 K is reached in the very deep interior ($560 - 630$ km below the surface) at an early stage of the evolution ($\sim 10^5$ yr), persisting for $\sim 10^6$ yr, before appreciable cooling sets in. As for Varuna, the interior cools, towards an almost steady temperature of ~ 200 K, within more than 60% of the bulk. The long-term thermal profile (from $\sim 3 \times 10^6$ yr to the end of the evolution) is split into two components: a warm interior ($T \gtrsim 150$ K, within $\sim 60\%$ of the bulk) and a cold outer region ($T \approx 100$ K, within the outer $\sim 30\%$of the bulk). The surface and immediate sub-surface (~ 3 km below the surface) are kept close to the equilibrium temperature of ~ 50 K. The high temperatures are confined more closely to the core due to the higher thermal conductivity resulting from the lower porosity.

The porosity map reflects the effect of compaction due to hydrostatic pressure (see discussion about the treatment of compaction in Sec. 2.4). Most of the bulk has a porosity $\lesssim 0.1$, gradually increasing from a depth ~ 130 km towards the surface. This structure is maintained from the beginning to the end of the evolution, with marginal variations in different periods, and attests to the significant role self-gravity pl ayes in such large objects. The densification increases the thermal conductivity almost to that of solid ice or dust (Prialnik *et al.*, 2004). The higher density also raises the tensile strength of the interior, due to reduced void volume between the solid components of each aggregate layer (Greenberg *et al.*, 1995).

As a result of the high internal temperatures, amorphous ice crystallizes rapidly, and thus starting from $\sim 3 \times 10^6$ yr there is no amorphous ice to be found, except for the sub-surface layers (~ 25 km to the surface), where the abundance is kept at its initial value. The persisting high temperatures cause the deep interior ($z/R \geq 0.9$) to become depleted of volatiles altogether. However, unlike the case of Varuna, the process here is faster and compaction stronger (larger size, bulk density and solid component), causing the depleted pores to shrink and establishing an almost uniform porosity throughout. It is worth noting that the depleted core has a density very close to that of rocky silicate dust ($\rho = 3.25$ g cm^{-3}), and progressively outer layers have lower densities, up to the surface, with a density of ~ 1 g cm^{-3}. The outer region is enriched in ice (mainly crystalline water ice) that has condensed on the pore walls, somewhat reducing the pore sizes.

As seen in the bottom right panel of Fig. 3.2, volatile ices have an obvious stratified pattern, in the outer $\sim$ 190 km of the object, with mass fractions of $0.1 - 1\%$. This enrichment of the outer layers of Quaoar is again the consequence of the rapid heating, crystallization and sublimation of the interior bulk, flow of gas (CO_2, HCN and H_2O) towards low-temperature outer layers and condensation on the pore walls. Small dust particles are also dragged along with the flow, but as the porosity is very low, most of the particles do not migrate to any appreciable distances within the object. Closer to the surface, where the porosity is higher, particles of various sizes may migrate from slightly deeper layers, although there the gas fluxes are low. The resulting sub-surface (down to $\sim$ 20 km below the surface) of Quaoar exhibits a complex composition, where amorphous and crystalline water ice layers may be found adjacent to volatile-enriched ice layers. Since the gas flow drags small dust particles with it, when it refreezes, these particles remain embedded in the ice. The particular stratification pattern depends on the particular initial configuration assumed, but some stratification pattern is obtained regardless of the initial configuration.

From about 100 km outwards ($z/R \lesssim 0.15$), the porosity is larger than 0.4. In addition, the initial volatile composition of amorphous ice with occluded gases is kept unaltered (unless affected by collisions) at depths of 30 km or less, and traces of organic volatile ices may be found at these depths. This material structure and composition strongly resembles that of known JFC nuclei.

(136199) Eris

As this object has the largest size and bulk density in our sample (see Table 3.1), it should also experience pressure-induced densification, even more so than Quaoar. We thus assumed a very low initial bulk porosity (the lowest in our sample – 10 times the lower threshold of 0.01), which lead to the highest initial dust/ice ratio in our sample (see Table 3.2). We ran one model configuration, applying the B-M EOS and all available radioactive isotopes. As this object was followed for a shorter time than the others (see beginning of Sec. 3.1.3), we present "snapshots" of the thermal and structural profiles near the end of the evolution run, at $\sim 10^7$ yr, in Fig. 3.3.

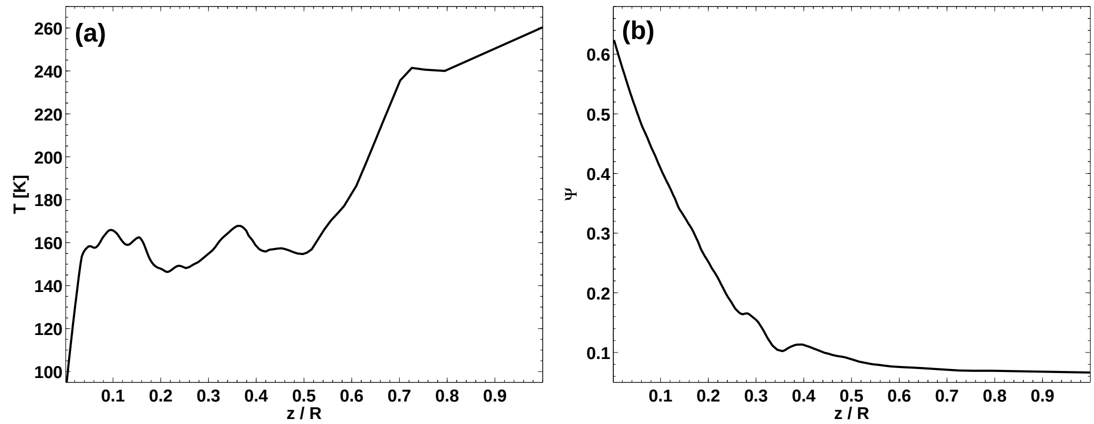

Figure 3.3 Depth profiles for a model of (136199) Eris. Shown here are the temperature (a) and porosity (b). The depth scale is normalized to the radius of the object ($\sim$ 1200 km), from surface (denoted by 0) to core (denoted by 1). This is a "snapshot" of the thermal and structural conditions inside the objects, near the end of the evolution run.

Fig. 3.3a shows the temperature variation with depth. The peak temperature is $\sim$ 260 K, lower than the maximal temperature of $\sim$ 450 K reached during the evolution (at $\sim 3 \times 10^6$ yr). As in the case of Quaoar, the high temperatures of the deep interior (from $\sim$ 950 km deep down to the center) are reached at an early stage of the evolution ($\sim 4 \times 10^5$ yr) and are kept for the entire duration, with a slow cooling rate. At the end of the evolution run, presented in the temperature distribution, we can identify two thermal regions in the interior of Eris: (i) $z/R = 0.05 - 0.5$ (corresponding to a depth of $\sim 60 - 600$ km), with a mean temperature of $\sim$ 155 K; (ii) $z/R = 0.7 - 1.0$ (corresponding to a depth of $\sim 840 - 1200$ km), with the temperature gradually increasing from 240 to 260 K. Each of these regions is preceded by a transition layer, where the temperature increases sharply. The first transition layer, from the surface to a depth of $\sim$ 60 km, is just the cooling length, $l_{cool} = \sqrt{\kappa_{eff}\tau}$. Here $\tau \simeq 10^7$ yr and κ_{eff} is the effective diffusivity of the medium, which is a calculation of the mass-weighted diffusivity of each component (in this case it is mostly a mixture crystalline ice and dust, at a ratio very close to the initial dust/ice ratio). The second transition layer, $z/R = 0.5 - 0.7$, is due to the decrease of porosity that quenches sublimation in these depths. This configuration is not in steady-state, but it is slowly-evolving. This means that from this point on the shallower region will gain some heat (due to uneven rates of heating from the interior and cooling to the exterior) and the deeper region will cool. The slow thermal evolution will proceed until most of the bulk of Eris will have $T_{mean} \simeq 200$ K, with slight variations. Since this slow thermal evolution should not cause any appreciable changes in composition or structure in the future, we can expect the entire object to retain its mean temperature during the lifetime of the solar system, according to

$$\tau_{tot} \approx \tau \left(\frac{R_{Eris}}{l_{cool}}\right)^2 \approx 10^7 \left(\frac{1200}{60}\right)^2 = 4 \times 10^9 \text{yr}. \tag{3.1}$$

Fig. 3.3b shows the porosity distribution. As in the case of Quaoar, the deep interior is completely depleted of any volatiles, including water. This results in a compacted interior, as the depleted pores are shrunk by compression (hydrostatic pressures on the order of 1 GPa). Porosity is kept very low ($\Psi \lesssim 0.1$) in most of the bulk, and rises towards the surface, from a depth of ~ 400 km outwards. The "kinks" in the porosity distribution, in the range of $z/R = 0.2 - 0.4$, are related to the variations in temperature, seen in Fig. 3.3a. This is because a slight rise in temperature and the subsequent onset of crystallization increase the abundance of crystalline ice in a certain layer, while decreasing the abundance of other ices in adjacent layers, due to induced sublimation. These variations are not visible from $z/R = 0.2$ outwards because temperature variations here are smaller and porosity values already higher. Close to the surface, from ~ 120 km outwards ($z/R \lesssim 0.1$), porosities are larger than 0.4, which renders the sub-surface layers of such an object an extremely porous medium with low mechanical strength. Similar to the case of Quaoar, volatile ices may be found at $z/R \lesssim 0.1$ (although this is a much greater depth than found in the case of Quaoar), where the initial composition of amorphous ice with occluded gases is kept almost unchanged. This leads to a configuration similar to that of a JFC nuclei, in terms of composition, porosity and internal temperature.

3.1.4 Re-distribution of Pore Sizes

Pore sizes change during evolution, due to sublimation and re-condensation of ices, as well as pore breaking because of mechanical stresses. Since these processes are sensitive to temperature, which varies considerably with depth and time (as described in Sec. 3.1.3), an initially uniform pore size distribution may soon cease to be uniform. The relative change in the pore size distribution, for each depth, may be written as

$$\frac{1}{N}\frac{dN}{dz} \propto -\ln\left(\bar{r}_p\right)\frac{d\alpha}{dz}, \tag{3.2}$$

where z goes from surface to center and $\bar{r}_p$ is the average pore radius at each depth (keeping in mind that depth is discretized).

For the models of Quaoar, we tracked the evolution of N over time, up to 10^8 yr, throughout the depth of the object, from the subsurface layer (at $\sim$ 200 m depth) to the center ($\sim$ 630 km depth). Our results indicate this length of evolution the pore size distribution at any depth differs from the initial (homogeneous) state, but – regardless of the equation of state or energy input – the variation is small and does not exceed $\sim$ 0.5%, between adjacent grid points. Once all of the volatile material is depleted, or internal energy sources exhausted, the porous structure no longer evolves. The surface layers may continue to evolve due to space weathering, although this effect should be reduced and slowly-accumulating, because of the low flux values in the Kuiper belt region (Hudson *et al.*, 2008). Occasional impacts may also alter the structure of both ice and dust components in the surface and sub-surface layers.

In Fig. 3.4, we present a comparison of the profiles of the surface to volume ratio (SVR) and the permeability (Φ), which are the controlling parameters of sublimation and gas flow, respectively. These are results from the evolution of Quaoar models, with either the B-M or Vinet EOS and either ^{26}Al solely or all radionuclides as energy source, given for early ($\sim 10^5$ yr) and late ($\sim 10^8$ yr) stages of the evolution. Both the permeability and the surface to volume ratio depend on the exponent of the pore size distribution and on the porosity at each depth (see Sec. 2.4 for the parameter definitions). We normalize each parameter value with the maximal value in the initial configuration. This is done in order to focus on the overall evolution trend of Φ and SVR.

If we compare the top panels (Fig. 3.4a and 3.4b) to the bottom panels (Fig. 3.4c and 3.4d), we can see that in the two different structural and thermal configurations the overall behavior is similar. Permeability, and thus gas flow, at initial stages is higher than at the final stages, throughout the outer and mid layers of the object, while in the inner parts the situation is reversed. Surface to volume ratio, and thus rate of volatile sublimation, is lower at initial stages than at final stages throughout the outer and mid layers, while in the inner parts the situation is reversed.

We should note that although the details of each evolution model are different, the

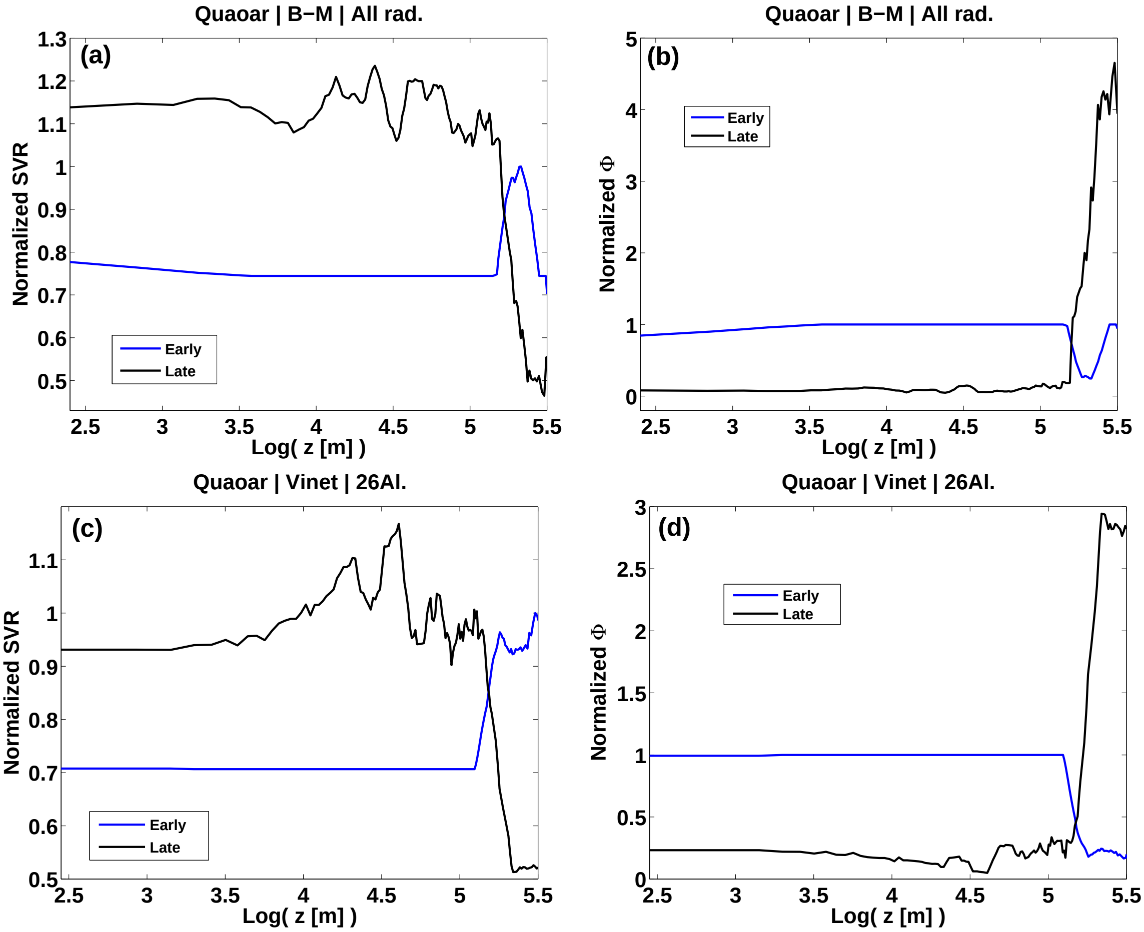

Figure 3.4 Depth profiles of the permeability Φ and surface-to-volume ratio SVR, for a model of Quaoar, from the subsurface (left) to the center (right). For a model including the B-M EOS and all radionuclides, (a) and (b) present SVR and Φ, respectively. For a model including the Vinet EOS and only ^{26}Al, (c) and (d) present SVR and Φ, respectively. In all panels we compare early stages (∼100 Kyr, blue) and late stages (∼ 100 Myr, black) of the evolution.

overall behavior is very similar between the two distinct configurations. This is true if we look at the depth distributions in similar time frames (compare same color curves for Φ and SVR) and also if we compare the variation from early to late evolution.

3.1.5 Effect of the Equation of State

In an attempt to investigate the influence of the EOS on the internal evolution of an icy object, we ran simulations of Quaoar, with the same initial conditions (identical dust/ice ratio and volatile composition), changing between "stiff" and "soft" EOS (see Sec. 2.7.3). All radioactive elements were included, so as to achieve the maximum heating power for the duration of the evolution ($\sim 10^8$ yr). We present results as a function of the relative volume (rather than depth), because the EOS affects the mass distribution (see Sec. 2.7), and mass is a volumetric property.

Fig. 3.5 shows a comparison of the temperature distribution for the simulations described above. A snapshot at an early stage of the simulations ($\sim 1.25 \times 10^5$ yr), presented in Fig. 3.5a, shows the two most conspicuous features: (i) A much higher core (and near-core) temperature in the B-M case; (ii) A much shallower slope of the temperature distribution in the Vinet case. A snapshot at a late stage of the simulations ($\sim 10^8$ yr), presented in Fig. 3.5b, shows the slow cooling of the interior, when the decay of short-lived radionuclides no longer contributes to the heat balance. It is clear that in both cases the temperature distribution follows a similar slope throughout most of the volume. However, the Vinet case exhibits higher temperatures. This is due to the fact that earlier in the evolution, the maximal (and central) temperature did not exceed ~ 350 K (see Sec. 3.1.6 and Fig. 3.7). As a result, sublimation, or melting, of water ice was slower and absorbed less heat, than in the B-M case.

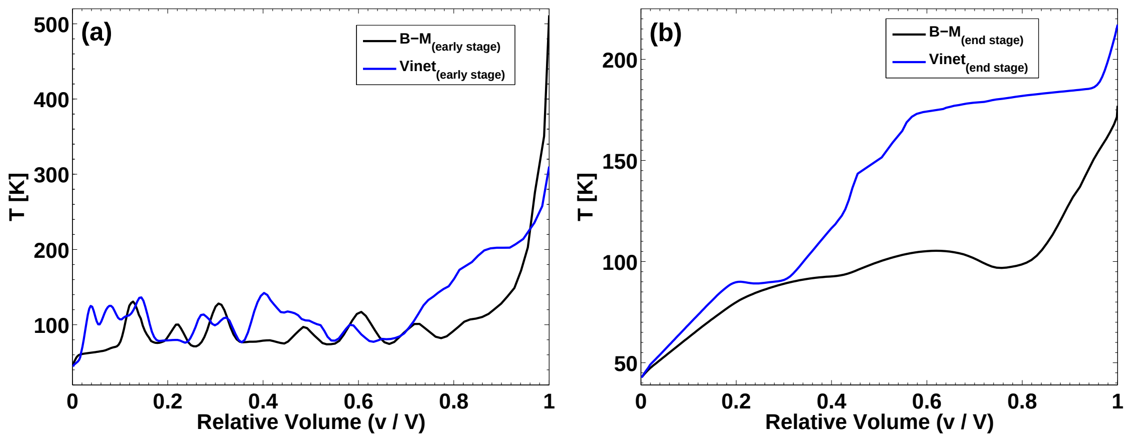

Figure 3.5 Depth profiles of temperature, for a model of Quaoar. The curves shown are for the B-M (black) and the Vinet (blue) EOS, at an initial stage of the evolution (a) and at the end of the evolution run (b). Depth scale given in relative volume, from the sub-surface (left) to the core (right). Both EOS cases experienced internal heating by all available radioactive sources.

The cooling rate, given by $(3KT)\,/\,(R^2\rho)$ (Prialnik and Podolak, 1999), depends not only on the temperature, but also on the porosity profile. The conductivity K depends on the characteristics of the porous medium (Prialnik *et al.*, 2004), predominantly on the porosity, at each layer.

Fig. 3.6 shows a comparison of the porosity distribution for the same simulations. At an early stage, presented in Fig. 3.6a, the porosity within most of the object's bulk is higher in the Vinet case, but the two curves show a similar behavior – porosity decreases from the surface inwards, reaches a minimum value in the deep interior and increases sharply close to the core. This suggests that early on, due to thermal effects and gas flow, the central layers are depleted of volatiles, leaving a "Swiss cheese" structure. Close to the end of the simulation, presented in Fig. 3.6b, porosity values are similar to the early stage, but the distribution in the deep interior is slightly altered. In the Vinet case, the deep interior is compacted locally. This means that pores are eventually quenched. At $\sim 60 - 70\%$ of the bulk porosities are slightly higher, due to further slow sublimation of the water ice in the interior. In the B-M case, the distribution remains the same as in the early stage, except for slight compaction of the layers close to the core, at a depth of more than $\sim 95\%$ of the bulk.

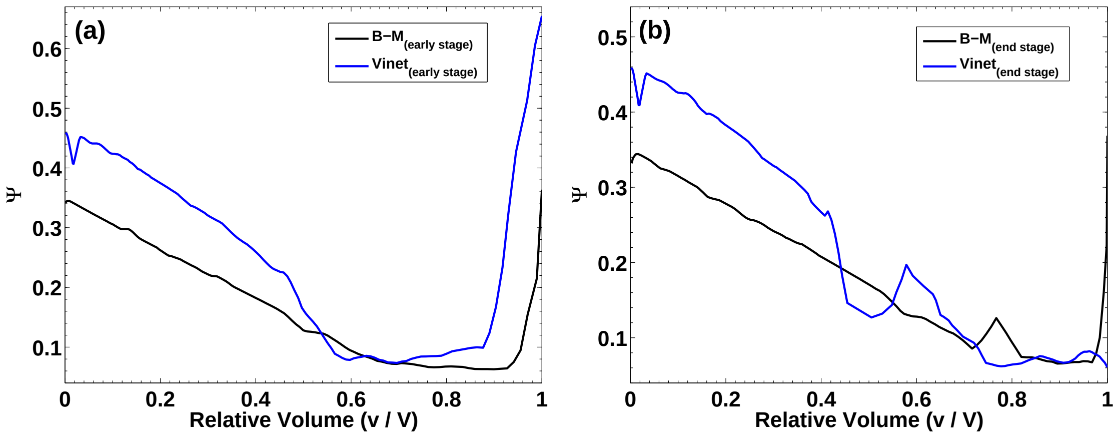

Figure 3.6 Depth profiles of porosity, for a model of Quaoar. The curves shown are for the B-M (black) and the Vinet (blue) EOS, at an initial stage of the evolution (a) and at the end of the evolution run (b). Depth scale given in relative volume, from the sub-surface (left) to the core (right). Both EOS cases experienced internal heating by all available radioactive sources.

Presumably, we would expect some effect of temperature on the stiffness of the ice component. At a constant temperature it should be constant, and the effect of hydrostatic pressure on the porosity could be well approximated with a constant bulk modulus in the equation of state (either Vinet or B-M). However, a temperature-dependent ice stiffness should have an influence on the mechanical response of the solid ice matrix, as there is no observed steady-state creep (plastic deformation) for polycrystalline ice (Petrenko and Whitworth, 1999). We neglect this secondary effect, because, for known laboratory measurements of water ice, the deformation rate is much smaller than the heating rate and subsequent sublimation/evaporation rate (see Petrenko and Whitworth, 1999, for a discussion of the minimum strain rate for ice). As a result, we still regard our implementation of the EOS as isothermal (see Sec. 2.7). Thus, although the stiffness of ice is reduced by increasing temperature (and pressure), the rise in temperature removes most of the ice component, by massive flow through the pores.

The above argument can be seen in Fig. 3.2, where all objects are left with very little (if any) ice, in their deep interior, from a very early stage in their evolution. The porosities in the deep layers can still remain high (up to 60%), but this reflects the stiffness of the dust component (rock/mineral), which can balance the hydrostatic pressure, depending on the density profile and the size. This is expressed in Fig. 3.2 (second row from the top) and Fig. 3.3, as the smaller and less-dense objects maintain high porosities, while the bulk volume of the larger and denser objects are much less porous ($< 10\%$).

3.1.6 Effect of Various Radioactive Species

In order to compare the relative importance of the short and long-lived radionuclides on the overall thermal evolution, we evolved a model of Quaoar, keeping the same initial conditions and using the Vinet EOS, for different sources of radioactive heating.

Fig. 3.7 shows the evolution of the maximal, central and surface temperatures, calculated for a complete evolutionary sequence, with either of the short-lived radionuclides, ^{26}Al and ^{60}Fe and with all relevant radioactive isotopes (see Sec. 2.5). These are given in Fig. 3.7a, 3.7b and 3.7c, respectively. Surface temperature is given just as a reference, as there is negligible heating of the surface by solar radiation (Choi *et al.*, 2002). We note that for the entire duration of the simulations, the maximal temperature is attained at, or very near, the center. Obviously, the highest peak temperature is reached in the case where all available radioactive sources are present. However, this peak temperature (~ 350 K) is not reached around the characteristic decay time of ^{26}Al, the most potent radioactive isotope. Rather, it is reached closer to the characteristic time of ^{60}Fe. The energy release from the decay of this radionuclide takes over when the energy release rate of ^{26}Al becomes marginal.

Since the difference in characteristic decay timescales is smaller that the heat diffusion timescale, there is no appreciable cooling in between these energy release processes. The

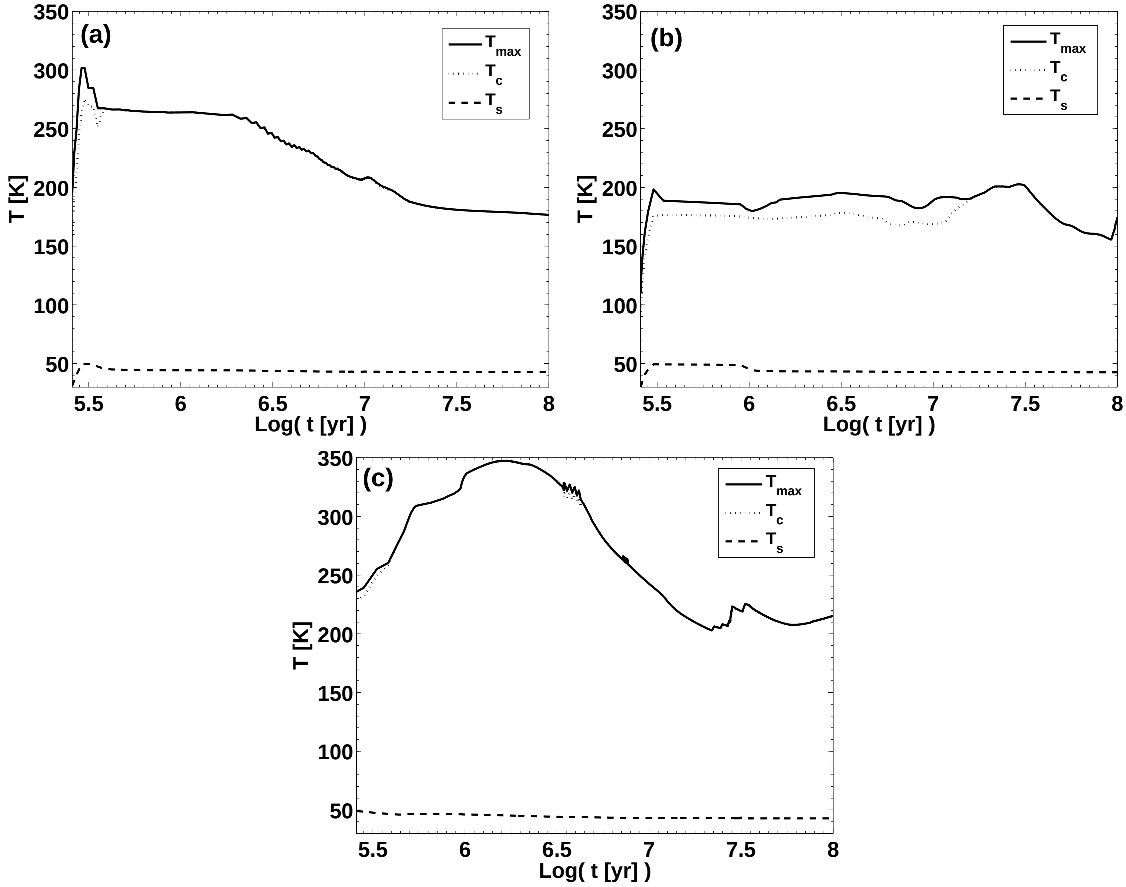

Figure 3.7 Evolution of temperature for maximal (T_{max} - solid), central (T_c - dotted) and surface (T_s - dashed) values, for a model of Quaoar. The three panels differ by the internal radioactive heating source: (a) ^{26}Al only; (b) ^{60}Fe only; (c) All available radionuclides. All cases were evolved using the Vinet EOS.

other radionuclides do not contribute at this stage of the evolution because of their much longer decay times and much lower energy release rates (see Sec. 2.5).

It is also clear that regardless of the power of the internal heating source, the surface layers remain at the equilibrium temperature with the environment. This is due to the fact the thermal timescale for diffusion of heat from the interior to the surface is of the order of 10^9 yr, for icy-rocky objects of 100 km scale (see Prialnik *et al.*, 2004). For the orbit of Quaoar, this results in a temperature of ~ 50 K throughout its evolution. This temperature corresponds to insolation at the present value of the solar luminosity, but other energy sources, such as impact heating by smaller bodies or dust particles, or space weathering effects, are negligible in the region of the Kuiper belt (Hudson *et al.*, 2008).

3.1.7 Possible Liquid Water

In our model we do not treat the kinematic contributions of the liquid phase of water, i.e., there is no EOS or flow equation for liquid water. Nevertheless, we do include the liquid phase transition by considering ice and water as one substance – the non-gaseous form of H_2O. We have no occurrence of mixed gas and liquid phases in the pores. We calculate the transition between gas and non-gas, based on the balance between the saturated vapor pressure and the partial pressure of the vapor (ideal gas). The liquid fraction of the non-gas phase may then be approximated by using a smooth step-function of the temperature:

$$X_l = \frac{\rho_l}{\rho_w} = \frac{1}{f(T)}; \quad \rho_w = \rho_c + \rho_l; \quad f(T) = 1 + e^{\beta(1-T/T_m)}, \tag{3.3}$$

where subscripts c and l refer to crystalline ice and liquid, respectively, $\beta \gg 1$ is the steepness parameter of the transition and T_m is the melting temperature (see Prialnik and Merk, 2008). Obviously, X_l can be between 0 and 1, as we cannot obtain a higher liquid abundance than the available water ice abundance, for each layer that experiences the appropriate conditions for melting.

In Fig. 3.8 we plot the (T, P) data points (the pressure P being the total gas pressure in the pores and T the temperature) obtained throughout the bodies at all times during evolution, superimposed on the phase-diagram of H_2O, in order to get a general idea about the possible occurrence of liquid water within our icy objects. Clearly, this leads to a great deal of overlap. At the same time, it shows which of the objects considered is likely to contain liquid water at some point during its evolution.

The density of points in Fig. 3.8 represents the chance for occurrence of the various phases of water. The more points at the different regimes, the more prevalent this phase is during the evolution of a given object, throughout the bulk. Also, the denser the points are in each phase (solid, liquid and vapor), the more stable these thermodynamic conditions will be during the evolution of a given object, throughout the bulk. For example, 1992 QB1 (magenta dots) retains water in mostly a stable phase of crystalline ice, at $P < 10^4$ Pa and $T \lesssim 220$ K. The points that cross the sublimation curve represent an unstable phase of vapor, resulting from temperatures of $\sim 200 - 300$ K, at very low pressures.

The smaller objects, 1992 QB1 and Varuna, only rarely develop conditions sufficient for sustaining liquid water (the upper right "third" of Fig. 3.8). The dominant phase for these objects is the solid one, with Varuna tending towards higher pressures, and 1992

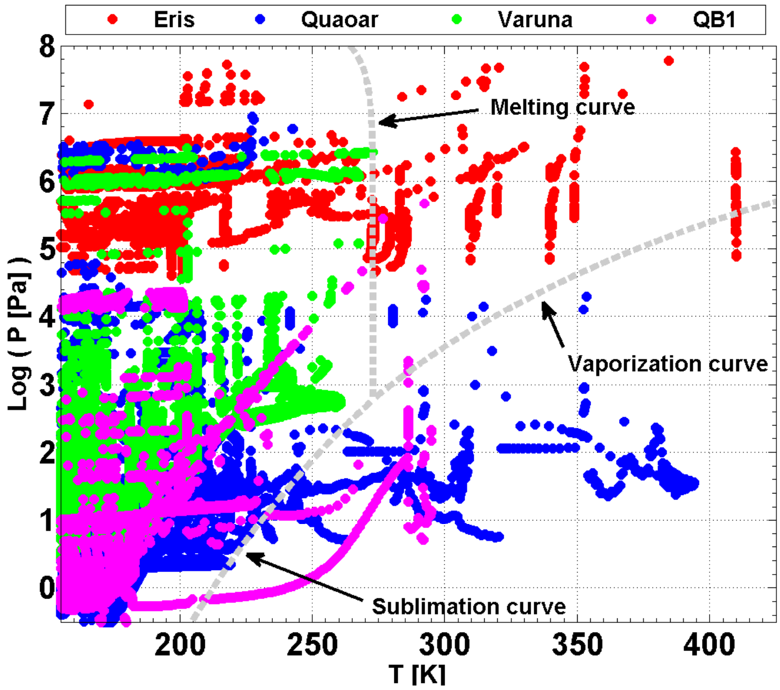

Figure 3.8 Thermodynamic conditions of H_2O phases. Each filled circle represents a point in the $T - P$ phase space, for Eris (red), Quaoar (blue), Varuna (green) and 1992 QB1 (magenta). These are given for any depth inside the object and any time during the evolution. The data is superimposed over the phase diagram of water, denoted by the dotted gray lines (the melting, vaporization and sublimation curves). Thus the diagram indicates which object is more likely to contain the different phases of water (vapor, liquid or ice).

QB1 remaining closer to the solid-vapor transition regime (denoted as the sublimation curve). This is mostly a result of the lower internal porosity of Varuna (see Fig. 3.2 and Sec. 3.1.3) compared with that of 1992 QB1. There are, however, a few points indicating a "near-liquid" phase for both objects. These points represent bursts of heating and pressure build-up that quickly subside.

Quaoar, about 3-6 times larger in radius than 1992 QB1 and Varuna, is able to maintain conditions that allow it to have a liquid or "near-liquid" phase more often and for longer durations. The dominant phase for this object is, of course, the solid phase, with a tendency toward a build-up of pressure at lower temperatures. This is due to partial sublimation as well as gas release from amorphous ice upon crystallization. The points corresponding to the vapor phase (the lower right "third" of Fig. 3.8) represent either water vapor that is supported in regions depleted of ice and volatiles, such as the hot interior.

Eris, the largest object in our sample, is the most likely to maintain the liquid phase of water. Most of the (T, P) points for Eris in Fig. 3.8 occupy the regions on either sides of the melting curve. We may interpret this as relative dominance of the liquid phase in the central part of the object, where heat release is strongest and the cooling rate is slowest, due to higher temperatures and very low porosities at these depths (see Fig. 3.3).

Another way to examine the likelihood of the liquid phase in large TNOs is to look at the volume occupied by the liquid inside the void volume of the pores. This parameter, which is a property of the porous medium, can be referred to as *saturation* an has values between 0 and 1. We can define it as

$$\chi = \frac{\rho_l/\varrho_l}{\rho_l/\varrho_l + \Psi}, \tag{3.4}$$

where $\varrho_l = 0.997$ g cm^{-3} is the specific density of water (Petrenko and Whitworth, 1999) and Ψ is the local porosity. For $\chi = 0$ we have $\rho_l = 0$, no matter the porosity, which means no water is present. For $\chi = 1$ (and $\rho_l \neq 0$), we have $\Psi = 0$, which means all available void volumes are filled with water. Since we know that ρ_l is a function of T and ρ_c (see Eq. 3.3), χ can be derived directly for each layer, from the local temperature, porosity, and ice density. Thus, we can produce a map of the saturation level throughout the bulk of an object. Assuming zero permeability for liquid water, we can expect non-negligible values of saturation.

Fig. 3.9 shows such a saturation map, where only values of $\chi \gtrsim 1\%$ are presented. Below this level, we have $\rho_l/\varrho_l \lesssim 0.01\Psi$ (see Eq. 3.4). The expected low porosities at the depths corrsponding to non-negligible ρ_l, $\Psi \leq 0.1$ (see Sec. 3.1.3 and Fig. 3.2), would imply liquid water abundance lower than 0.1%. The occurrence of high values of saturation, corresponding to liquid (melt) water phases, at increasing depths inside each object, is clear from the distribution of points in Fig. 3.9. We also note the relative absence of significant saturation values within the core (denoted by $z/R \gtrsim 0.9$) of each object, with the possible exception of the Varuna model. However, Varuna has only occurrences of saturation levels greater than 1%, which indicates its interior liquid phase conditions are un-stable and may be very short-lived.

From this figure we can conclude that the larger the object, the more likely it is to have significant amounts of liquid water, with the biggest objects (like Eris) basically containing "lakes" or "pools". However, these large liquid water masses are located deep inside each object, at depths of a few 100 km below the surface. This region should be

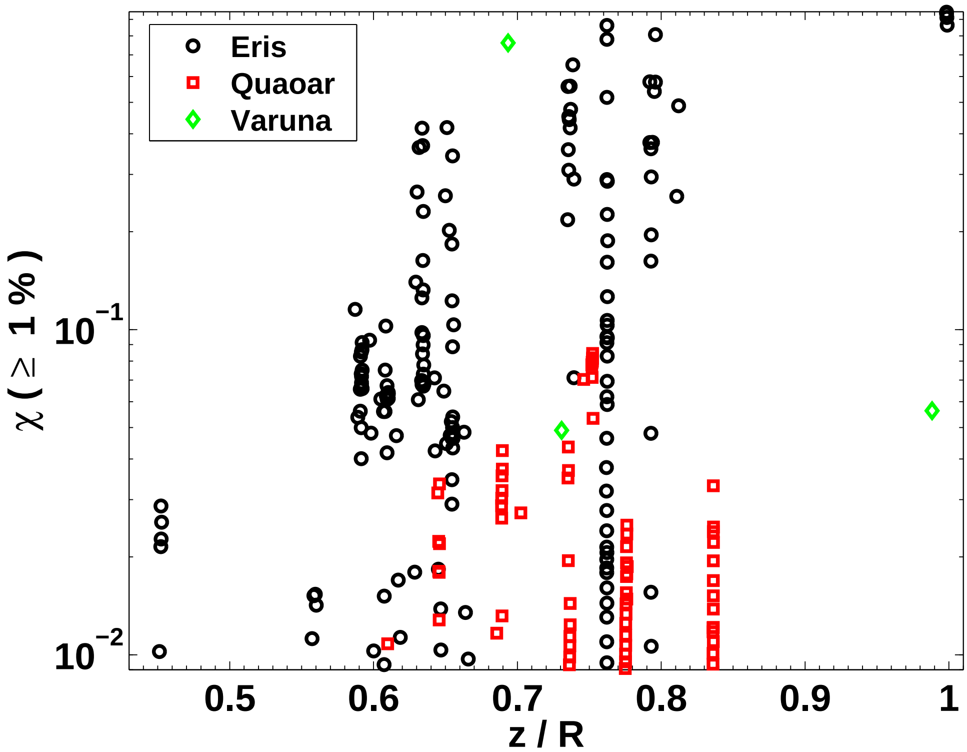

Figure 3.9 Level of saturation as a function of relative depth, Eris (black circles), Quaoar (red squares) and Varuna (green diamonds). Below the level of $\sim$ 1% saturation is practically negligible.

protected from all but the most catastrophic events (such as a collision with a similar sized object). The density of points in Fig. 3.9 represents the stability of a saturated "near-liquid" state, at a given layer (relative depth). Thus, Eris (black dots) has the most stable saturated layers, among the three large TNOs presented. These layers are at relative depths of $z/R = 0.6 - 0.65$. The saturated layer at $z/R \simeq 0.77$ spans all the range of relevant saturation levels represents an early occurrence of a highly saturated layer that loses its possible liquid content.

3.2 End-States of Some Evolved Objects

3.2.1 (50000) Quaoar - Extended Evolution

Here we focus on a single TNO, (50000) Quaoar, and present an extended long-term evolution of its interior. This simulation was done in order to be able to relate the early and late internal evolution of a large representative TNO. Also, its end-state configuration can be used to infer the initial internal states of objects that are collisionally produced and dispersed as fragments of a larger parent body. Such objects are speculated to be some of the Centaurs and JFCs. We include in the calculation water ice in solid (amorphous and crystalline) and liquid phase, as described in Sec. 3.1.7, as well as the major volatiles CO, CO_2 and HCN. These organic compounds are present initially as occluded gases in the amorphous ice, but can appear as solid ices in the evolved composition profiles, due to internal heating, which triggers crystallization of amorphous ice, release of its trapped volatiles, outward flow and subsequent condensation within the porous layers. This processing, which affects the phase of water ice and various volatiles in different depths inside the object, is triggered and maintained by heat produced from the decay of all relevant radioactive isotopes (see Sec. 2.5). Another heating contribution comes from the subsequent exothermic transition of amorphous to crystalline ice (Prialnik *et al.*, 2004).

The model of Quaoar was evolved up to $\sim 10^9$ yr, from a homogeneous initial state, with the full numerical model described in Ch. 2. It is basically an extension of one model of Quaoar that appears in Table 3.4 – B-M EOS and all radioactive species. All the assumptions and physical processes described in Ch. 2, for a general model of an icy body, and in Sec. 3.1, for an application to TNO modeling, apply for this simulation.

Bulk Composition

As time progresses, the interior cools, because heat production by the decay of short-lived radionuclides diminishes, until after several half-lives it becomes negligible. Since Characteristic half-lives of long-lived radionuclides are on the order of 10^9 yr or longer (see Sec. 2.5), they will not contribute significantly to the evolution at earlier times than that. This contribution is even further diminished because the interior has already been thermally processed – no amorphous ice is present, which means no induced heating by crystallization and no volatiles. Crystalline ice is almost extinct in the deep interior, because of high-temperature periods earlier in the evolution (see Sec. 3.1.3). Thus what little heat is added by the decay of long-lived radionuclides is dissipated from the deep interior by conduction of the solid component and radiation through the porous layers.

The earlier evolution phases (up to a few 10^6 yr), which were already discussed in Sec. 3.1.3, resulted in a configuration with no water ice or volatiles present in the deep interior, leaving only the solid, porous matrix. The slow-varying peak temperature that is reached after 10^7 yr, $T \approx 180$ K, is similar to that of the comparable case of the Vinet EOS, shown in Fig. 3.7, and also close to the sublimation temperature of crystalline ice (see Table 2.1). Thus, the rate of internal sublimation of the crystalline ice is lower than the cooling rate of the interior. Other volatile compounds are not as steady. As the temperature gradient settles to a range of $T \simeq 43 - 180$ K, from the surface to the deep interior, the conditions are such that CO_2 and HCN ices can sublimate and recondense on timescales shorter than the thermal timescale of the bulk. This results in migration of volatiles outwards and stratification of the ice layers. The early intense heating of the interior and the subsequent slow cooling cause a net loss of material, as some of the gas escapes through the porous outer layers. Since CO is completely extinct at an early stage of the evolution (see Sec. 3.1), it only survives as occluded gas in the diminished amorphous water ice component.

Table 3.5 shows a comparison of the bulk composition, presented in mass fractions, between the initial and final ($\sim 10^9$ yr) internal states. The first and second columns are the mass fractions of water ice (representing the dust/ice ratio) and amorphous water ice (representing the extent of internal crystallization). The third column is constant, because the abundance of gas species trapped in the amorphous ice does not change in time. The fourth column is the combined mass fraction of the volatile ices (CO_2 and HCN), representing the process of condensation on the pore walls, while the last column is simply the total volatile abundance, relative to all other components.

These final abundances can be interpreted as an upper limit, with regards to the initial composition assumptions (see Table 3.1, 3.2 and 3.3). This is because the choice of the B-M equation yields a temperature distribution, after long-term evolution, which is lower than a model with implementation of the Vinet EOS (see Sec. 3.1.5 and Fig. 3.5). Since our representations of the B-M and Vinet EOSs can be taken as upper and lower limits of simple "universal" EOSs (see Sec. 2.7), other choices will result in a slower cooling

Table 3.5 Bulk composition (by mass fractions), for an extended model of Quaoar

	X_{ice} [1]	$X_{am.}$ [2] ($\times 10^{-3}$)	$X_{occl.}$ [3] ($\times 10^{-2}$)	$X_{vol.}$ [4] ($\times 10^{-3}$)	Total [5] ($\times 10^{-3}$)
Initial:	0.30	1000	1.25	–	3.750
Final:	0.22	5.211	1.25	1.557	1.571

[1] Ratio of water ice to total mass. [2] Ratio of amorphous water ice content to water ice. [3] Abundance of occluded volatile species in the amorphous ice. [4] Ratio of volatile ices (CO_2 and HCN) to total mass. [5] Total mass fraction of volatile content (gaseous or solid), other than water.

rate than the present model. The excess heat, in comparison to this model's results, will expedite the sublimation and crystallization rates.

It is clear that the final bulk composition differs significantly from the initial one. During the 1 Gyr evolution, about 27% of the water component initially stored inside the object was lost, as ice sublimated and escaped outwards. The volatile component (either as ices or trapped gases) was depleted by about 60%, as some of the gases released upon crystallization of the amorphous ice escaped altogether and some condensed on the pore walls in colder regions, just to be sublimated away once these regions warmed up. The total mass loss was $\Delta M = 1.14 \times 10^{22}$ g, which is $\sim 0.75\%$ of the total mass of the object. The change in ice content changes the dust-to-ice ratio, which was initially 2.33 (see Table 3.2), to a higher value of 3.2. This results in a slight variation in bulk density (or bulk porosity) of about 5% (about 10% for porosity). However, this variation is well within the uncertainty ranges for determining the mass and size of an object at the heliocentric distances of the Kuiper belt.

Outer Layers

The outer layers of a large TNO, such as Quaoar, are much more prone to further evolution by external physical effects, than its interior. These effects include the bombardment by cosmic ray and solar wind ions, which is restricted to the outermost mm-deep layers of the surface and may accumulate in very low doses in the heliocentric distances of the Kuiper belt (Hudson *et al.*, 2008), and collisions by small impactors. The thermal-mechanical effects of the latter process are still poorly understood, as collisional rates in the trans-Neptunian region are not well-constrained (Kenyon *et al.*, 2008) and the evolved structural and compositional configurations of TNOs are not fully accounted for in current impact models (Leinhardt *et al.*, 2008). The first limitation might be addressed by further observations to discover smaller-end members of the TNO size distribution (Kenyon *et al.*, 2008) and by the discovery and characterization of collisional families in the Kuiper belt, such as that of Haumea (aka, 2003 EL61 Brown *et al.*, 2007).

Fig. 3.10 presents the extended long-term evolution of internal properties of the Quaoar model discussed in this section. We focus on the outer 20% of the object's radius, which are at a depth of $\sim$ 125 km, assuming a radius of 630 km (see Table 3.1). This depth roughly corresponds to the size of the largest intact fragment that can result from a catastrophic disruption of a 1000-km diameter parent body (see Sec. 4.3 in Benz and Asphaug, 1999), and is also roughly the size of the largest known Centaur object, 10199 Chariklo (Dotto *et al.*, 2003).

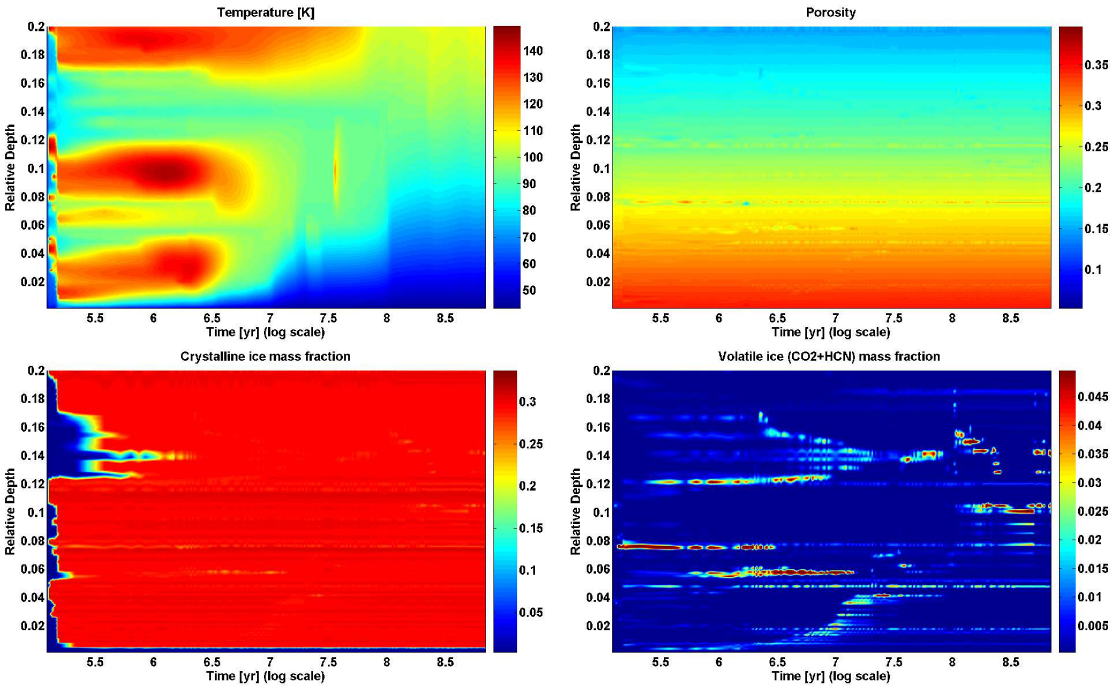

Figure 3.10 Evolution profiles of an extended thermal model of (50000) Quaoar. Shown here are distributions of temperature (top left), porosity (top right), crystalline water ice abundance (bottom left) and volatile ice abundance (bottom right). Time is given on a logarithmic scale, up to $\sim 10^9$ yr and the depth scale is normalized by the objects radius, R, from the surface (denoted by 0) inwards.

It is clear that these outer layers have gone through extensive thermal alteration, resulting also in compositional and structural alterations. During the evolution, temperatures (top left panel of Fig. 3.10) rise to $\sim$ 150 K, as a result of radioactive heating and the triggered exothermic transition of amorphous water ice to crystalline form. After several half-lives of ^{26}Al and ^{60}Fe, when these radioactive energy sources have decayed, the layers start to cool off, from about a few Myr on. Eventually a smooth temperature gradient is established, between 50K to about 100-110K. However, this gradient is not constant, as there is no actual steady-state, and successively deeper sub-surface layers reach the radiation-equilibrium temperature with the outside, of $\sim$ 45 K. The conditions shown in Fig. 3.10 are such that the conduction timescale is larger than the age of the Solar system, meaning that these outer layers are currently not in thermal equilibrium (Jewitt, 2008).

In terms of structure and composition, the regions shown in Fig. 3.10 are moderately porous and have a stratified multi-ice component. Porosity values in the sub-surface layers ($\sim$ 15 km deep, see to right panel of Fig. 3.10) are higher than 0.3, but are not comparable with values estimated for cometary nuclei, of $\sim 0.6 - 0.7$ (Weissman *et al.*, 2004), which are perhaps fragments derived from TNO parent bodies (see Sec. 1.3.2). This discrepancy could be explained by the minor fracture processes of the collision that produces small fragments, some further collisional evolution of the small fragments later on, or by later thermal evolution (either in the giant planet region, as Centaurs, or in the inner parts of the planetary system, as new JFCs). The latter effect results in sublimation and escape of water and minor volatiles, which increases the void volume of the pores.

The two bottom panels of Fig. 3.10 show the abundance of crystalline H_2O ice and volatile ice (CO_2 and HCN). In light of the above discussion on temperature, it is expected that most of the water ice would be in crystalline form, at a relatively early stage of the evolution ($\sim 10^6$ yr). However, at a depth of $\sim 3 - 4$ km, amorphous ice survives and is the prevalent form of ice, throughout the evolution. Volatile ices (bottom left panel of Fig. 3.10), which were not present at the initial configuration of the object, migrate towards the surface throughout the evolution and may be found, at different times, in non-negligible abundances close enough to the surface. By 'close enough' we mean that at a depth of 1-5% of the object's radius, relatively stable pockets of volatile ices are found, persist for several 10^6 yr. This depth is slightly higher than the roughness scale found for the main-belt Asteroid Ceres (Li *et al.*, 2006), another dwarf-planet class member, like Quaoar. However, we should note that TNOs probably contain more ices than MBAs, which generally means lower densities and corresponding higher porosities, at layers near the surface. This may suggest that deep depression features can easily arise on surfaces of TNOs (either as primordial topography or as impact cratering), exposing the water and volatile ice contents.

3.2.2 1992 QB_1 and 1998 WW_{31} – Smaller and Colder Objects

In this section we focus on the end-state configuration of two relatively small TNOs, as it results from a long-term thermal evolution. The physics and scheme of these calculation are the same as in Sec. 3.1, with the addition of the smaller object, 1998 WW_{31}. The end-state configurations can be used to infer the initial internal states of objects that dynamically transported inwards form the trans-Neptunian region to the giant planets region, becoming part of the Centaur population. We include in the calculation water ice in solid (amorphous and crystalline), as well as the major volatiles CO, CO_2 and HCN. These organic compounds are present initially as occluded gases in the amorphous ice, but can appear as solid ices in the evolved composition profiles, due to internal heating, which triggers crystallization of amorphous ice, release of its trapped volatiles, outward flow and subsequent condensation within the porous layers. This processing, which affects the phase of water ice and various volatiles in different depths inside the object, is triggered and maintained by heat produced from the decay of all relevant radioactive isotopes (see Sec. 2.5). Another heating contribution comes from the subsequent exothermic transition of amorphous to crystalline ice (Prialnik *et al.*, 2004).

Table 3.6 lists the initial physical model parameters used for the evolution calculations of 1992 QB_1 and 1998 WW_{31}. Determining the initial bulk density, ρ, and dust-to-ice ratio, $\Upsilon_{d/i}$, sets the initial bulk porosity of an object, as discussed in Sec. 2.3. For the objects examined here, this results in porosity values of ~ 0.54 and ~ 0.33 for 1992 QB_1 and 1998 WW_{31}, respectively. We choose density values that are slightly smaller than stated in the references (by$\sim 3-6\%$), in order to account for the forming conditions of these objects, as smaller objects would contain more voids (gravitational compaction is very weak and more ices survive the accretion phase). The dust-to-ice ratio was chosen to represent the more efficient coagulation of ice-rich particles into larger objects in the cold region of the outer Solar system (Weidenschilling, 2004).

The input physics parameters appear in Table 3.7. These are essentially the same as those for the simulations presented in Sec. 3.1. The volatile content was taken to roughly

Table 3.6 Initial model parameters for TNO models

	1998 WW_{31}	1992 QB_1
a [AU]	39.13	43.73
e	0.270	0.064
R [km]	65	100
ρ [g/cm^3]	1.45	0.70
$\mathcal{A}$	0.07	0.04
$\Upsilon_{d/i}$ [1]	4	1.2
Ref.[2]	(Veillet *et al.*, 2002)	(Jewitt and Luu, 1993)

[1] Initial bulk dust-to-ice ratio. [2] References for the radius, density and albedo estimates.

represent the abundances known from cometary measurements (Bockelée-Morvan *et al.*, 2004), but reduced in order to take into account the chemical differentiation in the early solar system (Bergin *et al.*, 2007). For all the other parameters we have values chosen so as to maximize the effects of thermal evolution. For example, the pore-size exponent and range correspond to a maximum of the sublimation rate correction factor (see Sec. 2.4) and the radionuclide abundances correspond to the maximum values, deduced from meteorite studies (e.g. Tachibana and Huss, 2003). The values for the thermodynamic parameters of ice and dust are the ones commonly used for modeling comets and larger icy objects (e.g. Prialnik *et al.*, 2004; Huebner *et al.*, 2006; McKinnon *et al.*, 2008).

Fig. 3.11 shows the internal configuration of 1998 WW_{31} at the end of the simulation ($\sim 5 \times 10^7$ yr). Presented are the depth distributions of temperature, local density, local porosity and abundances of ices (amorphous and crystalline water ice and volatile ices), as a function of the sub-surface depth, in logarithmic scale. The peak temperature that was reached during the evolution was $T \simeq 190$ K. The surface temperature remained almost unchanged throughout, at $T \simeq 45$ K (the radiation-equilibrium temperature). After the main heating source, radioactive decay, is quenched, which happens around several 10^6 yr (a few times the half-lives of the dominant radionuclides, ^{26}Al and ^{60}Fe), the object starts to cool off gradually. Eventually, a slowly-evolving state is reached (see Fig. 3.11a), where the deep interior, from a depth of ~ 20 km inwards, the temperature slowly cools towards 100 K, and the outer parts are cooling towards the equilibrium temperature.

Density is almost constant throughout the evolution. Fig. 3.11b shows a slight increase in density, as a function of depth, but the maximum to surface variation is only about

Table 3.7 Common input physics parameters for TNO models

Parameter	Value	Units
Specific H_2O ice density	0.917	g/cm^3
Specific dust density	3.25	g/cm^3
Heat capacity of ice	7.49×10^4T$+9 \times 10^5$	erg/g/K
Heat capacity of dust	1.3×10^7	erg/g/K
Conductivity of C-Ice	5.67×10^7/T	erg/cm/s/K
Conductivity of dust	10^6	erg/cm/s/K
Diffusivity of A-Ice	3×10^{-3}	cm^2/s
Pore-size exponent [1]	-3.5	
Pore-size range [2]	10^4	
$X_{rad.,SL}$ [3]	^{26}Al: 4.79×10^{-9}	
	^{60}Fe: 2.81×10^{-8}	
$X_{rad.,LL}$ [4]	^{40}K: 8.78×10^{-7}	
	^{232}Th: 4.39×10^{-8}	
	^{238}U: 1.76×10^{-8}	
	^{235}U: 5.02×10^{-9}	
$X_{vol.}$ [5]	CO: 0.005	
	CO_2: 0.005	
	HCN: 0.0025	

[1] Initial value for the power-law exponent of the pore-size distribution (see Sarid *et al.*, 2005).
[2] Ratio of maximal-to-minimal pore radius (see Sarid *et al.*, 2005).
[3] Initial mass fraction of short-lived radioactive species.
[4] Initial mass fraction of long-lived radioactive species.
[5] Initial mass fractions of volatile species occluded in the amorphous ice.

1% of the initial homogeneous density of 1.45 g/cm^3. This is due to the fact that this model was run, for consistency, with the implementation of self-gravity (see Sec. 2.6). At the size and mass of 1998 WW_{31} the effect is almost negligible. We note that the final density in most of the object's bulk is much closer to the reference value of 1.5 g/cm^3 (Veillet *et al.*, 2002).

Porosity, which is shown in Fig. 3.11c, also experiences only minor changes throughout the evolution. At the end-state of the evolution, down to a depth of ~ 10 km, porosity is at the initial homogeneous value of ~ 0.33. Below this depth there are a few changes, of the order of $\sim 10\%$ of the initial value, related to the peaks of recondensed volatile ices and the slow sublimation of the deeply buried crystalline ice.

During the entire evolution a crystallization front advances from the interior outwards,

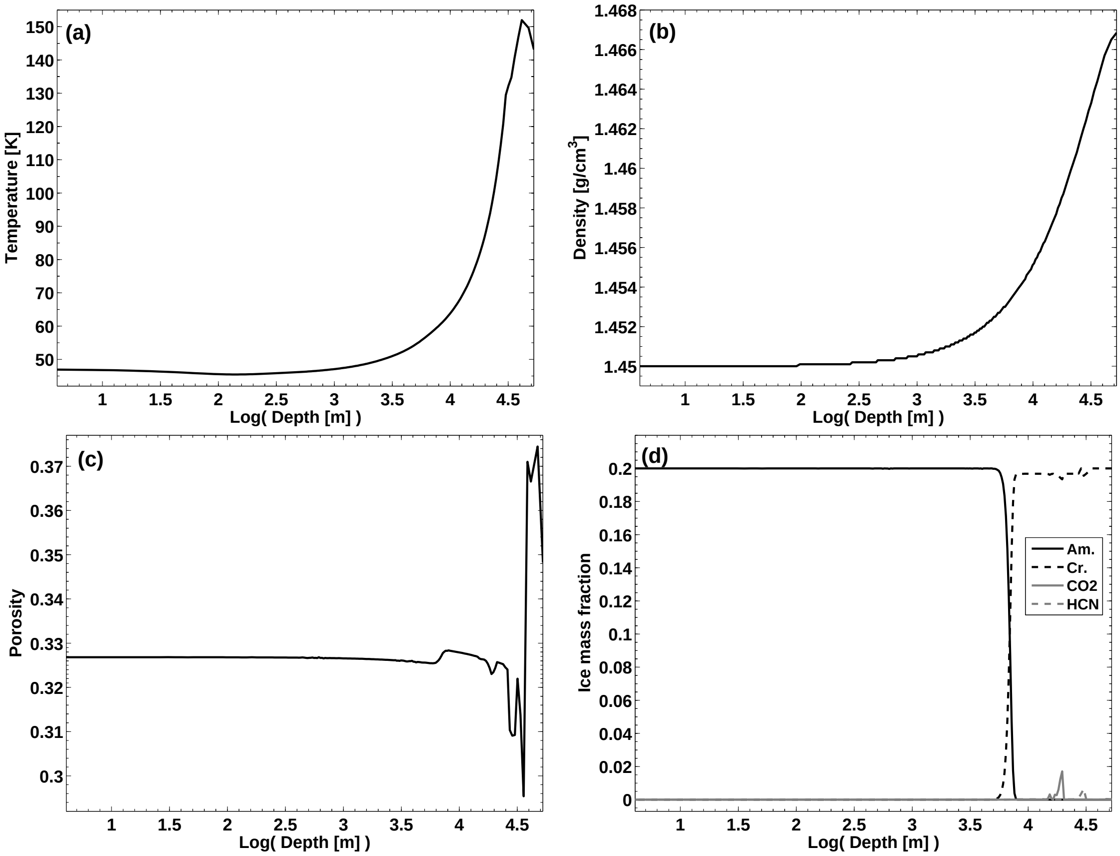

Figure 3.11 End-state internal profiles of a model for 1998 WW_{31}. Shown here are temperature (a), density (b), porosity (c) and mass fractions of ices (d), which include amorphous (solid black) and crystalline (dashed black) H_2O, CO_2 (gray) and HCN (dashed gray). Depth is in logarithmic scale, from $\sim$ 4 m below the surface to the center, and the evolution time is 50 Myr.

causing the initial amorphous ice to transition to crystalline ice (see Fig. 3.11d). This is because radioactive heating is a bulk energy source, resulting in highest temperatures where most of the mass resides (see Ch. 2). Similarly to what can happen in comets, the crystallization front finally reaches a region where it stops advancing. At this point the rate of heat conduction is matched by the rate of crystallization and the amorphous ice from that location outwards is unscathed. For this model of 1998 WW_{31} the depth of amorphous-to-crystalline crossover is about 6 km (the intersection of the solid and dashed black lines). From this figure we can also note that there are two minor sublimation fronts of the volatiles species. These are located deeper than the crystallization front, at depths of $\sim$ 17.5 km and $\sim$ 28 km, for CO_2 and HCN, respectively. This is result of the combined effect of crystallization and sublimation, as gas pressures peak near the location of the fronts and the flow's direction can be inward or outward (Prialnik *et al.*, 2004). Temperatures are higher then the sublimation temperatures of the two minor volatile species, so we would expect the two "bumps" representing the maximum mass fraction of volatile ices (Fig. 3.11d) to disappear. However, since the temperatures are not very high ($T = 100 - 130$ K) and temperatures drop to below the appropriate range of sublimation temperatures ($T = 80 - 95$ K, see Table. 2.1) towards the crystallization front, the volatile ices would just migrate outwards, with maximum abundances either close to the crystallization front, or, if water ice is depleted, close to their individual sublimation front, depending on their enthalpy of vaporization.

Fig. 3.12 shows the internal configuration of 1992 QB_1 at the end of the simulation ($\sim 5 \times 10^7$ yr). Presented are the depth distributions of temperature, local density, local porosity and abundances of ices (amorphous and crystalline water ice and volatile ices), as a function of the sub-surface depth, in logarithmic scale. The peak temperature that was reached during the evolution was $T \simeq 300$ K. The surface temperature remained almost unchanged throughout, at $T \simeq 43$ K (the radiation-equilibrium temperature). After the main heating source, radioactive decay, is quenched, which happens around several 10^6 yr (a few times the half-lives of the dominant radionuclides, ^{26}Al and ^{60}Fe), the object starts to cool off gradually. Eventually, a slowly-evolving state is reached (see Fig. 3.12a), where the deep interior, from a depth of ~ 10 km inwards, the temperature slowly cools towards 100 K, and the outer parts are cooling towards the equilibrium temperature. It should be noted that because this is a larger object than 1998 WW_{31}, its peak central temperatures are higher, maintained for longer durations and drive a more pronounced internal processing. The small "bump" in the temperature distribution, at a ~ 30 km, is a caused by the sublimation of crystalline water ice and subsequent outward flow of vapor. This process is endothermic and the vapor flow carries excess heat, thus slightly lowering the local temperate (Huebner *et al.*, 2006).

Density is almost constant throughout the evolution. Fig. 3.12b shows an increase in density, as a function of depth, with a maximum to surface variation of about 5% of the initial homogeneous density of 0.7 g/cm^3. This is due to the fact that this model was run, for consistency, with the implementation of self-gravity (see Sec. 2.6). At the size and mass of 1992 QB_1 the effect is more pronounced than in the case of 1998 WW_{31}, but still weak. We note that the final density in most of the object's bulk is much closer to the reference value of 0.75 g/cm^3 (Luu and Jewitt, 2002)

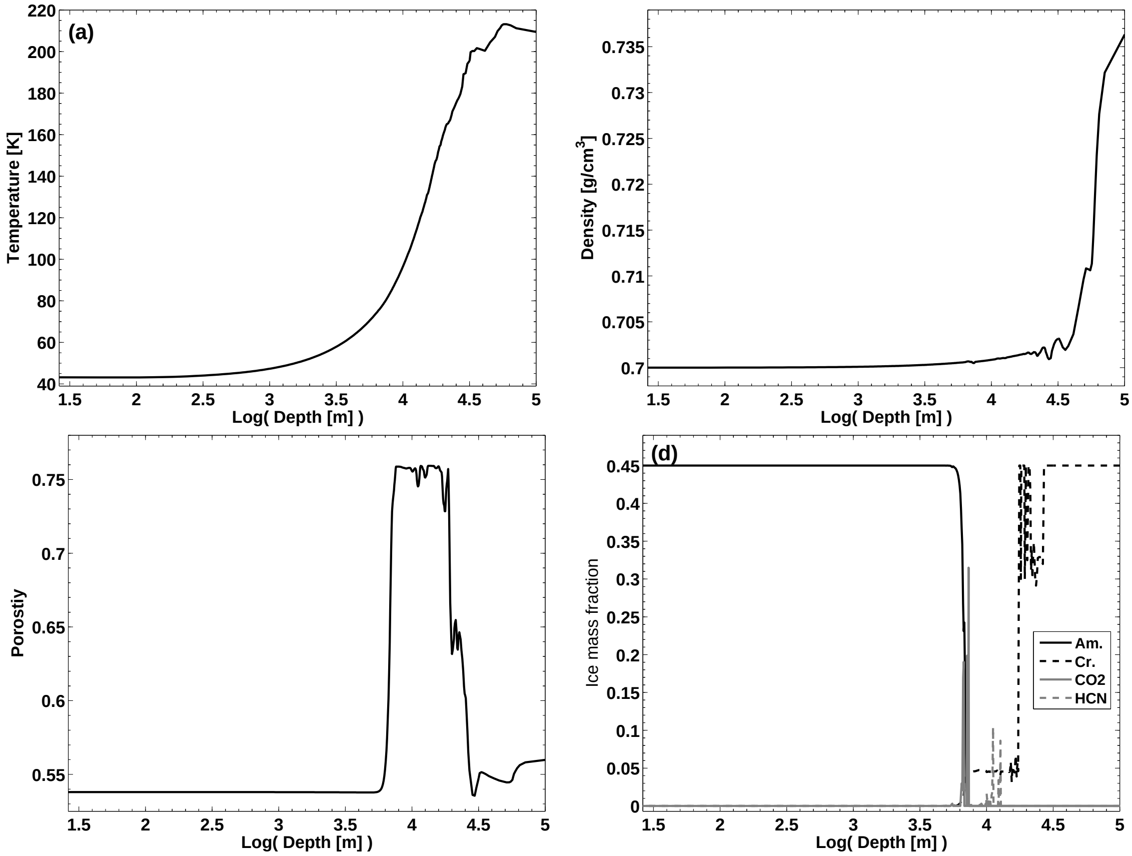

Figure 3.12 End-state internal profiles of a model for 1992 QB_1. Shown here are temperature (a), density (b), porosity (c) and mass fractions of ices (d), which include amorphous (solid black) and crystalline (dashed black) H_2O, CO_2 (gray) and HCN (dashed gray). Depth is in logarithmic scale, from $\sim$ 25 m below the surface to the center, and the evolution time is 50 Myr.

Porosity, which is shown in Fig. 3.12c, experiences some interesting changes throughout the evolution. At the end-state of the evolution, down to a depth of $\sim$ 5 km, porosity is at the initial homogeneous value of $\sim$ 0.54. Below this depth there is a notable jump in porosity values, from roughly 5-25 km deep. Deeper than 25 km, the porosity is again around the initial value, with a slight increase, as material was depleted during the thermal evolution.

By examining Fig. 3.12d, we can clearly relate the region of high porosity values with a region, at the same depth, which is relatively depleted in material, mostly crystalline water ice. As discussed in Sec. 3.1.3 for a similar model of 1992 QB_1, this cavity is a result of the sublimation of water ice and subsequent outflow of all material except for the largest dust grains. Eventually, as temperatures decrease, there is slow condensation of residual vapor on the pore walls and the porosity decreases. This is evident in Fig. 3.12d, at a depth of 18-30 km, where the mass fraction of crystalline ice exhibits some "oscillations", resulting from re-condensation and some release of latent heat. Similarly as for 1998 WW_{31}, we can identify the crystallization front, near the amorphous-to-crystalline intersection, at a depth of $\sim$ 6.5 km. We can also clearly see the two sublimation fronts, for CO_2 and HCN, at depths of $\sim$ 7 km and $\sim$ 11 km, respectively. Since 1992 QB_1 has had a more intense thermal processing history than 1998 WW_{31}, the location of the minor volatiles' sublimation could be thought of as the extreme extent of the migration these ices can experience, sublimating and recondesing, until reaching very close to the crystallization front (the CO_2 sublimation front location), or at at an individual sublimation front, somewhat deeper (the HCN sublimation front location), where the water ice has been largely depleted.

4 Evolution of Centaurs

In this chapter we present results of two studies dealing with the evolution of specific Centaur objects, as representing the intrinsic population.

The first study, described in Sec. 4.1, is aimed at characterizing the dynamical properties of individual Centaur objects. This is achieved through statistical analysis of the orbital behavior of many test particles, cloned by slight variations of the orbital elements from the known Centaur orbits.

In the second study, described in Sec. 4.2, we utilize the general thermal evolution model described in Ch. 2. We apply it to the modeling of a few specific objects (a subgroup of the those examined through dynamical evolution). These objects represent a sample of the various physical characteristics attributed to the population of Centaurs.

4.1 Dynamics Within the Centaur Population

4.1.1 Introduction

Dynamical simulations of large sets of test particles, with initial orbital elements slightly varied around the known values of Centaur objects, can yield estimates for individual dynamical lifetimes and orbital stability. We describe here the results of orbital evolution simulations, with regards to the mean dynamical lifetime of a sample of five Centaur objects – 8405 Asbolus, 10199 Chariklo, 2060 Chiron, 5145 Pholus and 32532 Thereus. These objects were chosen with forethought towards thermal modeling. They were the subject of several observation campaigns, resulting in estimates about some of their physical characteristics (e.g. Fernández *et al.*, 2002; Dotto *et al.*, 2003; Groussin *et al.*, 2004; Barucci *et al.*, 2005; Tegler *et al.*, 2005). We ran several simulations for initial populations of 500 test particles, having initial orbital elements randomly chosen around the currently known values.

Table 4.1 lists the orbital elements for each Centaur. Fig. 4.1 shows the projection onto the ecliptic plane of the Centaurs' orbits. We note that this projection can already indicate some of the characteristics of the current orbits of these Centaurs: Chariklo, not actually crossing any of the planets' orbits; Pholus, reaching from just beyond Neptune to Saturn, but staying clear of Jupiter; Asbolus, having the closest perihelion, coming closest to Jupiter; Thereus, avoiding the outer planets and staying mainly closer to Jupiter and Saturn. Thus, these objects may also represent different qualitative behaviors of Centaur orbits.

Table 4.1 Orbital elements of Centaur objects

Des. & name	a [1]	e [2]	i [3]	ω [4]	Ω [5]	M [6]
8405 Asbolus	17.908	0.618	17.637	290.291	6.062	358.913
10199 Chariklo	15.828	0.174	23.365	241.334	300.395	351.034
2060 Chiron	13.613	0.381	6.938	339.041	209.349	44.775
5145 Pholus	20.348	0.574	24.704	354.863	119.233	41.584
32532 Thereus	10.629	0.197	20.356	86.758	205.301	33.237

[1]–[6] Osculating semi-major axis (AU), eccentricity, inclination (deg.), argument of pericentre (deg.), longitude of ascending node (deg.) and mean anomaly (deg.), at epoch JD 2452400.5 (compiled from JPL's HORIZONS system).

Previous Studies

The dynamics of the intrinsic Centaur population has been investigated in several previous studies. These studies differ mainly by the choice of initial sample and the criterion used to define what object can be regarded as a Centaur. As already mentioned in Sec. 1.2.2, there are several definitions of the Centaur population, using somewhat different constraints on the main orbital elements (semi-major axis, perihelion and aphelion distances).

Dones *et al.* (1996) simulated the evolution of ~ 100 test particles for each object from a sample of six Centaurs known at that time. Initial orbital elements were taken as that of the known object, with an addition of a random variation in the semi-major axis, of order 10^{-5} AU. They focused on the dynamical lifetimes and found it to be in the range of $0.5 - 5 \times 10^6$ yr, with the strongest dependence being on the perihelion distance. As smaller perihelia, there is a greater chance for particles to suffer a large gravitational

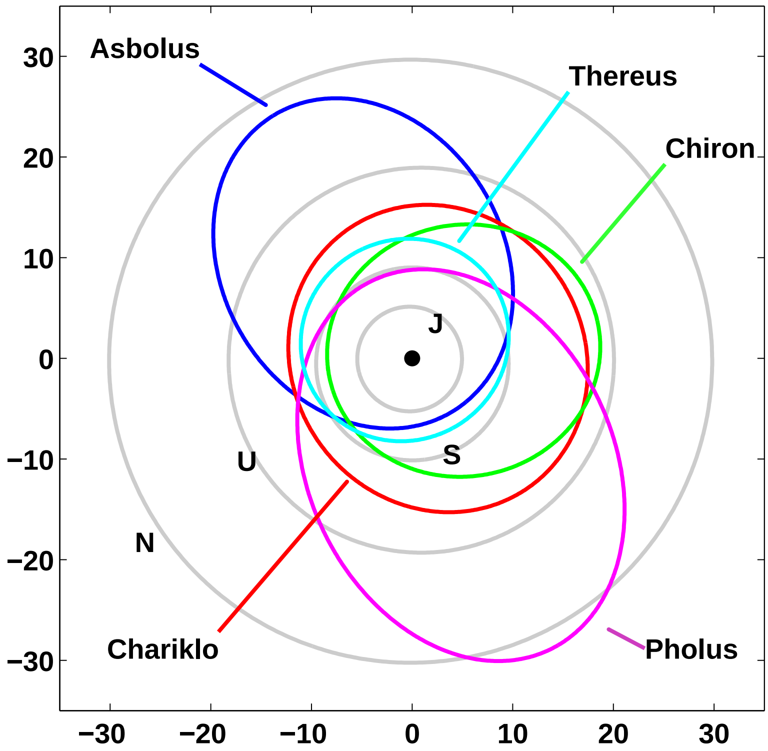

Figure 4.1 Projection onto the ecliptic plane of the orbits of the five sample Centaurs: 8405 Asbolus (blue), 10199 Chariklo (red), 2060 Chiron (green), 5145 Pholus (magenta) and 32532 Thereus (cyan). Shown for reference are the orbits of the four giant planets, in gray. Orbital elements for all orbits pertain to epoch JD 2452400.5 (compiled from JPL's HORIZONS system).

perturbation from the more massive planets (Jupiter or Saturn), thus being ejected from the solar system.

Levison and Duncan (1997) followed the evolution of a sample of hypothetical KBOs, as they dynamically evolved inward, toward becoming JFCs (see also Sec. 1.3.2). En route, some of these objects may be defined as Centaurs. In this paper, they argued for the use of the Tisserand parameter as the basis of dynamical classification in the solar system, as it is more appropriate for planet-crossing orbits than semi-major axis. In the context of the circular restricted 3-body problem, the Tisserand parameter is defined as (Murray and Dermott, 2000)

$$T_p = \frac{a_p}{a} + 2\sqrt{(1-e^2)\frac{a}{a_p}}\cos(i), \tag{4.1}$$

where a_p is the semi-major axis of the planet and a, e and i are the semi-major axis, eccentricity and inclination of the small body, respectively. The Tisserand parameter remains almost constant for a given particle before and after an encounter with a planet

(Levison and Duncan, 1997). Values of T_p close to 3 generally indicate that the orbit of the small body and that of the planet are similar. Thus, the planet can strongly influence the small body's orbit. In particular, Levison and Duncan (1997) identify Centaurs as objects having $T_J > 3$ and $a > 5.2$ AU (Jupiter's semi-major axis). They calculated that, starting with Neptune, each planet could scatter a particle just far enough inward to reduce its perihelion distance so that the particle could cross the orbit of the next planet.

Tiscareno and Malhotra (2003) presented a study of the dynamics of all known Centaur objects as of 2002. They included 53 Centaur objects, using the criterion $5.2 < q < 30$ AU, to constrain initial population. Orbits were followed for 10^8 yr and particles were removed from the simulation if they reached heliocentric distances, $r_H > 20,000$ AU or $r_H < 2.5$ AU. Their results suggest a median dynamical lifetime of 9×10^6 yr for their selected sample, although they also found a large dispersion in individual lifetimes, in the range of $1 - 100 \times 10^6$ yr. This paper also describes the orbital behavior the sample objects as more chaotic than the dynamical evolution found by Levison and Duncan (1997), connected more to transfer between resonances and random-walk in the phase space of orbital elements.

Horner *et al.* (2004a,b) conducted a study that examined both the the bulk statistics and the individual behavior of the Centaur population. They integrated the orbits of more than 23,000 test particles that were cloned from a sample of 32 known Centaurs, for 3×10^6 yr forward and backward in time. For the calculations they define Centaurs as having perihelion $q > 4$ AU and aphelion $Q < 60$ AU. Results of this study indicate a relatively wide range of half-lives for each Centaur, between $0.5 - 32 \times 10^6$ yr. The half-life time was defined as the time when half of the clone population of each Centaur was ejected from the simulation, either by reaching a heliocentric distance greater than 1000 AU or colliding with a planet. Another implication of this paper's results is an estimate of the total population of Centaur objects larger than 1 km in diameter, based on the fraction of simulated particles that become JFCs and an assumed influx to the inner solar system of 0.005 yr^{-1}. Finally, Horner *et al.* (2004a,b) apply the classification scheme suggested in Horner *et al.* (2003), in which the planets closest to the perihelion and aphelion distances are those who control the dynamics (e.g. Table 4.2).

Table 4.2 presents the orbital class, according to Horner *et al.* (2004a), of each of the Centaur objects in our sample. We also calculate the current Tisserand parameters, with respect to each of the four planets (see Eq. 4.1). These two forms of classification are somewhat inconsistent in what we can directly learn from them. For example, Asbolus has its perihelion and aphelion controlled by Saturn and Uranus, respectively. However, the Tisserand parameter closest to 3 is the one with respect to Jupiter, indicating that the strongest orbital perturbations should be due to this planet. This means that while we have a clear distinction of Asbolus, choosing either of the two classifications, we do not know much about its intrinsic orbital evolution.

Table 4.2 Orbital classification of Centaur objects

Des. & name	Class [1]	T_J [2]	T_S [3]	T_U [4]	T_N [5]
8405 Asbolus	SN	3.0704	2.5859	2.5191	2.8355
10199 Chariklo	U	3.4821	2.9317	2.8544	3.2115
2060 Chiron	SU	3.3513	2.8936	2.9558	3.4439
5145 Pholus	SN	3.1979	2.6419	2.4752	2.7017
32532 Thereus	SU	3.1170	2.8380	3.1737	3.9219

[1] Following the classification scheme of (Horner *et al.*, 2004a), where letters designate the planet that dominates the perihelion and aphelion of the object, respectively.

[2]–[5] Tisserand parameters with respect to Jupiter, Saturn, Uranus and Neptune.

di Sisto and Brunini (2007) examined the origin and distribution of the Centaur population, as derived from the SDOs population. Their choice of initial conditions was to debias the orbital elements distribution (mainly semi-major axis and inclination) of 95 observed SDOs. The numerical integration was advanced for 10^8 yr and included 1000 test particles, randomly chosen from the debiased distributions, that evolved into the Centaur region. Their results indicate a mean dynamical lifetime, for the entire population, of 7.2×10^7 yr, a dependence of lifetime on perihelion distance, an estimate for the intrinsic Centaur population of $\sim 2.8 \times 10^8$ objects, and a JFC injection chance of $\sim 30\%$.

4.1.2 Integration Scheme

For the calculations of orbital evolution we used a symplectic integrator, as it is implemented in the SWIFT integration package (Levison and Duncan, 1994). This is a commonly-used and well-known tool, in the planetary science community, for the study of planetary system dynamics. It allows to integrate a set of massive, mutually interacting bodies, and massless “test particles”. This package includes four integration methods:

Wisdom-Holman Mapping (WHM or MVS, Wisdom and Holman, 1991), Regularized Mixed Variable Symplectic (RMVS, Levison and Duncan, 1994), fourth order T+U Symplectic (TU4, Gladman *et al.*, 1991) and Bulirsch-Stoer (BS, Press *et al.*, 1992).

In the WHM approach (2nd order symplectic map) for an N-body problem, the integration consists of dividing the Hamiltonian of the system into two separate integrable parts, such that $\mathcal{H} = \mathcal{H}_{\mathcal{A}} + \mathcal{H}_{\mathcal{B}}$. This means that the equations of motion given by $\mathcal{H}_{\mathcal{A}}$ and $\mathcal{H}_{\mathcal{B}}$ can be explicitly solved. The two parts of the Hamiltonian usually represent the independent Keplerian motion and terms associated with the gravitational perturbations of massive bodies on the particles and among themselves. The advantage of the symplectic map technique over other methods comes from the fact that the energy and angular momentum of the system oscillate slightly, but with no secular trend. Thus long-term integrations are enabled, without introducing spurious numerical outcomes. Under this integration scheme, the state of the system after a time step τ is computed by first following the equations of motion of $\mathcal{H}_{\mathcal{B}}$ for a time $\tau/2$, then following the equations of motion of $\mathcal{H}_{\mathcal{A}}$ for a time τ, and finally following again the equations of motion of $\mathcal{H}_{\mathcal{B}}$ for a time $\tau/2$ (for a concise derivation, see Chambers, 1999). Symplectic mapping theory ensures that there exists an integrable Hamiltonian, which can exactly interpolate the same resulting orbits, to an order τ^2. However, there is one additional degree of freedom, resulting from this scheme, which can produce spurious chaos, due to resonances between the time step and the shortest period T in the system. These resonances have widths proportional to $e^{-(T/\tau)^{\alpha}}$, forcing the choice of a small fraction of the orbital period to be taken as the time step, in order to minimize the error encountered at each time step.

The preferred integration method used in our studies is the RMVS one, which is a variant of the WHM. In this approach, close encounters of test particles with massive bodies and the behavior of planet-crossing orbits is handled more accurately. During a close approach to a massive body, the perturbing part of the Hamiltonian becomes increasingly more dominant over the Keplerian part. As a result, the splitting of the perturbing part, $\mathcal{H}_{\mathcal{B}}$, into two distinct $\tau/2$ time steps, imparts an error on the total computation of the τ time step, which is on the same order. In order resolve this, the Regularized MVS method (Levison and Duncan, 1994) first reduces the time step and then re-arranges the division of the Hamiltonian, when within a few Hill's radii of the perturbing body. The focus now shifts to the massive body – the Keplerian part describes the two-body interactions of the test particle with the body and the perturbation part addresses the interactions with the Sun and other perturbers. Thus, the dominant part is always the Keplerian and there is no need to reduce the time step any further. However, the consequence of varying the time step and the Hamiltonian partition is that the scheme is no longer strictly symplectic (there is no single interpolating Hamiltonian). This can produce a variation in the system's energy, which can, through a sequence of close encounters, accumulate to a significant error for the conservation properties of the system. This drawback is not too severe, as most particles experiencing many close approaches will be preferably scattered by the massive perturbers, rather then have their orbits evolve slowly. See Morbidelli (2002b) for a more detailed discussion of the properties and implementations of this method.

4.1.3 Initial Configuration

We tracked the variations in the orbital elements of 2500 massless test particles, which were cloned from the selected sample of five Centaur objects and moved under the influence of gravitational perturbations from the four planets in the outer solar system. A particle was removed from the simulation in the following situations: evolution of orbit to a heliocentric distance smaller than 5.2 AU (Jupiter's orbit), heliocentric distance greater than 100 AU, or collision onto a planet (particle-planet distance smaller than a 'closest approach' distance, taken as the planet's radius). The time step was constrained to be 1 yr, results were recorded every 1000 yr and the overall duration of the simulations was 10^7 yr.

Fig. 4.2 shows the distribution of all known Centaurs and SDOs, as a function of their perihelion and aphelion distances. The objects that are the focus of this study are identified by name.

It is clear that heliocentric distances smaller than 5.2 AU require even smaller perihelion distances. These are not observed among the Centaurs, as such perihelion distances mostly lead to a JFC orbit. In this study we are interested only in the intrinsic dynamics of Centaur objects, so transfer to the JFCs region constitutes a removal from the intrinsic population. Heliocentric distances greater than 100 AU require even greater aphelion distances. Such aphelion distances are only compatible with the broader definition of Centaurs. However, objects on such orbits spend most of their time well beyond the orbit of Neptune, and only a fraction reach to within the perihelion distance of Neptune. The SDOs are a much better fit to such orbits. Thus, the boundaries for keeping the

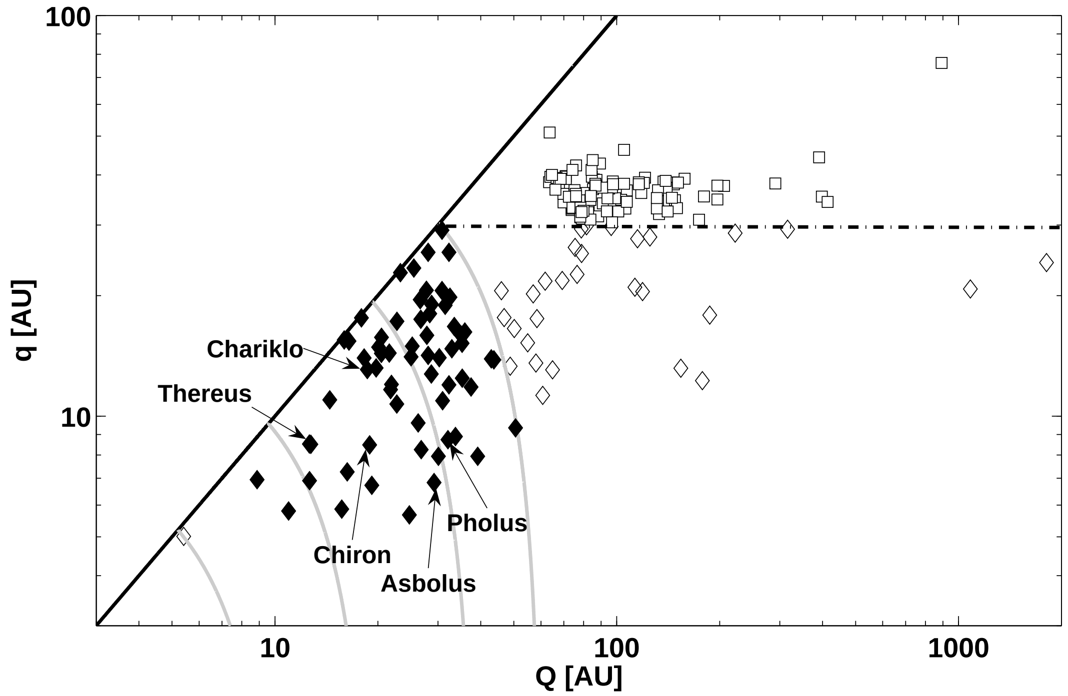

Figure 4.2 Map of all known Centaurs and SDOs, in aphelion-perihelion space. Open squares represent the SDOs and diamonds represent Centaurs. The distinction between open and solid diamonds follows the two standard dynamical divisions of the Centaurs/SDOs population, as mentioned in the Sec. 1.2.2. The horizontal dash-dotted line marks Neptune's perihelion distance, while the curved gray lines represent constant semi-major axis contours for Jupiter, Saturn, Uranus, and Neptune. Marked by their names, are the Centaur objects that we focus on. Data compiled from the Minor Planet Center website, as of November 2008.

Centaur population well-defined should be between 5.2-100 AU. The duration of the integration, 10^7 yr, was chosen to coincide with the current estimate of median lifetime, for the intrinsic Centaur population (Tiscareno and Malhotra, 2003).

The time step for the integrations was taken to be 1 yr. This is less than 10% of the smallest orbital period in the system (that of Jupiter), which constitutes the boundary for evolving particles. It is also a few percent of the smallest initial orbital period of the test particles – those pertaining to Thereus, with 35 yr (see Table 4.1). We experimented with some toy integrations of shorter and longer time steps. These integrations were followed for 10^5 yr, with 100 test particles, randomly distributed between $a = 10 - 20$ AU (semi-major axis) and $e = 0.3 - 0.5$ (eccentricity), and suffering close encounters with the planets at a distance equal to the Hill radius of the planet. Boundaries of the integration were as discussed above. We concluded that a time step of 1 yr constitutes a very good compromise between computational constraints (size of output files and real-time duration of computer runs) and dependence of integration results on time step. The latter is evident, as various statistics (initial population depletion times, planet encountering probabilities and survival probabilities) remain very similar for time steps up to a year, but change drastically beyond that.

The number of test particles to fill the initial population was chosen after experimenting with a few toy integrations, where we varied the initial size of the population and examined the number of surviving particles. These integrations had a time span of 10^6 yr, time step of 1 yr, and a random distribution of particles between $a = 10-20$ AU, with eccentricity of 0.4 and inclination of 10°. Boundaries of the integration were as discussed above. We concluded that an initial population size between $50-100$ is the minimum required. In order to reconcile computational constraints (size of output files and real-time duration of computer runs) and accuracy of statistics, we converged on an initial number of 500 test particles per object.

The cloned test particles of each object have similar initial orbits. Since Centaur objects suffer strong planetary perturbation throughout most of their lifetime on the outer solar system, their orbits are rendered chaotic (Tiscareno and Malhotra, 2003; Horner *et al.*, 2004a). In order to account for this chaotic nature, the initial conditions of each particle in the clone sample of 500 particles were chosen randomly, with orbital elements slightly varied with respect to the known orbital elements of the Centaur object that was cloned. Each initial clone population of 500 test particles was distributed through a small cube of $a - e - i$ (semi-major axis, eccentricity and inclination), with $da/a = de/e = di/i = 10^{-5}$. The other orbital angles were chosen randomly between $0 - 360°$. This choice of initial conditions ensures both that the clones can be considered as initially essentially identical to one another, and that the subsequent chaotic orbital evolution, due to various gravitational perturbations, will rapidly disperse their orbits through the orbital elements phase space (Dones *et al.*, 1996; Horner *et al.*, 2004a).

The last parameter to determine was the 'closest approach' distance. If a test particle gets to within this distance of the a planet it is removed from the integration. This parameter can be defined for each planet. Since Centaur objects are prone to frequent gravitational interactions, deciding on what constitutes a 'close encounter' with a planet can have a decisive effect on the outcomes of an integration. We experimented with several options for this parameter, ranging between $\sim 0.001 - 1$ Hill radius, which is the boundary between the gravitational dominance of the Sun and a perturbing planet, in the circular restricted 3-body problem. The value of ~ 0.001 Hill radius is actually the radius of the planet. Full integrations were calculated, including all the above mentioned considerations and the same initial populations of cloned test particles.

Fig. 4.3 shows the results of a set of integrations for the Centaur 2060 Chiron, aimed at examining the above mentioned parameter. We compare the cumulative distribution functions of semi-major axes and lifetimes, as recorded for the last stable orbit of each clone. It is clear that the limiting cases are those where the 'closest approach' distance is 1 Hill radius (blue curve) and the planet's radius (red curve). It is also clear that the lower bound has statistically similar outcomes to distances up to 0.1 Hill radius, while the upper bound has similar outcomes to the case of 0.5 Hill radius.

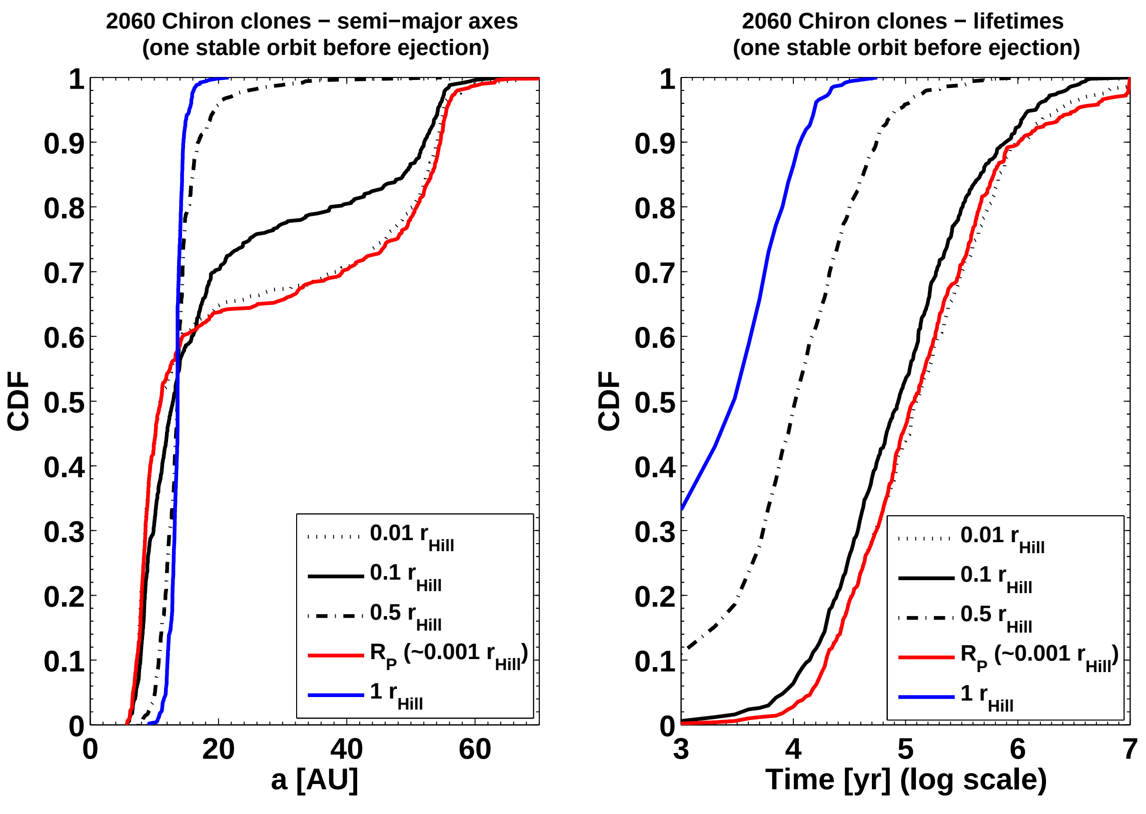

Figure 4.3 Comparison of orbital stability for Chiron's clone population, as dependent on the 'closest approach' distance to the planets. Shown here are distances corresponding to the each planet's radius (red) and factors of each planet's Hill radius of 1 (blue), 0.5 (dash-dot), 0.1 (solid), 0.01 (dot). *Left*: cumulative distribution function of semi-major axes, one orbit before each particle was ejected from the boundaries of the simulation. *Right*: cumulative distribution function of lifetimes, one orbit before each particle was ejected from the boundaries of the simulation.

Fig. 4.4 shows the difference between the two limiting cases of 'closest approach' distances, in terms of the evolution of orbital elements for an individual test particle. For the sake of illustration, we chose particle #93 of the Asbolus clone population and display its perihelion distance, eccentricity and inclination. It is clear that evolution is identical until the orbit begins to de-stabilize, at around 2×10^4 yr, for the case of 1 Hill radius. Near the ejection instance, where the red curve stops, variations of the orbital elements arise between the two cases, but they are small in amplitude. Thus, a 'closest approach' distance of a planetary radius was taken to represent the close encounter of a test particle with a planet, meaning that objects are removed by physically colliding onto the surface of a planet.

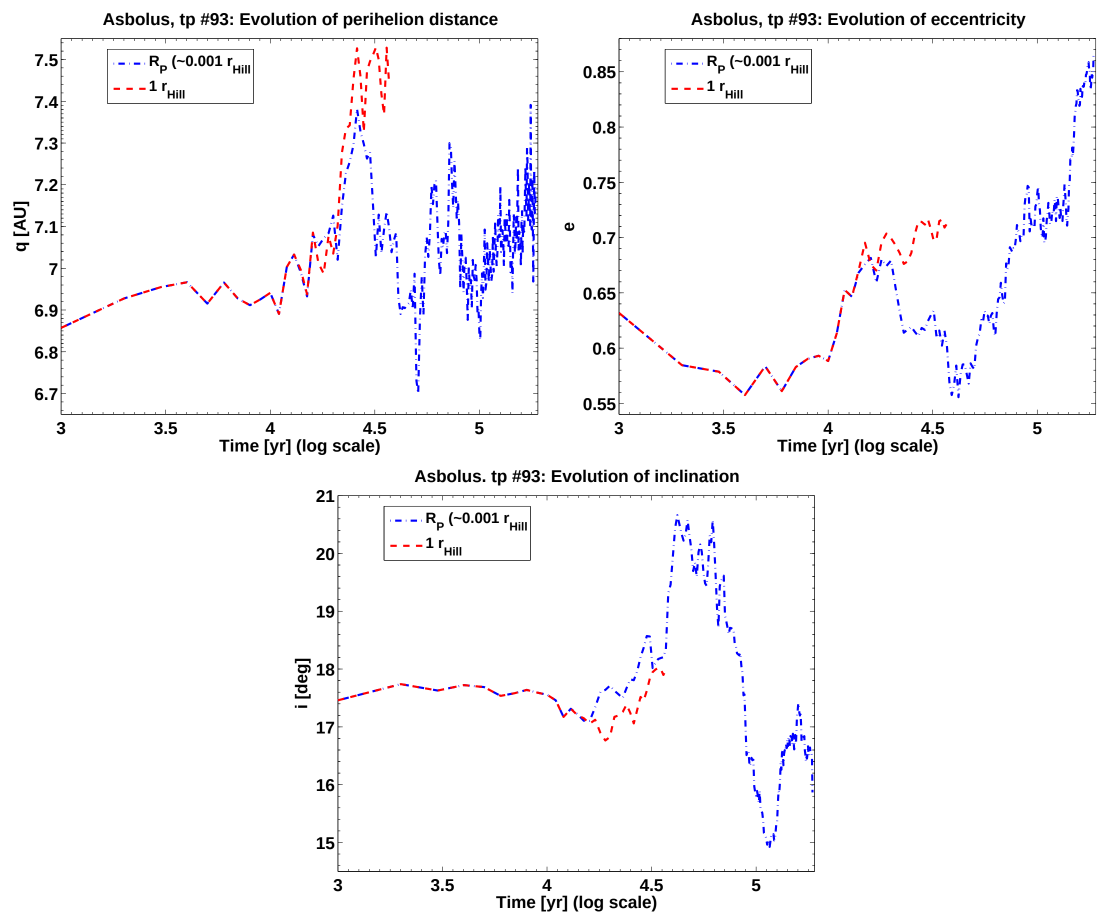

Figure 4.4 Evolution of orbital elements for Asbolus tp93. Compared here are the two limiting cases of the 'closest approach' distance to the planets, 1 Hill radius (blue) and planet's radius (red), as they affect the evolution of perihelion distance (top left), eccentricity (top right) and inclination (bottom). Note that the evolution is identical until the orbit begins to de-stabilize.

4.1.4 Summary of Results

Here we analyze the orbital stability of our samples, through the statistics of the ensemble of test particles, for each clone population of a specific Centaur object. Results are discussed in terms of dynamical lifetimes, survival probabilities, mean orbital elements, planetary encounter probabilities and representative individual orbital evolution.

Fig. 4.5 shows the cumulative distribution function of the lifetimes for each clone population of 500 particles, pertaining to a specific Centaur object. These lifetimes are the time from beginning of integration (t=0) to the time of the last stable orbit, for each test particle. The different Centaur objects are shown in different colors, as a function of time. We can see that Chariklo is the most stable of our sample objects, as actual depletion of its representative population of test particles begins only after $\sim 3 \times 10^5$ yr. At the end of the simulation, $\sim 20\%$ of the particles are still active. At early times, the clone population of Chiron is the one that scatters most rapidly, where at 10^5 yr about 50% of the particles are already removed from the simulation. At later times, more than 80% of the particles of all clone populations, except that of Chariklo, are already ejected and the cumulative distributions level off towards the 90% value.

Table 4.3 summarizes the lifetimes and ejection/survival probabilities, which were derived from the full integration of all test particles. These values are stated for each Centaur object, as resulting from the dynamical evolution of all 500 clones.

t_{50} is the median dynamical lifetime, representing the time during the integration, at which 50% of the clones have been removed. t_{90} is the time during the evolution, at which 90% of the clones have been removed (See Fig. 4.5 for the graphical representation of these times). While the median lifetime is usually taken as the canonical dynamical lifetime, we prefer to take t_{90} as such. This is because all t_{50}'s are much shorter than the median dynamical lifetime for the entire Centaurs population, as derived by Tiscareno and Malhotra (2003). Therefore, we wait until most of the clone population has been depleted, but ensure that there are still enough particles to make the statistics robust (see discussion in Sec. 4.1.1). $\mathrm{t}_{diff.}$ is a median lifetime, calculated from an approximated diffusion model, $t_{diff.} = 4.77 \times 10^4 10^{q/3.5AU} (1AU/a)^{1/2}$ yr (see Dones *et al.*, 1996, and references therein). Since orbits are expected to be chaotic, a diffusion model, such as given by Yabushita (1980), may provide a reasonable estimate of the dynamical lifetimes. However, there is a notable discrepancy between these times and the two former definitions

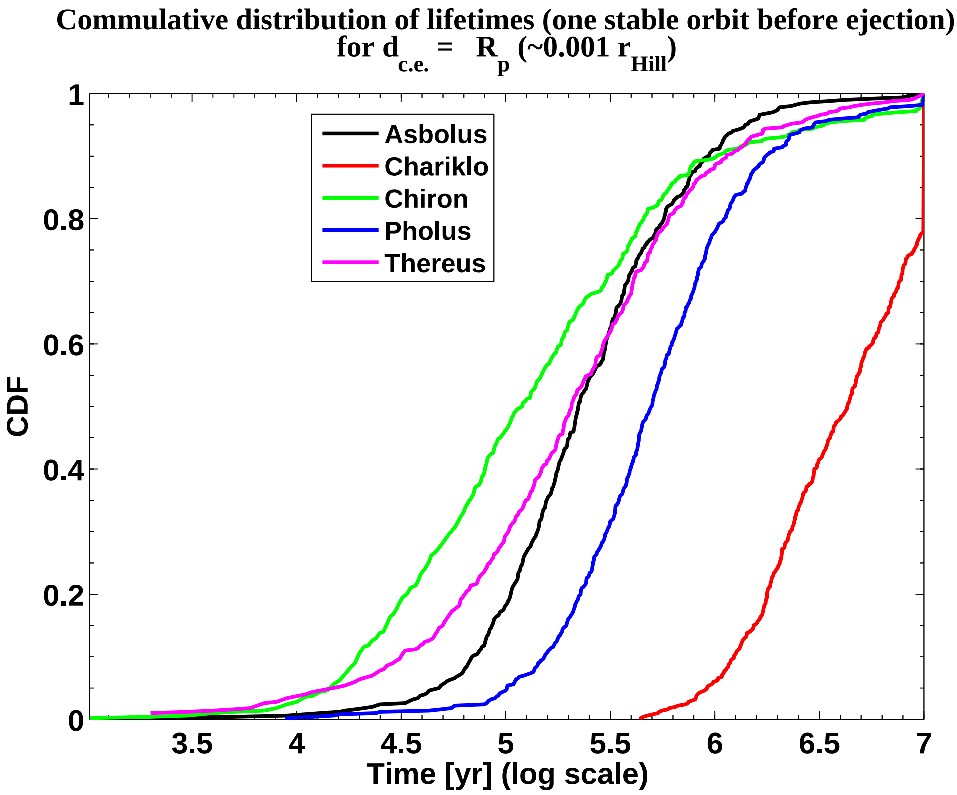

Figure 4.5 Cumulative distribution function of lifetimes, for the complete 500 clones sample of each Centaur object. The different colored curves represent the number of stable orbits just before ejection from the simulation boundaries. Time is shown on a logarithmic scale. See table 4.3 for the summary of main results from this figure.

of dynamical lifetimes. Clearly, the t_{50}'s are in complete disagreement with the diffusion estimate.

The discrepancy in values between t_{90} and $t_{diff.}$ seems to indicate that as eccentricities are higher the diffusion median lifetime is closer to the dynamical lifetime. Thus, within the scheme of our integrations, t_{90} is probably the best estimate for the lifetimes of the chaotically evolving particles.

Ejection and survival probabilities, presented in the last three columns of Table 4.3, record the fraction of particles, for each clone population, that were removed from the integration, either inward or outward, or that survived the whole 10^7 yr duration of the integration. We note that survival probabilities are not necessarily correlated with dynamical lifetimes. Chiron has the second shortest dynamical lifetime t_{90}, but its survival probability as a proper Centaur is larger than that of Thereus and Pholus. This probably attests to the more chaotic nature of Chiron's orbit, in comparison to the other two

Table 4.3 Lifetimes (in Myr) and statistics for the different Centaur objects

	t_{50} [1]	t_{90} [2]	$t_{diff.}$ [3]	Ej.$_{(out)}$ [4]	Ej.$_{(in)}$ [5]	Surv. [6]
8405 Asbolus	0.22	0.94	1.01	0.692	0.302	0.006
2060 Chiron	0.12	1.02	3.32	0.348	0.626	0.026
32532 Thereus	0.21	1.14	4.0	0.35	0.64	0.01
5145 Pholus	0.5	1.76	3.17	0.734	0.248	0.018
10199 Chariklo	4.3	> 10	65.3	0.446	0.33	0.224

[1] Time in Myr at which 50% of the clones survive the integration (see Fig. 4.5, for the lifetime distributions).
[2] Time in Myr at which 10% of the clones survive the integration (see Fig. 4.5, for the lifetime distributions).
[3] Median lifetime in Myr, as calculated from an approximated diffusion model (Dones *et al.*, 1996).
[4] Fraction of particles that were ejected beyond the outer boundary of the integration.
[5] Fraction of particles that were ejected beyond the outer boundary of the integration.
[6] Fraction of particles that survived for the whole 10 Myr duration of the integration.

objects. The inward ejection probability, Ej.$_{(in)}$, can be regarded as the probability of the Centaur object to become a JFC, or at least be observed as a JFC-like object, during the time span of the simulation. Thus, Thereus and Chiron are the Centaurs most probable to evolve inwards and may display cometary activity at some point in their evolution. Indeed, Chiron is well-known for its cometary activity patterns (Jewitt, 2009). The inhomogeneous surface properties observed for Thereus (Licandro and Pinilla-Alonso, 2005), might be a result of some cometary activity, causing outgassing or exposure of ices, from below the surface. The other three Centaurs are more likely to be ejected to large heliocentric distances, leaving the region bounded by the orbits of the outer planets.

Table 4.4 summarizes the relative influence of each of the four outer planets on the orbital stability of our sample objects. The values represent the number of particles that suffered a fatal encounter with a specific planet. This interaction drives them to an unbound orbit, or forces them outside the boundaries of the simulation. These can also be interpreted as the probability of a certain Centaur object to be ejected by a certain planet.

An obvious result is that all of our objects, who have different stability characteristics

Table 4.4 Last planetary encounters for each Centaur object

	J †	S †	U †	N †
8405 Asbolus	0.118	0.634	0.096	0.146
10199 Chariklo	0.094	0.516	0.074	0.094
2060 Chiron	0.258	0.612	0.042	0.064
5145 Pholus	0.066	0.756	0.076	0.084
32532 Thereus	0.204	0.67	0.066	0.05

† Fraction of particles, for each object sample of 500 clones, that encountered the designated planet, before being ejected outside the boundaries of the integration (either outwards or inwards).

for their orbits, suffer most likely from the hands of Saturn. Thus, although Jupiter is commonly considered as the main de-stabilizer of orbits in the outer solar system, Saturn may play the dominant role in the orbital stability of the intrinsic Centaur population. We see that Chariklo, which has the most stable orbit according to our lifetime and ejection analysis above (see Table 4.3), has the lowest probability of our Centaur sample to encounter Saturn. However, it is more likely than most objects to be ejected by Neptune (although this probability is lower than 10%). This is due to the fact that Chariklo's clones evolve more diffusively in the orbital phase space, with their scattering timescales being longer than the other clone populations.

Fig. 4.6 and 4.7 show the aphelion/perihelion and inclination/semi-major axis distributions of the clone populations of Chariklo and Asbolus, respectively, at different times during the orbital evolution. The initial conditions (see Sec. 4.1.3) are concentrated in the tiny red region, also marked by an arrow.

Fig. 4.6 demonstrates the slower rate at which the Chariklo clones fill up the orbital phase space. The 'snapshots' of the evolution are given at 10^5, 10^6, 5×10^6 and 10^7 yr. We see that the diffusion through phase space advances slowly, with $\gtrsim 10^6$ yr for particles to reach close to the boundaries of the simulation. Even then, most particles are still concentrated in the region between $Q \simeq 18 - 26$ AU and $q \simeq 10 - 16$ AU in the left panel of Fig. 4.6 and $i \simeq 20 - 27$ deg and $a \simeq 12 - 22$ AU in the right panel. This means that the eccentricity of the orbits is bound between $e \simeq 0.059 - 0.444$. Thus, the ratio of the minimum to maximum specific angular momentum, $l = \sqrt{GM_{\odot}a(1-e^2)}$, for the orbits that most of the clone inhabit, is ~ 0.663. The corresponding ratio of the minimum to

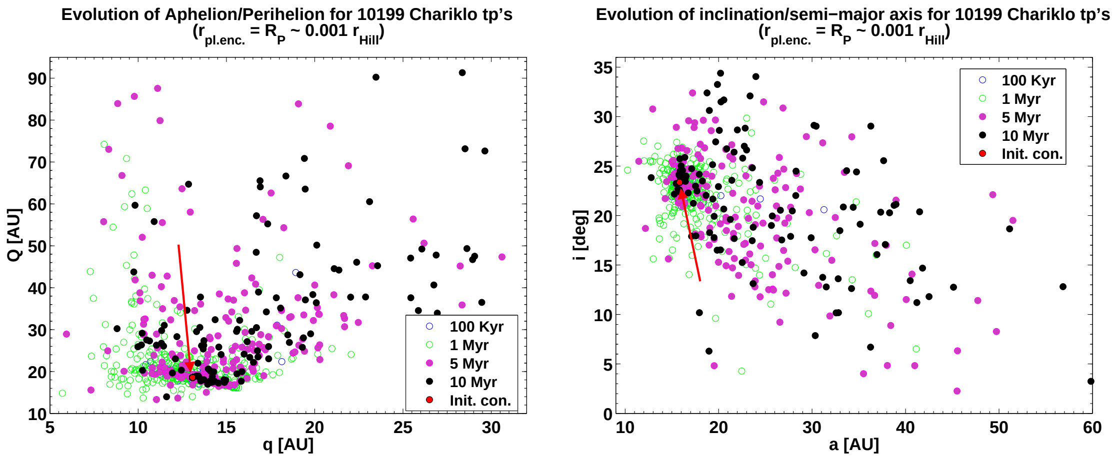

Figure 4.6 *Left*: Perihelion and aphelion distribution of the clone population of 10199 Chariklo, as it evolves in time in q-Q space. *Right*: Semi-major axis and inclination distribution of the clone population of 10199 Chariklo, as it evolves in time in a-i space. Shown here are snapshots of the particles' locations at 10^5 yr (blue circles), 10^6 yr (green circles), 5×10^6 yr (magenta) and 10^7 yr (black). The initial population, which is highly concentrated around the known elements of Chariklo (see Table 4.1), is marked with a red arrow.

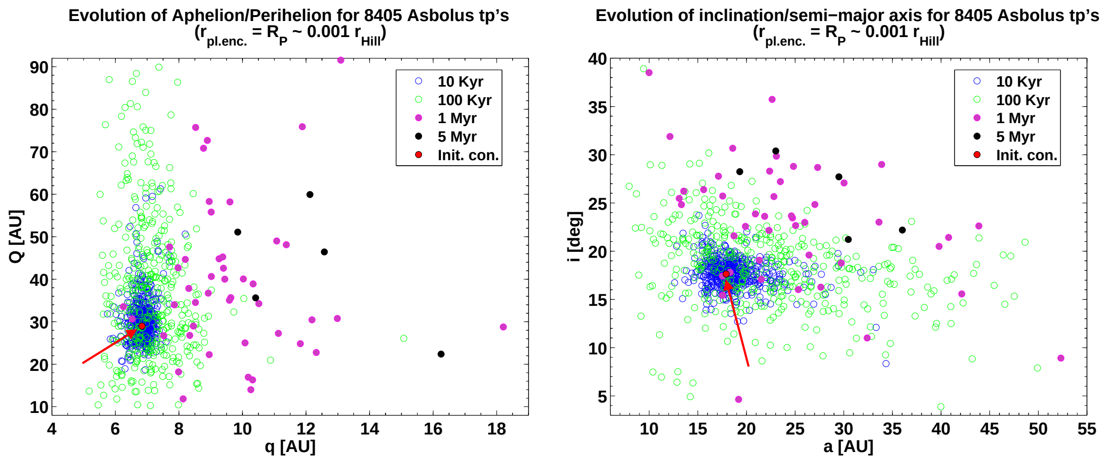

Figure 4.7 *Left*: Perihelion and aphelion distribution of the clone population of 8405 Asbolus, as it evolves in time in q-Q space. *Right*: Semi-major axis and inclination distribution of the clone population of 8405 Asbolus, as it evolves in time in a-i space. Shown here are snapshots of the particles' locations at 10^4 yr (blue circles), 10^5 yr (green circles), 10^6 yr (magenta) and 5×10^6 yr (black). The initial population, which is highly concentrated around the known elements of Chariklo (see Table 4.1), is marked with a red arrow.

maximum specific orbital energy, $|\epsilon| = \frac{GM_\odot}{2a}$, is ~ 0.54.

Fig. 4.7 shows that for Asbolus the diffusion through phase space is much more rapid than for Chariklo, with $\lesssim 10^5$ yr for particles to reach close to the boundaries of the simulation. The 'snapshots' of the evolution are given at 10^4, 10^5, 10^6 and 5×10^6 yr. Only a handful of particles remain active around 5×10^6 and they are already on relatively excited orbits, with high inclinations and aphelion distances. Before most of the population has been dispersed and ejected, $t \lesssim 10^5$, the bulk of the orbits occupied by the particles are in the range of $Q \simeq 20 - 45$ AU and $q \simeq 6 - 8$ AU in the left panel of Fig. 4.7 and $i \simeq 15 - 21$ deg and $a \simeq 15 - 25$ AU in the right panel. This means that the eccentricity of the orbits is bound between $e \simeq 0.428 - 0.765$. Thus, the ratio of the minimum to maximum specific angular momentum, for the orbits that most of the clone inhabit is ~ 0.55. The corresponding ratio of the minimum to maximum specific orbital energy is ~ 0.6.

Detailed evolution of the orbital elements of representative particle clones, chosen from the Chariklo population, are presented in Fig. 4.8, 4.9 and 4.10. We show the time evolution of semi-major axis, eccentricity, inclination, perihelion, aphelion and argument of perihelion. We identify the strongest mean-motion resonances, between the particle and either of the four outer planets, according to the scheme presented in Gallardo (2006).

Fig. 4.8 shows the dynamical evolution of Chariklo clone #163. Its evolution goes through two periods of strong mean-motion resonance interactions with Uranus or Neptune (4:3 or 8:3, respectively), at around 3×10^5 yr, and with Saturn or Uranus (1:2 or 7:5, respectively), at around 2.2×10^6 yr. This object is one of the shorter-lived particle of the clone population, with a last stable orbit recorded at 3.9×10^6 yr. It is ejected outside of the simulation (to beyond 100 AU) by Saturn. The orbit remains between those of Saturn and Uranus, up to $\sim 3 \times 10^6$ yr, with only a few instances where it crosses the orbit of Uranus. During this time there are two possible events of capture into a Kozai resonance (Morbidelli, 2002a), as indicated by the libration of the argument of perihelion around $\sim 90°$ ($t \simeq 2 \times 10^6$ yr) $\sim 270°$ ($t \simeq 3 \times 10^6$ yr). However, these appear to be weak, as there are no clear periodic exchange between the eccentricity and inclination. After that time it experiences a strong interaction with Saturn and the orbit becomes much less stable. This is demonstrated by the much sharper oscillations in eccentricity and inclination, after $\sim 3 \times 10^6$ yr, also accompanied by larger amplitudes of semi-major axis variations. The final ejection occurs shortly after another interaction with Saturn.

Fig. 4.9 shows the dynamical evolution of Chariklo clone #251. Its evolution goes through many periods of mean-motion resonance interactions, most of them with Uranus. The most pronounced ones are at around 3×10^5 yr with Uranus (4:3,11:8, or 13:10), at

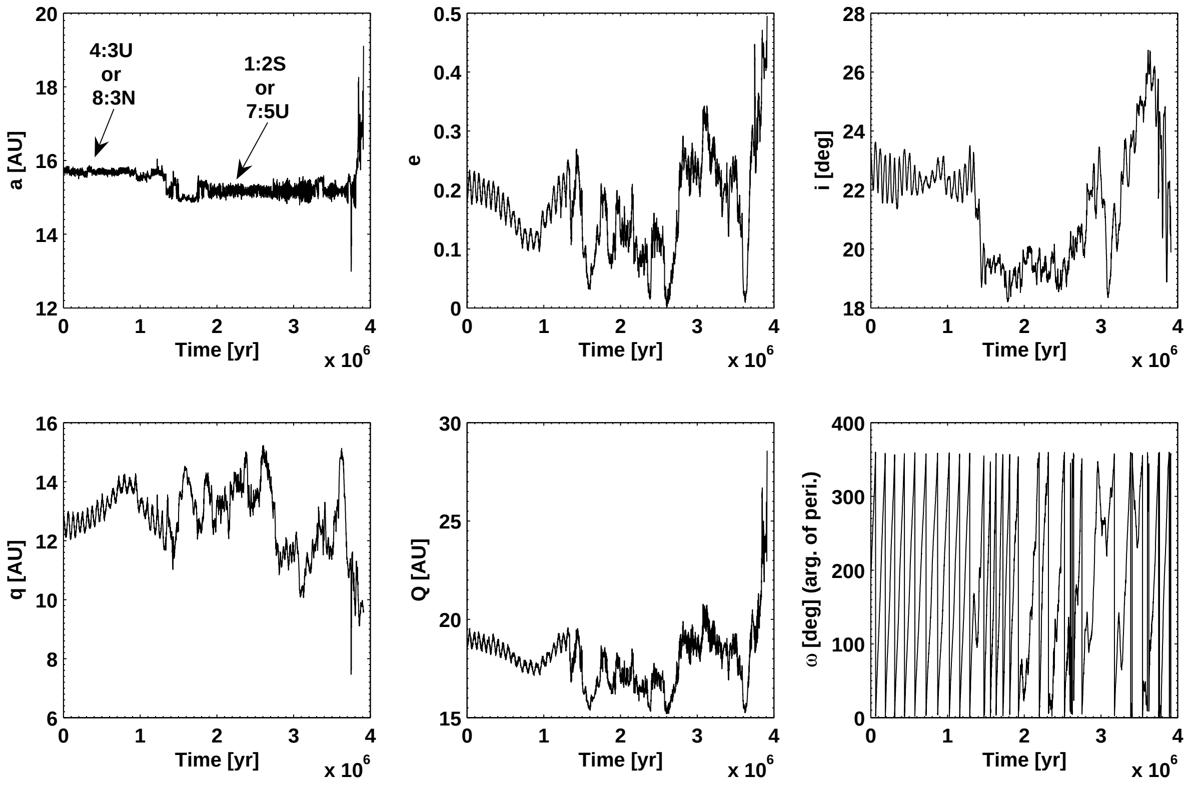

Figure 4.8 Evolution of the orbital elements of 10199 Chariklo clone 163. Shown here are semi-major axis, a, eccentricity, e, inclination, i, perihelion and aphelion distances, q and Q and argument of perihelion, ω. The evolution of these elements is a result of the gravitational perturbations in the outer Solar system. We note that this object has a relatively stable orbit, until just after 3.9×10^6 yr it is ejected from the simulation (reaching beyond 100 AU) by a close encounter with Saturn.

around 1.6×10^6 yr with Uranus (7:6), at around 2.5×10^5 yr with Uranus or Jupiter (6:5 and 7:6 or 1:6, respectively) and at around 3.3×10^6 yr with Uranus or Saturn (4:3, 5:4 and 9:7 or 4:9, respectively). This object has a longer lifetime than clone #163, coinciding with the median lifetime of the entire clone population of Chariklo (see Table 4.3), with the last stable orbit recorded at 4.3×10^6 yr. It is ejected outside of the simulation by Uranus. Its eccentricity and inclination experience a jump, with eccentricity sharply decreasing and inclination sharply increasing, at $t \simeq 3.9 \times 10^6$ yr. Just prior to this, the orbit becomes more tightly concentrated around that of Saturn, as indicated by the perihelion and aphelion values. It experiences strong interactions with Saturn, which could be attributed to the Kozai mechanism, as indicated by the confined libration of the argument of perihelion (Morbidelli, 2002a), ω, around 200°. This is the cause for the large eccentricity variations, which subsequently leads to a close encounter of this particle with

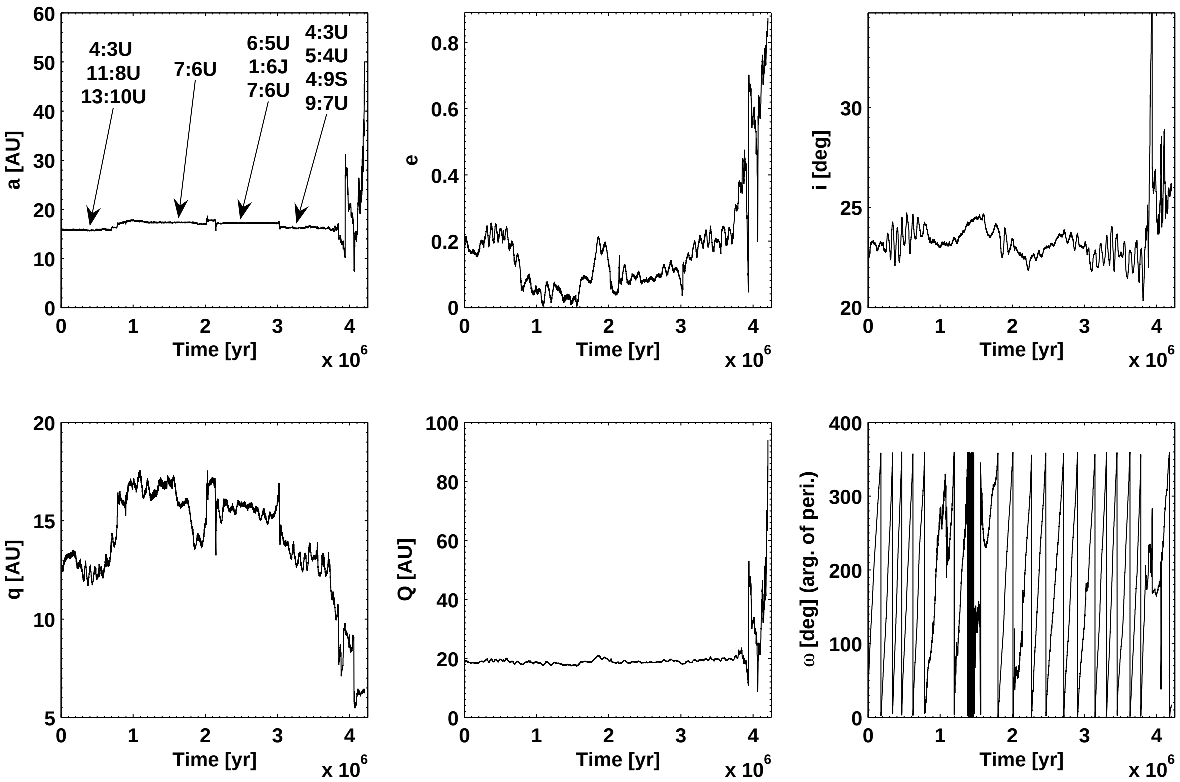

Figure 4.9 Evolution of the orbital elements of 10199 Chariklo clone 251. Shown here are semi-major axis, a, eccentricity, e, inclination, i, perihelion and aphelion distances, q and Q and argument of perihelion, ω. The evolution of these elements is a result of the gravitational perturbations in the outer Solar system. We note that this object has a stable orbit, with a lifetime of 4.2×10^6 yr, similar to the mean dynamical lifetime (see Table 4.3), until it is ejected from the simulation (reaching beyond 100 AU) by a close encounter with Uranus.

Uranus and an orbit bringing it to beyond 100 AU.

Fig. 4.10 shows the dynamical evolution of Chariklo clone #399. Its evolution goes through three distinct periods of mean-motion resonance interactions: At around 1.2×10^6 yr with Saturn (1:5), Uranus (4:7), or Neptune (9:8, 10:9); At around 2.9×10^6 yr with Saturn (1:7) or Neptune (4:5); At around 5.1×10^6 yr with Neptune (3:4) or Uranus (3:8). This object has a much longer lifetime than the two other clones discussed, with the last stable orbit recorded at $\sim 7 \times 10^6$ yr. It is ejected outside of the simulation (to beyond 100 AU) by Neptune. The behavior of the argument of perihelion does not exhibit any notable signs for possible instances of capture into a Kozai resonance, as was the case for the other two clones. The orbital eccentricity gradually increases, mostly due to secular perturbations, causing the aphelion distance to gradually increase as well. At around

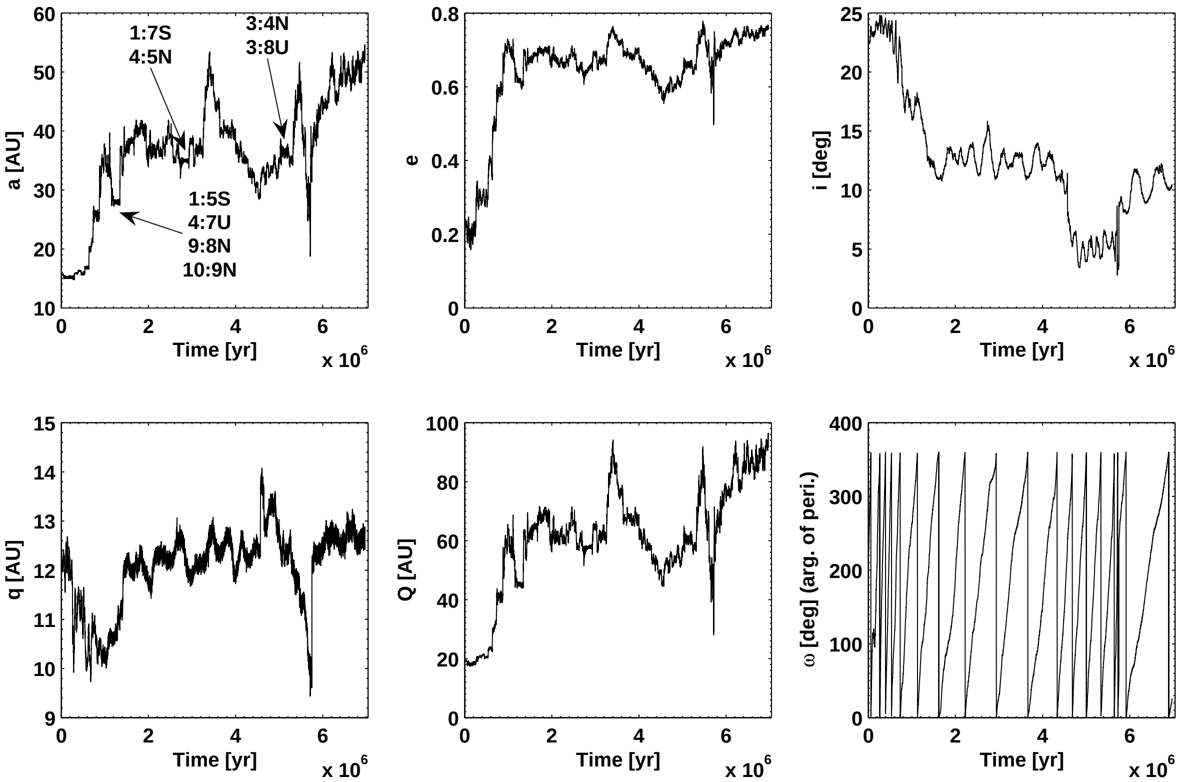

Figure 4.10 Evolution of the orbital elements of 10199 Chariklo clone 399. Shown here are semi-major axis, a, eccentricity, e, inclination, i, perihelion and aphelion distances, q and Q and argument of perihelion, ω. The evolution of these elements is a result of the gravitational perturbations in the outer Solar system. We note that this object has a very stable orbit, with a lifetime of $\sim 7 \times 10^6$ yr, until it is ejected from the simulation (reaching beyond 100 AU) by a close encounter with Neptune.

5.7×10^6 yr a sharp decrease of perihelion distance to the vicinity of Saturn. As the eccentricity decreases, the aphelion distance moves inward to Neptune and there is a brief period where the orbit is confined between those of Saturn and Neptune. A subsequent outwards scatter due to interactions with Saturn causes the semi-major axis to increase beyond the orbit of Neptune ($a \gtrsim 40$ AU). Thus, with $e \gtrsim 0.6$, the aphelion distance continues to increase gradually. Finally, secular perturbations by Neptune drive the orbit to diffuse further and the particle is removed from the simulation.

Fig. 4.11 and 4.12 show the mean value of the eccentricity and inclination of the entire population of clones, for each Centaur objects, as a function of time. The evolution time for each population is the dynamical lifetime, t_{90}, taken from Table 4.3. The additional frame in each panel depicts the coefficient of variation, or relative standard deviation (standard deviation divided by the mean), RSD, for each corresponding value.

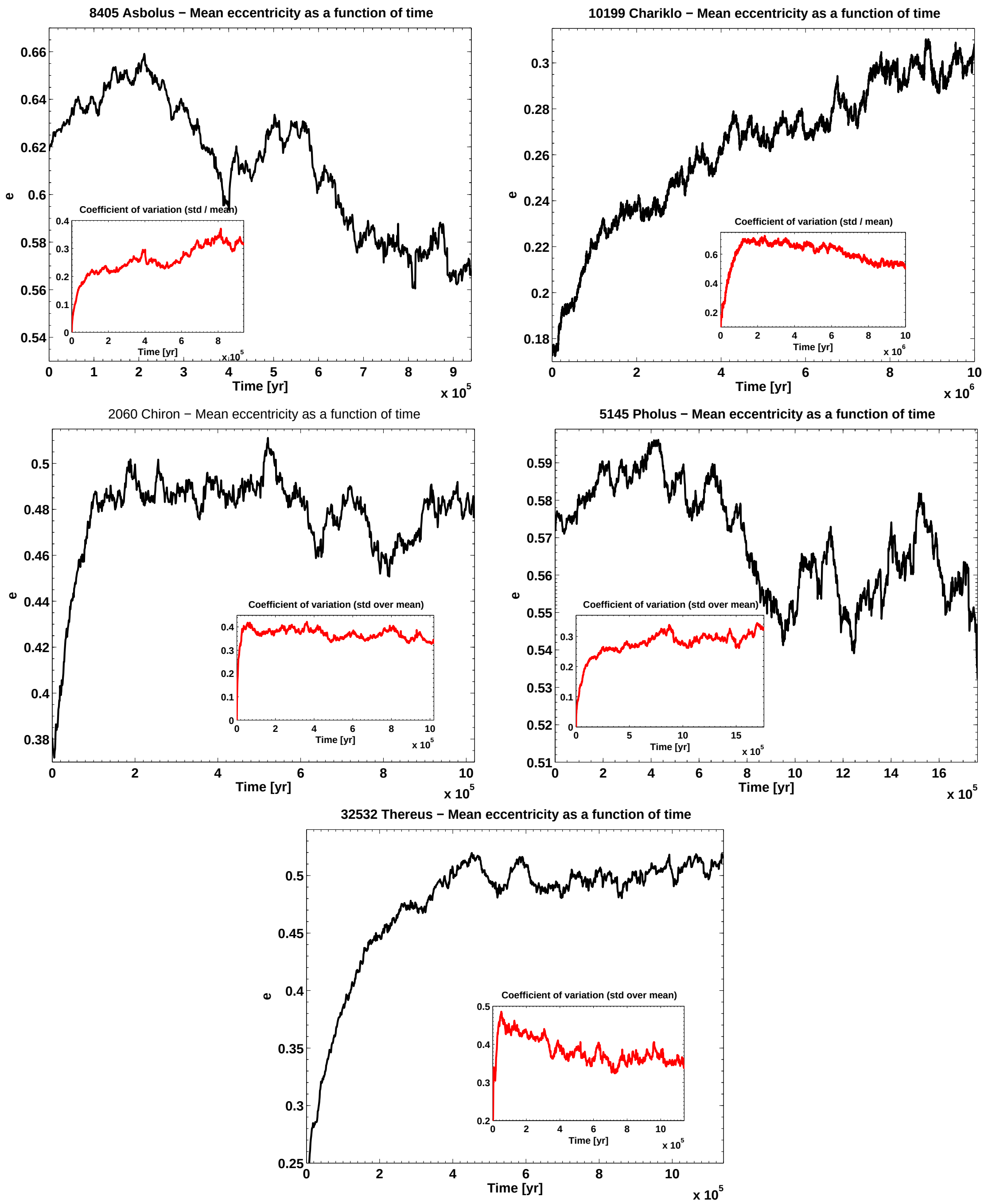

Figure 4.11 Mean value of the eccentricity, for the clone populations of each Centaur object, as a function of time. Shown for each time step, are the average of all orbital eccentricities (black) and the coefficient of variation (red), which is the relative standard deviation (standard deviation divided by the mean). Maximum time for each Centaur clone population is the dynamical lifetime, $t_9$0, from Table 4.3.

For Asbolus, the mean eccentricity of the clone population is only slightly varied, from an initial value of 0.62 to 0.57, and remains in the range $e = 0.56 - 0.66$. The mean

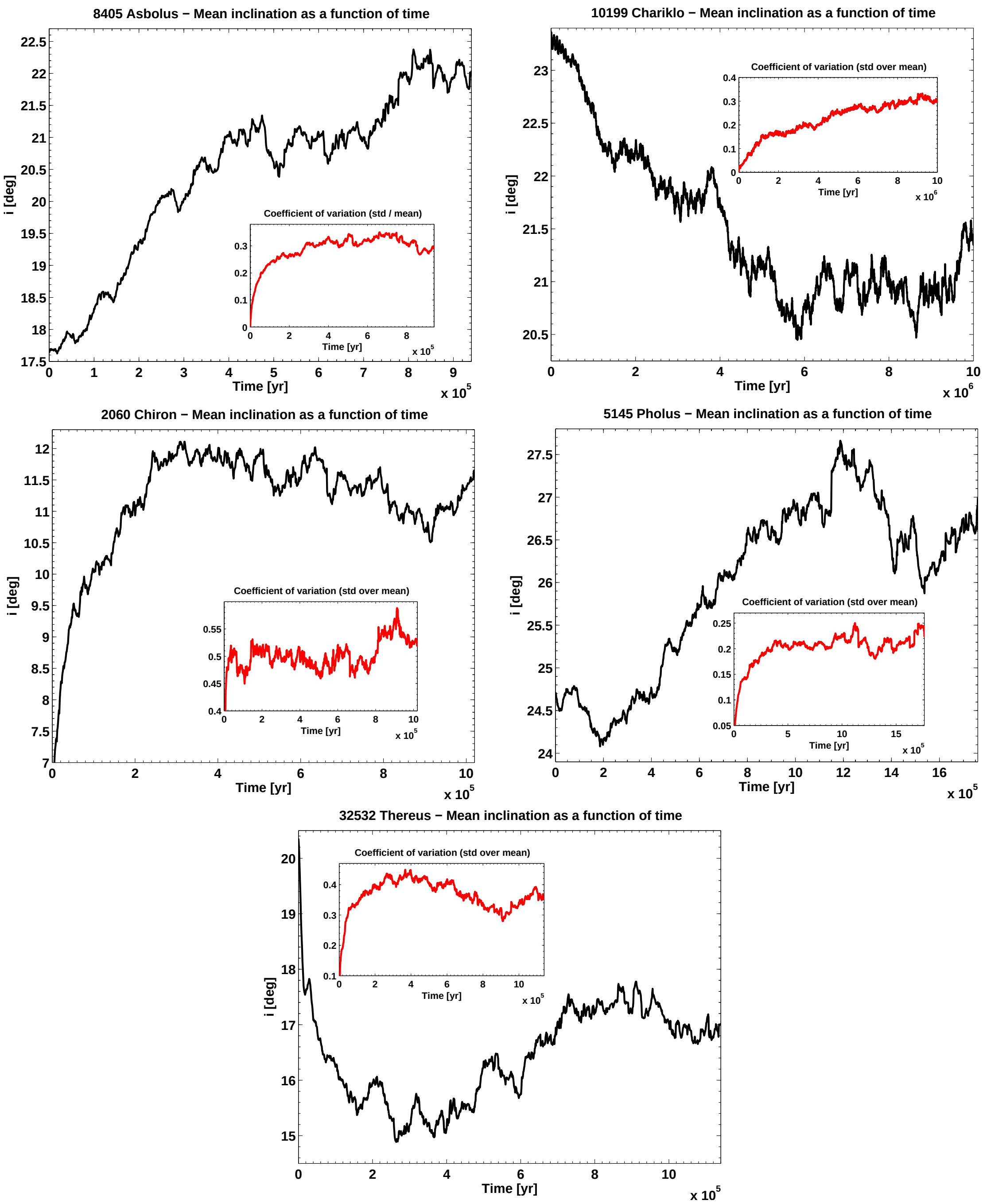

Figure 4.12 Mean value of the inclination (in degrees), for the clone populations of each Centaur object, as a function of time. Shown for each time step, are the average of all orbital inclinations (black) and the coefficient of variation (red), which is the relative standard deviation (standard deviation divided by the mean). Maximum time for each Centaur clone population is the dynamical lifetime, t_{90}, from Table 4.3..

inclination increases, almost monotonically, from 17.6° to $\sim 22°$. For Chariklo, the mean eccentricity is almost doubled, from an initial value of 0.175 to ~ 0.35, with an almost monotonic trend of evolution. The mean inclination decreases from 23.4° to $\sim$ 21.5°. For Chiron, the mean eccentricity sharply increases, from an initial value of 0.38 to 0.49, within $\sim 10^5$ yr of evolution. After this time, it remains in the range $e = 0.46 - 0.52$, with a mean value of $\sim$ 0.48. The mean inclination displays a similar behavior, sharply increasing from 7° initially to 12°, within $\sim 2 \times 10^5$ yr. After this time, it is also confined to a narrow range of $\sim$ 1.5° of variation, around a value of 11.5°. For Pholus, the mean eccentricity displays a similar behavior to that of Asbolus. It is only slightly varied from an initial value of 0.575 to 0.545. The mean inclination increases from 24.7° initially to 26.6°, but it does so less monotonically than for Asbolus. Thereus displays a similar behavior in mean eccentricity to that of Chiron. Its clone population experience a sharp increase in mean eccentricity, within $\sim 3 \times 10^5$ yr, from 0.2 initially to 0.48. After this time the eccentricity continues to vary, in the range $e = 0.48 - 0.52$. The mean inclination displays an opposite behavior to that of Chiron, sharply decreasing, from 20.4° initially to $\sim$ 15°, on the same time span as the eccentricity "jump". After further evolution, in the range $i = 15 - 18°$, the final mean inclination is $\sim$ 17°.

The relative standard deviations, RSD's, shown in Fig. 4.11 and 4.12 as red curves in a smaller panel, for each object, are a measure of the dispersion of eccentricities and inclinations. The orbits of individual test particles, in each clone population, quickly evolve from the very small phase space volume of initial conditions and fill the orbital elements phase space. Inclinations and eccentricities are a measure of how 'dynamically hot' is a population of particles. By examining the RSD's of eccentricity and inclination for all objects we can see that after a short initial period, the dispersion settles around values of 0.2-0.4 for all objects, except Chariklo's eccentricity and Chiron's inclination, which have larger-valued ranges. This short initial period is $\sim$ 7% of the dynamical lifetime, for the eccentricity RSD's, and $\sim$ 20% for the inclination RSD's.

The different trend of eccentricity evolution and larger dispersion of Chriklo's RSD are due to the fact that its clone population is much more stable than the other clone populations. Thus, although their orbits remain confined to our defined 'Centaur region' (heliocentric distances between 5.2-100 AU), on average not changing in orbital energy by much from one time step to another, their average angular momentum changes. This implies that the more likely eventual fate of Chariklo-like orbits will be to gradually diffuse, either inwards (becoming JFCs), or outwards (returning to the TNO parent population).

Tiscareno and Malhotra (2003) find that in their integrations of the intrinsic Centaur population, the characteristic inclination increases with time by $\sim 4°$, with higher inclinations of $19 - 20°$ somewhat more abundant. Our clone populations for the sample Centaurs show the same range of variation in inclination, with respect to the dynamical lifetimes, although Chariklo and Thereus exhibit a decreasing trend, rather than an increase. There is a preference towards higher inclinations (or lower, in the cases of Chariklo and Thereus), as larger fractions of the dynamical lifetimes are characterized by larger values of the inclination. However, we should remember that these populations are mostly unstable, so their sizes decrease, making mean values more susceptible to the least stable orbits at each time step. We also note the difference in the configuration of our simulations and those of Tiscareno and Malhotra (2003), starting from different initial populations, putting different boundaries on particle removal and following the orbital evolution for different times (10^8 yr, in Tiscareno and Malhotra, 2003).

4.2 Thermal Evolution In the Region of the Outer Planets

4.2.1 Introduction

We present results of thermal evolution calculations for objects originating in the Kuiper belt and transferring inwards, to the region of the outer planets. Kuiper belt objects (KBOs) are considered to be part of a reservoir that supplies the flux of small icy bodies, mainly Centaurs and Jupiter-family comets, to regions interior to the orbit of Neptune. We use the end-states of a long-term thermal evolution of some typical KBOs as initial conditions for evolutionary calculations of several representative Centaurs. These calculations span periods of time compatible with the Centaurs' dynamical lifetimes. The subsequent evolution in the Centaur region results in both specific features for each modeled object (mainly surface and sub-surface composition) and common characteristics of thermally evolved Centaurs.

We apply two scenarios for the trans-Neptunian origin of the Centaur population: (I) A TNO fragment, where the Centaur object is considered a piece of the debris produced by a disruptive collision suffered by a much larger parent body; (II) A TNO immigrant, where the Centaur object is considered a former member of the TNOs population, which dynamically evolved (by means of chaotic diffusion or scattering) to the region of the giant planets. The first scenario may be relevant mostly to the smaller Centaurs, as smaller fragments of disruption events are more numerous and will have higher escape velocities that will enable them to dynamically diffuse inward (Benz and Asphaug, 1999). The second scenario could apply for Centaurs of all sizes, but mostly for the larger ones, as small KBOs (several tens of km in radius) have suffered more frequent destructive collisions during the formation and evolution of the Kuiper belt (Pan and Sari, 2005; Kenyon *et al.*, 2008).

The end results of these sets of simulations should provide insight into the current internal state of Centuars and the initial configurations of evolving JFC nuclei (cf. Coradini *et al.*, 2008).

4.2.2 Initial Parameters

The sample Centaur objects chosen are 10199 Chariklo, 8405 Asbolus, 5145 Pholus and 32532 Thereus. They are among the best-characterized Centaur objects and their surface features have been measured and classified by several studies (e.g. Fernández *et al.*, 2002; Dotto *et al.*, 2003; Barucci *et al.*, 2004; Tegler *et al.*, 2005; Cruikshank *et al.*, 1998; Licandro and Pinilla-Alonso, 2005; Merlin *et al.*, 2005). From a dynamical point of view, these objects probably represent distinct sub-groups within the Centaur population (Horner *et al.*, 2004a), as also apparent from their orbital stability and lifetimes (see Sec. 4.1).

Table 4.5 lists the known parameters for each of the Centaur objects, relevant for our modeling of the thermal evolution.

Table 4.5 Known parameters for each of the modeled Centaurs

	10199 Chariklo	8405 Asbolus	5145 Pholus	32532 Thereus
a [AU] [1]	15.795	18.096	20.431	10.616
e [1]	0.172	0.622	0.572	0.198
R [km] [2]	140	33	95	40
$\mathcal{A}$ [2]	0.05	0.12	0.04	0.0975

[1] Orbital parameters from the Minor Planet Center database.
[2] Average radius and albedo estimates from Dotto *et al.* (2003), for Chariklo, Fernández *et al.* (2002), for Asbolus, Davies *et al.* (1993), for Pholus and Stansberry *et al.* (2005), for Thereus.

Asbolus and Pholus have high-eccentricity orbits, with perihelion distances of 6.84 AU and 8.74 AU, respectively. The relatively low-eccentricity orbits of Chariklo and Thereus have perihelion distances of 13.08 AU and 8.51 AU, respectively. This means that Asbolus receives the highest peak insolation input energy (maximum incident solar radiation, at perihelion), Chariklo receives the least and, interestingly enough, Pholus and Thereus experience roughly the same peak energy input. However, if we want to examine which object receives the most input energy throughout its orbit, we can look at the average incoming power of solar radiation per unit area.

We begin from the energy balance on the surface of an object, which can be written as,

$$\frac{(1-\mathcal{A})\mathrm{L}_\odot}{16\pi d_H^2(t)} = (\text{Rad. term}) + (\text{Subl. term}) + (\text{Cond. term}), \tag{4.2}$$

where $\mathcal{A}$ is the surface albedo, $\mathrm{L}_\odot$ is the solar luminosity and $d_H(t)$ is the heliocentric distance (see Sec. 2.1).

The sum of the input energy flux, per orbit, can be found by integrating the LHS term from the last, with respect to time, over an entire orbit. For this purpose, we may use the relation of the polar angle, given by

$$dt = \frac{d\theta}{\dot{\theta}} = \frac{d\theta}{l}r^2 = \frac{d\theta}{l}d_H^2, \tag{4.3}$$

where l is the angular momentum per unit mass, which is constant. Thus, using the above relation, we can find the input energy per orbit as

$$S = \int_0^{2\pi} \frac{(1-\mathcal{A})\mathrm{L}_\odot}{16\pi}\frac{d\theta}{l} = \frac{(1-\mathcal{A})\mathrm{L}_\odot}{8\sqrt{G\mathrm{M}_\odot}}\frac{1}{\sqrt{a(1-e^2)}}, \tag{4.4}$$

where the standard expression for the specific angular momentum was used (Murray and Dermott, 2000). If we now divide the above expression by the orbital period, we get the average incoming power per unit area, as

$$\frac{S}{P} = \frac{(1-\mathcal{A})\mathrm{L}_\odot}{16\pi}\frac{1}{a^2\sqrt{(1-e^2)}}. \tag{4.5}$$

We can now calculate the average incoming power per unit area for each of our Centaur object, by using the orbital elements from Table 4.5. We get the following values (in erg/s/cm^2): 2832, for Thereus, 1340, for Chariklo, 1190, for Asbolus and 972, for Pholus. Thus, although Asbolus comes closest to the Sun, it does not linger around perihelion too long, and it has a longer time to radiate its input heat to a colder environment than Chariklo or Thereus. So, we would expect objects like Pholus and Asbolus to experience less surface and sub-surface alterations, than Thereus and Chariklo. However, this is only a simple analytical consideration. We should note that the actual thermal and compositional evolution depends on the physical and chemical characteristics of each object.

In order to have some common ground to compare the different results of the evolution runs, we have to take structural and compositional parameters to be similar. For the composition, other than water ice, we take the three most common volatile compounds in planetary environments – CO, CO_2 and HCN (Bergin *et al.*, 2007). These are also among the most abundant cometary volatiles observed (Bockelée-Morvan *et al.*, 2004). The pore-size distribution parameters are taken to be close to the most commonly observed values of dust-size distribution in comets (see Sarid *et al.*, 2005). Other parameters, such as density, dust-to-ice ratio and mass fraction of volatiles, depend on the assumed circumstances for the origin of an object.

Table 4.6 describes the common physical parameters for all of the thermal. These are essentially the same as those stated for the TNOs, in Sec. 3.1.

Table 4.6 Common input physics parameters for all models of Centaurs

Parameter	Symbol	Value	Units
Specific H_2O ice density	$\varrho_{\rm ice}$	0.917	gc m^{-3}
Specific dust density	$\varrho_{\rm dust}$	3.25	g cm^{-3}
Ice heat capacity	$c_{\rm ice}$	$7.49 \times 10^4 T + 9 \times 10^5$	erg g^{-1} K^{-1}
Dust heat capacity	$c_{\rm dust}$	1.3×10^7	erg g^{-1} K^{-1}
C-Ice conductivity	$K_{\rm C-ice}$	$5.67 \times 10^7/T$	erg cm^{-1} s^{-1} K^{-1}
Dust conductivity	$K_{\rm dust}$	10^6	erg cm^{-1} s^{-1} K^{-1}
A-Ice diffusivity	$\kappa_{\rm A-ice}$	3×10^{-3}	cm^2 s^{-1}
Pore-size distribution [1]	α	3.5	
Pore size range [2]	X	10^4	

[1] Exponent for initial power-law distribution of pore sizes, as in comets (Sarid *et al.*, 2005).
[2] Ratio of maximal to minimal pore radius, as in comets (Sarid *et al.*, 2005).

Another consideration for the thermal simulation of these objects is their dynamical lifetime. Since the Centaurs are considered a transient population, most objects occupy stable orbits for a relatively short period of time. However, this does not necessarily hold true for each specific object and there is a wide dispersion in calculated lifetimes (Tiscareno and Malhotra, 2003). To address this issue, we use the results for dynamical lifetimes of the specific Centaur objects, derived in Sec. 4.1. For the purpose of our thermal evolution simulations we chose the time span for calculation as a fraction of the dynamical lifetime estimates.

Since we wish to explore the evolution of cometary-like objects, as they transfer from the Kuiper belt to the region of the outer planets, the initial conditions for the simulations of already thermally-processed objects were derived from the end-states of KBO evolution calculations. These were discussed in Sec. 3.2, for (5000) Quaoar, 1992 QB_1 and 1998 WW_{31}. The internal evolution of these KBOs was followed, from an initially homogeneous configuration. and until a slowly-evolving state was reached (see Sec. 3.1 for a discussion on the conditions to terminate a KBO thermal evolution run). Quaoar was followed up to $\sim 10^9$ yr, while QB_1 and WW_{31} were followed up to $\sim 5 \times 10^7$ yr. We have confirmed previously derived results about the depletion of highly-volatile species at an early stage of a moderate-to-large sized KBO evolution (Choi *et al.*, 2002). These species were represented by CO in our initial compositions at the trans-Neptunian region and not even a residual abundance is present at the end of the evolution, except for what survives as occluded gas in the amorphous ice. Thus, we do not consider CO ice as a component of initial configurations of Centaurs.

4.2.3 Initial State Scenarios – The Fragment and Immigrant Cases

In order to follow the evolution of Centaurs, as objects having early thermal histories in the trans-Neptunian region, we assume a physical connection between the objects simulated. Two scenarios are considered: (I) a relatively small fragment of a much larger, thermally processed, KBO evolves dynamically to become a Centaur; (II) a smaller KBO evolves thermally beyond Neptune's orbit and then diffuses inwards to become a Centaur. In the first case, we assume that the collision that produced the fragment imparted mostly kinetic energy. Thus, the fragment quickly becomes a Centaur and the heat deposition during the collision is too small to induce thermal alteration of the fragment's interior. In the second case, no external effects are taken into account and the final state of the KBO simulation becomes the initial state of the Centaur simulation. According to the current understanding of the collisional history of the Kuiper belt (Kenyon *et al.*, 2008), the first scenario may be applicable to smaller objects, such as Asbolus, Thereus and maybe even Pholus, while the latter scenario could represent the larger Centaur objects, such as Chariklo (although it is also relevant for the smaller objects).

For the fragment scenario, we assume that objects similar to the smaller Centaurs in our sample were initially ejected debris, after a catastrophic collision, from a KBO resembling Quaoar. Accordingly, we take the final state of the upper $\sim 20\%$ of Quaoar's radius, corresponding to less than 1% of the volume, and use it to construct a homogeneous initial models for the Centaur object's bulk . These are the outer layers that experienced about 10^9 yr of evolution and were discussed in Sec. 3.2.1. As the initial bulk density we take the weighted average of the density profile in the outer layers of the evolved Quaoar model. The initial temperature is chosen as the smallest between the equilibrium temperature at perihelion in the Centaur's orbit and the average temperature of the upper layers of the evolved Quaoar model. The initial composition is taken as a weighted average of the mass fractions in the outer layers. We use weight average values in order to enable the application of the same fragment model to Centaur objects of different sizes and albedos. Since the initial state of is derived from an already thermally-evolved model, it is composed of both amorphous and crystalline water ice and volatiles (CO_2 and HCN) are present in both gaseous and solid phases. We assume that there is no contribution of heat from radioactive isotopes, as the short-lived ones have already decayed. The long-lived radionuclides are still of negligible importance and the duration of the evolution ($\sim 3\times10^4$ yr) is not long enough to enable their on-going decay to accumulate any significant heat.

For the immigrant scenario, where a smaller KBO acquires a Centaur-like orbit, we assume both larger objects, like Chariklo, and smaller objects, like Asbolus, are equally likely to be transferred. We assume that a KBO resembling 1992QB$_1$, which has similar size and albedo as Chariklo, diffused inwards of Neptune's orbit, after a thermal evolution period of $\sim 10^8$ yr in the Kuiper belt zone. Thus, the initial structure is identical to that of the evolved model of QB1 and the initial temperature distribution is that of the final orbit calculated in the Kuiper belt. Table 4.7 lists the initial parameters for the model of Chariklo, where the previous KBO thermal evolution is evident in the mass fractions of amorphous and crystalline water ice and the presence of non-negligible abundances of volatile ices.

Table 4.7 lists the initial configurations of the interior models, pertaining to the two scenarios discussed above. We note that the immigrant cases do not start from a homogeneous configuration. Thus, the values for the ice mass fraction (either amorphous/crystalline water ice or volatiles) are the average values throughout the bulk. Fig. 3.11 and 3.12, in Sec. 3.2.2, represent the detailed distribution of the composition, as a function of depth. By comparing the dust-to-ice ratios, $\Upsilon_{d/i}$, in Table 4.7 to Table 3.6, we can see that for the case of 1998 WW$_{31}$ there was no depletion of eater ice and the volatile ices are a minor component. However, case of 1992 QB$_1$ the water ice component is nearly half depleted and the volatile ices have a more pronounced contribution. This indicates that objects coming from the trans-Neptunian region as "intact immigrants", should resemble the smaller KBOs in appearance and behavior during their initial injection to the giant planet region.

4.2.4 Thermal Evolution As A TNO Fragment

For Asbolus, we assume that a KBO resembling (5000) Quaoar has undergone a catastrophic collision, producing fragments in various sizes. This kind of collision requires the impactor to be at least about half the size of the parent body (Benz and Asphaug, 1999), which means the impact is more like a mutual collision of 100-km sized objects. Other

Table 4.7 Initial internal configurations for the fragment and immigrant cases

	Fragment case	Immigrant case I (1992 QB_1)	Immigrant case II (1998 WW_{31})
ρ [g/cm^3] [1]	1.1	0.703	1.46
$\Upsilon_{d/i}$ [2]	2.33	2.4	4
$X_{am.}$; $X_{cry.}$ [3]	0.065 ; 0.23	0.197 ; 0.093	0.149 ; 0.051
$X_{vol.,gas}$ [4]	CO: 0.005	CO: 0.005	CO: 0.005
	CO_2: 0.005	CO_2: 0.005	CO_2: 0.005
	HCN: 0.0025	HCN: 0.0025	HCN: 0.0025
$X_{vol.,ice}$ [5]	CO_2: 0.004	CO_2: 0.003	CO_2: 2.4×10^{-4}
	HCN: 0.001	HCN: 0.0014	HCN: 1.1×10^{-4}

[1] Average bulk density.
[2] Initial dust-to-ice ratio.
[3] Initial average mass fractions of amorphous and crystalline water ice.
[4] Initial fractions of volatiles occluded in the amorphous ice.
[5] Initial average mass fractions of volatile ices.

mechnisms for producing fragments or debris of larger parent objects could be tidal disruptions or grazing impacts (so-called "hit-and-run") between the more massive members of the population (Ip, 2003; Asphaug *et al.*, 2006).

In the present-day Kuiper belt, the timescales for these sort of collisions are very long (Durda and Stern, 2000) and the probabilities for such an encounter render the population of large KBOs not significantly altered by collisions (Davis and Farinella, 1997). Thus, violent collisions of large KBOs, could have occurred only in the early phases of the Kuiper belt's evolution, when relative velocities were greater and more massive objects were present (Kenyon *et al.*, 2008; Morbidelli *et al.*, 2008). We assume that some re-accumulation of the smaller debris occurred with a relatively low velocity dispersion, before the fragment was injected to a Centaur-like orbit. Thus, a homogeneous starting point for the initial configuration is not too crude of an assumption. The initial configuration appears in Table 4.7, as the fragment case.

Fig. 4.13 and 4.14 show the internal evolution of Asbolus, in terms of temperature distribution and structure and composition distributions (density, porosity, amorphous ice and volatile ice mass fractions), respectively. Early and final evolution states are presented, where the final state corresponds to a few precent of the adopted dynamical lifetime for the Asbolus clone population, in Table 4.3.

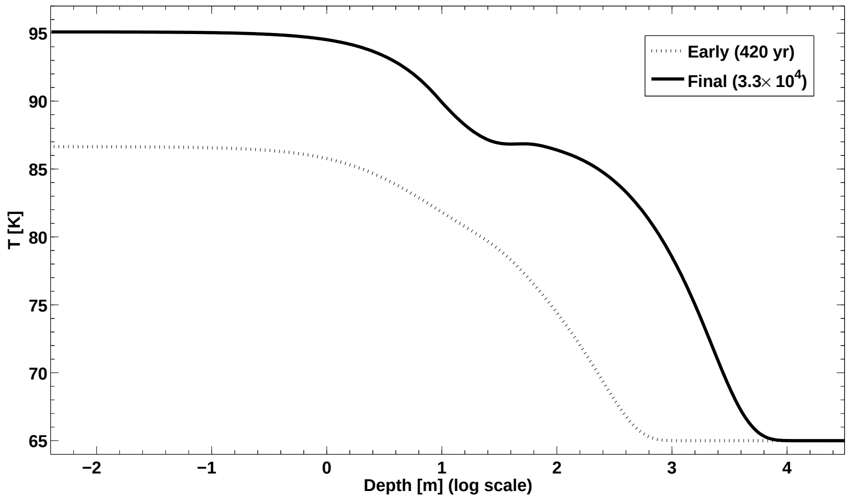

Figure 4.13 Temperature profiles for 8405 Asbolus. Displayed for comparison are early and final evolution times in the simulation: 420 yr (dotted) and 3.3×10^4 yr (solid). Depth is given on a logarithmic scale, from left (surface) to right (center). Note the larger temperature variations, in comparison to Fig. 4.17.

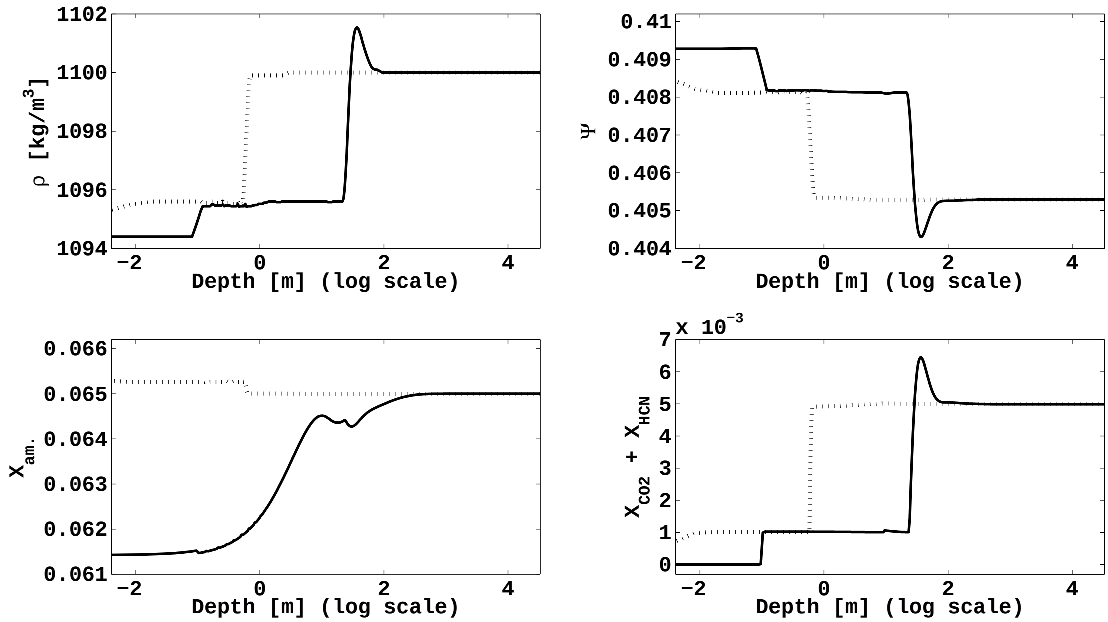

Figure 4.14 Profiles of density (top left), porosity (top right), amorphous ice (bottom left) and volatile ice (bottom right) mass fractions for 8405 Asbolus. Depth is given on a logarithmic scale, from left (surface) to right (center). Displayed for comparison are early and final evolution times in the simulation: 420 yr (dotted) and 3.3×10^4 yr (solid).

The surface is heated by the successive passages at less than 7 AU from the Sun. At this distance the equilibrium temperature is ~ 110 K and thermal processing occurs, as the heat absorbed near-perihelion is conducted inwards. The progressing heat front is evident in Fig. 4.13, as there is clear heating at all depths, down to ~ 5 km. After reaching its highest temperatures at its orbital skin depth (~ 25 m), Asbolus continues to heat up slowly. The boundary region between the colder interior and the hotter outer layers reaches ~ 3 km at $\sim 10^4$ yr. From this point on, the heat front progresses much more slowly inwards. This is due to the change in abundances of amorphous and crystalline water ice and volatile ices resulting from the earlier thermal processing. Only slight variations in density and porosity occur during the evolution. However, the penetrating heat front produces more pronounced variations in abundances of amorphous water ice (up to $\sim 5\%$) and volatile ices (up to $\sim 80\%$). In the profiles shown in Fig. 4.14 it is also clear that around a depth of 1 km there is a boundary region between thermally-processed and relatively pristine material (relative to the initial state).

Fig. 4.15 shows the early and final states of the evolution of 5145 Pholus. It was evolved from an initial homogeneous state, assuming a recent history as a fragment of a thermally-evolved object similar to (5000) Quaoar. The thermal evolution timescale corresponds to the dynamical lifetime, defined in Sec. 4.1.4 and Table 4.3. We present here the distributions of temperature, porosity, crystalline ice abundance and volatile ices abundance, as a function of depth (on a logarithmic scale).

We see that temperature slightly increases, down to a depth of ~ 50 km, while the deeper half of its bulk remains close to the initial temperature. Since the temperature never exceeds 70 K and there is very little amorphous ice, crystallization is negligible and it does not contribute, as a secondary heat source. Thus, most of the bulk is 'inactive', in terms of thermal and compositional changes. However, since $T \gtrsim 55$ K in the subsurface layers (at a depth of ~ 10 m) from an early stage and there are ices of volatiles present, in the initial configuration, a slow sublimation of these volatiles (CO_2 and HCN) is maintained. These volatiles become slightly depleted at these depths (see Fig. 4.15, bottom right) and some of the gas flows inward, where temperatures are lower, and recondense. Thus, porosity in these depths is somewhat decreased, after being increased, where the partial disappearance of volatile ices has left more empty pore space. Crystalline ice is slightly enriched in depths down to ~ 10 m, as the small amount of amorphous ice (see Table 4.7) experiences very slow crystallization. The slight decrease in crystalline ice

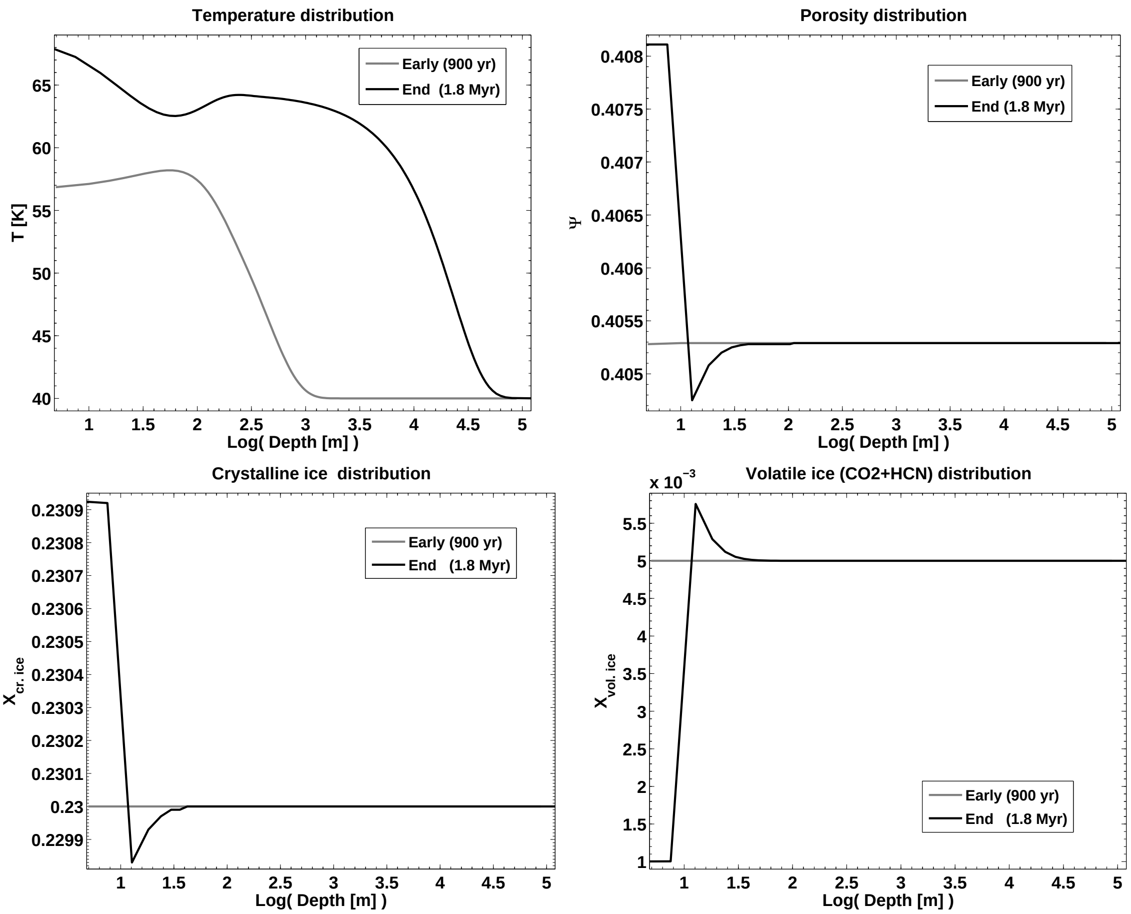

Figure 4.15 Internal profiles for 5145 Pholus – temperature (top left), porosity (top right), crystalline ice abundance (bottom left) and volatile ice abundance (bottom right). Depth is given on a logarithmic scale, from left (surface) to right (center). Displayed for comparison are early and final evolution times in the simulation: 900 yr (gray) and 1.8×10^6 yr (black).

mass fraction, just inside of a depth of 10 m, is due to the slight increase in bulk density of the layers, resulting from the decrease in porosity and volatile ice recondensation.

Fig. 4.16 shows the early and final states of the evolution of 32532 Thereus. It was also evolved from an initial homogeneous state, assuming a recent history as a fragment of a thermally-evolved object similar to (5000) Quaoar. The thermal evolution timescale corresponds to $\sim$ 10% of the dynamical lifetime, defined in Sec. 4.1.4 and Table 4.3. We present here the distributions of temperature, porosity, crystalline ice abundance and volatile ices abundance, as a function of depth (on a logarithmic scale).

We see a similar behavior in the temperature distribution to that of Pholus, only now values are higher, as Thereus orbits closer to the Sun. The peak temperature at the end

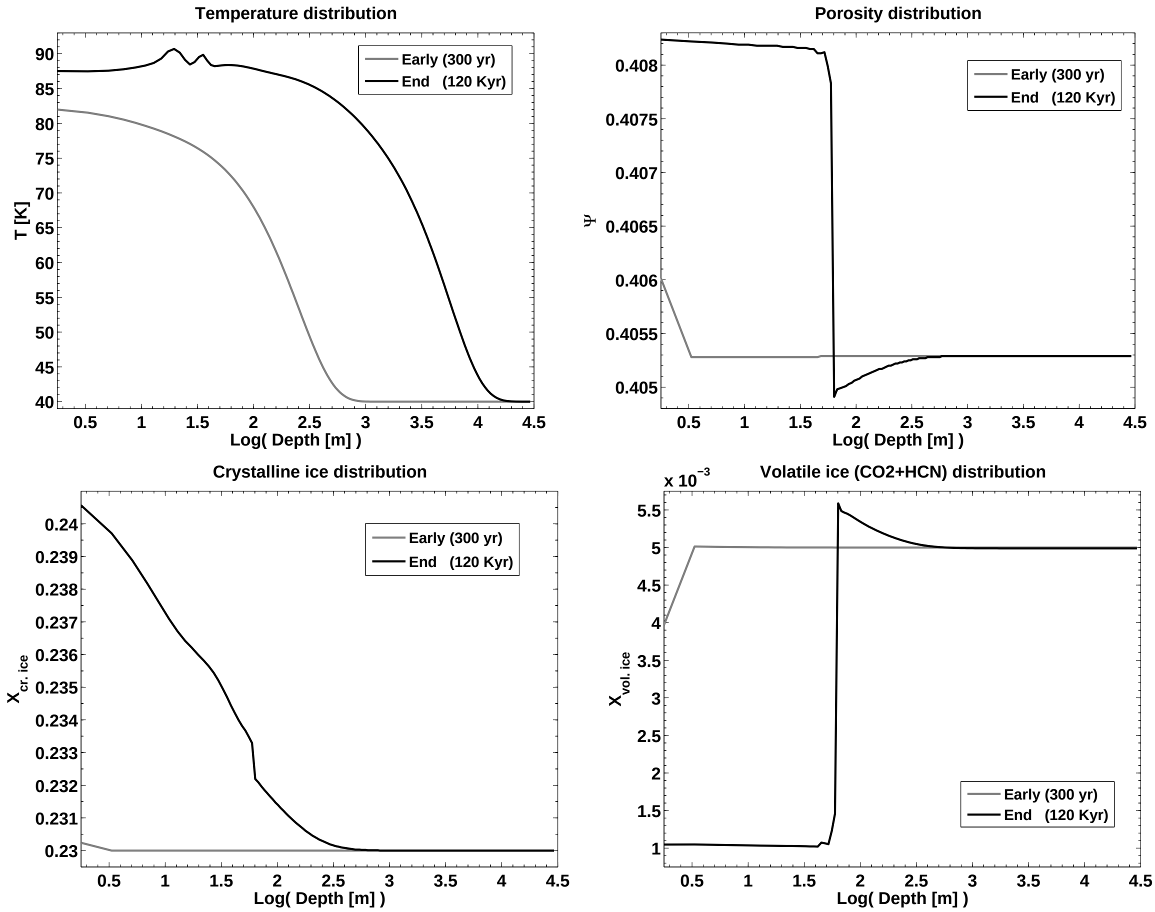

Figure 4.16 Internal profiles for 32532 Thereus – temperature (top left), porosity (top right), crystalline ice abundance (bottom left) and volatile ice abundance (bottom right). Depth is given on a logarithmic scale, from left (surface) to right (center). Displayed for comparison are early and final evolution times in the simulation: 300 yr (gray) and 1.2×10^5 yr (black).

of the evolution is 90 K, whereas for Pholus it was only 68 K. Interestingly, although Thereus is $\sim$ 40% of the size of Pholus and it receives much higher average incoming power of solar radiation (see Sec. 4.2.2), the fraction of the bulk that remains unaltered is the same as for Pholus. The behavior of the volatile ice abundance and porosity is more pronounced for Thereus, because of the higher temperatures, which expedite the thermal processing. Regarding the crystalline ice distribution, we see that abundances increase as a function of depth below the surface, until the location where $T \lesssim 85$ K and the changes (relative to the early stage of evolution) in porosity and volatile ices are quenched. This is caused due to the temperature-dependent crystallization of the residual amorphous ice, which proceeds at a reasonable rate for this range of temperatures.

4.2.5 Thermal Evolution As A TNO Immigrant

For Chariklo, we assume that a KBO resembling 1992 QB_1, which has similar size and albedo as Chariklo, diffused inwards of Neptune's orbit, after a thermal evolution period of $\sim 5 \times 10^7$ yr the Kuiper belt zone. Thus, the initial structure and the temperature distribution are identical to that of the evolved QB1 model (see Fig. 3.12). The composition appears in Table 4.7, as immigrant case I.

Fig. 4.17 (temperature distribution) and 4.18 (structure and composition distribution) show the internal evolution of Chariklo.

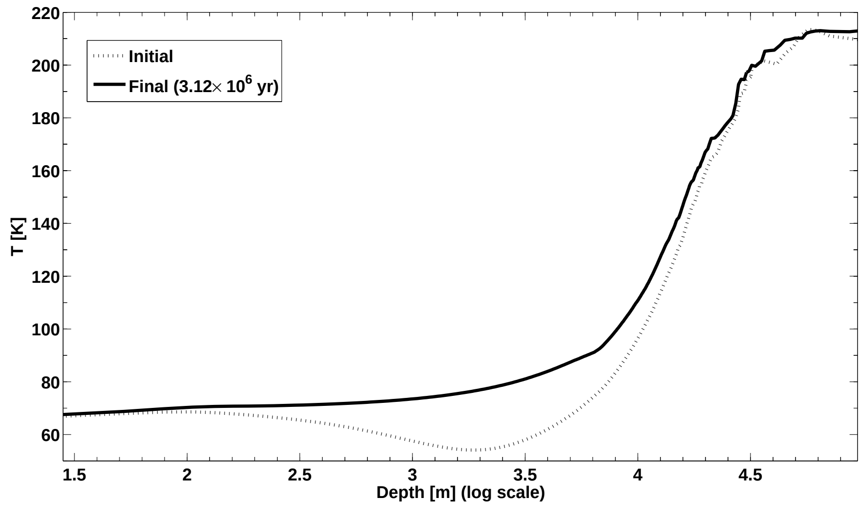

Figure 4.17 Temperature profiles for 10199 Chariklo. Displayed for comparison are initial and final (3.12×10^6 yr) evolution states of the simulation. Depth is given on a logarithmic scale, from left (surface) to right (center). Note that the temperature is almost constant in time, except for layers at a depth of 1-10 km below the surface, where heat builds-up around the orbital skin depth.

The surface very rapidly cools to the ambient temperature of $\sim$ 70 K and remains so, as the cooling and heating rate of the surface are similar. From that point on, the only change in temperature is the slow heating of the sub-surface depths corresponding to the penetration depth of heat from solar radiation. At the end of the simulation, most of its interior retained the initial temperature distribution and the outer few 100 m are at equilibrium with the surroundings. The minor increase of temperature at a depth of 1-10 km is not enough to trigger any appreciable sublimation or crystallization. Considering the internal structure and composition, we note that there is almost no change from the initial state. Density and porosity distributions remain almost constant in time and the

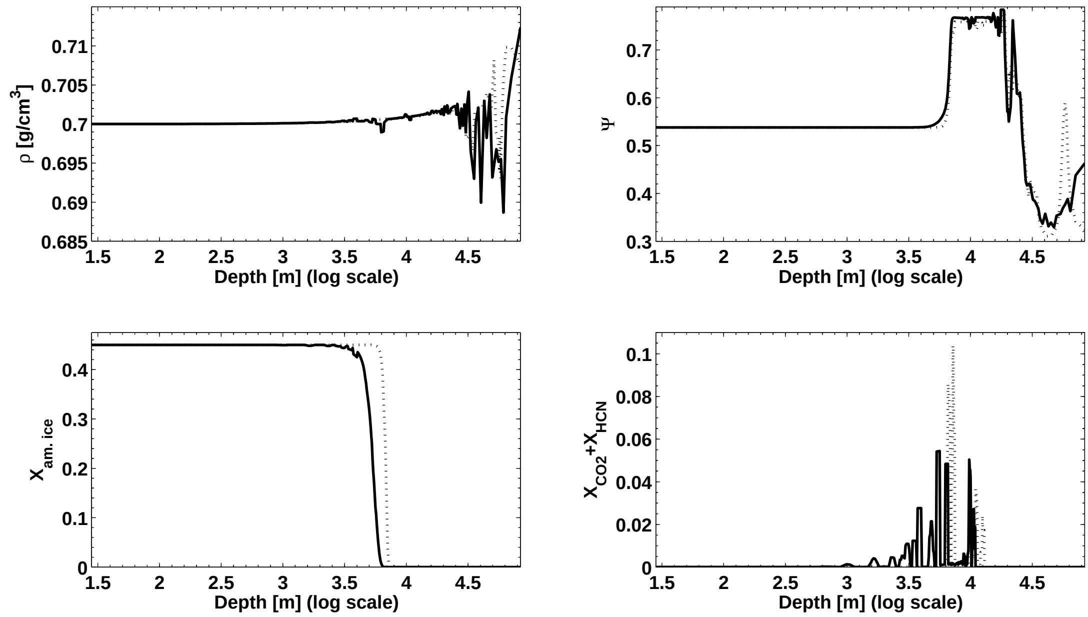

Figure 4.18 Profiles of density (top left), porosity (top right), amorphous ice (bottom left) and volatile ice (bottom right) mass fractions for 10199 Chariklo. Depth is given on a logarithmic scale, from left (surface) to right (center). Displayed for comparison are the initial non-homogeneous state (dotted) and final state of the simulation (solid) at 3.12×10^6 yr.

amorphous ice abundance is slightly diminished, as it crystallizes at a very slow rate, as can be seen in the bottom-left panel of Fig. 4.18. Volatile ices remain at the same depth, just under the skin depth (heat penetration depth), with slight variations. These variations are slow and minor, because the corresponding temperature at this depth (3-10 km) is 80-90 K, which is the range of sublimation temperatures for CO_2 and HCN (Meech and Svoren, 2004).

Fig. 4.19 shows a comparison of the temperature, volatile ice and amorphous ice abundance between the final state in the Kuiper belt (end of the evolution for 1992 QB_1) and long-term evolution of two possible Centaur-like orbits. These orbits are taken as that of Asbolus and Chariklo, with the appropriate semi-major axis, eccentricity and albedo. Evolution times are on the order of twice the dynamical lifetime of Asbolus and the median lifetime of Chariklo (Sec. 4.1.4 and Table 4.3). All other physical characteristics are those of 1992 QB_1 and 'immigrant case I' in Table 4.7.

We see that there are changes in the temperature distributions, which are the result

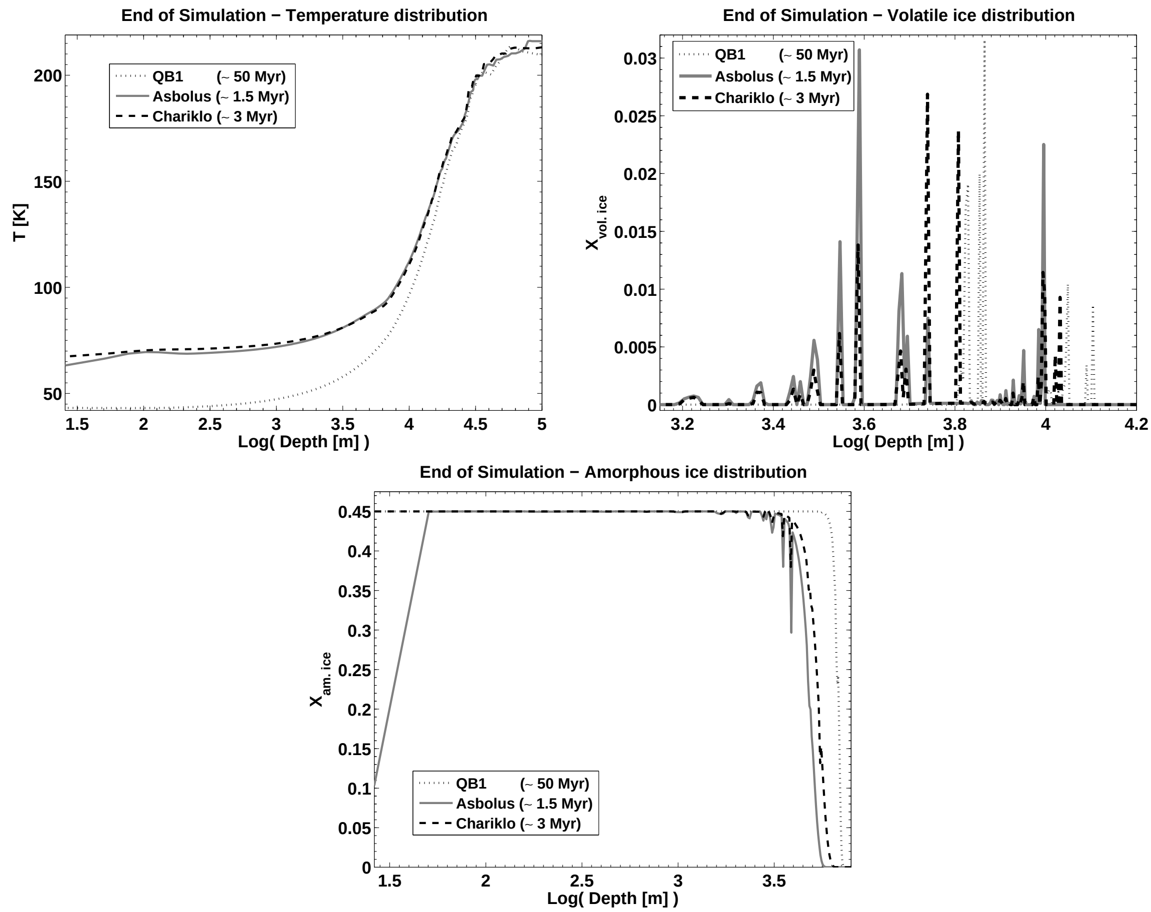

Figure 4.19 Depth distributions of temperature (right), volatile ice abundance (left) and amorphous water ice abundance (bottom). Compared here are the final configurations of 1992 QB_1 (dotted black - 5×10^7 yr), Asbolus (solid gray - 1.5×10^6 yr) and Chariklo (dashed black - 3×10^6 yr). Depth is given on a logarithmic scale, from left (surface) to right (center). The right panel is focused around the region of maximum volatile ice mass fractions. The bottom panel is focused around the region of maximum amorphous ice mass fraction. Note that both models of Asbolus and Chariklo are continued evolution simulations from the end state of 1992 QB_1.

of stronger insolation, as clearly seen at sub-surface depths down to $\sim$ 30 m. Internal crystallization of the amorphous water ice component is evident in the bottom panel, at a depth of $\sim$ 10 km. This transition releases latent heat and changes the ice conductivity, thus we see a marked difference between the temperature curves, from a depth of $\sim$ 10 outwards. Volatile ices (right panel), which are mostly located at depths of 3-12 km, experience only minor changes as they migrate slowly outwards. However, his migration, caused by sublimation, outflow and subsequent recondensation of the CO_2 and HCN ices, does not transfer any appreciable abundances of volatile ices close to the surface.

Fig. 4.20 shows a comparison of the temperature and volatile ice abundance distributions between the final state in the Kuiper belt (end of the evolution for 1998 WW_{31}) and long-term evolution of two possible Centaur-like orbits. These orbits are taken as that of Asbolus and Chariklo, with the appropriate semi-major axis, eccentricity and albedo. Evolution times are on the order of the dynamical lifetime of Asbolus and 10% of the dynamical lifetime of Chariklo (Sec. 4.1.4 and Table 4.3). All other physical characteristics are those of 1998 WW_{31} and 'immigrant case II' in Table 4.7.

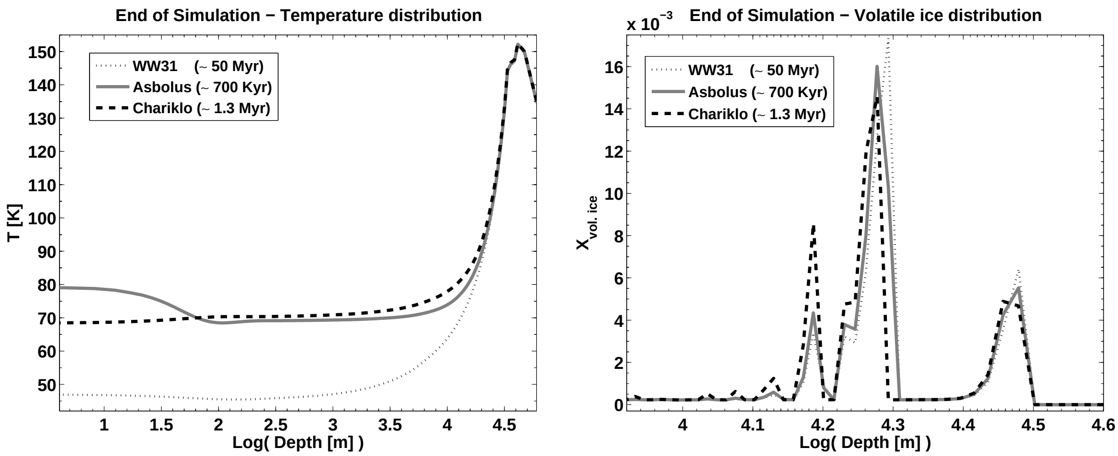

Figure 4.20 Depth distributions of temperature (right) and volatile ice abundance (left). Compared here are the final configurations of 1998 WW_{31} (dotted black - 5×10^7 yr), Asbolus (solid gray - 7×10^5 yr) and Chariklo (dashed black - 1.3×10^6 yr). Depth is given on a logarithmic scale, from left (surface) to right (center). The right panel is focused around the region of maximum volatile ice mass fractions. Note that both models of Asbolus and Chariklo are continued evolution simulations from the end state of 1998 WW_{31}.

We see that there are changes in the temperature distributions, which are the result of stronger insolation, as clearly seen at sub-surface depths down to ~ 30 m. Asbolus, having a smaller perihelion has the highest sub-surface temperatures. Chariklo has a higher value of average incoming power from solar radiation (see Sec. 4.2.2), but it experiences a weaker heat wave at perihelion, and so the thermal response of its ice components is more subdued. Volatile ices behave similarly as in the former case of 1992 QB_1, except for the deeper locations where ices accumulate.

5 Evolution of Jupiter-Family Comets

In this chapter we present studies of two sample JFCs. These examples should be typical of this cometary population and were chosen as representing characteristic properties.

Section 5.1 presents a detailed study of the internal evolution, activity and impact modeling of comet 9P/Tempel 1. It is based on Sarid *et al.* (2005).

Section 5.2 presents several results regarding the dust activity of comet 22P/Kopff and its connection to internal thermal evolution.

5.1 Thermal Evolution and Activity of Comet 9P/Tempel 1 and Simulation of a Deep Impact

5.1.1 Introduction

Comet 9P/Tempel 1 was the target of NASA's *Deep Impact* mission (A'Hearn *et al.*, 2005). The spacecraft, successfully launched on January 12 2005, encountered the comet on July 4 2005 and collected many images of the nucleus. It also released a smaller projectile probe, which maneuvered and impacted the surface. This collision dug a crater into the comet and released a large cloud of material from both the surface and deeper within. The results of this impact were followed by many observing facilities, both Earth- and space-based, and combined with observations prior to the event itself to reveal various properties of this "typical" Jupiter-family comet (A'Hearn, 2008).

In anticipation of the mission, comet 9P/Tempel 1 has been intensively observed by both professional and amateur astronomers (Lamy *et al.*, 2001; Meech, 2002) and data about its size, rotation, production rates, etc., has accumulated (Fernández *et al.*, 2003; Belton *et al.*, 2005). On the theoretical side, models have been developed to simulate the impact and its consequences (Schultz *et al.*, 2005; Richardson *et al.*, 2005). It is impossible, however, to simulate the impact accurately, since very little is known about the properties of cometary material. Clearly, the impact energy – originally kinetic – will divide between mechanical and thermal energies, but the proportion will be strongly determined by the nature of cometary material: its strength, porosity, thermal conductivity, and so forth.

Since the dynamical side of this kind of impact has already been investigated in detail (Nolan *et al.*, 1996; Holsapple *et al.*, 2002; Leinhardt *et al.*, 2008), we focus in this study on the thermal aspect. We first choose an initial model that matches as well as possible the observations of comet 9P/Tempel 1 (prior to the *Deep Impact* observing campaign). This is achieved by running a number of models, for different assumptions and parameter combinations, through several orbital revolutions. The composition of these models is assumed to include water ice, dust and five additional volatile species. A "thermal" impact on this model is then simulated.

The evolution – both long-term, prior and following the impact, and short-term during the event itself – is calculated by means of a quasi-3D code (Prialnik *et al.*, 2004). This code takes into account diurnal and latitudinal variations, but neglects lateral heat conduction, and is an extended version of the code used in Cohen *et al.* (2003).

5.1.2 Some Ground-Based Observations

In order to prepare for the *Deep Impact* encounter, the *Deep Impact* team has undertaken a large observing campaign to characterize the nucleus and the levels of activity (Meech *et al.*, 2005). From past apparitions it was known that this comet typically exhibits a sharp rise in brightness near 200 days pre-perihelion (see references in Meech *et al.*, 2005). Optical CCD images have been obtained regularly since 1997, by a collaborating observational team (led by Karen Meech, from the Institute for Astronomy, Univ. of Hawaii), to monitor the development of activity and the cessation of activity as the comet moved to aphelion in early 2002. Tempel 1 is well placed for observing every other apparition, and the early 2000 perihelion passage was only moderately good for dust dynamical modeling, but was the first chance to measure dust parameters for this comet. Nevertheless, a large data set has been accumulated for this purpose, beginning in January and March 1999 pre-perihelion, and continuing from August 2000 through January 2001.

A Finson-Probstein dust-dynamical model, based on the work by Finson and Probstein (1968) and Farnham (1996), was utilized. This model uses the observed extent and morphology of the dust coma to determine the relative velocity distribution, size distribution and production rates of the dust leaving the nucleus as a function of heliocentric distance. The model evaluates the motion of a suite of particles after leaving the nucleus under the influence of solar radiation pressure and gravity. The scattered light from the dust is added together and fit to the surface brightness of the observed coma.

The details of the imaging and observing schemes are given in Sarid *et al.* (2005) and will not be repeated here. The resultant composite images are shown in Fig. 5.1. Using a code developed by Farnham (1996), Finson-Probstein models were fit to the images. Contour fits to the images are shown in Fig. 5.2. Results of the fitted parameters are shown in Table 5.1.

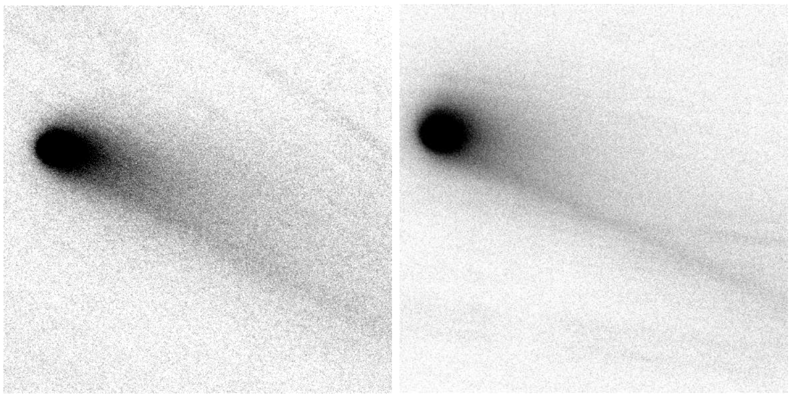

Figure 5.1 Composite images of comet 9P/Tempel 1 (left) from 2000 Aug. 21 (r=2.54 AU), composed of 26 × 300 sec R images and (right) from 2000 Sep. 30 (r=2.77 AU) composed of 42 × 300 sec R images. Images are 180×180″, with N at the top and E to the left. These images were taken using the University of Hawaii 2.2m telescope on Mauna Kea.

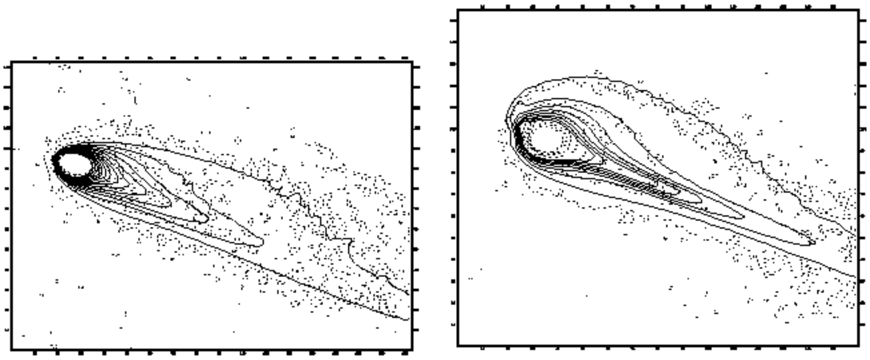

Figure 5.2 Finson-Probstein dust dynamical model fits to the data on Aug. 21 (left) and Sep. 30 (right), 2000. These are plotted on contours from the composite images.

Guided by the dust grain size distribution derived from observations, we adopted for the pore size distribution inside the nucleus a slightly steeper power law, with $\alpha = 3.5$,

Table 5.1 Finson-Probstein model fit to 9P/Tempel 1 images

Parameter	Value
Smallest particles	3 μm
Largest particles	3 mm
Emission start	$perihelion - 100$ days
Maximum dust output	$perihelion - 60$ days
Emission decline	$perihelion + 260$ days
Velocity ($v(\beta)$)[1]	$v(r_{\min})/v(r_{\max}) \approx 40$
α[2]	3.1

[1] $\beta = F_{rad}/F_{grav} = 5.74 \times 10^{-4} Q/\varrho_d r$, is a proxy for grain size, where Q is the radiation pressure scattering efficiency, ϱ_d is the dust grain density and r the grain size.
[2] Fitted value for the slope of the particle size distribution.

an average pore size of 100 μm, and the ratio of minimal-to-maximal pore radius to be $X = 10^{-4}$. According to the discussion in Sec. 2.4, $\bar{r} \approx \sqrt{r_{\min} r_{\max}}$, which results in a size range between $r_{\min} = 1$ μm and $r_{\max} = 1$ cm. The range was chosen to be wider than the dust grain size range indicated in Table 5.1. This was done in order to account for micro-pores at the low-end, and to enable the flow of a few mm-size grains requiring somewhat larger pores at the high-end. A steeper power law was chosen for pore sizes than indicated by grain observations, because dust grains are also lifted off the surface, where pore size does not constitute an impediment, and hence the relative proportion of larger grains coming from the surface should be larger than for those originating from the interior.

5.1.3 Numerical Model and Initial Parameters

Our model assumes a porous, spherical and initially homogeneous nucleus composed of amorphous and crystalline water ice, dust, and five other volatile species: CO, CO_2, HCN, NH_3, and C_2H_2. The basic numerical model and input physics used for the simulation of this system are already summarized in Ch. 2. However, here we use a quasi-3D approach, where diurnal and latitudinal temperature variations are calculated as they result from uneven surface heating by solar radiation onto a spinning comet. Lateral heat conduction is neglected, and so heat is assumed to flow radially (perpendicular to the surface). Thus, different points on the surface do not interact. This simple approach is justified by the low thermal conductivity of cometary ice mixtures and by the thinness of the skin-depth (see Cohen *et al.*, 2003).

As mentioned in Sec. 2.1, one of the boundary conditions used is obtained from the requirement of energy balance at the surface:

$$F(R) = \epsilon\sigma T(R,t)^4 + \mathcal{F}P_{\rm vap}(T)\sqrt{\frac{\mu}{2\pi}R_g T}\mathcal{H} - (1-\mathcal{A})\frac{L_\odot}{4\pi d_H(t)^2}\cos z, \tag{5.1}$$

where $\cos z = cos\theta \cos\varphi$. In the simple case considered here, of a rotational axis that is perpendicular to the orbital plane, θ is the latitude angle and $\varphi = (2\pi/P_{\rm rot})t$ is the hour angle, both defined relative to the equator of the nucleus.

With the spin vector perpendicular to the orbital plane, results for six hour angles are recorded: $\varphi = 0/360°$, 60°, 120°, 180°, 240°, 300°, a different one at each time-step. Separate calculations are carried out for latitudes corresponding to $\cos\theta = 1$, 0.75, 0.5, 0.25, that is, between the equator ($\theta = 0°$) and a near-pole angle ($\theta = 75.5°$).

Table 5.2 lists the main physical parameters that were applied to the model calculations together with their relevant values.

Table 5.2 Orbital elements and nucleus properties for 9P/Tempel 1

Parameter	Symbol	Value	Units
Semi-major axis	a	3.12	AU
Eccentricity	e	0.5175	
Effective radius	R	3.3	km
Geometric albedo	$\mathcal{A}$	0.04	
Spin period	$P_{\rm rot}$	41.85	hr
Dust mass fraction	$X_{\rm d}$	0.5	
Ice mass fraction	$X_{\rm ice}$	0.5	
Porosity	Ψ	0.5	
Dust density	$\varrho_{\rm d}$	3250	kg m^{-3}
H_2O ice density	$\varrho_{\rm ice}$	917	kg m^{-3}
Dust heat capacity	$c_{\rm d}$	1.3×10^3	J kg^{-1} K^{-1}
Ice heat capacity	$c_{\rm ice}$	$7.49T + 90$	J kg^{-1} K^{-1}
Dust conductivity	$K_{\rm d}$	10	J m^{-1} s^{-1} K^{-1}
C-Ice conductivity	$K_{\rm c}$	$5.67 \times 10^2/T$	J m^{-1} s^{-1} K^{-1}
A-Ice diffusivity	$K_{\rm a}/(c_{\rm ice}\varrho_{\rm ice})$	3×10^{-7}	m^2 s^{-1}

Initial *Working* Model

Since little is known about any comet's structure and composition, our first task was to choose the structural and compositional parameters. The composition was chosen by running full simulations of several models of various generic compositions, but identical structure – as listed in Table 5.3 – and comparing the resulting production rates to the available relevant past observations (Cochran *et al.*, 1992; Osip *et al.*, 1992). This is shown in Fig. 5.3, where the activity was derived from the simulations after an advanced evolution time, so that a regular periodic activity pattern could be established.

Table 5.3 Initial compositions for 9P/Tempel 1 evolution models.

mass fraction [1]	Trapped gas No mantle [2] (*Working* model)	Trapped gas Dust mantle [2]	Ice mixture No mantle	Ice mixture Dust mantle
X_a	0.5	0.5	0	0
X_c	0	0	0.45	0.45
X_d	0.5	0.5	0.5	0.5
X_{CO}	0.05	0.05	0.025	0.025
X_{CO_2}	0.0125	0.0125	0.00625	0.00625
X_{HCN}	0.0035	0.0125	0.00625	0.00625
X_{NH_3}	0.0125	0.0125	0.00625	0.00625
$X_{C_2H_2}$	0.0012	0.0125	0.00625	0.00625

[1] Mass fraction is either occluded volatiles in the amorphous ice for the 'trapped gas' case, or solid ices in the 'ice mixture' case.
[2] The distinction between 'no mantle' and 'dust mantle' depends on the choice of the dust drag efficiency factor (see Sec. 2.1).

The model for which reasonable agreement was obtained for all available observed species was then chosen as the *working* model. Fig. 5.4 shows the dust production rate of this model. We can see that it agrees very well with the results derived from ground-based observations described in Sec. 5.1.2. We note, in particular, the times of rise, maximum and decline in the rate of dust emission, compared to those in Table 5.1. The magnitude corresponding to the dust production rate at maximum is ~ 9. Varying the average grain size and/or dust grain density may result in a change of ± 0.5 mag. For a correlation between dust production and magnitude, and perihelion magnitudes, see Meech (2002) and Meech *et al.* (2005).

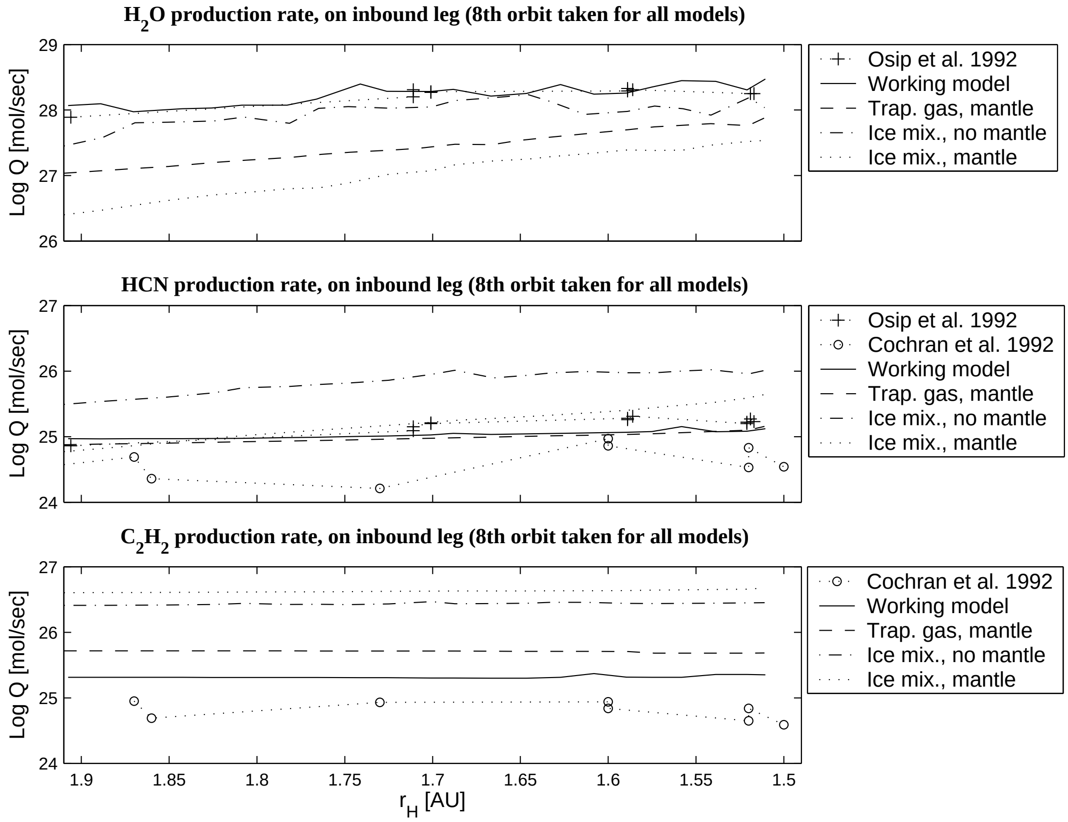

Figure 5.3 Comparison of observations and results from simulations for the four generic models (see Table 5.3). These are presented in production rates of the various volatile species(on a log scale) as a function of heliocentric distance (in AU). Measured production rates of OH, as the product of H_2O, CN, as the product of HCN, and C_2, as the product of C_2H_2, were taken from Cochran *et al.* (1992) and Osip *et al.* (1992).

5.1.4 Results of Evolutionary Calculations

Assuming the spin axis to be perpendicular to the orbital plane and starting with a uniform low temperature, we followed the evolution of the *working* model for several orbits. The thermal and compositional evolution in the interior of the nucleus is illustrated in Fig. 5.5, for the subsolar point on the equator and for a point near the pole. These represent extreme cases – maximum and minimum – with respect to absorption of solar radiation, and hence activity, of a spinning nucleus in the orbit of 9P/Tempel 1, among **all** possible inclinations of the spin axis.

We should note that the model nucleus is spherical, whereas in reality the nucleus was found to be elongated, with semi-axes $a \approx 7.2$ km, $b \approx c \approx 2.2$ km (Belton *et al.*, 2005). Thus the "absorbing area" of the nucleus may vary, according to inclination, between

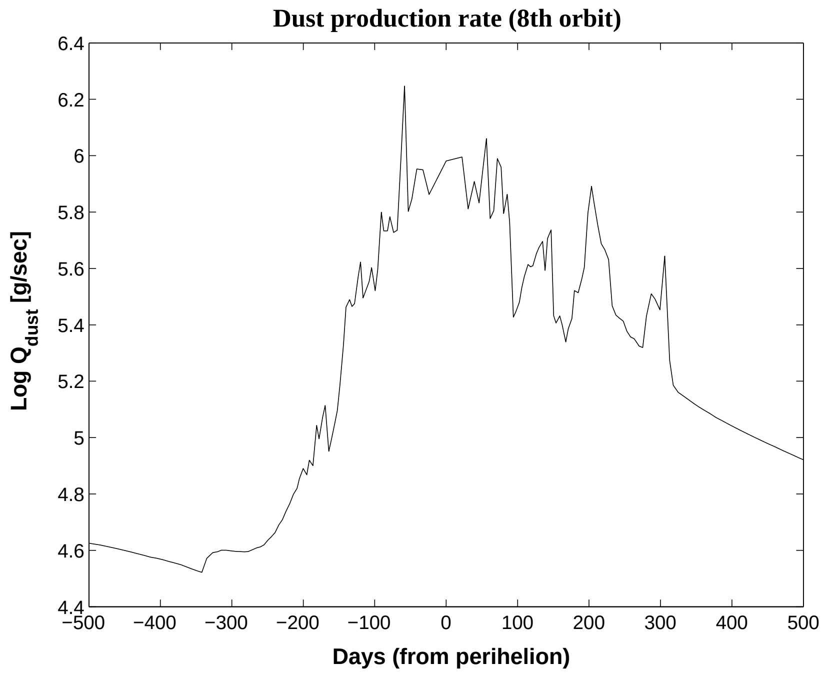

Figure 5.4 Dust production rate pre- and post-perihelion for the fitted working model. This is presented as production rate of dust as a function of time, in days, relative to time of perihelion passage.

about 15-50 km^2, compared to 34 km^2 in our model. This would place an error bar of up to a factor of 2 on the results regarding production rates, since most of the solar heat is spent in sublimation of volatiles. The shape itself should be of lesser importance, since the depth of the affected layer is much smaller than the radius.

The outstanding feature emerging from these calculations is the complicated stratification pattern as a function of depth, where layers enriched in various volatiles alternate. Moreover, several layers enriched in the same volatile may appear at different depths. The effect is illustrated by the mass fraction of amorphous ice, shown in the right panels of Fig. 5.5. We recall that the model's composition includes five volatile species trapped in amorphous water ice. These volatiles cover a wide range of sublimation temperatures (see Prialnik *et al.*, 2004). As the surface of the nucleus is heated and the heat wave propagates inward, the amorphous ice crystallizes and the trapped gas is released. The gas pressure in the pores peaks at the crystallization front. As a result, gas flows in part outward and escapes, and in part, inward into colder regions. Eventually, each species reaches a sufficiently cold region for it to recondense. Since recondensation releases heat, it affects the composition of its surroundings and thus a complicated pattern results, of alternating ices mixed with the amorphous water ice.

When another heat wave reaches these regions, on a subsequent perihelion passage, the heat is absorbed in sublimation of the recondensed volatiles rather than in crystallization of amorphous ice. This is how alternating layers of crystalline and amorphous ice arise, rather than a single boundary between a crystalline exterior and an amorphous interior. Finally, the *terraced* behavior that appear in the outer crystalline/amorphous ice boundary (especially notable in Fig. 5.5d) is due to erosion of the nucleus, which brings this boundary closer to the surface.

The evolution of local noon temperature profiles is shown in the left panels of Fig.5.5. It indicates that a steady state is reached after a few revolutions at about the same depth, both near the pole and at the equator. This depth corresponds to the orbital skin depth

$$\left(\frac{2Ka^{3/2}}{\sqrt{GM_{\odot}}\rho c}\right)^{1/2} \approx 10\mathrm{m}. \tag{5.2}$$

We note, however, that the maximum temperatures at the two locations differ by about 40 K; accordingly, the skin depth, which is roughly inversely proportional to temperature, is slightly larger near the pole.

The stratified layers extend from a depth of about 10 m below the surface and down to a few hundred meters. Since the former is roughly the orbital skin depth for 9P/Tempel 1, this structure should cause activity variations on the orbital time scale. This means that activity may differ from orbit to orbit and occasional spurious outbursts may arise, when the heat wave propagating in from the surface reaches a region enriched in ice of some volatile species. Such outbursts of gas should be accompanied by ejection of dust particles. This variable behavior is exhibited in Fig.5.6, where we note an outburst of CO, CO_2 and dust following several orbits of "regular" emission. Water production, with its main source being sublimation from the surface, follows a much more regular pattern.

Applying the correction of the SVR parameter (see Sec. 2.4) has a notable effect the simulation results. Temperature profiles at the equator are compared in Fig. 5.5 in the two lower left panels, and the evolution of crystallization in the two lower right panels. The correction factor increases internal pore surface, enhances sublimation from pore walls and hinders the heat wave from penetrating deeper, causing internal temperatures to be lower. As a result, the depth of amorphous ice is slightly shallower, as illustrated in Fig. 5.5d. At higher latitudes, due to the diminished insolation, it is still shallower, as illustrated in Fig. 5.5b.

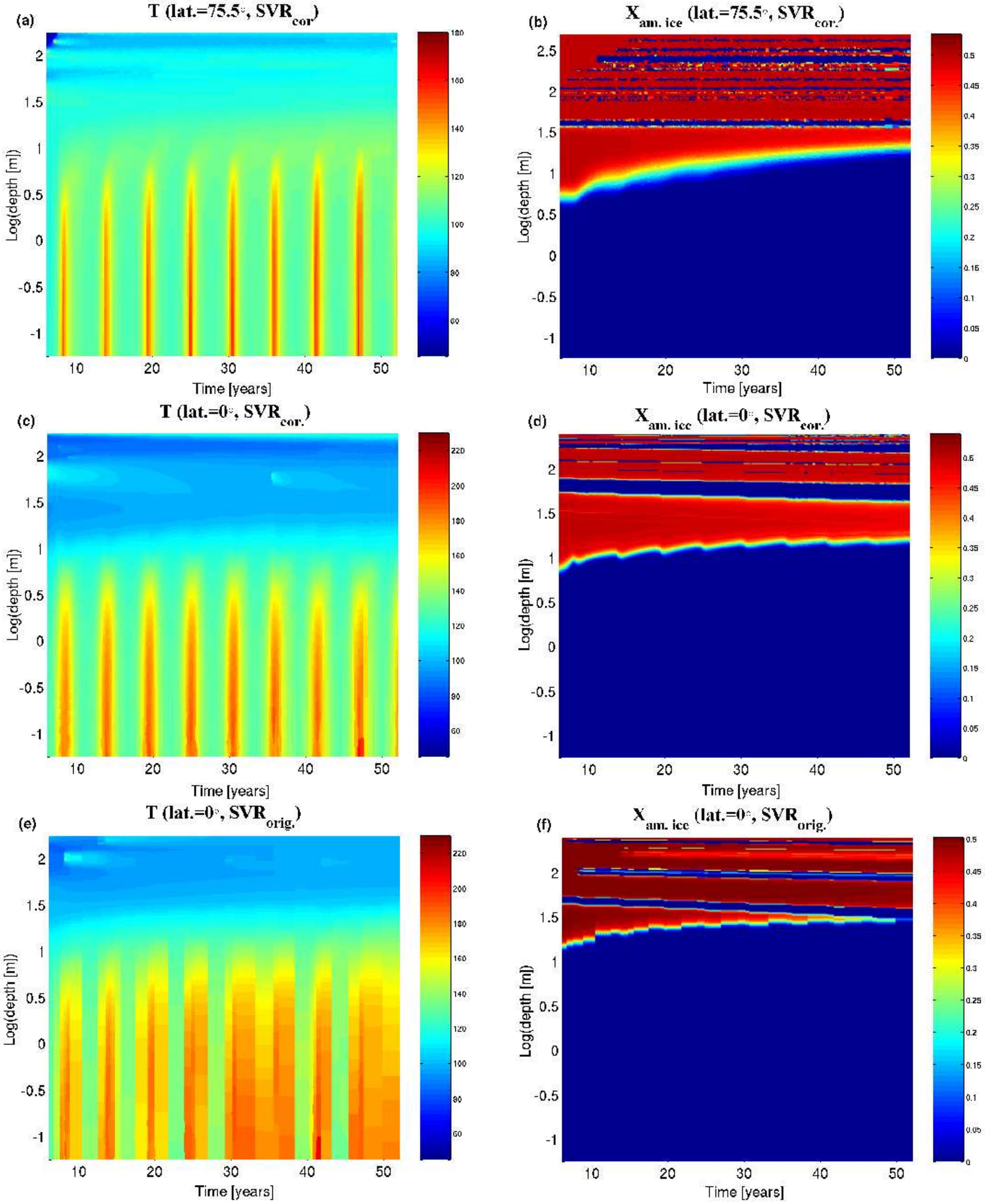

Figure 5.5 Evolution of the nucleus of 9P/Tempel 1, with an initial configuration of the *working* model. Temperature and amorphous ice abundance are shown as a function of time (in years) and depth (on a log scale, from the surface to the interior). (a) and (b) present near-pole latitude, with the corrected SVR term; (c) and (d) present equator (subsolar), with the corrected SVR term; (e) and (f) present equator (subsolar), with the non-corrected SVR term.

Fig. 5.6 shows a comparison of the production rates obtained for long-term evolution with and without the SVR correction (see Sec. 2.4 for description of the correction factor). As expected, surface properties, such as temperature and H_2O production rate, are not affected. The production rates of gases released in the interior, either escape from crystallizing ice or by sublimation of recondensed ice, are affected to a larger extent, but preserve the same pattern of behavior. This is not surprising, since the driving energy source is the same. We note that the complex stratified structure of the outer layer of the nucleus gives rise to occasional outbursts.

Clearly, the orbital evolution of production rates differs considerably among different volatiles. This means that observed volatile abundances do not necessarily reflect nucleus abundances (cf. Huebner and Benkhoff, 1999; Prialnik *et al.*, 2004).

Fig. 5.7 presents surface maps of water and dust production rates. It is a spherical projection of the quasi-3D model results, where each patch corresponds to a specific value of the latitude and the hour angle (longitude). The panels on the left column present the evolution of water production rates, starting from perihelion (top), through mid-orbit (middle) and to aphelion (bottom). Note that the colorbar scales vary, as production rates are quenched when the comet moves away from the Sun. Since the spin axis alignment is taken as perpendicular to the orbital plane, the equator is always at the sub-solar, receiving the largest energy input and producing the highest production rates.

We can see that the variations in production rates between perihelion and aphelion are more pronounced at the near-pole latitude – the production rate of water is higher by 9 orders of magnitude, at perihelion. This means that, for our model, most of the surface of the comet is active at perihelion, while at aphelion only minor activity can be expected from the region of the equator. We can see that regarding the variation of dust production rates (right column panels) between perihelion and aphelion, the opposite is true. The largest variations are on the equator, with a difference of ~ 1.5 orders of magnitude,whereas the near-pole latitude rates are almost the same (factor of 2 difference).

What is also notable is that in the case of the dust production rates, there is almost no dependence on the longitude, except when at aphelion. this is because dust production rates are sensitive to the total gas flow, which peaks for water at perihelion, but can be maintained at more distant locations by the sublimation of volatile species, due to triggered sublimation of the sub-surface volatile or amorphous water ice layers. This is especially true for the more volatile species, CO and C_2H_2 (see Fig. 5.6).

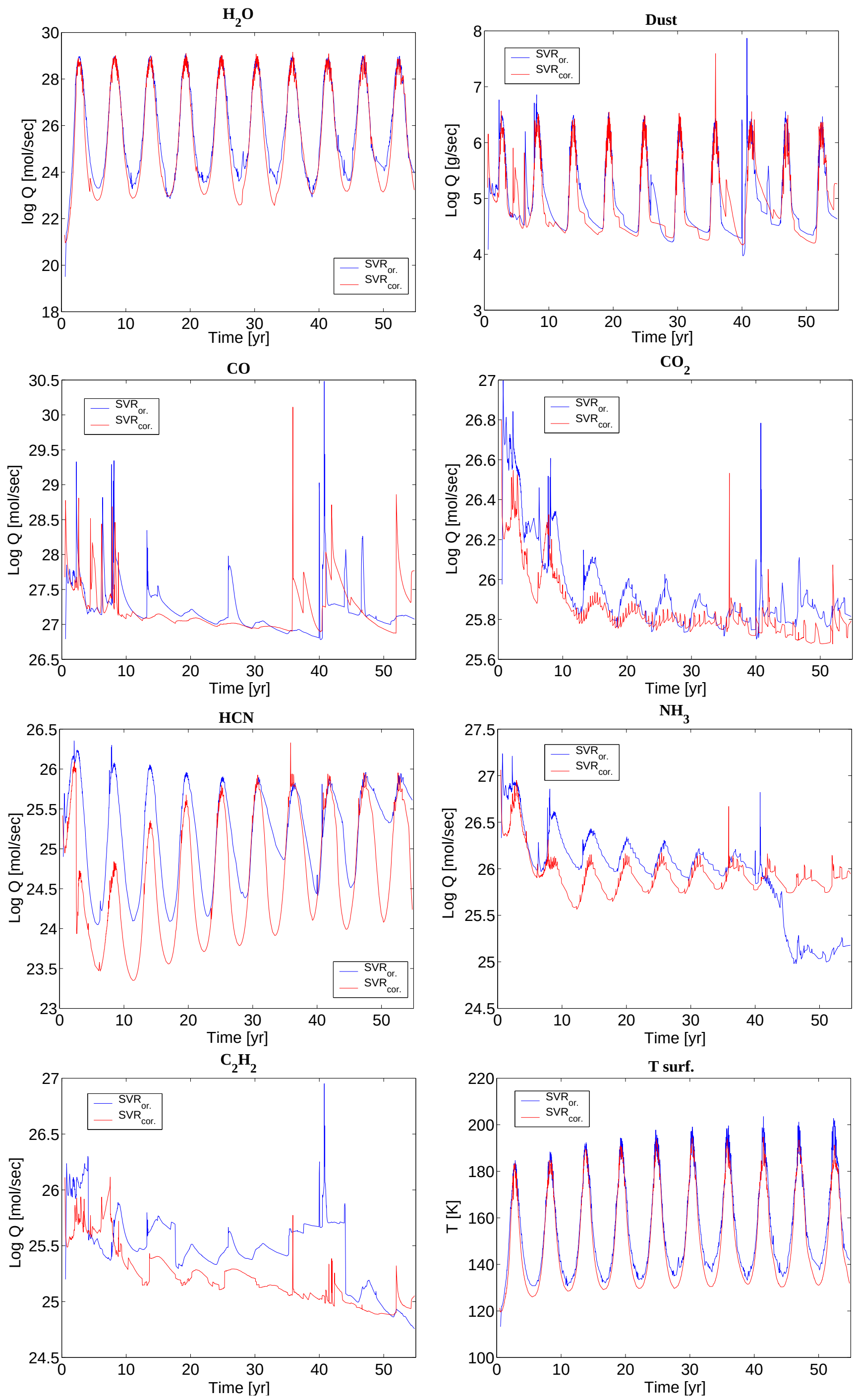

Figure 5.6 Time-dependent external activity resulting from a simulation of 9P/Tempel 1. Presented here are production rates of water, dust, all volatile species and surface temperature (at subsolar point), as a function of time. We note here the differences in resulting activity between the cases of non-corrected (blue) and corrected (red) SVR parameter.

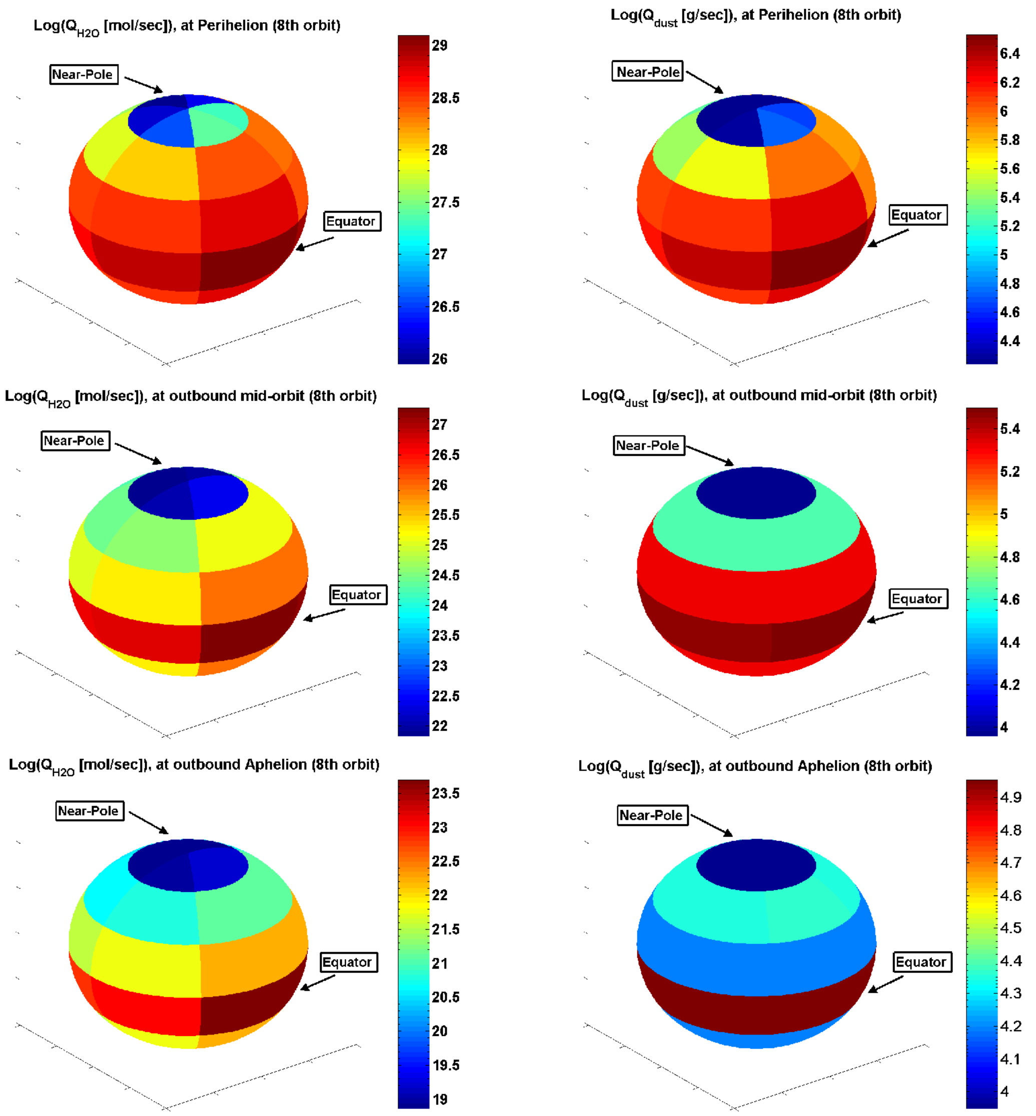

Figure 5.7 Surface maps of the resulting production rates of H_2O (left) and dust (right). Here we show three sample positions along the 8th orbit: perihelion, at 1.5 AU (top); outbound lag mid-orbit, at 3.1 AU (middle); outbound lag near-aphelion, at 4.7 AU (bottom). Presented here are 4x6 "patches" of latitude and longitude, respectively, calculated as described in Sec. 5.1.3. Note the different colorbar scales, as production rates of volatiles, responsible for dragging the dust along, are quenched all over the surface, due to decrease in solar input.

5.1.5 Simulation of a Thermal Impact

The aim of the *Deep Impact* mission was the collision of the impactor spacecraft with the nucleus, in order to form a crater. This has enabled the flyby spacecraft to perform observations and measurements of the impact itself, the ejected material and the interior composition, as revealed by the exposed crater.

We simulate this thermal impact by assuming an additional energy flux in the form an procedure described in Sec. 2.8. The impact is applied to an evolved model of comet 9P/Tempel 1 – the *working* model, described in Sec. 5.1.3 and 5.1.4. In order to maximize the effect of the impact on the thermal properties, we assume that the entire kinetic energy of the impactor is turned into heat.

The parameter values used are listed in Table 5.4. The resulting peak energy flux is about 300 times higher than the solar energy flux at that distance at the subsolar point. At a distance of 1.5 AU, the actual impact distance, the contrast would be reduced by a factor of ~ 0.6, but this change should not be significant.

Table 5.4 Properties of the simulated impact for a model of 9P/Tempel 1.

Parameter *	Symbol	Value	Units
Total energy	E_{tot}	1.9×10^{10}	J
Crater area	A	1000	m^2
Crater depth	ΔL	30	m
Heliocentric distance	d_0	2	AU
Revolutions before impact	n	7	
Timescale	τ	180	s
Peak energy flux	F_0	10^5	J m^{-2} s^{-1}

* See Sec. 2.8 for the parameter definitions.

Two impact calculations were carried out for two different locations on the nucleus surface: one at the equator (subsolar point), and another near the pole. The purpose was to find out to what extent is the point of impact expected to affect the outcome.

Fig. 5.8 shows the comparison of the two impact locations. We can see that, to within a fraction of a magnitude, the production rates of the major constituents (H_2O, dust, CO and CO_2) are indistinguishable at the moment of impact. However, since the flyby spacecraft is supposed to conduct the observation for a period of ~ 15 minutes after the impact, the emission of dust, CO and CO_2 may vary by ~ 2 orders of magnitude during this time.

The low production rates before impact are an artifact of our simulation: when we remove an outer layer of several tens of meters, we expose cold material. Since the energy is supplied slowly at first, production rates drop. The total amount of dust ejected upon impact amounts to $\sim 1.7 \times 10^5$ tons at the near-pole location, and $\sim 2.2 \times 10^5$ tons near

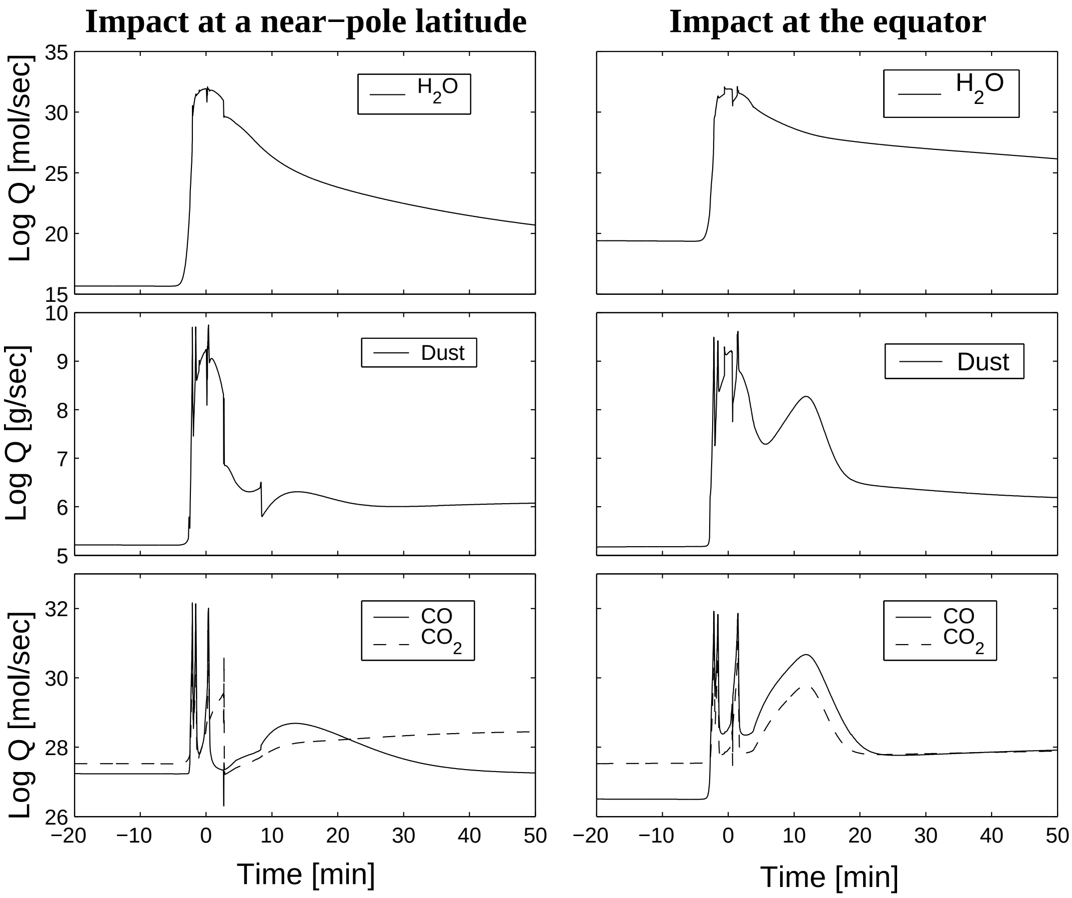

Figure 5.8 Results of the thermal impact simulation. Presented here are the production rates as a function of time, relative to the moment of impact. We compare between the two extreme of impact latitudes: near-pole (75.5°) and equator (0°). The dominant volatiles, H_2O, CO and CO_2, and the dust component, are presented at high temporal resolution, around the peak of the impact. Note that the general shape of production rates is similar at both impact sites.

the equator. Compared with the dust production rate over the entire comet at perihelion, these amounts are equivalent to the total dust output of 2 days and 2.6 days, respectively, at perihelion.

We note that the CO and CO_2 production rates are not smooth: they show two spikes and a somewhat later peak (see lower panels of Fig. 5.8). This is due to the layered structure of the nucleus described in the previous sub-section. The fact that the behavior pattern of these volatiles can also be noted in the rate of dust ejection indicates that a significant fraction of the dust originates in layers beneath the surface. Small dust grains are thus dragged by volatiles through the pores. This effect is less marked near the pole, where the subsurface layers have been processed to a far lesser extent during evolution, prior to the impact.

We thus conclude for the outcome of the simulated impact that:

- The increase in production rates of volatiles and dust is of several orders of magnitude, and thus readily observable. The total dust output, for example, is equivalent to the output of about two days at perihelion. We should bear in mind, however, that these results provide an upper limit, since it is assumed that the entire energy is spent in thermal effects.

- An important conclusion of these calculations is that the place on the nucleus where the impact occurs is not as significant as one might expect. The total dust output, for example, differs by only a factor of ~ 1.3.

- Variability in activity may be detected even on the short timescale of an impact, as the heat wave propagates into a stratified layer, where amorphous water ice may crystallize and ices of various volatile species may sublimate.

- Subsequent long-term thermal evolution is also affected to some extent, but not in a way that would be recognized by observations as an aftermath of an impact (or collision). The variation of volatile production rates with time (or heliocentric distance) will retain a general uneven pattern, but whether this pattern differs from that of an undisturbed comet may be difficult to establish.

A similar effect may be expected of a random collision with a large meteor. Provided that such a collision will create a deep crater and expose layers a few tens of meters deep, an outburst of gas and dust ejection is expected to result.

An interesting result of the long-term evolution, is that even though the thermal energy influx due to the impact is confined in both time (by the Gaussian function) and space (by the depth of penetration), the effect lingers and shows deviations in production rates – as compared with the un-impacted model – long after the event. However, this effect cannot be used to characterize a comet that has undergone an “impact”, because the general evolution and activity patterns are similar to that of a comet model that did not suffer an impact. The difference is in the detailed variations of production rates with heliocentric distance, but these also depend to a similar extent on model parameters and assumptions.

5.2 Internally-Driven Dust Activity of Comet 22P/Kopff

5.2.1 Introduction

Comet 22P/Kopff was one of the targets of the CRAF (Comet Rendezvous Asteroid Flyby) mission, which was canceled by NASA in 1992. As such, it has been observed extensively on different occasions. It was discovered in 1906 by German astronomer August Kopff. During the 20th century it underwent about eight close approaches to planets, the most dominant of them with Jupiter. These perturbations affected mostly its inclination, decreased from 18° to 4.7°, and perihelion distance, decreased from ~ 2 AU to 1.5 AU (Lamy *et al.*, 2002). Its current orbit lies between those of Mars and Jupiter, has a small inclination angle ($i = 4.27°$) and a period of 6.453 yr (Lamy *et al.*, 2002). Thus, it is a bona-fide JFC.

The comet has been recovered at every apparition since its discovery, and has had relatively repeatable behavior. It has a significant coma activity, even before perihelion (Lamy *et al.*, 2002; Lowry and Weissman, 2003), and a dust trail, distinguishable as an extended feature in both optical and IR measurements, mostly (Ishiguro *et al.*, 2002, 2007).

Spitzer observations show that the comet has a radius of $R_N = 1.89 \pm 0.16$ km and a low thermal inertia of $I \leq 30$ J/K/m^2/s$^{1/2}$ (Groussin *et al.*, 2009). Radiometric measurements suggest a low albedo of $p_V = 0.042 \pm 0.006$ (Lamy *et al.*, 2002). The rotation period is estimated to be ~ 13 hr (see Lowry and Weissman, 2003). Optical CCD observations were obtained during four nights, between 1989-1992, using the UH 2.2-m telescope on Mauna Kea. These were used to make deep composite images to search for dust activity (A. R. Zenn, private communication).

Dust-dynamical models were developed by Zenn & Meech for the available observations datasets, using the Finston-Probstein method (F-P). This method models a cometary tail in order to determine onset and cessation of emission, particle production rates, sizes, and velocities. Three of the models (1989 observations) corresponded to pre-perihelion activity, with a sunward emission function. The latter model (1992 observations) corresponded to post-perihelion activity and displayed an interesting result with emission directed from a specific location ("jet") on the nucleus.

Thermal evolution models of the nucleus of 22P/Kopff are calculated here, by means of a quasi-3D code (Prialnik *et al.*, 2004). This code takes into account diurnal and latitudinal variations, but neglects lateral heat conduction. For these specific models we have focused on the location of the directed emission, as derived from the dust-dynamical modeling. We examine the dependence of the activity on a few key parameters by following the outgassing of volatiles, ejection of dust and heat transport inside the nucleus.

5.2.2 Dust-Dynamical Modeling Results

Four models of comet 22P/Kopff were constructed by Zenn & Meech, from four composite images, with each image corresponding to a data set for a single night (Feb. 9, Apr. 6, and Aug. 2, 1989, and Jan. 6, 1992). The 1989 observations, taken pre-perihelion, were of poor quality, had some scatter in the data and the dust tail was not very extended. The 1992 observations were taken post-perihelion and displayed a distinct tail feature and directed emission.

The dust tail was modeled using a method first employed in Farnham (1996), as a modified F-P method (Finson and Probstein, 1968). Dust grains are entrained in the gas flow (due to sublimation of volatiles, predominantly water ice) and are dragged from the nucleus, to within a few nuclear radii, where they are decoupled from the gas. The motion of the refractory dust grains are controlled by solar gravity and solar radiation pressure. The net result may be regarded as a reduced solar gravitational force acting on each grain.

The F-P modeling technique involves computing the trajectories of dust grains ejected from the nucleus at a certain velocity and moving under the influence of the reduced gravity force. The scattered light from a distribution of particles emitted from the nucleus is then added up to produce a surface brightness of a synthetic tail. This is compared to the surface brightness derived from the real data. The data can be inverted and information about the grain size distribution, ejection velocity and onset and cessation of activity can be obtained.

The onset of emission in the 1989 models began $\sim$ 500 days before perihelion and continued until the observation date, with increased emission in the sunward direction. The particle sizes ranged between 30-300μm, with velocities inversely proportional to particle size. All of these pre-perihelion models displayed similar characteristics, with identical times of emission onset, particle sizes, emission function (sunward-directed), and production rates.

The 1992 post-perihelion data (corresponding to 715 days post-perihelion) were fit with a substantially different model. The best-fit models required emission near the south pole of the nucleus, with the southern rotation pole located at $RA = 270°$ and $DEC = -50°$. The post-perihelion dust tail appeared somewhat detached, as there was a gap in the dust between the nucleus and the tail (see Fig. 5.9). This is caused by the cessation of activity post-perihelion, with the dust slowly moving away from the nucleus. The particle production varied slightly and peaked near perihelion. Since the emission consisted of relatively large particles, there was a smaller rate relative to the 1989 models. The velocities of the particles decreased slightly with size, and were generally close to 2 m/s. The contour plots for the data and the model are shown in Fig. 5.9.

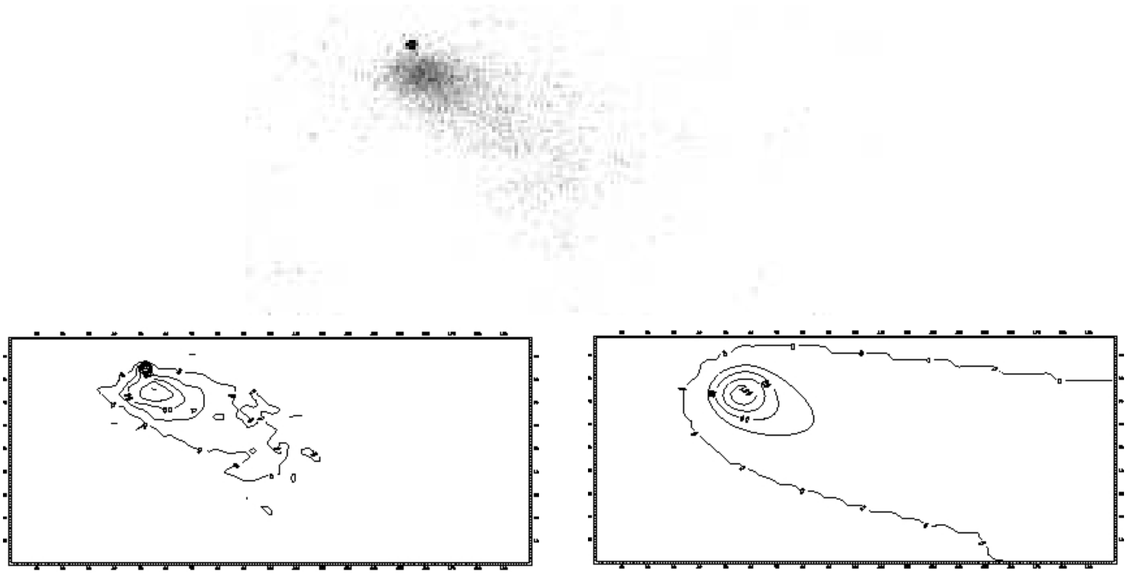

Figure 5.9 *Top*: Median combined composite image of comet 22P/Kopff, from Jan. 6, 1992. Note that the tail is disconnected from the nucleus. *Bottom-left*: Contour plot for the median combined composite image of Kopff, from Jan. 6, 1992. *Bottom-right*: Contour plot of the best-fit model for the Jan. 6, 1992 image of Kopff. For all figures, North is up and East is to the left. Images are 3.95×10^5 by 1.90×10^5 km in the plane of the sky. Images are courtesy of A. R. Zenn, IfA, U of Hawaii (private communication).

Table 5.5 summarizes the characteristics of the best-fit model to the 1992 data. The onset of particle emission for the jet was modeled to begin $T-200$ days pre-perihelion and continue until $T+500$ days. The date of observation corresponds to $T+715$ days, and the detached dust tail suggests that there was very little recent emission. The particle sizes range between 300-3000μm. However, it should be noted that if particles smaller than 300μm were ejected 500 days before perihelion, they would have traveled so far from the nucleus, that by the time observations were made they would have cleared the image's field of view.

Table 5.5 Finson-Probstein model fit to 1992 Kopff observations

Parameter	Value
Smallest particles	300 μm
Largest particles	3 mm
Emission start	$perihelion - 200$ days
Maximum dust output	$perihelion$
Emission decline	$perihelion + 500$ days
Velocity ($v(\beta)$)[1]	$v(r_{\min})/v(r_{\max}) \approx 1.2$
α[2]	1

Data is courtesy of A. R. Zenn & K. J. Meech, IfA, U of Hawaii (private communication).
[1] $\beta = F_{rad}/F_{grav} = 5.74 \times 10^{-4} Q/\varrho_d r$, is a proxy for grain size, where Q is the radiation pressure scattering efficiency, ϱ_d is the dust grain density and r the grain size.
[2] Fitted value for the slope of the particle size distribution.

There is a general agreement between the 1989 models and that of 1992. Although there was earlier emission in the 1989 models, the emission consisted of small particles that would have moved far from the nucleus and would not be observed in the 1992 observations. The 1992 model would therefore not take into account these smaller particles, and the modeled emission only took into account larger particles. The Kopff modeling results seem to suggest that initial emission consisted of particles smaller than 300μm, but that once larger particle emission turned on it continued until $\sim$ 500 days post-perihelion.

5.2.3 Numerical Model and Initial Parameters

For the purpose of our thermal modeling, we assume a similar model to that employed in Sec 5.1, for modeling 9P/Tempel 1. The nucleus is assumed to be spherical, initially homogeneous and composed of amorphous water ice (at the initial stage), occluded gas species (CO, CO_2 and HCN), and a dust component (grains of silicates and minerals). The volatile species, other than water, were taken as the most common compounds in planetary environments (Bergin *et al.*, 2007), which are also among the most abundant cometary volatiles observed (Bockelée-Morvan *et al.*, 2004). This is because there are no observations to date of the gas coma or tail of 22P/Kopff and no constraints on the volatile capacity of this object. However, its activity, orbital configuration and known physical parameters, place it well inside the group of JFCs. The basic numerical model and input physics are already summarized in Ch. 2.

Since we aim to model the dust activity of Kopff, as originating from a directed emission ("jet") configuration (according to the dust modeling results, see Sec. 5.2.2), we use the quasi-3D approach, as described in Sec. 5.1.3. For the given latitude, $\theta = 50°$, we record 12 hour angles (or longitudes) from $\varphi = 0°$ to $\varphi = 330°$, in increments of 30°, a different one at each time-step. In this way we can follow the evolution of activity from the location around $\varphi = 270°$, through repeated perihelion passages and diurnal variations (due to uneven heating of a spinning object). According to the location of the "jet", our choice of grid and a fiducial error estimate of $10\% - 20\%$ in the sub-solar latitude location, the active patch on the surface of the comet is between $\sim 0.5\% - 2\%$ of the total surface area, which translates to a circular patch of $\sim 265 - 535$ m in radius.

The physical parameter values used in the model calculations are given in Table 5.6. These are the same as for the model of Tempel 1 (see Sec. 5.1.3), except for those taken from recent observations (see references in the table).

Table 5.7 lists variant models we set, in order to investigate the influence of some key parameters on the dust activity emanating from the nucleus.

For the bulk density we take a value derived from non-gravitational forces and light curve analysis (Sosa and Fernández, 2009). However, since there are some uncertainties and scatter in the compiled light curve of Kopff (see discussion in Sosa and Fernández, 2009), we choose the upper limit of the mass estimate. Abundances of volatile species were taken as a few times their upper limit estimates, from cometary gas production measurements (Bockelée-Morvan *et al.*, 2004), in order to facilitate extended gas emission around perihelion. We also varied the Hertz factor, f_H, which accounts for the effect of a porous aggregation of grains on the thermal conductivity, reducing it by the ratio of the inter-grain contact area to the mean grain cross-section (Huebner *et al.*, 2006). Reduced thermal conductivity of the sub-surface material allows for prolonged volatile sublimation post-perihelion. Finally, the last three parameters in Table 5.7 are the largest grain radius, exponent of the power law and range of the pore-size distribution. These are related to the dust-dynamical modeling results of Sec. 5.2.2, since we assume that the pore-size distribution follows the dust-size distribution (see Sec. 2.4). The range was chosen to be wider than the dust grain size range indicated in Table 5.5. This was done in order to

Table 5.6 Orbital elements and nucleus properties for 22P/Kopff

Parameter	Symbol	Value	Units
Semi-major axis [1]	a	3.466	AU
Eccentricity [1]	e	0.543	
Effective radius [2]	R	1.89	km
Geometric albedo [1]	$\mathcal{A}$	0.042	
Spin period [3]	P_{rot}	13.0	hr
Dust mass fraction	X_d	0.5	
Ice mass fraction	X_{ice}	0.5	
Bulk density [4]	ρ	300-400	kg m^{-3}
Dust density	ϱ_d	3250	kg m^{-3}
H_2O ice density	ϱ_{ice}	917	kg m^{-3}
Dust heat capacity	c_d	1.3×10^3	J kg^{-1} K^{-1}
Ice heat capacity	c_{ice}	$7.49T + 90$	J kg^{-1} K^{-1}
Dust conductivity	K_d	10	J m^{-1} s^{-1} K^{-1}
C-Ice conductivity	K_c	$5.67 \times 10^2/T$	J m^{-1} s^{-1} K^{-1}
A-Ice diffusivity	$K_a/(c_{ice}\varrho_{ice})$	3×10^{-7}	m^2 s^{-1}

[1] Lamy *et al.* (2002). [2] Groussin *et al.* (2009). [3] Lowry and Weissman (2003). [4] Sosa and Fernández (2009) – based on non-gravitational forces analysis and the updated radius from Groussin *et al.* (2009).

Table 5.7 Variants of the basic thermal model of 22P/Kopff

	Run1	Run2	Run3	Run4	Run5	Run6	Run7
ρ [g/cm^3]	0.4	0.4	0.4	0.4	0.4	0.3	0.3
X_{CO}, X_{CO2} [1]	0.1	0.1	0.1	0.1	0.1	0.1	0.05
X_{HCN} [1]	0.05	0.05	0.05	0.05	0.05	0.05	0.005
f_H [2]	0.1	0.01	1.0	1.0	1.0	0.1	0.1
a_{max} [cm] [3]	0.01	0.01	0.01	0.1	0.3	0.3	0.3
α [4]	1.9	1.9	1.9	2.2	2.1	1.95	1.9
X_p [4]	1000	1000	1000	5000	1000	1000	1000

[1] Initial abundance of gas species occluded in amorphous ice.
[2] Correction to the thermal conductivity of a porous medium (Huebner *et al.*, 2006).
[3] Maximal dust grain radius, in cm.
[4] Parameters of the initial pore-size distribution – exponent of the power law (α) and the ratio of maximal to minimal pore radius (X_p).

account for micro-pores at the low-end, and to enable the flow of a few mm-size grains requiring somewhat larger pores at the high-end. A steeper power law was chosen for pore sizes than indicated by dust observations and modeling, because grains are also lifted off the surface, where pore size does not constitute an impediment, and hence the relative proportion of larger grains coming from the surface should be larger than for those originating from the interior.

5.2.4 Thermal Evolution Modeling Results

Each of the models, which appear in Table 5.7 (Runs 1-7), was evolved from an initial homogeneous configuration through 10-15 orbits, equivalent to a time span of 65-97 yr. The simulation results give a record of both the internal evolution and external activity. The internal profile is presented in terms of temperature, porosity/density and volatile ice abundances, as dependent on depth and time. External activity is recorded as production rates of water, volatile compounds and dust, which result from the processing of the nucleus's interior as it approaches and departs perihelion. We have a high enough temporal resolution in our models, to try and find the orbits that best reproduce the behavior of the dust emission, as described in Sec. 5.2.2.

Fig. 5.10 presents the production rates of dust, as a function of days relative to perihelion. Included here are all 7 models, each represented by the two orbits that best fit the behavior of dust emission from the F-P modeling. The production rates are normalized by the maximum rate of each orbit in order to examine the qualitative behavior of the dust emission.

An immediate distinction is that none of the orbits reproduce exactly the dust emission in terms of onset (at -200 days), development through perihelion and cessation (at 500 days). However, considering the large number of free parameters in a full thermo-chemical simulation such as this (see Ch. 2), we do not expect a complete reconstruction of the dust behavior. Thus, we can determine that the most likely models/orbits are: Run1/Orb10, Run4/Orb4 and Run5/Orb14. The leading parameters for this determination are the onset and cessation times and the extended production rate in the close vicinity of the perihelion passage.

Fig. 5.11 presents the internal profiles (temperature, porosity and ice abundances) of the most likely orbits (from runs 1, 4 and 5), before perihelion passage. The internal distributions presented are snapshots of the evolved compositional and structural config-

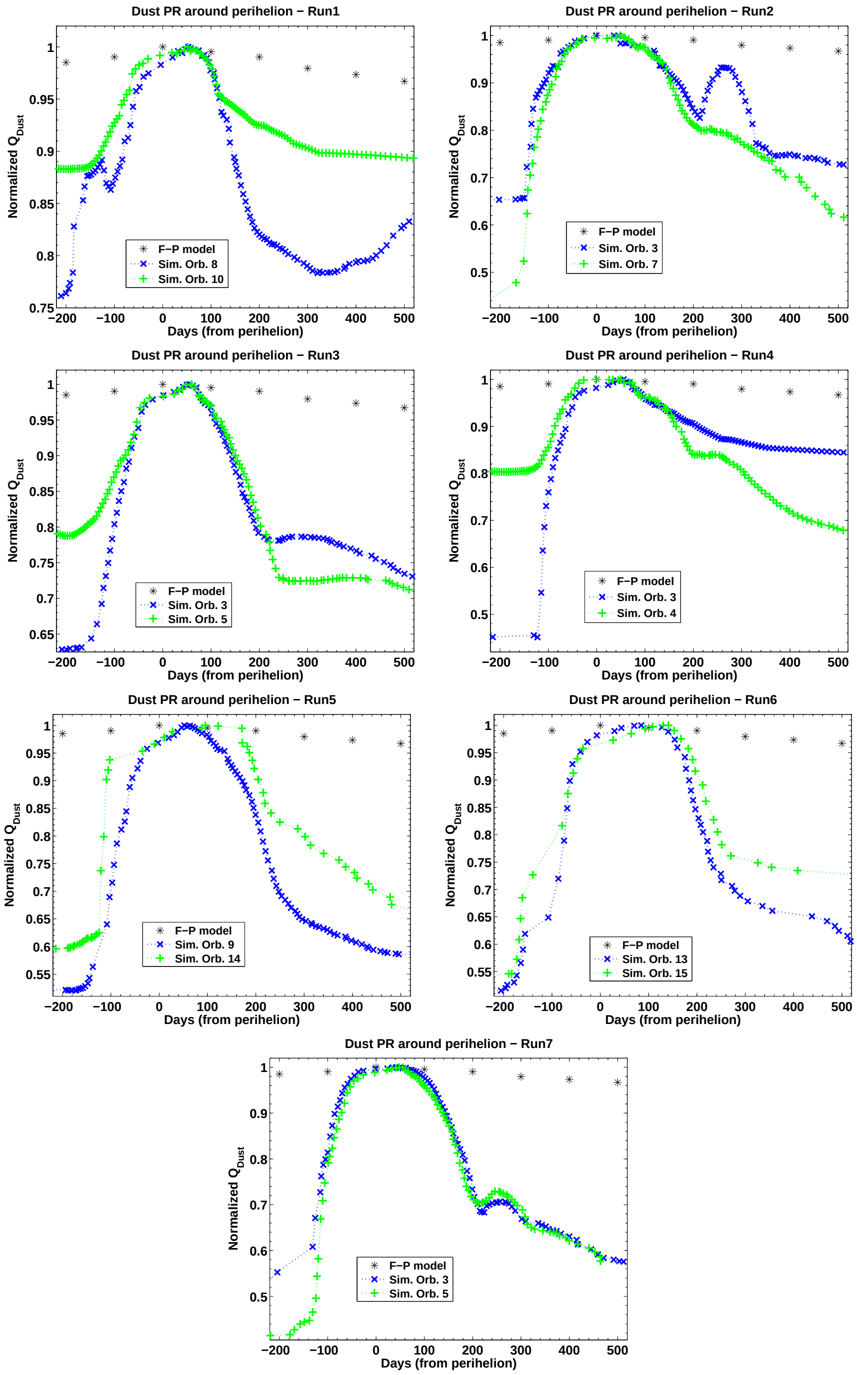

Figure 5.10 Dust production rates of the two most akin orbits, for all models of comet 22P/Kopff. The production rate is normalized to the maximum rate of the orbit, in order to examine the qualitative behavior of the dust emission. Time is presented in days relative to perihelion and only the near-perihelion parts of the orbits are shown. We compare in each panel the results of the dust-dynamical modeling (black "$*$"'s), the earlier orbit (blue "x"'s) and the later orbit (green "+"'s).

urations at $\sim$ 5 days pre-perihelion (Run1), $\sim$ 6 days pre-perihelion (Run4) and $\sim$ 140 days pre-perihelion (Run5). We note that for all models, below a depth of 100-300 m, the temperature is constant and under 40K. This means that throughout most of its bulk, this comet is pristine. Since the initial temperature was 30K (low enough so that initial sublimation rates would be negligible) and only amorphous ice was present, there is no chemical alteration of the deep interior. This is also clear from the panels on the right column of Fig. 5.11, showing ice mass fraction of amorphous and crystalline water ice, as well as CO_2 and HCN ices. The latter are not present in the initial configuration, but are a result of the thermal evolution.

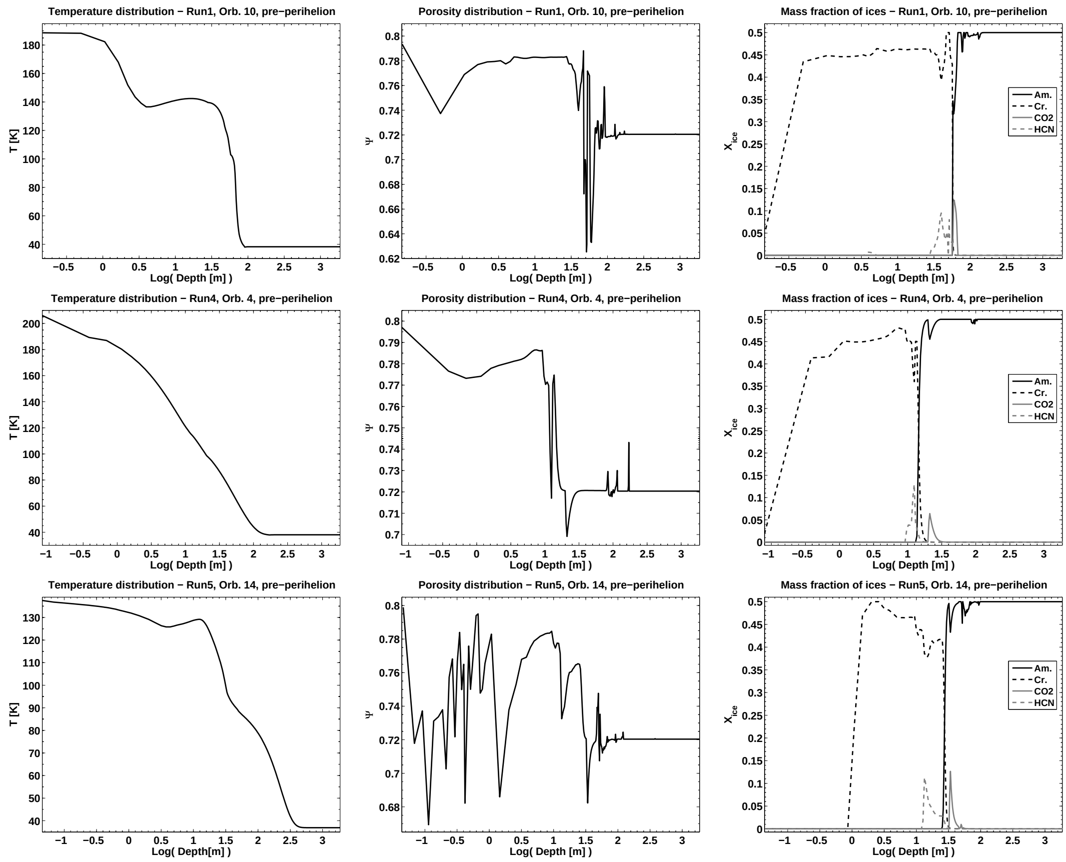

Figure 5.11 Depth distributions of temperature (left column), porosity (middle column) and ice abundances (right column). These are for the three best-fit orbits presented in Fig. 5.10 - Run1/Orb10 (top row), Run4/Orb4 (middle row) and Run5/Orb14 (bottom row). Values are presented as a function of the sub-surface depth, on a log scale.

On perihelion approach, solar radiation heats the surface and a heat wave propagates inward. This input energy can cause either sublimation of ice (if the threshold temperature is reached), or crystallization of the amorphous ice and release of its trapped volatile gases.

Gas pressure in the pores peaks at the crystallization front causing gas to flow in part outward to escape, and in part, inward. When each of the species reaches a sufficiently cold region, it recondenses. This recondensation releases heat and affects the heat balance and composition of its surrounding. Thus, a complicated pattern emerges, containing alternating ices mixed with amorphous and crystalline ice. Since the orbital skin depth is at 11 m and the pre-dominant location of the crystallization front is close to the skin depth, it is not surprising to find stratified layers around this depth.

What is interesting from the simulation results is the width of this transition region, at depths of $\sim 10 - 50$ m. The actual locations of the crystallization fronts are also interesting to examine, as they depend on the parameters of the model and the stage of the evolution. This is clearly visible in the panels on the right column of Fig. 5.11.

The middle column of Fig. 5.11 shows the internal porosity, which exhibits several distinct features. First, we can see that at the depths where there is no thermal alteration, the porosity remains almost constant at the initial value of 0.72. Second, it is clear that at the location of the amorphous-to-crystalline transition (where the solid and dashed black lines intersect, in the left column panels) there is a sharp variation of local porosity values, between adjacent layers, related with the change in local ice densities. For Run5/Orb14 there are also sharp variations in the outer layers. However, these are connected with the blocking of pores by dust grains dragged from the interior. This is because, as can be seen in the bottom right panel, there is no ice left at all, from a depth of 1 m outwards. The last prominent feature is the high porosity, in all model variants and at different evolution instances, of the shallow sub-surface layers. From a depth of ~ 30 cm to the surface, porosities increase (albeit not monotonically) to a value of ~ 0.8 – a 10% increase in bulk porosity of the sub-surface layers. This agrees well with the low thermal inertia of this object, $I \leq 30$ J/K/m^2/s$^{1/2}$ (Groussin *et al.*, 2009), indicating that an assumption of a fine thick regolith may not be necessary.

If we now consider the initial parameters of the variant models, as they appear in Table 5.7, and the results presented in Fig. 5.10 and 5.11, we can try and constrain the interior configuration of comet 22P/Kopff. We refer to the following parameters.

- *Density*: A value of 0.3 g/cm^3 is not compatible, making it necessary to take a value that is twice the mean value calculated by Sosa and Fernández (2009). This could indicate that the large scatter in the light curve data used to infer the mass of the comet results in an incompatible fit. Since 22P/Kopff exhibits extended emission features and activity both pre- and post-perihelion, a better understanding of its dust coma is needed in order to de-bias the optical light curve and its relation to the gas production curve.

- *Abundance of volatiles*: These should probably be enhanced in their initial abundances as trapped gases in the amorphous ice, in comparison to the mean abundance in comet nuclei. However, until there is no spectroscopic measurements of the gas coma or tail, even the identity of the volatile species is fiducial.

- *Hertz factor*: Although fits to laboratory data yielded values between 0.1 and 0.001 (Huebner *et al.*, 2006), it seems that Kopff may need a higher value. Since the porosity is high throughout the bulk of the comet, it is probable that the Hertz factor is not actually unity. So, a range between 0.1 and 1 could be constrained for the nucleus.

- *Pore-size distribution*: Since the two orbits of Run4 seem to be the closest fit to the dust behavior, we are inclined to promote a large range of pore radii. This is not strictly supported by the dust-dynamical modeling. However, since the observations were taken at $T + 715$ days, there may be a vast amount and range of smaller dust grains, which have already left by then the image's field of view. Also, an enhanced outgassing activity is needed in order to sustain the prolonged dust emission near-perihelion. This kind of gas flow would be able to entrain within it smaller and smaller dust grains, to be subsequently ejected from the nucleus. These same arguments apply for the exponent of the power-law size distribution. More resolved observations of the the dust coma and tail are needed, in order for the composite images and model fits to be more accurate. We argue that a large range of dust grain sizes and a size distribution slope of $\alpha \approx 2$ should be sufficient for reproducing the dust activity of comet 22P/Kopff.

6 Summary and Conclusions

Our study started with long-term evolutionary simulations of TNOs, including detailed calculations of gas flow through the porous interior and allowing for sublimation and re-condensation on the pore walls. A crucial element that was missing from all previous studies was the consideration of hydrostatic configurations in conjunction with the full calculation of heat and gas flow within a porous medium. Following the evolution of each model for significant durations is important in order to track long-term trends of non-linear effects and their attenuation.

Long-term evolutionary models of TNOs have been calculated in the past by Choi *et al.* (2002), but simplifying assumptions were adopted there for the flow of gas through the porous nucleus that were avoided in this work. The significant result of that work was that highly volatile species – if present in the initial composition – would have been completely depleted in the early stages of evolution. Evolution of TNOs, including limited release and flow of volatiles in the interior, was also studied by De Sanctis *et al.* (2001), but only for a relatively short period of time, less than the decay time of the active short-lived radioactive species. Hence the full-scale effect of radiogenic heating could not be assessed. This study showed that volatiles flowing toward the interior may re-condense and form new ice layers. Shchuko *et al.* (2006) focused on a single TNO, (20000) Varuna, mainly on the relation between the formation scenario and its early thermal evolution. However, this study was much simplified as it did not include volatile species other than water, only applied radioactive heating by the decay of the long-lived species ^{238}U, ^{232}Th and ^{40}K, and did not include the full parametrization of a porous medium.

We found that a wide range of evolutionary outcomes is possible, depending on several properties of the models. The physical characteristics of the objects, mainly sizes and bulk densities, are important factors in the overall evolution, both as reference values and for scaling the various processes. The amount and type of radioactive species, applied as an internal heat source, determine the extent and duration of the internal activity.

Assumptions regarding the constitution of the porous medium affect various thermal and structural parameters (such as conductivity, permeability, etc.), which influence the major physical processes of heat transfer, phase transition and gas flow. To these we must add the assumptions on initial compositions, specifically the abundances of volatile species with and the dust/ice ratio. Considering, for example, the internal configurations of 1992 QB_1 and 1998 WW_{31}, presented in Sec. 3.2.2, which should roughly represent the structure and composition in the interiors of similar sized TNOs (specifically classical KBOs, which are the dynamical group members of these objects), we found that the results depended more on the group of observable parameters (or those that can be directly derived from observations), such as radius, mass/density and composition. Thus, as observations and their related statistics accumulate, models can be further refined and constrained and will enable us to estimate the thermodynamic and mechanical properties of such icy objects more accurately.

Nevertheless, we found that a general trend does emerge regardless of assumptions and uncertain parameters: TNOs with radii larger than $\sim$ 100 km are not pristine objects throughout their bulk. The larger objects may even be depleted of ice altogether in the deep interior. For these objects, some further internal decay of long-lived radionuclides is expected, but this should probably not alter the structure and composition significantly, as most of the interior bulk had been already processed at higher temperatures. In particular, although initial compositions (as we have chosen them - representing early evolution) did not include ices of volatile compounds other than water, the final compositions did, and in non-negligible fractions. The stratification in composition exhibited "pockets" of volatile ices, confined in depth and longevity. These might even be found, under certain conditions, at relative depths that could be accessible to excavation by collisions. No CO ice was found in any of the evolution calculations we followed, although CO was included as trapped gas in the amorphous ice structure. As CO is considered super-volatile, once released from its amorphous ice "casing" it flows rapidly outwards, to low-temperature and low-pressure regions. Since its sublimation temperature is lower than the equilibrium temperature with the environment (Coradini *et al.*, 2008), it does not condense and simply escapes through the porous sub-surface. If any CO is preserved, it will probably only be as trapped gas in the sub-surface amorphous ice layers.

The large TNOs (a few 100 km in size) were found to be considerably affected by self-gravity. Their final structure is stratified not only in composition, but also in its porous structure, with the larger objects (over 1000 km in diameter) experiencing compaction, which reduces bulk porosities in their deep interior to under 10%. Unfortunately, we conclude that although the two equations of state we implemented represnted different hydrostatic properties (i.e., stability regimes and pressure dependence), the subsequent long-term thermal evolution is very similar, given the same initial conditions for the smae specific TNO model.

Objects larger than a few 100 km in radius were also found to maintain appropriate thermodynamic conditions for liquid, or at least "slush" (partially melted), water. These conditions may persist even up to a few 10^6 yr. However, this requires an internal heating mechanism, which is comprised of energetic radioactive decay (i.e. the more potent radionuclides, such as ^{26}Al ^{60}Fe) and efficient heat retention conditions (i.e. large size and low thermal diffusivity, or equivalently, low porosity). This form of liquid phase can be found in the deep interior of large objects, where it may be mixed with the ice phase, as indicated by the large range of saturation values (see Sec. 3.1.7).

Only the outer layers of TNOs remain almost pristine, although they may be slightly enriched in volatile ices, as a result of the re-condensation of outward flux from a sublimating interior. Volatile ices that migrate towards the surface throughout the evolution may be found, at different times, in non-negligible abundances, at depths of 1-5% of the object's radius, compatible with the roughness scale, and they can persist for several 10^6 yr. The depths are only slightly higher than what was found for other dwarf planets (i.e. Ceres, Li *et al.*, 2006), but the formation region of KBOs probably contained more ices than the Main belt. This generally means lower densities and correspondingly higher porosities, at layers near the surface. Thus, deep depression features may easily arise on surfaces of KBOs as the result of impact cratering, exposing water and volatile ice spectral signatures.

The abundance of amorphous ice, and super-volatile species that may be occluded within it, also depends on the physical properties of the object, as they influence its overall evolution. However, what is independent of the individual characteristics is the depletion of amorphous ice from all but the shallow sub-surface layers (a few percent to a few tenths of the radius). For example, at a depth of $\sim 3-4$ km, amorphous ice survives in an object similar to (50000) Quaoar and is the prevalent form of ice, throughout the evolution. This, of course, does not take into account bombardment by energetic particles and impacts of small objects, which can easily mask the composition of the sub-surface layers by altering the top few cm to meters.

In summary, the internal structure resulting from the evolutionary simulations is not uniform, and the composition not homogeneous. However, the stratified structure that emerges, exhibits outer layers that are far less altered by evolution.

On the assumption that Centaurs are thermally-processed objects, derived from a parent population in the Kuiper belt, we thus continued our study by calculating evolution sequences for models of several Centaurs. After a slowly-evolving state was attained for the parent KBOs (see Sec. 3.2), we used the final structure as input for evolutionary calculations of the Centaurs.

Applying the same modeling procedure but for different initial configurations, which represent different scenarios for the origin of Centaur objects and different orbital behavior, it was possible to distinguish between degrees of thermo-chemical processing based on dynamical features and origin. A general common result for the Centaurs simulations is that regardless of the specific thermal behavior during the evolution, a “quiet” configuration, with no further variations of internal properties, was reached throughout most of the object’s volume (mid-layers to the deep interior) on a time scale of a few percent of the dynamical lifetime.

The issue of dynamical lifetimes, and related properties of orbital stability, was examined for a small sample of real Centaur objects. Several of these objects were also the subject of the thermal modeling mentioned above. We found that, although previous studies showed that the intrinsic Centaur population is highly dispersed in orbital configurations, the statistics of large clone samples of specific objects can yield valuable information about their current states and future fates. The comparison of mean orbital elements of different objects, with respect to dynamical lifetimes, can serve to better classify the highly unstable and diffusive orbits in the outer planets region.

By contrast, the surface and sub-surface layers, which may span up to $\sim 10\%$ of the radius in depth, may experience continuous heating, as in the case of 8405 Asbolus. This depends on the perihelion distance and eccentricity, as objects that come closer to the Sun absorb more heat and objects with larger eccentricities experience a greater difference between maximal and minimal ambient temperature at the surface. Composition differences between different Centaurs, as revealed in photometry and spectroscopy of their surfaces, could be the result of relatively recent thermal evolution, rather then a consequence of different initial states. We must keep in mind that in the case of Centaurs the main heat source is absorption of solar energy at the surface rather than radioactive heating of the interior. Therefore, continued evolution in the Centaurs region results in a two-component division of the objects bulk - most of the volume reaches a slowly-evolving state on relatively short evolution time scales for all objects, while the surface and sub-surface layers may exhibit diverse features in composition and structure.

We recall that the bulk is a relic of the outer, largely unprocessed layers of the parent KBOs, which have undergone only moderate (or little) thermal processing during the Centaur phase. Eventually, as a result of further dynamical evolution, Centaurs will become comets. The main heat source will still be solar radiation, but now more intense. As a result, the outer layers that were altered during the Centaur phase, are likely to be eroded sooner or later. This should expose the deeper layers, which we now know to be almost pristine. Their structure and composition is now easier to derive, due to the activity of comets that can be observed and analyzed. This requires close interaction between models and observations. Far more than in the case of KBOs and Centaurs, model predictions can be confronted with observations.

We have thus completed our study by following the evolution of two Jupiter-family comets — 9P/Tempel 1 and 22P/Kopff — with the aim of deriving internal properties by matching the observed and calculated activity patterns, keeping in mind that models are simplified versions of reality. For both calculations we used the evolution code in the quasi-3D mode.

For Comet 9P/Tempel 1, we were able to determine the abundances of volatile species. Refreezing of migrating gases released from the amorphous ice — a process that was amply encountered during the evolution of KBOs and Centaurs as well — resulted in a stratified structure of the subsurface layers in terms of composition. This resulted in a "noisy" activity, ridden by multiple outbursts due to evaporation of volatiles whenever the heat wave propagating inwards from the surface reached a volatile-enriched layer. This behavior is confirmed by the detailed observations of this comet. Interestingly, even at relatively high cometocentric latitudes the nucleus developed a complex pattern of volatile stratification with depth.

For Comet 22P/Kopff, we explored several internal configurations for the nucleus, in order to match its observed unusual dust activity around perihelion. A further constraint from the dust-dynamical modeling was that activity is connected with a localized region on the surface, around latitude and longitude of 50° and 270°, on the southern hemisphere. The outstanding features emerging from the quasi-3D thermal simulation for comet 9P/Tempel 1 are present here as well. We conclude that more volatile materials may be trapped at depths much greater than the diurnal skin depth, which is about 0.01 of the orbital skin depth. When the heat wave from perihelion eventually reaches these layers, activity is triggered and maintained by internal sublimation of volatile ices, even when there is no longer incident solar radiation on the surface.

Thus comets are still capable of revealing primordial properties of icy bodies despite the long and complicated evolution of these bodies, both dynamical and thermal, before reaching the brief phase of intense cometary activity.

Bibliography

A'Hearn, M. F. 2008. Deep Impact and the Origin and Evolution of Cometary Nuclei. *SSRv* **138**, 237–246.

A'Hearn, M. F., M. J. S. Belton, W. A. Delamere, J. Kissel, K. P. Klaasen, L. A. McFadden, K. J. Meech, H. J. Melosh, P. H. Schultz, J. M. Sunshine, P. C. Thomas, J. Veverka, D. K. Yeomans, M. W. Baca, I. Busko, C. J. Crockett, S. M. Collins, M. Desnoyer, C. A. Eberhardy, C. M. Ernst, T. L. Farnham, L. Feaga, O. Groussin, D. Hampton, S. I. Ipatov, J.-Y. Li, D. Lindler, C. M. Lisse, N. Mastrodemos, W. M. Owen, J. E. Richardson, D. D. Wellnitz, and R. L. White 2005. Deep Impact: Excavating Comet Tempel 1. *Science* **310**, 258–264.

Asphaug, E., C. B. Agnor, and Q. Williams 2006. Hit-and-run planetary collisions. *Nature* **439**, 155–160.

Bar-Nun, A., J. Dror, E. Kochavi, and D. Laufer 1987. Amorphous water ice and its ability to trap gases. *Phys. Rev. B* **35**, 2427–2435.

Barucci, M. A., I. N. Belskaya, M. Fulchignoni, and M. Birlan 2005. Taxonomy of Centaurs and Trans-Neptunian Objects. *AJ* **130**, 1291–1298.

Barucci, M. A., A. Doressoundiram, and D. P. Cruikshank 2004. *Surface characteristics of transneptunian objects and centaurs from photometry and spectroscopy*, pp. 647–658. In Comets II, eds. Festou, M. C. and Keller, H. U. and Weaver, H. A., University of Arizona Press.

Belton, M. J. S., K. J. Meech, M. F. A'Hearn, O. Groussin, L. McFadden, C. Lisse, Y. R. Fernández, J. Pittichová, H. Hsieh, J. Kissel, K. Klaasen, P. Lamy, D. Prialnik, J. Sunshine, P. Thomas, and I. Toth 2005. Deep Impact: Working Properties for the Target Nucleus Comet 9P/Tempel 1. *SSRv* **117**, 137–160.

Benz, W., and E. Asphaug 1999. Catastrophic Disruptions Revisited. *Icarus* **142**, 5–20.

Bergin, E. A., Y. Aikawa, G. A. Blake, and E. F. van Dishoeck 2007. *The Chemical Evolution of Protoplanetary Disks*, pp. 751–766. In Protostars and Planets V, eds. Reipurth, B. and Jewitt, D. and Keil, K., University of Arizona Press.

Bernstein, G. M., D. E. Trilling, R. L. Allen, M. E. Brown, M. Holman, and R. Malhotra 2004. The Size Distribution of Trans-Neptunian Bodies. *AJ* **128**, 1364–1390.

Birch, F. 1947. Finite Elastic Strain of Cubic Crystals. *Phys. Rev.* **71**, 809–824.

Bizzarro, M., D. Ulfbeck, A. Trinquier, K. Thrane, J. N. Connelly, and B. S. Meyer 2007. Evidence for a Late Supernova Injection of ^{60}Fe into the Protoplanetary Disk. *Science* **316**, 1178–1181.

Blake, D., L. Allamandola, S. Sandford, D. Hudgins, and F. Freund 1991. Clathrate hydrate formation in amorphous cometary ice analogs in vacuo. *Science* **254**, 548–551.

Blum, J., R. Schräpler, B. J. R. Davidsson, and J. M. Trigo-Rodríguez 2006. The Physics of Protoplanetesimal Dust Agglomerates. I. Mechanical Properties and Relations to Primitive Bodies in the Solar System. *ApJ* **652**, 1768–1781.

Blum, J., and G. Wurm 2008. The Growth Mechanisms of Macroscopic Bodies in Protoplanetary Disks. *ARA&A* **46**, 21–56.

Bockelée-Morvan, D., J. Crovisier, M. J. Mumma, and H. A. Weaver 2004. *The composition of cometary volatiles*, pp. 391–423. In Comets II, eds. Festou, M. C. and Keller, H. U. and Weaver, H. A., University of Arizona Press.

Brown, M. E. 2001. The Inclination Distribution of the Kuiper Belt. *AJ* **121**, 2804–2814.

Brown, M. E. 2008. *The Largest Kuiper Belt Objects*, pp. 335–344. In The Solar System Beyond Neptune, eds. Barucci, M. A. and Boehnhardt, H. and Cruikshank, D. P. and Morbidelli, A., University of Arizona Press.

Brown, M. E., K. M. Barkume, D. Ragozzine, and E. L. Schaller 2007. A collisional family of icy objects in the Kuiper belt. *Nature* **446**, 294–296.

Brown, M. E., E. L. Schaller, H. G. Roe, D. L. Rabinowitz, and C. A. Trujillo 2006. Direct Measurement of the Size of 2003 UB313 from the Hubble Space Telescope. *ApJ Lett.* **643**, L61–L63.

Brown, M. E., and C. A. Trujillo 2004. Direct Measurement of the Size of the Large Kuiper Belt Object (50000) Quaoar. *AJ* **127**, 2413–2417.

Brown, R. H., D. P. Cruikshank, and Y. Pendleton 1999. Water Ice on Kuiper Belt Object 1996 TO_66. *ApJ Lett.* **519**, L101–L104.

Capria, M. T., A. Coradini, M. C. De Sanctis, and R. Orosei 2000. Chiron Activity and Thermal Evolution. *AJ* **119**, 3112–3118.

Chambers, J. E. 1999. A hybrid symplectic integrator that permits close encounters between massive bodies. *MNRAS* **304**, 793–799.

Choi, Y.-J., M. Cohen, R. Merk, and D. Prialnik 2002. Long-Term Evolution of Objects in the Kuiper Belt Zone-Effects of Insolation and Radiogenic Heating. *Icarus* **160**, 300–312.

Cochran, A. L., E. S. Barker, T. F. Ramseyer, and A. D. Storrs 1992. The McDonald Observatory Faint Comet Survey - Gas production in 17 comets. *Icarus* **98**, 151–162.

Cohen, M., D. Prialnik, and M. Podolak 2003. A quasi-3D model for the evolution of shape and temperature distribution of comet nuclei-application to Comet 46P/Wirtanen. *NewA* **8**, 179–189.

Coradini, A., M. T. Capria, M. C. de Sanctis, and W. B. McKinnon 2008. *The Structure of Kuiper Belt Bodies: Link with Comets*, pp. 243–256. In The Solar System Beyond Neptune, eds. Barucci, M. A. and Boehnhardt, H. and Cruikshank, D. P. and Morbidelli, A., University of Arizona Press.

Crifo, J. F., and A. V. Rodionov 1997. The Dependence of the Circumnuclear Coma Structure on the Properties of the Nucleus. *Icarus* **129**, 72–93.

Cruikshank, D. P., T. L. Roush, M. J. Bartholomew, T. R. Geballe, Y. J. Pendleton, S. M. White, J. F. Bell, J. K. Davies, T. C. Owen, C. de Bergh, D. J. Tholen, M. P. Bernstein, R. H. Brown, K. A. Tryka, and C. M. Dalle Ore 1998. The Composition of Centaur 5145 Pholus. *Icarus* **135**, 389–407.

Czechowski, L., and J. Leliwa-Kopystyński 2005. Convection driven by tidal and radiogenic heating in medium size icy satellites. *P&SS* **53**, 749–769.

Davidsson, B. J. R., and Y. V. Skorov 2002. On the Light-Absorbing Surface Layer of Cometary NucleiII. Thermal Modeling. *Icarus* **159**, 239–258.

Davidsson, B. J. R., and Y. V. Skorov 2004. A practical tool for simulating the presence of gas comae in thermophysical modeling of cometary nuclei. *Icarus* **168**, 163–185.

Davies, J. K., T. L. Roush, D. P. Cruikshank, M. J. Bartholomew, T. R. Geballe, T. Owen, and C. de Bergh 1997. The Detection of Water Ice in Comet Hale-Bopp. *Icarus* **127**, 238–245.

Davies, J. K., M. V. Sykes, and D. P. Cruikshank 1993. Near-infrared photometry and spectroscopy of the unusual minor planet 5145 Pholus (1992AD). *Icarus* **102**, 166–169.

Davis, D. R., and P. Farinella 1997. Collisional Evolution of Edgeworth-Kuiper Belt Objects. *Icarus* **125**, 50–60.

De Sanctis, M. C., M. T. Capria, and A. Coradini 2001. Thermal Evolution and Differentiation of Edgeworth-Kuiper Belt Objects. *AJ* **121**, 2792–2799.

Desch, S. J. 2007. Mass Distribution and Planet Formation in the Solar Nebula. *ApJ* **671**, 878–893.

di Sisto, R. P., and A. Brunini 2007. The origin and distribution of the Centaur population. *Icarus* **190**, 224–235.

Dones, L., B. Gladman, H. J. Melosh, W. B. Tonks, H. F. Levison, and M. Duncan 1999. Dynamical Lifetimes and Final Fates of Small Bodies: Orbit Integrations vs Öpik Calculations. *Icarus* **142**, 509–524.

Dones, L., H. F. Levison, and M. Duncan 1996. On the Dynamical Lifetimes of Planet–Crossing Objects. In T. Rettig & J. M. Hahn (Ed.), *Completing the Inventory of the Solar System*, Volume 107 of *Astronomical Society of the Pacific Conference Series*, pp. 233–244.

Dones, L., P. R. Weissman, H. F. Levison, and M. J. Duncan 2004. *Oort cloud formation and dynamics*, pp. 153–174. In Comets II, eds. Festou, M. C. and Keller, H. U. and Weaver, H. A., University of Arizona Press.

Dotto, E., M. A. Barucci, C. Leyrat, J. Romon, C. de Bergh, and J. Licandro 2003. Unveiling the nature of 10199 Chariklo: near-infrared observations and modeling. *Icarus* **164**, 122–126.

Duncan, M., H. Levison, and L. Dones 2004. *Dynamical evolution of ecliptic comets*, pp. 193–204. In Comets II, eds. Festou, M. C. and Keller, H. U. and Weaver, H. A., University of Arizona Press.

Duncan, M., T. Quinn, and S. Tremaine 1988. The origin of short-period comets. *ApJ Lett.* **328**, L69–L73.

Duncan, M. J., and H. F. Levison 1997. A scattered comet disk and the origin of Jupiter family comets. *Science* **276**, 1670–1672.

Durda, D. D., and S. A. Stern 2000. Collision Rates in the Present-Day Kuiper Belt and Centaur Regions: Applications to Surface Activation and Modification on Comets, Kuiper Belt Objects, Centaurs, and Pluto-Charon. *Icarus* **145**, 220–229.

Durham, W. B., W. B. McKinnon, and L. A. Stern 2005. Cold compaction of water ice. *GeoRL* **32**, 18202–18206.

Edgeworth, K. E. 1949. The origin and evolution of the Solar System. *MNRAS* **109**, 600–609.

Fanale, F. P., and J. R. Salvail 1997. The Cometary Activity of Chiron: A Stratigraphic Model. *Icarus* **125**, 397–405.

Farnham, T. L. 1996. PhD Thesis, University of Hawaii.

Fernandez, J. A. 1980. On the existence of a comet belt beyond Neptune. *MNRAS* **192**, 481–491.

Fernández, Y. R., D. C. Jewitt, and S. S. Sheppard 2002. Thermal Properties of Centaurs Asbolus and Chiron. *AJ* **123**, 1050–1055.

Fernández, Y. R., K. J. Meech, C. M. Lisse, M. F. A'Hearn, J. Pittichová, and M. J. S. Belton 2003. The nucleus of Deep Impact target Comet 9P/Tempel 1. *Icarus* **164**, 481–491.

Finson, M., and R. Probstein 1968. A theory of dust comets. 1. Model and equations. *ApJ* **154**, 327–380.

Fulle, M. 1997. Injection of large grains into orbits around comet nuclei. *A&A* **325**, 1237–1248.

Fulle, M., H. Mikuz, and S. Bosio 1997. Dust environment of Comet Hyakutake 1996B2. *A&A* **324**, 1197–1205.

Gallardo, T. 2006. Atlas of the mean motion resonances in the Solar System. *Icarus* **184**, 29–38.

Ghosh, A., and H. Y. McSween 1998. A Thermal Model for the Differentiation of Asteroid 4 Vesta, Based on Radiogenic Heating. *Icarus* **134**, 187–206.

Gladman, B., M. Duncan, and J. Candy 1991. Symplectic integrators for long-term integrations in celestial mechanics. *CeMDA* **52**, 221–240.

Gladman, B., J. J. Kavelaars, J.-M. Petit, A. Morbidelli, M. J. Holman, and T. Loredo 2001. The Structure of the Kuiper Belt: Size Distribution and Radial Extent. *AJ* **122**, 1051–1066.

Gombosi, T. I. 1994. *Gaskinetic Theory.* pp. 311. Cambridge, UK: Cambridge University Press.

Gomes, R. S. 2003. The origin of the Kuiper Belt high-inclination population. *Icarus* **161**, 404–418.

Gomes, R. S., J. A. Fern Ndez, T. Gallardo, and A. Brunini 2008. *The Scattered Disk: Origins, Dynamics, and End States*, pp. 259–273. In The Solar System Beyond Neptune, eds. Barucci, M. A. and Boehnhardt, H. and Cruikshank, D. P. and Morbidelli, A., University of Arizona Press.

Gounelle, M., and A. Meibom 2008. The Origin of Short-lived Radionuclides and the Astrophysical Environment of Solar System Formation. *ApJ* **680**, 781–792.

Greenberg, J. M., H. Mizutani, and T. Yamamoto 1995. A new derivation of the tensile strength of cometary nuclei: Application to comet Shoemaker-Levy 9. *A&A* **295**, L35–L38.

Groussin, O., P. Lamy, and L. Jorda 2004. Properties of the nuclei of Centaurs Chiron and Chariklo. *A&A* **413**, 1163–1175.

Groussin, O., P. Lamy, I. Toth, M. Kelley, Y. Fernandez, M. A'Hearn, H. Campins, J. Licandro, C. Lisse, S. Lowry, K. Meech, and C. Snodgrass 2009. The size and thermal properties of the nucleus of Comet 22P/Kopff. *Icarus* **199**, 568–570.

Hahn, J. M., and R. Malhotra 1999. Orbital Evolution of Planets Embedded in a Planetesimal Disk. *AJ* **117**, 3041–3053.

Hama, J., and K. Suito 1998. Equation of state of MgSiO3 perovskite and its thermoelastic properties under lower mantle conditions. *JGR* **103**, 7443–7462.

Hanner, M. S., and J. P. Bradley 2004. *Composition and mineralogy of cometary dust*, pp. 555–564.

Harker, D. E., D. H. Wooden, C. E. Woodward, and C. M. Lisse 2002. Grain Properties of Comet C/1995 O1 (Hale-Bopp). *ApJ* **580**, 579–597.

Holman, M. J., and J. Wisdom 1993. Dynamical stability in the outer solar system and the delivery of short period comets. *AJ* **105**, 1987–1999.

Holsapple, K., I. Giblin, K. Housen, A. Nakamura, and E. Ryan 2002. *Asteroid Impacts: Laboratory Experiments and Scaling Laws*, pp. 443–462. In Asteroids III, eds. Bottke W. F. and Paolicchi, P. and Binzel, R. P. and Cellino, A., University of Arizona Press.

Horner, J., N. W. Evans, and M. E. Bailey 2004a. Simulations of the population of Centaurs - I. The bulk statistics. *MNRAS* **354**, 798–810.

Horner, J., N. W. Evans, and M. E. Bailey 2004b. Simulations of the population of Centaurs - II. Individual objects. *MNRAS* **355**, 321–329.

Horner, J., N. W. Evans, M. E. Bailey, and D. J. Asher 2003. The populations of comet-like bodies in the Solar system. *MNRAS* **343**, 1057–1066.

Hudson, R. L., M. E. Palumbo, G. Strazzulla, M. H. Moore, J. F. Cooper, and S. J. Sturner 2008. *Laboratory Studies of the Chemistry of Transneptunian Object Surface Materials*, pp. 507–523. In The Solar System Beyond Neptune, eds. Barucci, M. A. and Boehnhardt, H. and Cruikshank, D. P. and Morbidelli, A., University of Arizona Press.

Huebner, W. F., and J. Benkhoff 1999. From Coma Abundances to Nucleus Composition. *SSRv* **90**, 117–130.

Huebner, W. F., J. Benkhoff, M.-T. Capria, A. Coradini, C. de Sanctis, R. Orosei, and D. Prialnik (Eds.) 2006. *Heat and Gas Diffusion in Comet Nuclei*. Published for The

International Space Science Institute, Bern, Switzerland, by ESA Publications Division, Noordwijk, The Netherlands.

Ip, W. 2003. Tidal Breakup of Comets. *CeMDA* **87**, 197–202.

Ishiguro, M., Y. Sarugaku, M. Ueno, N. Miura, F. Usui, M.-Y. Chun, and S. M. Kwon 2007. Dark red debris from three short-period comets: 2P/Encke, 22P/Kopff, and 65P/Gunn. *Icarus* **189**, 169–183.

Ishiguro, M., J. Watanabe, F. Usui, T. Tanigawa, D. Kinoshita, J. Suzuki, R. Nakamura, M. Ueno, and T. Mukai 2002. First Detection of an Optical Dust Trail along the Orbit of 22P/Kopff. *ApJ Lett.* **572**, L117–L120.

Jewitt, D. 2008. *Kuiper Belt and Comets: An Observational Perspective*, pp. 1–78. In Trans-Neptunian Objects and Comets: Saas-Fee Advanced Course 35, Swiss Society for Astrophysics and Astronomy, eds. Altwegg, K. and Benz, W. and Thomas, N., Springer.

Jewitt, D. 2009. The Active Centaurs. *AJ* **137**, 4296–4312.

Jewitt, D., and J. Luu 1993. Discovery of the candidate Kuiper belt object 1992 QB1. *Nature* **362**, 730–732.

Jewitt, D. C. 2004. *From cradle to grave: the rise and demise of the comets*, pp. 659–676. In Comets II, eds. Festou, M. C. and Keller, H. U. and Weaver, H. A., University of Arizona Press.

Jewitt, D. C., and J. Luu 2004. Crystalline water ice on the Kuiper belt object (50000) Quaoar. *Nature* **432**, 731–733.

Jewitt, D. C., and S. S. Sheppard 2002. Physical Properties of Trans-Neptunian Object (20000) Varuna. *AJ* **123**, 2110–2120.

Jockers, K. 1997. Observations Of Scattered Light From Cometary Dust And Their Interpretation. *EM&P* **79**, 221–245.

Kavelaars, J., L. Jones, B. Gladman, J. W. Parker, and J.-M. Petit 2008. *The Orbital and Spatial Distribution of the Kuiper Belt*, pp. 59–69. In The Solar System Beyond Neptune, eds. Barucci, M. A. and Boehnhardt, H. and Cruikshank, D. P. and Morbidelli, A., University of Arizona Press.

Kawakita, H., J.-i. Watanabe, T. Ootsubo, R. Nakamura, T. Fuse, N. Takato, S. Sasaki, and T. Sasaki 2004. Evidence of Icy Grains in Comet C/2002 T7 (LINEAR) at 3.52 AU. *ApJ Lett.* **601**, L191–L194.

Kenyon, S. J. 2002. Planet Formation in the Outer Solar System. *PASP* **114**, 265–283.

Kenyon, S. J., B. C. Bromley, D. P. O'Brien, and D. R. Davis 2008. *Formation and Collisional Evolution of Kuiper Belt Objects*, pp. 293–313. In The Solar System Beyond Neptune, eds. Barucci, M. A. and Boehnhardt, H. and Cruikshank, D. P. and Morbidelli, A., University of Arizona Press.

Kenyon, S. J., and J. X. Luu 1998. Accretion in the Early Kuiper Belt. I. Coagulation and Velocity Evolution. *AJ* **115**, 2136–2160.

Kouchi, A., T. Yamamoto, T. Kozasa, T. Kuroda, and J. M. Greenberg 1994. Conditions for condensation and preservation of amorphous ice and crystallinity of astrophysical ices. *A&A* **290**, 1009–1018.

Kowal, C. T. 1989. A solar system survey. *Icarus* **77**, 118–123.

Kuiper, G. P. 1951. On the Origin of the Solar System. In J. A. Hynek (Ed.), *50th Anniversary of the Yerkes Observatory and Half a Century of Progress in Astrophysics*, pp. 357.

Lacerda, P., and D. C. Jewitt 2007. Densities of Solar System Objects from Their Rotational Light Curves. *AJ* **133**, 1393–1408.

Lacerda, P., and J. Luu 2006. Analysis of the Rotational Properties of Kuiper Belt Objects. *AJ* **131**, 2314–2326.

Lamy, P. L., I. Toth, M. F. A'Hearn, H. A. Weaver, and P. R. Weissman 2001. Hubble Space Telescope Observations of the Nucleus of Comet 9P/Tempel 1. *Icarus* **154**, 337–344.

Lamy, P. L., I. Toth, L. Jorda, O. Groussin, M. F. A'Hearn, and H. A. Weaver 2002. The Nucleus of Comet 22P/Kopff and Its Inner Coma. *Icarus* **156**, 442–455.

Leinhardt, Z. M., S. T. Stewart, and P. H. Schultz 2008. *Physical Effects of Collisions in the Kuiper Belt*, pp. 195–211. In The Solar System Beyond Neptune, eds. Barucci,

M. A. and Boehnhardt, H. and Cruikshank, D. P. and Morbidelli, A., University of Arizona Press.

Leliwa-Kopystyński, J., and K. J. Kossacki 2000. Evolution of porosity in small icy bodies. *P&SS* **48**, 727–745.

Leonard, F. C. 1930. The New Planet Pluto. *Leaflet of the Astronomical Society of the Pacific* **1**, 121.

Levison, H. F., and M. J. Duncan 1994. The long-term dynamical behavior of short-period comets. *Icarus* **108**, 18–36.

Levison, H. F., and M. J. Duncan 1997. From the Kuiper Belt to Jupiter-Family Comets: The Spatial Distribution of Ecliptic Comets. *Icarus* **127**, 13–32.

Levison, H. F., and A. Morbidelli 2003. The formation of the Kuiper belt by the outward transport of bodies during Neptune's migration. *Nature* **426**, 419–421.

Li, J.-Y., L. A. McFadden, J. W. Parker, E. F. Young, S. A. Stern, P. C. Thomas, C. T. Russell, and M. V. Sykes 2006. Photometric analysis of 1 Ceres and surface mapping from HST observations. *Icarus* **182**, 143–160.

Licandro, J., and N. Pinilla-Alonso 2005. The Inhomogeneous Surface of Centaur 32532 Thereus (2001 PT13). *ApJ Lett.* **630**, L93–L96.

Lowry, S. C., and P. R. Weissman 2003. CCD observations of distant comets from Palomar and Steward Observatories. *Icarus* **164**, 492–503.

Luu, J. X., and D. C. Jewitt 2002. Kuiper Belt Objects: Relics from the Accretion Disk of the Sun. *ARA&A* **40**, 63–101.

Lykawka, P. S., and T. Mukai 2005. Long term dynamical evolution and classification of classical TNOs. *EM&P* **97**, 107–126.

Malhotra, R. 1996. The Phase Space Structure Near Neptune Resonances in the Kuiper Belt. *AJ* **111**, 504–516.

McKinnon, W. B. 2002. On the initial thermal evolution of Kuiper Belt objects. In B. Warmbein (Ed.), *Asteroids, Comets, and Meteors: ACM 2002*, Volume 500 of *ESA Special Publication*, pp. 29–38.

McKinnon, W. B., D. Prialnik, S. A. Stern, and A. Coradini 2008. *Structure and Evolution of Kuiper Belt Objects and Dwarf Planets*, pp. 213–241. In The Solar System Beyond Neptune, eds. Barucci, M. A. and Boehnhardt, H. and Cruikshank, D. P. and Morbidelli, A., University of Arizona Press.

Meech, K. J. 2002. The Deep Impact Mission and the AAVSO. *JAAVSO* **31**, 27–33.

Meech, K. J., M. F. A'Hearn, Y. R. Fernández, C. M. Lisse, H. A. Weaver, N. Biver, and L. M. Woodney 2005. The Deep Impact Earth-Based Campaign. *SSRv* **117**, 297–334.

Meech, K. J., and J. Svoren 2004. *Using cometary activity to trace the physical and chemical evolution of cometary nuclei*, pp. 317–335. In Comets II, eds. Festou, M. C. and Keller, H. U. and Weaver, H. A., University of Arizona Press.

Mekler, Y., D. Prialnik, and M. Podolak 1990. Evaporation from a porous cometary nucleus. *ApJ* **356**, 682–686.

Merk, R., and D. Prialnik 2003. Early Thermal and Structural Evolution of Small Bodies in the Trans-Neptunian Zone. *EM&P* **92**, 359–374.

Merlin, F., M. A. Barucci, E. Dotto, C. de Bergh, and G. Lo Curto 2005. Search for surface variations on TNO 47171 and Centaur 32532. *A&A* **444**, 977–982.

Morbidelli, A. 1997. Chaotic Diffusion and the Origin of Comets from the 2/3 Resonance in the Kuiper Belt. *Icarus* **127**, 1–12.

Morbidelli, A. 2002a. *Modern celestial mechanics : aspects of solar system dynamics*. pp. 356. London: Taylor Francis.

Morbidelli, A. 2002b. Modern Integrations of Solar System Dynamics. *Annual Review of Earth and Planetary Sciences* **30**, 89–112.

Morbidelli, A. 2008. *Comets and Their Reservoirs: Current Dynamics and Primordial Evolution*, pp. 79–164.

Morbidelli, A., and M. E. Brown 2004. *The kuiper belt and the primordial evolution of the solar system*, pp. 175–191. In Comets II, eds. Festou, M. C. and Keller, H. U. and Weaver, H. A., University of Arizona Press.

Morbidelli, A., H. F. Levison, and R. Gomes 2008. *The Dynamical Structure of the Kuiper Belt and Its Primordial Origin*, pp. 275–292. In The Solar System Beyond Neptune, eds. Barucci, M. A. and Boehnhardt, H. and Cruikshank, D. P. and Morbidelli, A., University of Arizona Press.

Mostefaoui, S., G. W. Lugmair, and P. Hoppe 2005. ^{60}Fe: A Heat Source for Planetary Differentiation from a Nearby Supernova Explosion. *ApJ* **625**, 271–277.

Murray, C. D., and S. F. Dermott 2000. *Solar System Dynamics.* pp. 606. Cambridge, UK: Cambridge University Press.

Nolan, M. C., E. Asphaug, H. J. Melosh, and R. Greenberg 1996. Impact Craters on Asteroids: Does Gravity or Strength Control Their Size? *Icarus* **124**, 359–371.

Oort, J. H. 1950. The structure of the cloud of comets surrounding the Solar System and a hypothesis concerning its origin. *Bull. Astron. Inst. Neth* **11**, 91–110.

Osip, D. J., D. G. Schleicher, and R. L. Millis 1992. Comets - Groundbased observations of spacecraft mission candidates. *Icarus* **98**, 115–124.

Pan, M., and R. Sari 2005. Shaping the Kuiper belt size distribution by shattering large but strengthless bodies. *Icarus* **173**, 342–348.

Petrenko, J.-P., and R. W. Whitworth 1999. *Physics of Ice.* pp. 373. Oxford, UK: Oxford University Press.

Pinilla-Alonso, N., R. Brunetto, J. Licandro, R. Gil-Hutton, T. L. Roush, and G. Strazzulla 2009. The surface of (136108) Haumea (2003 EL61), the largest carbon-depleted object in the trans-Neptunian belt. *A&A* **496**, 547–556.

Podolak, M., and D. Prialnik 1996. Models of the structure and evolution of comet P/Wirtanen. *P&SS* **44**, 655–664.

Poirier, J.-P. 2000. *Introduction to the Physics of the Earth's Interior*. pp. 326. Cambridge, UK: Cambridge University Press.

Press, W. H., S. A. Teukolsky, W. T. Vetterling, and B. P. Flannery 1992. *Numerical recipes in FORTRAN: The art of scientific computing.* pp. 992. Cambridge, UK: Cambridge University Press.

Prialnik, D. 1992. Crystallization, sublimation, and gas release in the interior of a porous comet nucleus. *ApJ* **388**, 196–202.

Prialnik, D. 2000. *An Introduction to the Theory of Stellar Structure and Evolution.* pp. 320. Cambridge, UK: Cambridge University Press.

Prialnik, D., A. Bar-Nun, and M. Podolak 1987. Radiogenic heating of comets by Al-26 and implications for their time of formation. *ApJ* **319**, 993–1002.

Prialnik, D., J. Benkhoff, and M. Podolak 2004. *Modeling the structure and activity of comet nuclei*, pp. 359–387. In Comets II, eds. Festou, M. C. and Keller, H. U. and Weaver, H. A., University of Arizona Press.

Prialnik, D., N. Brosch, and D. Ianovici 1995. Modelling the activity of 2060 Chiron. *MNRAS* **276**, 1148–1154.

Prialnik, D., and R. Merk 2008. Growth and evolution of small porous icy bodies with an adaptive-grid thermal evolution code. I. Application to Kuiper belt objects and Enceladus. *Icarus* **197**, 211–220.

Prialnik, D., and M. Podolak 1999. Changes in the Structure of Comet Nuclei Due to Radioactive Heating. *SSRv* **90**, 169–178.

Prialnik, D., G. Sarid, E. D. Rosenberg, and R. Merk 2008. Thermal and Chemical Evolution of Comet Nuclei and Kuiper Belt Objects. *SSRv* **138**, 147–164.

Quinn, T., S. Tremaine, and M. Duncan 1990. Planetary perturbations and the origins of short-period comets. *ApJ* **355**, 667–679.

Richardson, J. E., H. J. Melosh, N. A. Artemeiva, and E. Pierazzo 2005. Impact Cratering Theory and Modeling for the Deep Impact Mission: From Mission Planning to Data Analysis. *SSRv* **117**, 241–267.

Sarid, G., D. Prialnik, K. J. Meech, J. Pittichová, and T. L. Farnham 2005. Thermal Evolution and Activity of Comet 9P/Tempel 1 and Simulation of a Deep Impact. *PASP* **117**, 796–809.

Schaller, E. L., and M. E. Brown 2008. Detection of Additional Members of the 2003 EL61 Collisional Family via Near-Infrared Spectroscopy. *ApJ Lett.* **684**, L107–L109.

Schmitt, B., S. Espinasse, R. J. A. Grim, J. M. Greenberg, and J. Klinger 1989. Laboratory studies of cometary ice analogues. In J. J. Hunt and T. D. Guyenne (Eds.), *Physics and Mechanics of Cometary Materials*, Volume 302 of *ESA Special Publication*, pp. 65–69.

Schultz, P. H., C. M. Ernst, and J. L. B. Anderson 2005. Expectations for Crater Size and Photometric Evolution from the Deep Impact Collision. *SSRv* **117**, 207–239.

Scott, E. R. D. 2007. Chondrites and the Protoplanetary Disk. *ARE&PS* **35**, 577–620.

Shchuko, O. B., A. Coradini, R. Orosei, and S. D. Shchuko 2006. Varuna: Thermal evolution. *AdSpR* **38**, 1946–1951.

Sheppard, S. S., D. C. Jewitt, C. A. Trujillo, M. J. I. Brown, and M. C. B. Ashley 2000. A Wide-Field CCD Survey for Centaurs and Kuiper Belt Objects. *AJ* **120**, 2687–2694.

Smoluchowski, R. 1981. Amorphous ice and the behavior of cometary nuclei. *ApJ Lett.* **244**, L31–L34.

Sosa, A., and J. A. Fernández 2009. Cometary masses derived from non-gravitational forces. *MNRAS* **393**, 192–214.

Stansberry, J. A., D. P. Cruikshank, W. G. Grundy, J. L. Margot, J. P. Emery, Y. R. Fernandez, and G. H. Rieke 2005. Albedos, Diameters (and a Density) of Kuiper Belt and Centaur Objects. In *Bulletin of the American Astronomical Society*, Volume 37 of *Bulletin of the American Astronomical Society*, pp. 737.

Stern, S. A. 1995. Collisional Time Scales in the Kuiper Disk and Their Implications. *AJ* **110**, 856–868.

Stern, S. A. 1996. Signatures of collisions in the Kuiper Disk. *A&A* **310**, 999–1010.

Stern, S. A. 2003. The evolution of comets in the Oort cloud and Kuiper belt. *Nature* **424**, 639–642.

Stern, S. A., and J. E. Colwell 1997. Accretion in the Edgeworth-Kuiper Belt: Forming 100-1000 KM Radius Bodies at 30 AU and Beyond. *AJ* **114**, 841–849.

Stern, S. A., and L. M. Trafton 2008. *On the Atmospheres of Objects in the Kuiper Belt*, pp. 365–380. In The Solar System Beyond Neptune, eds. Barucci, M. A. and Boehnhardt, H. and Cruikshank, D. P. and Morbidelli, A., University of Arizona Press.

Tachibana, S., and G. R. Huss 2003. The Initial Abundance of ^{60}Fe in the Solar System. *ApJ Lett.* **588**, L41–L44.

Tegler, S. C., W. Romanishin, G. J. Consolmagno, J. Rall, R. Worhatch, M. Nelson, and S. Weidenschilling 2005. The period of rotation, shape, density, and homogeneous surface color of the Centaur 5145 Pholus. *Icarus* **175**, 390–396.

Tiscareno, M. S., and R. Malhotra 2003. The Dynamics of Known Centaurs. *AJ* **126**, 3122–3131.

Toth, I., and C. M. Lisse 2006. On the rotational breakup of cometary nuclei and centaurs. *Icarus* **181**, 162–177.

Trigo-Rodriguez, J. M., and J. Blum 2009. Tensile strength as an indicator of the degree of primitiveness of undifferentiated bodies. *P&SS* **57**, 243–249.

Trujillo, C. A., and M. E. Brown 2001. The Radial Distribution of the Kuiper Belt. *ApJ Lett.* **554**, L95–L98.

Urey, H. C. 1955. The Cosmic Abundances of Potassium, Uranium, and Thorium and the Heat Balances of the Earth, the Moon, and Mars. *Proc. Nat. Ac. Sci.* **41**, 127–144.

Valencia, D., R. J. O'Connell, and D. Sasselov 2006. Internal structure of massive terrestrial planets. *Icarus* **181**, 545–554.

Valencia, D., D. D. Sasselov, and R. J. O'Connell 2007. Detailed Models of Super-Earths: How Well Can We Infer Bulk Properties? *ApJ* **665**, 1413–1420.

Veillet, C., J. W. Parker, I. Griffin, B. Marsden, A. Doressoundiram, M. Buie, D. J. Tholen, M. Connelley, and M. J. Holman 2002. The binary Kuiper-belt object 1998 WW31. *Nature* **416**, 711–713.

Vinet, P., J. Ferrante, J. H. Rose, and J. R. Smith 1987. Compressibility of solids. *JGR* **92**, 9319–9325.

Wallis, M. K. 1980. Radiogenic melting of primordial comet interiors. *Nature* **284**, 431–433.

Weidenschilling, S. J. 2004. *From icy grains to comets*, pp. 97–104. In Comets II, eds. Festou, M. C. and Keller, H. U. and Weaver, H. A., University of Arizona Press.

Weissman, P. R., E. Asphaug, and S. C. Lowry 2004. *Structure and density of cometary nuclei*, pp. 337–357. In Comets II, eds. Festou, M. C. and Keller, H. U. and Weaver, H. A., University of Arizona Press.

Wisdom, J., and M. Holman 1991. Symplectic maps for the n-body problem. *AJ* **102**, 1528–1538.

Yabushita, S. 1980. On exact solutions of diffusion equation in cometary dynamics. *A&A* **85**, 77–79.

תקציר תזה

הכינוי "גופים קטנים" בלימודי מערכת השמש מתייחס לגופים אסטרונומיים הקטנים מכוכבי לכת, עבורם השמש היא מוקד הכבידה הראשי. מגוון התכונות הדינאמיות של גופים אלו עשוי להיגרם כתוצאה משוני באזורי ההיווצרות המסוימים של כל מחלקה של גופים, או מהשפעות ההתפתחות המסלולית שלהם, בעיקר בשל הפרעות כבידתיות מצד כוכבי הלכת החיצוניים. ישנן מחלקות דינאמיות רבות, אך אלו החולקות סכימת התפתחות מסלולית מקובלת, או שרשרת היווצרות מקובלת הן המחלקות של השביטים, הסנטאורים והגופים הטרנס-נפטוניים.

בעבודה המוצגת כאן עקבנו אחר ההתפתחות התרמו-כימית של הגופים הקטנים המוזכרים לעיל. עשינו זאת על ידי שימוש בקוד נומרי מתוחכם, חד ממדי או "מעין תלת-ממדי", הפותר את משוואות מעבר החום והזרימה עבור גוף נקבובי ורב-רכיבי, עם התחשבות מלאה בתנאי השפה הפנימיים והחיצוניים.

יישמנו קוד התפתחות כללי זה לבחינת מצבם והתפתחותם של מספר כופים טרנס-נפטוניים, המייצגים מדגם מהתכונות הפיזיקאליות האופייניות של אוכלוסיה זו. התוצאות שקיבלנו מצביעות על מגמה כללית של תצורות פנימיות יותר דחוסות, מעובדות חומנית וחסרות בחומרים נדיפים, כאשר גודלו וצפיפותו של העצם גדולים יותר. עם זאת, בשכבות התת-קרקעיות ניתן למצוא הרכב מעורב ומסובך של תרכובות נדיפות. תוצאה מעניינת היא ההיקרות הנפוצה יחסית וברת-הקיימא של תנאים למים נוזליים בעומקם של הגופים הגדולים יותר.

יישום נוסף של הקוד היה למטרת בחינת מצבם והתפתחותם של הסנטאורים. בחלק זה בחנו את ההשפעה שיש לתנאי ההתחלה על ההתפתחות החומנית עבור מסלולים לא-יציבים שונים. למטרה זו, קבענו מספר תרחישים לגבי רצף המקור וקביעת מיקומם של גופים אלו – או כחלקים שנשברו מגופים טרנס-נפטוניים גדולים יותר והתפזרו לכיוון פנים, או כעצמים מקוריים מעבר למסלולו של נפטון שהתקדמו פנימה בניחותא יחסית. תוצאות הסימולציות הללו יכולות לספק תובנה לגבי מצבם הנוכחי של הסנטאורים ותצורותיהם ההתחלתיות של שביטים ממשפחת צדק.

מצבם הדינאמי של מספר סנטאורים מסוימים נבחן גם הוא, על ידי שימוש בסימולציות רבות חלקיקים. מכיוון שעצמים אלו מועדים ביותר לאינטראקציות כבידתיות עם כוכבי הלכת החיצוניים, מסלוליהם כאוטיים ביותר. מכיוון שכך, אפיון היציבות המסלולית מהוו המשימה מאתגרת. אנו מראים מספר תוצאות מייצגות של מאמץ זה וקובעים תוך כדי כך מספר תכונות כלליות של ההתפתחות המסלולית עבור כל עצם שנבדק.

אנו מסיימים בבדיקה מפורטת, על ידי שימוש במודל "מעין תלת-ממדי", של שני מייצגים טיפוסיים של שביטים ממשפחת צדק. במקרה של טמפל 1 (9P/Tempel 1), חקרנו את התפתחותו הפנימית, פעילות חיצונית והשפעות פגיעת גוף חיצוני בו. עבור קופף (22P/Kopff), בדקנו את פעילות האבק ואת הקשר בינה לבין ההתפתחות החומנית הפנימית. תכונה יוצאת-דופן, שהתגלתה מניתוח הסימולציות, היא שאף בקווי רוחב גבוהים, על פני השביט, הגרעין יכול להתפתח למצב מורכב ומסובך של ריבוד בקרח נדיף, כתלות בעומק מפני השפה.

אנו טוענים כי התוצאות המפורטות של מחקר זה לגבי העיבוד החומני, ששינה את תצורותיהם הפנימיות של גופים טרנס-נפטוניים, סנטאורים ושביטים, מספקות תובנה והבנה של ההיסטוריות של פלנטסימלים עשויי קרח ואבק ומצבו הקדום של חומר שביטי.

TEL AVIV UNIVERSITY אוניברסיטת תל-אביב

RAYMOND AND BEVERLY SACKLER
FACULTY OF EXACT SCIENCES
GEOPHYSICS AND PLANETARY SCIENCES

הפקולטה למדעים מדוייקים
ע״ש ריימונד ובברלי סאקלר
המחלקה לגיאופיזיקה ומדעים פלנטאריים

התפתחות חומנית ומבנית
של גופים קטנים במערכת השמש

חיבור לשם קבלת התואר *דוקטור לפילוסופיה*

מאת

גל שריד

עבודה זו נעשתה בהנחייתה של

פרופ' דינה פריאלניק

החוג לגיאופיזיקה ומדעים פלנטאריים

הוגש לסנאט של אוניברסיטת תל-אביב

אוקטובר 2009